Strong Electronic Correlations
in Low-Dimensional Systems

Von der Fakultät für Mathematik, Informatik und Naturwissenschaften der RWTH Aachen University zur Erlangung des akademischen Grades eines Doktors der Naturwissenschaften genehmigte Dissertation

vorgelegt von

Dipl.-Phys. Andreas Dolfen

aus Köln

Berichter:	Univ.-Prof. Dr.rer.nat. Erik Koch
	Univ.-Prof. Eva Pavarini, Ph.D.
Tag der mündlichen Prüfung:	16.09.2010

Diese Dissertation ist auf den Internetseiten der Hochschulbibliothek online verfügbar.

Contents

Introduction

It has always been a dream of physicists to understand and predict properties of materials without resorting to direct experimental measurements. In principle, the fundamental laws describing our world between the nuclear and astronomical scales are well-known. All we need to do is solve the time-dependent many-body Schrödinger equation providing direct access to all properties. Neglecting relativistic effects it takes the form

$$i\frac{\partial}{\partial t}|\Psi\rangle = \mathcal{H}|\Psi\rangle \,,$$

where $|\Psi\rangle$ is the many-body wavefunction and

$$\mathcal{H} = \sum_{\alpha=1}^{N_n} \frac{\boldsymbol{P}_\alpha^2}{2M_\alpha} + \sum_{j=1}^{N_e} \frac{\boldsymbol{p}_j^2}{2m} - \sum_{j=1}^{N_e}\sum_{\alpha=1}^{N_n} \frac{Z_\alpha e^2}{|\boldsymbol{r}_j - \boldsymbol{R}_\alpha|} + \sum_{j<k}^{N_e} \frac{e^2}{|\boldsymbol{r}_j - \boldsymbol{r}_k|} + \sum_{\alpha<\beta}^{N_n} \frac{Z_\alpha Z_\beta e^2}{|\boldsymbol{R}_\alpha - \boldsymbol{R}_\beta|} \,,$$

denotes the many-body Hamiltonian of the system. Z_α is the atomic number, M_α the mass, $\boldsymbol{R}_\alpha$ the position, and $\boldsymbol{P}_\alpha$ the momentum of nucleus α. $\boldsymbol{p}_j$ and $\boldsymbol{r}_j$ denote the jth electron's momentum and position. N_e, N_n are the number of electrons and nuclei, respectively. This equation does not only describe essentially all everyday phenomena but also unusual quantum effects. Striking examples are macroscopic quantum states such as superconductivity, superfluidity, or the entanglement of states that lies at the heart of quantum computing.

Soon after Schrödinger formulated his equation [1], Dirac realized that this "Theory of Almost Everything" comes with a catch [2]:

> The underlying laws necessary for the mathematical theory of a large part of physics and the whole of chemistry are thus completely known, and the difficulty is only that exact applications of these laws lead to equations which are too complicated to be soluble. It therefore becomes desirable that approximate practical methods of applying quantum mechanics should be developed, which can lead to an explanation of the main features of complex atomic systems without too much computation.

The complexity, Dirac refers to, arises from the quantum many-body nature of the problem. As illustration let us consider a simplified iron atom. With its $N_e = 26$ electrons the total electronic wavefunction depends on 26 times 3 coordinates. Choosing a very crude approximation by specifying the wavefunction on a grid with 10 points per coordinate yields 10^{78} numbers to store – let alone process. This huge amount of data cannot even be stored on a hard drive as large as our home galaxy, the milky way.

The most successful, "approximate practical method" of applied quantum mechanics for condensed matter systems is density-functional theory. It works well for many classes of materials, where it is a good approximation to think of each electron as an individual entity, moving in the static mean-field created by the other electrons and atomic nuclei. This is justified, when the electronic structure can be described by well-defined quasiparticles. However, for many materials of scientific as well as technological interest, density-functional theory fails to give even qualitative insights. In these strongly correlated materials the electronic interaction is so strong that the phenomena produced cannot be predicted by studying the electrons individually – instead, we need to describe them collectively.

Strongly correlated systems often show unusual physics: they can be Mott insulators, exhibit heavy-fermion behavior, orbital ordering, or, in one dimension, show spin-charge separation (e.g. in TTF-TCNQ). Effects such as the colossal magnetoresistance in manganites for spintronics or high-T_c superconductivity in cuprates are hot topics and highly interesting for real-world applications.

A characteristic quantity for strongly correlated systems is the ratio of the local Coulomb interaction, the Hubbard-U, and the bandwidth W. While it is small for ordinary materials, the ratio is about or even greater than 1 for systems with strong correlations. Typical representatives have partially filled d- or f-electron bands, where the large ratio stems from the strong localization and thus large Coulomb repulsion in these orbitals. A second class of strongly correlated materials are molecular crystals. Here, the relevant orbitals are quite extended so that the corresponding Us are small. However, the bandwidth originating from a very small overlap of the molecules is even smaller.

The electronic structure of strongly correlated materials is often studied with angular-resolved photo-emission spectroscopy (ARPES) and neutron-scattering experiments. In general, these materials are very sensitive to external perturbations. Theoretically, ARPES and neutron-scattering results are closely related to the spectral functions and spin susceptibilities. A direct calculation of these functions poses, however, a hard problem. Since the single-particle picture breaks down and related techniques are not applicable, we have to deal with a full non-perturbative many-body problem. Even with the latest generation of supercomputers only the simplest model-Hamiltonians can be solved. Therefore, we have to make every effort to capture the most relevant physics in these simple models.

Obviously, the models have to be constructed in such a way that only the relevant degrees of freedom are taken into account. Even though a systematic down-folding approach exists, in practice the basic models are usually derived from intuition.

The prime and simplest model to treat strongly correlated systems is the Hubbard model. It describes itinerant electrons in a single tight-binding band and their mutual

local Coulomb repulsion in an orbital. A slightly generalized Hamiltonian which also contains the next-neighbor interaction is

$$H = -\sum_{\sigma,ij} t_{ij} c_{i,\sigma}^\dagger c_{j,\sigma} + U \sum_i n_{i\uparrow} n_{i\downarrow} + V \sum_{\langle i,j \rangle} n_i n_j \ ,$$

where t_{ij} denotes the tight-binding hopping matrix, U the local, and V the next-neighbor interaction. The simplest model applicable to heavy-fermion systems is the periodic Anderson model. It describes localized and correlated impurities (f-orbitals) coupled to a band of non-interacting, conduction electrons via a small hybridization V:

$$H_{\mathrm{PAM}} = \sum_{\boldsymbol{k}\sigma} \varepsilon_{\boldsymbol{k}\sigma} a_{\boldsymbol{k}\sigma}^\dagger a_{\boldsymbol{k}\sigma} + V \sum_{l\sigma} \left(f_{l\sigma}^\dagger c_{l\sigma} + c_{l\sigma}^\dagger f_{l\sigma} \right) + \epsilon_f \sum_{l\sigma} f_{l\sigma}^\dagger f_{l\sigma} + U \sum_l n_{l\uparrow}^f n_{l\downarrow}^f \ .$$

One of the most successful techniques to actually solve these models is dynamical mean-field theory, where the lattice Hamiltonian is self-consistently mapped onto an artificial single-impurity Anderson model. Among the many different DMFT-impurity solvers such as different flavors of quantum Monte Carlo we use exact diagonalization. The solution gives direct access to the impurity- as well as the lattice spectral function, where the latter contains a local approximation to the correct self-energy Σ. Formally, the spectral functions are the imaginary parts of the corresponding single-particle (2-point) Green's functions. Local susceptibilities are also readily obtained from this method.

The evaluation of general *lattice* susceptibilities like the aforementioned spin-spin correlation function proves, however, difficult. The problem lies not only in its many-body nature but also in the complexity of one of the ingredients – the vertex function. As we will see in chapter 3 it is built from two-particle Green's functions being expectation values of four field-operators, evaluated at, in general, four different times. Their evaluation is challenging due to the computational complexity of the quantity itself and the amount of data needed to obtain reliable results. Even working with relatively small baths in the Anderson impurity model, we need supercomputers for actual calculations.

Having the two-particle Green's function and particle-hole bubbles originating from the local and lattice Green's function we can employ a Dyson-like equation to obtain arbitrary lattice susceptibilities, enabling us to study the exotic correlation effects in these strongly correlated materials.

As input for realistic calculations we need model parameters. Traditionally, they have been guessed, estimated by comparison with experiment, or semi-empirically determined. This approach is, obviously, unsatisfactory. Still, for general materials these procedures are "state-of-the-art", as no feasible other way is known. For organic crystals, however, we devise an approach to systematically evaluate realistic, material-specific model parameters. It will be covered in chapter 2. In a nutshell: Taking the positions and orientations of the molecules from X-ray experiments we construct a new crystal from DFT-relaxed molecules. For dimers within this crystal we obtain the hopping matrix elements from the bonding/anti-bonding splitting of the relevant molecular orbitals. The Coulomb parameters are harder to determine. If we treated all electrons in the Hubbard model, we would need to use the bare Coulomb integrals. However, the neglect of all but the

relevant electrons leads to a renormalization of the parameters. In a two-step process we first use DFT to obtain the screening due to the electrons inside the molecules, giving the intra-molecularly screened Coulomb parameter U_0 and V_0.

To obtain the screening contribution ΔU and ΔV of all the other molecules in the system we proceed with a classical electrostatic approach, where we represent the molecules by polarizable point dipoles. Building a cluster of N unit cells containing these dipole molecules we extract the energetic response to an additional charge on one or two molecules. Extrapolating to infinitely large N we obtain the screening contributions ΔU and ΔV. This approach is developed in chapter 1.

Finally, we apply this procedure to two compounds, TTF-TCNQ and $(BEDT-TTF)_2I_3$ and obtain the parameters for a realistic description in terms of an extended Hubbard model. We find relatively small hopping matrix elements in comparison to the effectively strongly-screened Coulomb integrals – a situation typical of organic crystals.

For $(BEDT-TTF)_2I_3$ we observe a strong dependence of the characteristic ratio U/W on the molecular orientations in the crystal, suggesting experiments for pressure exerted on the sample. The realistic parameters for TTF-TCNQ help to resolve a long-standing problem in the interpretation of the experimental data and demonstrating the importance of longer-range Coulomb interactions in organic crystals.

Electrostatic Screening in Dielectrics

Inside a material an external electric potential $V(\boldsymbol{r}, \omega)$ is shielded by the mobile charges of the system. This screening leads to a change, usually a reduction, of the external potential, which in linear response can be described in terms of a new effective potential $V^{\text{eff}}(\boldsymbol{r}, \omega)$.

In chapter 2 we will study organic crystals which belong to the group of non-polar dielectrics. The basic building blocks of these systems are molecules or atoms that are only weakly bound. Hence, we can unambiguously assign a charge density to each lattice site. In systems where the hybridization is too strong we would have to resort to the modern theory of polarization based on the Berry phase (e.g. refer to Resta [3]).

Usually the molecules forming an organic crystal do not carry permanent dipole moments, e.g. due to their spatial symmetry. Therefore, we can describe the screening by considering the molecules as sets of polarizable point dipoles. With these new building blocks we rebuild the crystal giving a microscopic point dipole model (MPDM). Within this model we can then derive effective parameters for organic crystals.

This chapter introduces and discusses the MPDM and its solutions for several dimensions. It is structured in four sections. We start with an introduction to the general theory. The following two sections describe low-dimensional systems embedded in three-dimensional space. Three-dimensional systems are covered in the final section of this chapter.

1.1. Introduction

Given a general charge distribution $\varrho(\boldsymbol{x})$ we define its electrostatic potential $\Phi(\boldsymbol{x})$ as

$$\Phi(\boldsymbol{x}) = \int_{\mathbb{R}^3} \mathrm{d}^3 x' \, \frac{\varrho(\boldsymbol{x}')}{|\boldsymbol{x} - \boldsymbol{x}'|} \ . \tag{1.1}$$

For a localized charge density $\varrho(\boldsymbol{x})$, such as a molecule in an organic crystal, it is possible to construct a sphere of radius R enclosing all charges (electrons and nuclei) around its center. Outside this sphere we can expand

$$\frac{1}{|\boldsymbol{x} - \boldsymbol{x}'|} = \sum_{n=0}^{\infty} \frac{1}{n!} \left(-\boldsymbol{x}' \cdot \boldsymbol{\nabla}\right)^n \frac{1}{|x|} = \frac{1}{|\boldsymbol{x}|} - \boldsymbol{x}' \cdot \boldsymbol{\nabla} \frac{1}{|\boldsymbol{x}|} + \cdots \tag{1.2}$$

yielding

$$\Phi(\boldsymbol{x}) = \frac{q}{|\boldsymbol{x}|} + \frac{\boldsymbol{p} \cdot \boldsymbol{x}}{|\boldsymbol{x}|^3} + \frac{1}{2} \sum_{ij} Q_{ij} \frac{x_i x_j}{|\boldsymbol{x}|^5} + \cdots \ , \tag{1.3}$$

where q denotes the total charge

$$q = \int \mathrm{d}^3 x' \, \varrho(\boldsymbol{x}') \ , \tag{1.4}$$

$\boldsymbol{p}$, the electric dipole moment

$$\boldsymbol{p} = \int \mathrm{d}^3 x' \, \boldsymbol{x}' \varrho(\boldsymbol{x}') \ , \tag{1.5}$$

and, Q_{ij}, the quadrupole moment tensor

$$Q_{ij} = \int \mathrm{d}^3 x' \ (3x'_i x'_j - |\boldsymbol{x}'|^2 \delta_{ij}) \varrho(\boldsymbol{x}') \ . \tag{1.6}$$

The electrostatic energy of this localized charge distribution within an external potential $\Phi^{\mathrm{ext}}(\boldsymbol{x})$ is given by

$$W = \int \mathrm{d}^3 x \ \varrho(\boldsymbol{x})\Phi^{\mathrm{ext}}(\boldsymbol{x}) \ . \tag{1.7}$$

Using expansion (1.3) we obtain

$$W = q\Phi^{\mathrm{ext}}(\boldsymbol{0}) - \boldsymbol{p}\cdot\boldsymbol{E}^{\mathrm{ext}}(\boldsymbol{0}) - \frac{1}{2}\sum_{ij} Q_{ij}\frac{\partial E_j^{\mathrm{ext}}(\boldsymbol{0})}{\partial x_i} + \cdots \ , \tag{1.8}$$

where the electric field $\boldsymbol{E}^{\mathrm{ext}}(\boldsymbol{x})$ is

$$\boldsymbol{E}^{\mathrm{ext}}(\boldsymbol{x}) = -\boldsymbol{\nabla}\Phi^{\mathrm{ext}}(\boldsymbol{x}) \ . \tag{1.9}$$

Usually the external potentials vary rather slowly. Contributions of order higher than the dipole term can be neglected since the quadrupole and higher tensors are small and decay fast. Hence, we neglect all but the first two terms in the microscopic point-dipole model.

From equations (1.9) and (1.3) we obtain the electric field of a point charge at the origin

$$\boldsymbol{E}^{\mathrm{pc}}(\boldsymbol{x}) = \frac{q\boldsymbol{n}}{|\boldsymbol{x}|^2} \ , \tag{1.10}$$

and that of a dipole at the origin

$$\boldsymbol{E}^{\mathrm{dip}}(\boldsymbol{p}, \boldsymbol{x}) = \frac{3\boldsymbol{n}(\boldsymbol{p}\cdot\boldsymbol{n}) - \boldsymbol{p}}{|\boldsymbol{x}|^3} \ , \tag{1.11}$$

where $\boldsymbol{n} = \boldsymbol{x}/|\boldsymbol{x}|$.

1.1.1. Microscopic Point-Dipole Model

If an atom or molecule is exposed to an external electric field, it responds by rearranging the electrons with respect to the nuclei in such way that the resulting field depolarizes, i.e. weakens, the original external field. As a first approximation we regard the molecule as a set of polarizable point dipoles defining the microscopic point-dipole model (MPDM).

In linear response the polarization of a single dipole costs an energy of $\boldsymbol{p}^2/2\alpha$, where α denotes its polarizability. Obviously the higher the polarizability the larger the response. According to equation (1.8) the energy of a dipole placed inside an external electric field is $-\boldsymbol{p} \cdot \boldsymbol{E}^{\text{ext}}$.
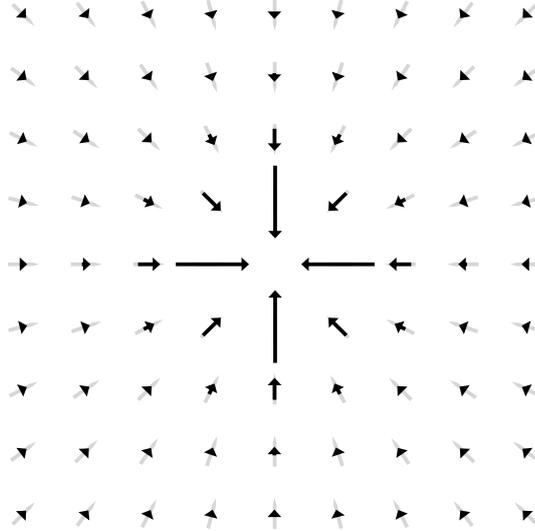
Figure 1.1.: Dipole arrangement in the x-y-plane induced by a negative point charge in the center of a three-dimensional cubic crystal of atoms regarded as polarizable point dipoles ($\alpha \approx 0.076$).

Describing the full crystal within the MPDM we have at least a single point dipole per lattice site (see figure 1.1). Let $\boldsymbol{R}_i$ be the position of site i, $\boldsymbol{p}_i$ and α_i the corresponding dipoles and their polarizabilities. The energy of a dipole in the lattice not only depends on the external field but also on the field of all other dipoles in the system, $-\boldsymbol{p}_i \cdot \boldsymbol{E}_i^{\text{local}}$. Using the dipole fields (1.11), we obtain for the microscopic local field at lattice site i

$$\boldsymbol{E}_i^{\text{local}} = \boldsymbol{E}_i^{\text{ext}} + \sum_{j, j \neq i} \boldsymbol{E}^{\text{dip}} \left(\boldsymbol{p}_j, \boldsymbol{R}_i - \boldsymbol{R}_j \right) \ . \tag{1.12}$$

Consequently, the change in energy due to fixed dipoles $\boldsymbol{p}$ and an external electric field $\boldsymbol{E}^{\text{ext}}$ is

$$\Delta W = \sum_i \left(\frac{\boldsymbol{p}_i^2}{2\alpha_i} - \boldsymbol{p}_i \cdot \left(\frac{1}{2} \sum_{j, j \neq i} \boldsymbol{E}^{\text{dip}} \left(\boldsymbol{p}_j, \boldsymbol{R}_i - \boldsymbol{R}_j \right) + \boldsymbol{E}_i^{\text{ext}} \right) \right) \ , \tag{1.13}$$

external field $\mathbf{E}_i^{\text{ext}} = \dfrac{q\mathbf{n}}{|\mathbf{R}_i - \mathbf{R}_0|^2}$

initialize $\mathbf{E}_i^{\text{micro}} = \mathbf{E}_i^{\text{ext}}$

induced dipoles $\mathbf{p}_i = \boldsymbol{\alpha}_i \mathbf{E}_i^{\text{micro}}$

total field $\mathbf{E}_i^{\text{micro}} = \mathbf{E}_i^{\text{ext}} + \sum_{j \neq i} \dfrac{3\mathbf{n}(\mathbf{p}_j \cdot \mathbf{n}) - \mathbf{p}_j}{|\mathbf{R}_i - \mathbf{R}_j|^3}$

$\Delta U = \dfrac{1}{2} \sum \mathbf{p}_i^T \boldsymbol{\alpha}_i^{-1} \mathbf{p}_i - \sum \mathbf{p}_i \mathbf{E}_i^{\text{micro}}$
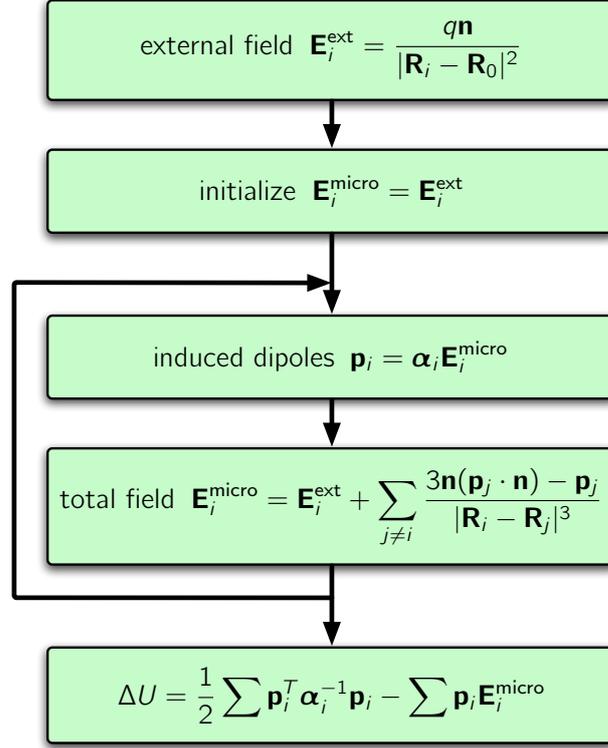
Figure 1.2.: Scheme to obtain the self-consistent solution for the screening problem.

where the dipole-dipole energy term has been reduced by a factor of 2 to avoid double counting.

Allowing the dipoles $\boldsymbol{p}_i$ to change to minimize their energy, the variational principle yields the actual dipole arrangement

$$\boldsymbol{p}_i = \alpha_i \boldsymbol{E}_i^{\text{local}} = \alpha_i \left(\boldsymbol{E}_i^{\text{ext}} + \sum_{j,j\neq i} \boldsymbol{E}^{\text{dip}} \left(\boldsymbol{p}_j, \boldsymbol{R}_j - \boldsymbol{R}_j \right) \right) . \tag{1.14}$$

Obviously, changing dipole i alters the local field for all the others. That in turn influences the local field at site i and therefore $\boldsymbol{p}_i$. To obtain a solution, the coupled system of equations (1.14) has to be solved self-consistently. For a real-space based MPDM code figure 1.2 shows a scheme to do so.

1.1.2. Vector-Space Notation

It is practical to reformulate the problem in a vector notation to use the methods of linear algebra. We define the dipole-dipole matrix $\Gamma_{i\mu,j\nu}$ which relates the Cartesian component

$\mu = x, y, z$ of the induced electric field at site i to the dipole component ν at site j

$$\Gamma_{i\mu,j\nu} = \frac{3R_{ij\mu}R_{ij\nu} - \delta_{\mu\nu}R_{ij}^2}{R_{ij}^5} \quad, \quad i \neq j \ , \tag{1.15}$$

where $\boldsymbol{R}_{ij} = \boldsymbol{R}_i - \boldsymbol{R}_j$. Using $\Gamma_{i\mu,j\nu}$ we can write the field caused by the induced dipoles as

$$|\boldsymbol{E}^{\mathrm{ind}}\rangle = \Gamma|\boldsymbol{p}\rangle \ , \tag{1.16}$$

where $|\boldsymbol{p}\rangle$ is

$$|\boldsymbol{p}\rangle = \begin{pmatrix} p_{1x} \\ p_{1y} \\ p_{1z} \\ p_{2x} \\ \vdots \end{pmatrix} \ , \tag{1.17}$$

and likewise for the electric field. This Dirac-like notation, introduced by Allen [4, 5], goes back to Luttinger and Tisca [6]. Following this notation the general change in energy due to the induced dipoles (1.13) reads

$$\Delta W = \frac{1}{2}\Big\langle \boldsymbol{p}\Big|\alpha^{-1} - \Gamma\Big|\boldsymbol{p}\Big\rangle - \langle\boldsymbol{p}|\boldsymbol{E}^{\mathrm{ext}}\rangle \ . \tag{1.18}$$

As self-consistent solution (1.14) we get the dipole arrangement

$$|\boldsymbol{p}\rangle = \left(\alpha^{-1} - \Gamma\right)^{-1}|\boldsymbol{E}^{\mathrm{ext}}\rangle \ , \tag{1.19}$$

which leads to an energy reduction

$$\Delta W_0 = -\frac{1}{2}\Big\langle \boldsymbol{E}^{\mathrm{ext}}\Big| \left(\alpha^{-1} - \Gamma\right)^{-1} \Big|\boldsymbol{E}^{\mathrm{ext}}\Big\rangle \ . \tag{1.20}$$

1.1.3. Obtaining the Screening Energy for Coulomb Parameters

To obtain Coulomb parameters we place point charges into the lattice of polarizable dipoles and calculate the energy correction (1.20) due to the newly induced dipoles. As an ingredient we need the energetic response Δu of the crystal to a *single* charge. It gives rise to the field $\boldsymbol{E}^{\mathrm{ext}}(\boldsymbol{R}) = \boldsymbol{E}^{\mathrm{pc}}(\boldsymbol{R})$, where $\boldsymbol{E}^{\mathrm{pc}}(\boldsymbol{R})$ is given by equation (1.10). According to (1.20) we obtain the energy correction $\Delta u = \Delta W_0^{\mathrm{1pc}}$.

From this we can readily obtain the screening contribution for the local Hubbard-U. It is the response of the crystal to *two* charges on the same site $\Delta W_0^{\mathrm{2pc}}$, corrected for the energy of two isolated additional charges, i.e. $\Delta U = \Delta W_0^{\mathrm{2pc}} - 2\Delta u$. Since the charge enters the correction (1.20) quadratically, we find $\Delta U = 2\Delta u$.

For the inter-site Coulomb parameters $V_{\boldsymbol{l}}$ we place two equal charges q into the crystal: one at site i and the other at site j such that $\boldsymbol{R}_i - \boldsymbol{R}_j = \boldsymbol{l}$. The resulting electric field is $\boldsymbol{E}^{\mathrm{ext}}(\boldsymbol{R}) = \boldsymbol{E}^{\mathrm{pc}}(\boldsymbol{R} - \boldsymbol{R}_i) + \boldsymbol{E}^{\mathrm{pc}}(\boldsymbol{R} - \boldsymbol{R}_j)$. Due to the linearity of equation (1.19) the superposition principle for the point charges holds for the dipoles, as well. Therefore,

we decompose the dipoles into a component $|\boldsymbol{p}^{(i)}\rangle$ induced by the charge at site i and likewise for j:

$$|\boldsymbol{p}\rangle = |\boldsymbol{p}^{(i)}\rangle + |\boldsymbol{p}^{(j)}\rangle \,. \tag{1.21}$$

Without dipoles in the system the external field is unscreened, i.e. $V_{\boldsymbol{l}}^0 = q^2/|\boldsymbol{l}|$. Within a lattice of dipoles the energy reduction (1.20) due to polarization is

$$
\begin{aligned}
\Delta W_{0,\boldsymbol{l}} = \ & - \left\langle \boldsymbol{E}_i \middle| \left(\alpha^{-1} - \Gamma\right)^{-1} \middle| \boldsymbol{E}_i \right\rangle/2 - \left\langle \boldsymbol{E}_j \middle| \left(\alpha^{-1} - \Gamma\right)^{-1} \middle| \boldsymbol{E}_j \right\rangle/2 \\
& - \left\langle \boldsymbol{E}_i \middle| \left(\alpha^{-1} - \Gamma\right)^{-1} \middle| \boldsymbol{E}_j \right\rangle/2 - \left\langle \boldsymbol{E}_j \middle| \left(\alpha^{-1} - \Gamma\right)^{-1} \middle| \boldsymbol{E}_i \right\rangle/2 \,,
\end{aligned} \tag{1.22}
$$

where $|\boldsymbol{E}_i\rangle$ denotes the electric field caused by the point charge at site i. Evidently, the first two terms yield the on-site Coulomb correction ΔU, which is not to be included in $\Delta V_{\boldsymbol{l}}$. Thus,

$$
\begin{aligned}
\Delta V_{\boldsymbol{l}} \ &= \ \Delta W_{0,\boldsymbol{l}} - 2\Delta u \tag{1.23} \\
&= \ -\left\langle \boldsymbol{E}_i \middle| \left(\alpha^{-1} - \Gamma\right)^{-1} \middle| \boldsymbol{E}_j \right\rangle/2 - \left\langle \boldsymbol{E}_j \middle| \left(\alpha^{-1} - \Gamma\right)^{-1} \middle| \boldsymbol{E}_i \right\rangle/2 \tag{1.24} \\
&= \ -\left\langle \boldsymbol{E}_0 \middle| \left(\alpha^{-1} - \Gamma\right)^{-1} \middle| \boldsymbol{E}_{\boldsymbol{l}} \right\rangle \,. \tag{1.25}
\end{aligned}
$$

In the final step we make i the origin of the system and exploit that the two summands are equal due to symmetry. For $i = j$, i.e. $\boldsymbol{l} = \boldsymbol{0}$, the correction to the Coulomb integral (1.25) obviously gives $\Delta V_{\boldsymbol{0}} = 2\Delta u = \Delta U$.

1.1.4. Ferroelectric Catastrophe and Reciprocal Space

Together with the polarizability, the dipole-dipole matrix Γ determines the physics of the system. It is practical to expand Γ in its spectral representation

$$\Gamma = \sum_\gamma \gamma \, |\gamma\rangle\langle\gamma| \,, \tag{1.26}$$

where γ denotes its eigenvalues and $|\gamma\rangle$ its eigenvectors. With this we can rewrite the dipole equation (1.19) for site i. In the presence of an external field it is

$$\boldsymbol{p}_i = \langle i|\boldsymbol{p}\rangle = \sum_\gamma \left(\alpha^{-1} - \gamma\right)^{-1} \langle i|\gamma\rangle\langle\gamma|\boldsymbol{E}^{\text{ext}}\rangle \,. \tag{1.27}$$

The energy reduction due to screening can be cast as

$$\Delta W_0 = -\frac{1}{2} \sum_\gamma \langle \mathbf{E}^{\text{ext}}|\gamma\rangle\langle\gamma|\mathbf{E}^{\text{ext}}\rangle \left(\alpha^{-1} - \gamma\right)^{-1} \,. \tag{1.28}$$

In ordinary dielectrics the polarizability is small enough that $\alpha^{-1} > \gamma_{\text{max}}$ holds, where γ_{max} is the largest eigenvalue of Γ. However, for $\alpha^{-1} = \gamma_{\text{max}}$ the dipoles and the energy reduction (1.28) diverge if the external field has a component parallel to $|\gamma_{\text{max}}\rangle$. Thus, the system becomes instable. This is a manifestation of the ferroelectric instability.

Ferroelectric instability Equation (1.18) gives the energy correction for an arbitrary arrangement of dipoles. In the absence of an external field it collapses to the quadratic form

$$\Delta W = \frac{1}{2}\left\langle \boldsymbol{p}\left|\alpha^{-1} - \Gamma\right|\boldsymbol{p}\right\rangle . \tag{1.29}$$

Usually $(\alpha^{-1} - \Gamma)$ is positive definite. Therefore, minimization leads to the trivial solution: $\Delta W_0 = 0$ with $|p_0\rangle = 0$, i.e. an entirely unpolarized system with no non-vanishing dipoles and reduction in energy. However, for $\alpha^{-1} = \gamma_{\max}$ the matrix $(\alpha^{-1} - \Gamma)$ becomes positive semi-definite and consequently, there is no unique solution. For even larger polarizabilities the system is not stable. $|p\rangle = 0$ becomes an instable fixed point and the energy correction diverges $\Delta W_0 \to -\infty$. At this ferroelectric instability the system is polarized spontaneously with the dipole pattern determined by the eigenvector $|\gamma_{\max}\rangle$ to $\gamma_{\max}$. This behavior can be found in infinite solids as well as finite clusters.

Reciprocal Space In infinite periodic crystals we can exploit translation symmetry. Γ can be thought of as a tight-binding Hamiltonian in elementary condensed matter physics. In that picture the hopping takes the role of the dipole-dipole interaction which, in contrast to usual hopping, is long range.

The eigenstates of Γ are Bloch-like waves,

$$\langle j\mu|\gamma\rangle = \langle j\mu|\boldsymbol{k}n\rangle = \frac{1}{\sqrt{N}}\exp\left(i\boldsymbol{k}\boldsymbol{R}_j\right)\varepsilon_\mu\left(\boldsymbol{k}n\right) , \tag{1.30}$$

where j is the site, $\mu = x, y, z$ the coordinate component, and n the band index. $\varepsilon_\mu\left(\boldsymbol{k}n\right)$ denotes the polarization vector which solves

$$\Gamma_{\mu\nu}(\mathbf{k})\varepsilon_\nu(\mathbf{k}n) = \gamma(\mathbf{k}n)\varepsilon_\mu(\mathbf{k}n), \tag{1.31}$$

where $\Gamma_{\mu\nu}(\boldsymbol{k})$ is the 3×3 dipole-dipole matrix (for one atom per unit cell) in Fourier space

$$\Gamma_{\mu\nu}(\mathbf{k}) = \frac{1}{N}\sum_{j\neq i}e^{-i\mathbf{k}\cdot\mathbf{r}_{ij}}\left(\nabla_\mu\nabla_\nu\frac{1}{R_{ij}}\right) = \frac{1}{N}\sum_{j\neq i}\exp\left(-i\mathbf{k}\cdot\mathbf{r}_{ij}\right)\frac{(3r_{ij}^\mu r_{ij}^\nu - r_{ij}^2\delta_{\mu\nu})}{r_{ij}^5}. \tag{1.32}$$

$\Gamma_{\mu\nu}(\mathbf{k})$ is a tracefree matrix, i.e. $\mathrm{Tr}\left(\Gamma_{\mu\nu}(\mathbf{k})\right) = 0$. This follows directly from (1.32) since $\sum_\mu \nabla_\mu^2 = \Delta$ and $\Delta 1/R_{ij}$ is only non-vanishing for $i = j$. These terms are, however, omitted in the summation.

A direct evaluation of the sum (1.32) converges very slowly. For numerical calculations we therefore resort to the Ewald method [7]. It decomposes the summation into two parts: a sum over the short-range interaction terms in real space and the longer-range terms in reciprocal space. This leads to an overall fast convergence (cf. [8] and appendix A).

Once we have the complete eigensystem we can directly obtain the self-consistent dipoles for arbitrary external fields according to equation (1.27)

$$|\mathbf{p}\rangle = \sum_{\mathbf{k}n}\frac{1}{\alpha^{-1} - \gamma(\mathbf{k}n)}|\mathbf{k}n\rangle\langle\mathbf{k}n|\mathbf{E}^{\mathrm{ext}}\rangle , \tag{1.33}$$
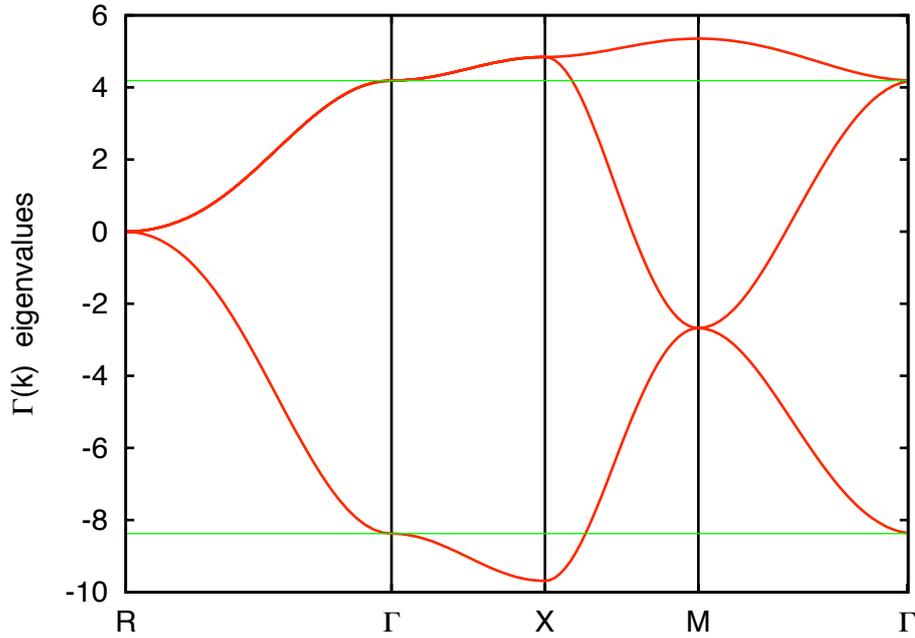
Figure 1.3.: The eigenvalue $\gamma_{\boldsymbol{k}}$ of the dipole-dipole interaction matrix Γ as a function of $\boldsymbol{k}$ for a simple cubic lattice of polarizable point dipoles. The largest eigenvalue is at the M-point $(\pi, \pi, 0)$. $\gamma_{\mathrm{CM}} = 4\pi/3$ is determined by the CM relation (largest eigenvalue at the Γ-point) and indicated by the upper green line. Since it is doubly occupied and $\mathrm{Tr}\left(\Gamma_{\mu\nu}(\mathbf{k})\right) = 0$ the lowest eigenvalue at the Γ-point is $-8\pi/3$ (lower green line). For the definition of the high-symmetry points see for instance [11, page 693].

and the corresponding energy reduction

$$\Delta W_0 = -\frac{1}{2} \sum_{\mathbf{k}n} \frac{\langle \mathbf{E}^{\mathrm{ext}} | \mathbf{k}n \rangle \langle \mathbf{k}n | \mathbf{E}^{\mathrm{ext}} \rangle}{\alpha^{-1} - \gamma(\mathbf{k}n)} \ . \tag{1.34}$$

For isotropic systems one Γ-point eigenvector and the corresponding eigenvalue have been independently derived by Mossotti [9] in 1850 and Clausius [10] in 1897. The eigenstate describes a uniformly polarized system, where all dipoles point along the same crystallographic axis with the same magnitude as does the induced field. Equation (1.16) shows that this configuration is an eigenvector whose eigenvalue is given by the Clausius-Mossotti relation, $\gamma_{\mathrm{CM}} = \gamma_{\Gamma} = 4\pi n/3$, where n denotes the density of the polarizable dipoles (cf. section 1.4.1).

Is γ_{CM} the maximal eigenvalue $\gamma_{\max}$ which – for fixed density – determines the critical polarizability α_c? Sauer [12], Luttinger and Tisza [6] showed that for body-centered and face-centered cubic crystals this ferroelectric eigenstate actually is one of the dominant

states (refer to figures A.1 and A.2 in appendix A). Luttinger and Tisza, however, also proved in the same paper that in simple cubic systems an anti-ferroelectric state provides a slightly larger eigenvalue. Figure 1.3 shows the "band structure". We indeed identify the maximum of the eigenvalues at the M-point (anti-ferroelectric state) [4]. As a consequence the ferroelectric catastrophe actually happens already for smaller polarizabilities than predicted by the Clausius-Mossotti relation (for simple cubic $\alpha_c \approx 0.1867$).

1.2. Screening in a One-Dimensional Chain

For an infinite one-dimensional chain of polarizable point dipoles with polarizability α there exists an analytical solution which we present in the beginning of this section. Then, we discuss peculiar screening processes found in these systems. In the final part we assess the convergence of numerical real-space approaches by comparing to the analytical solution.

1.2.1. Confinement to One Dimension

Let the one-dimensional chain run along the $\boldsymbol{e}_z$ axis. A single dipole p_m at position $R_m = ma$ causes an electric dipole field (1.11). At site n with position $R_n = na$ it is

$$
\boldsymbol{E}_m^{\mathrm{dip}}(n) = \begin{cases} \dfrac{2p_m\boldsymbol{e}_z}{|n-m|^3 a^3} \,, & \boldsymbol{p} \parallel \boldsymbol{e}_z \quad \text{(longitudinal)} \\[2mm] \dfrac{-\boldsymbol{p}_m}{|n-m|^3 a^3} \,, & \boldsymbol{p} \perp \boldsymbol{e}_z \quad \text{(transversal)} \end{cases} \quad \text{where } n \neq m \,, \qquad (1.35)
$$

and a denotes the lattice constant. Apart from the case of an external field with a component perpendicular to the chain, the dipole moments are forced to point along the chain direction. We will exclusively consider longitudinal dipole moments and fields.

The change in energy due to an arbitrary dipole arrangement (1.20) is

$$
\Delta W = \sum_n \left(\frac{p_n^2}{2\alpha_n} - \sum_{m \neq n} \frac{p_n p_m}{|n-m|^3 a^3} - p_n E_n^{\mathrm{ext}} \right) \,. \qquad (1.36)
$$

Minimization, $\delta W/\delta p_n = 0$, again gives the dipole arrangement

$$
p_{0n} = \alpha_n \left(E_n^{\mathrm{ext}} + E_n^{\mathrm{dip}} \right) = \alpha_n \left(E_n^{\mathrm{ext}} + \sum_{m \neq n} \frac{2p_m}{|n-m|^3 a^3} \right) \,. \qquad (1.37)
$$

In the absence of an external field and for a uniform polarizability $\alpha_n = \alpha$ for all sites the system is homogeneous and translationally invariant. Hence, all dipoles are equal $p_n = p$ and equation (1.37) collapses to

$$
p = \frac{4\zeta(3)\alpha}{a^3} p \,, \qquad (1.38)
$$

where $\zeta(s) = \sum_{n=1}^{\infty} 1/n^s$ is Riemann's zeta function ($\zeta(3) \approx 1.20206$). Obviously $p = 0$ is the trivial solution of this equation. It describes an unpolarized chain. For $\tilde{\alpha} = 4\zeta(3)\alpha/a^3 < 1$, this is the only solution. For $\tilde{\alpha} = 1$, any p is a solution. Finally, for $\tilde{\alpha} > 1$, the solution diverges for any non-vanishing p. $p = 0$ is an unstable fix point of equation (1.38). This is the ferroelectric instability in one dimension (cf. section 1.1.4).

For a homogeneous external field the translation invariance is retained and the microscopic local field at all sites reads

$$
E^{\mathrm{local}} = E^{\mathrm{ext}} + \frac{4p}{a^3}\zeta(3) \,, \qquad (1.39)
$$

where p is implicitly given by

$$p = \alpha E^{\text{local}} \ . \tag{1.40}$$

Solving for p explicitly and inserting the result in (1.39) yields

$$E^{\text{local}} = \frac{1}{1 - \tilde{\alpha}} E^{\text{ext}} \ . \tag{1.41}$$

Note that the external field is effectively *enhanced*. We discuss this enhancement in section 1.2.3, after presenting the analytical solution to the one-dimensional problem for inhomogeneous external fields.

1.2.2. Analytical Solution

The situation for arbitrary external fields is more complicated. To solve the linear system of equations (1.37) we rely on the vector-space notation introduced in section 1.1.2. In one dimension the Γ matrix has a very simple form

$$\Gamma_{nm} = \frac{2}{|n - m|^3 a^3} = \frac{1}{a^3} \begin{pmatrix} \ddots & \ddots & \ddots & \ddots & \ddots & \ddots & \ddots \\ \ddots & 0 & 2/1^3 & 2/2^3 & 2/3^3 & 2/4^3 & \ddots \\ \ddots & 2/1^3 & 0 & 2/1^3 & 2/2^3 & 2/3^3 & \ddots \\ \ddots & 2/2^3 & 2/1^3 & 0 & 2/1^3 & 2/2^3 & \ddots \\ \ddots & 2/3^3 & 2/2^3 & 2/1^3 & 0 & 2/1^3 & \ddots \\ \ddots & 2/4^3 & 2/3^3 & 2/2^3 & 2/1^3 & 0 & \ddots \\ \ddots & \ddots & \ddots & \ddots & \ddots & \ddots & \ddots \end{pmatrix} \ . \tag{1.42}$$

The translation invariance is immediately evident. Γ is equivalent to a one-dimensional single-band tight-binding Hamiltonian where the dipole interaction takes the role of the hopping matrix elements. The only difference is the slow decay of the off-diagonal elements ($\propto 1/r^3$).

To diagonalize Γ we use an ansatz of Bloch waves $\langle n|k\rangle = e^{inka}$. As eigenvalues we obtain a sum of cosines decaying with $1/r^3$

$$\gamma_k = \frac{2}{a^3} \sum_{m=1}^{\infty} \frac{e^{imka} + e^{-imka}}{m^3} = \frac{2}{a^3} \left(\text{Li}_3(e^{ika}) + \text{Li}_3(e^{-ika}) \right) = \frac{4}{a^3} \text{Re} \left(\text{Li}_3(e^{ika}) \right) \ , \tag{1.43}$$

where $\text{Li}_s(z)$ are the polylogarithms $\text{Li}_s(z) = \sum_{k=1}^{\infty} z^k / k^s$. This function is plotted in figure 1.4. We observe the highest eigenvalue γ_{max} at $k = 0$ causing the ferroelectric instability for $1/\alpha = \gamma_{\text{max}} = 4\zeta(3)/a^3$.

From the eigenfunctions and eigenvalues we obtain the energy reduction (1.34) in one dimension for arbitrary external fields

$$\Delta W_0 = -\frac{a}{4\pi} \int_{-\pi/a}^{\pi/a} dk \, \frac{\langle E^{\text{ext}}|k\rangle\langle k|E^{\text{ext}}\rangle}{1/\alpha - \gamma_k} \ . \tag{1.44}$$
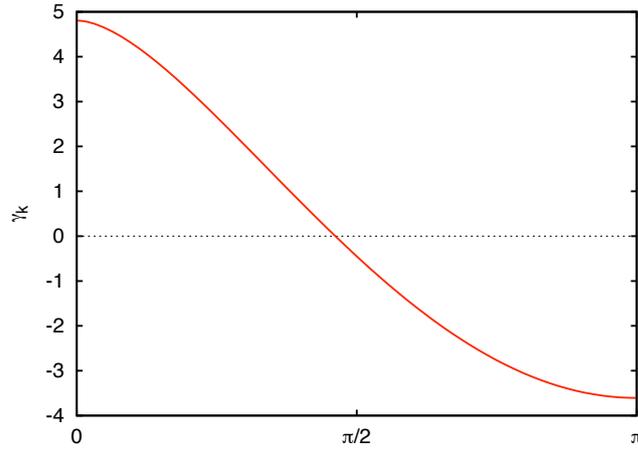
Figure 1.4.: Eigenvalue of the dipole interaction "matrix" Γ which in one dimension just is the k-dependent number $\Gamma_{zz}(k)$. $\gamma_{\max}$ is found at $k = 0$.

Similarly, we obtain the self-consistent dipoles from (1.33)

$$p_{0n} = \langle n | p \rangle = \langle n | (1/\alpha - \Gamma)^{-1} | E^{\text{ext}} \rangle = \frac{a}{2\pi} \int_{-\pi/2a}^{\pi/2a} \mathrm{d}k \, \frac{\langle n | k \rangle \langle k | E^{\text{ext}} \rangle}{1/\alpha - \gamma_k} \, . \tag{1.45}$$

Applying these formulæ to the special case of a point charge q at $n = 0$ gives the screening contribution to the local Coulomb integral ΔU. The charge causes an external field $E_n^{\text{ext}} = E_n^{\text{pc}} = qn/(a^2 |n|^3)$ for $n \neq 0$, giving

$$\Delta u = \Delta W_0 = -\frac{q^2}{2\pi a} \int_0^\pi \mathrm{d}\kappa \, \frac{\mathrm{Im} \left(\mathrm{Li}_2(e^{\mathrm{i}\kappa}) \right)^2}{\zeta(3)/\tilde{\alpha} - \mathrm{Re} \left(\mathrm{Li}_3(e^{\mathrm{i}\kappa}) \right)} \, , \tag{1.46}$$

which stems from the interaction of the point charge with the induced dipoles

$$p_{0n} = -\frac{qa}{2\pi} \int_0^\pi \mathrm{d}\kappa \, \sin(\kappa n) \, \frac{\mathrm{Im} \left(\mathrm{Li}_2(e^{\mathrm{i}\kappa}) \right)}{\zeta(3)/\tilde{\alpha} - \mathrm{Re} \left(\mathrm{Li}_3(e^{\mathrm{i}\kappa}) \right)} \, . \tag{1.47}$$

The screening contribution to the non-local Coulomb parameters ΔV_l follows for an external field composed of two charges $E_n^{\text{ext}} = E_n^{\text{pc}} + E_{n-l}^{\text{pc}}$. The resulting total energy correction is

$$\Delta W_0 = -\frac{a}{4\pi} \int_{-\pi/a}^{\pi/a} \mathrm{d}k \, \frac{|\langle E_0^{\text{pc}} | k \rangle|^2 + |\langle E_l^{\text{pc}} | k \rangle|^2 + \langle E_0^{\text{pc}} | k \rangle \langle k | E_l^{\text{pc}} \rangle + \langle E_l^{\text{pc}} | k \rangle \langle k | E_0^{\text{pc}} \rangle}{1/\alpha - \gamma_k} \, , \tag{1.48}$$

where the latter two terms give

$$\Delta V_l = -\frac{q^2}{\pi a} \int_0^\pi \mathrm{d}\kappa \, \cos(\kappa l) \, \frac{\left(\mathrm{Im} \, \mathrm{Li}_2(e^{\mathrm{i}\kappa}) \right)^2}{\zeta(3)/\tilde{\alpha} - \mathrm{Re} \left(\mathrm{Li}_3(e^{\mathrm{i}\kappa}) \right)} \, . \tag{1.49}$$

Figure 1.5 shows the screening corrections for different distances as a function of $\tilde{\alpha}$.
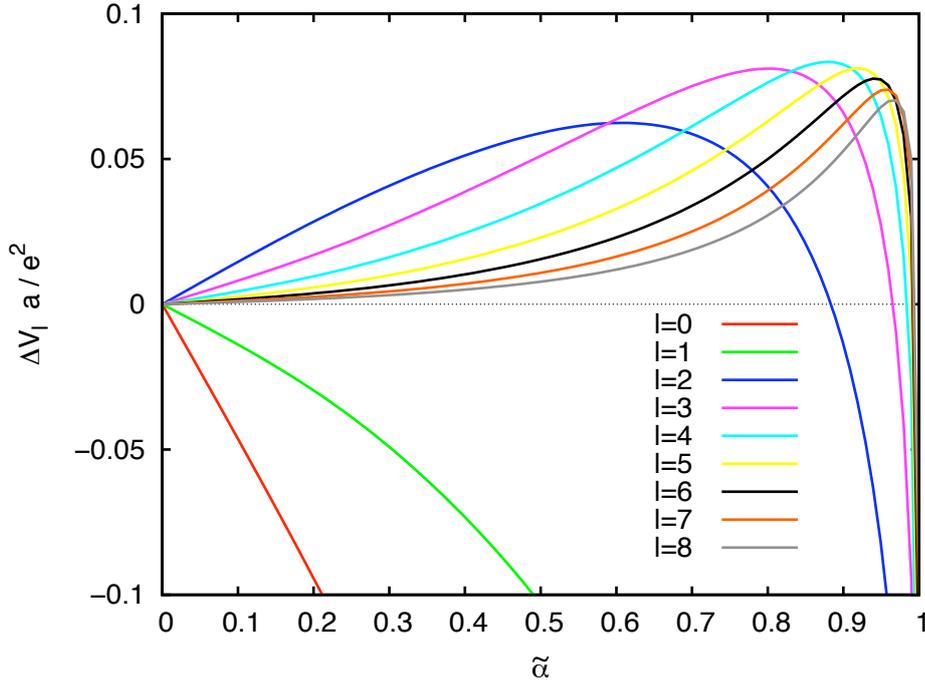
Figure 1.5.: Screening energy ΔV of Coulomb matrix elements for point charges on an infinitely long chain of polarizable point dipoles as a function of polarizability $\tilde{\alpha}$. The different curves denote on-site ($l = 0$) and different neighbor ($l > 0$) Coulomb terms. We see that the on-site Coulomb term ($l = 0$) as well as the interaction between charges of nearest-neighbors are screened for all $0 \leq \tilde{\alpha} < 1$. For longer range interactions and $\tilde{\alpha}$ not too close to the instability we observe anti-screening.

1.2.3. Screening Peculiarities

1.2.3.1. Electric Field

To study the screening effects in a one-dimensional chain of polarizable point dipoles, we define a dielectric-constant-like quantity ε_E with

$$\varepsilon_E = \frac{E^{\text{ext}}}{E^{\text{local}}} \,, \tag{1.50}$$

which in contrast to the actual dielectric constant is only defined at the lattice sites. In the presence of homogeneous external fields we find

$$\varepsilon_E = 1 - \tilde{\alpha} \,, \tag{1.51}$$

where we make use of equation (1.41). Since $\tilde{\alpha} < 1$, also $\varepsilon_E < 1$. Obviously, the effective local field at the sites is *stronger* than the original external field E^{ext}. Instead of screening
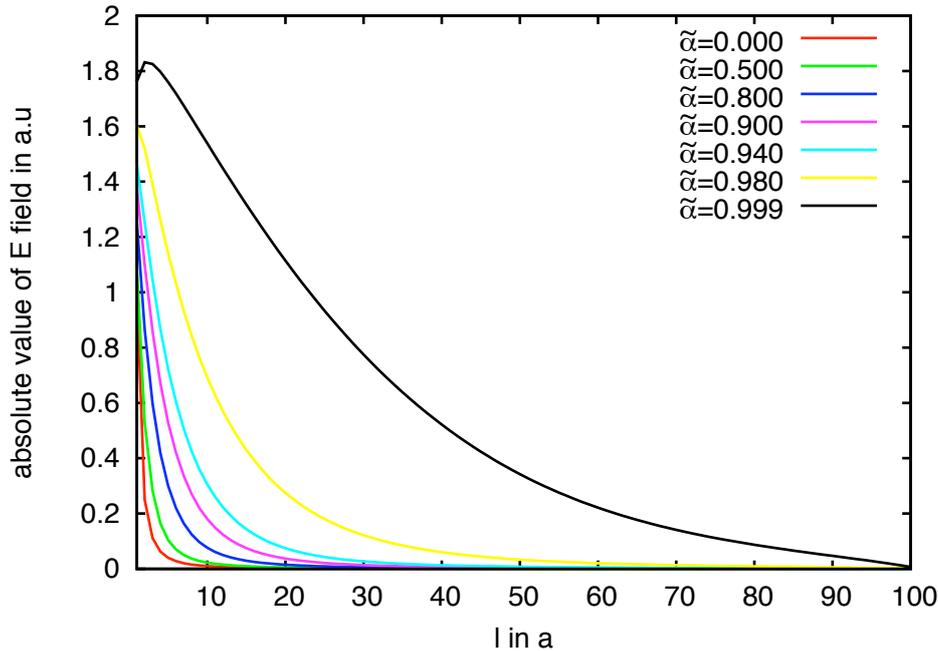
Figure 1.6.: Absolute value of the microscopic local electric field $E^{\text{local}} = p_{0n}/\tilde{\alpha}$ of a one-dimensional chain of polarizable point dipoles at the position of the dipoles. The lowest red curve represents the Coulomb law without screening due to $\tilde{\alpha} = 0$. With increasing $\tilde{\alpha}$ the effective electric field becomes stronger. We observe anti-screening.

we find *anti-screening.* Anti-screening does not only take place for homogeneous but also for more general external fields. For the example of a point charge, the microscopic field $E_n^{\text{local}} = p_{0n}/\tilde{\alpha}$ with p_{0n} from (1.47) is plotted in figure 1.6 for different polarizabilities $0 \leq \tilde{\alpha} < 1$. Compared to the unscreened bare field (red curve) we observe an enhancement of the local field, which is the stronger the larger $\tilde{\alpha}$. Moreover, close to the charge the field can behave non-monotonously.

It is instructive to study the inverse of ε_E since it directly describes the screening. For $\varepsilon_E^{-1} = 1$ we retain the bare field, whereas for $\varepsilon_E^{-1} < 1$ we have screening while $\varepsilon_E^{-1} > 1$ implies anti-screening. Figure 1.7 gives examples of ε_E^{-1} for different polarizabilities and distances from the point charge.

Far away from the charge the field varies slowly as $1/r$. Hence, is close to zero. The asymptotic behavior of $1/\varepsilon_E$ is approximately given by the inverse of equation (1.51) for homogeneous fields (horizontal lines). Close to the charge there is a strong deviation from this asymptotic limit due to local-field effects caused by the dipoles nearby. This effect gives rise to the non-monotonous behavior. The local-field effects become the stronger
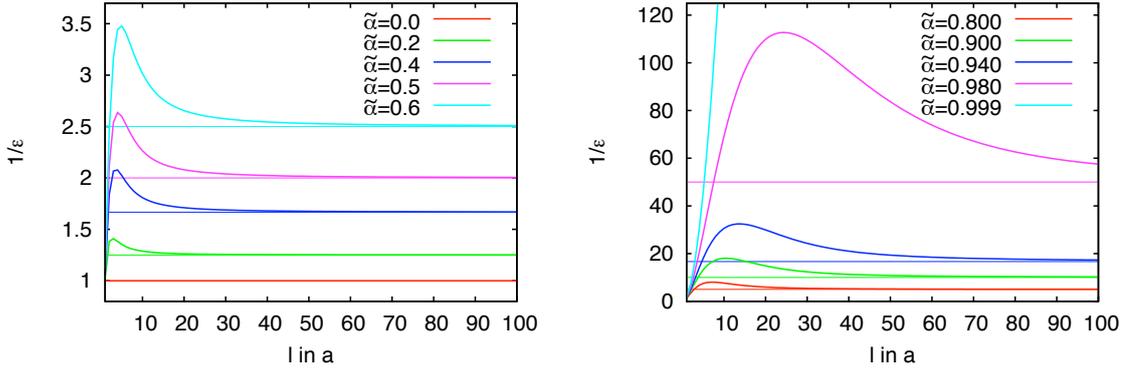
Figure 1.7.: $1/\varepsilon_E = E_l^{\text{local}}/E_l^{\text{ext}}$ for an infinite one-dimensional chain of polarizable point dipoles, where the external field is caused by a charge at site $n = 0$. Close to the charge there are strong local-field effects, which are more pronounced the larger $\tilde{\alpha}$. Sufficiently far away the asymptotic limit of ε_E^{-1} is given by $\varepsilon_E = 1 - \tilde{\alpha}$ (equation (1.51)).

and more extended the higher the polarizability. Close to the ferroelectric instability $\tilde{\alpha} \lesssim 1$ we find that ε_E^{-1} almost diverges (light blue curve in second plot).

To understand how the anti-screening behavior (always $\varepsilon_E^{-1} > 1$) comes about we consider the field of a single dipole in a homogeneous external field of a capacitor. The dipole is modelled as two particles of opposite charge fixed at a constant distance. Its dipole moment is aligned with the direction of the external field lines. The resulting dipole field within the dipole weakens the external field because it is opposed (plot (b) of figure 1.8). This process is called depolarization. Outside the dipole but along its axis, coinciding with the one-dimensional chain, the field is enhanced. This holds for both sides of the dipole. In one dimension and for point dipoles, which by definition have no extent, only these outside regions remain. Hence, we only find anti-screening.

It is also illustrative to look how the microscopic potential Φ reflects screening and anti-screening. Figure 1.9 sketches Φ. We find a linear potential (from the homogeneous external field), the two divergences of the dipole charges, and a relatively flat plateau between the two charges. This plateau shows the reduction of the field within the dipole – the depolarization – because of $E = -\nabla\Phi$. Similarly, close to the charges along their connection line we clearly identify the enhancement of the field due to an increased slope.

1.2.3.2. Coulomb Integrals

The energy correction ΔV_l for non-local Coulomb integrals $V_l = q^2/la + \Delta V_l$ is given by equation (1.49). Figure 1.10 shows the analytical solutions for V_l as a function of l and $\tilde{\alpha}$. We find that for short distances the Coulomb repulsion always is screened in contrast to the field. The screening is the stronger the higher the polarizability. At a
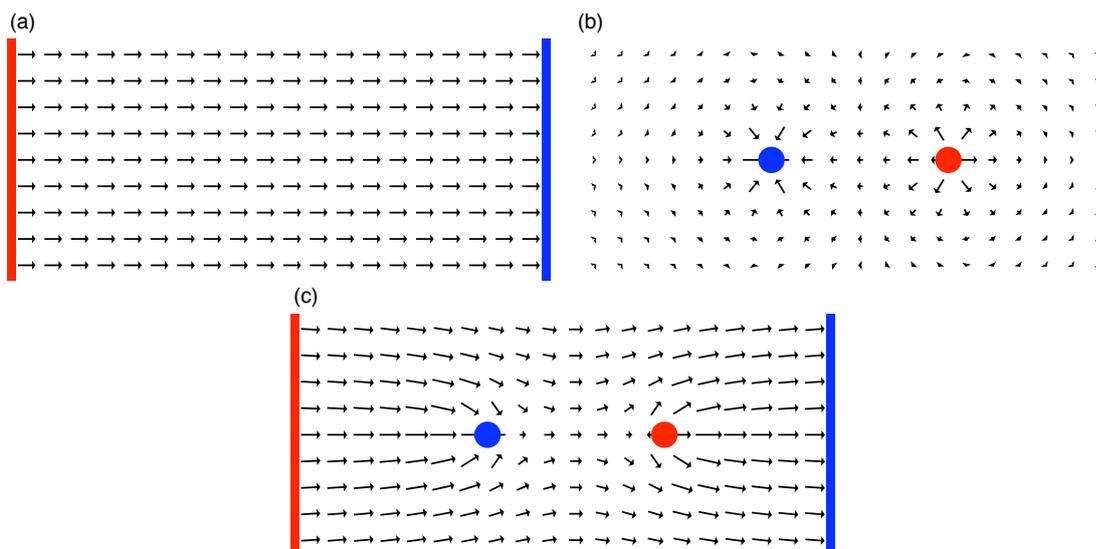
Figure 1.8.: Illustration for a dipole in an external homogeneous field. Within the dipole the electric field points in the opposite direction of the external field which is thus effectively reduced. Outside the dipole on the connection axis of both charges the external field is enhanced. For point dipoles only the outer region counts, leading to an effective increase of the field.
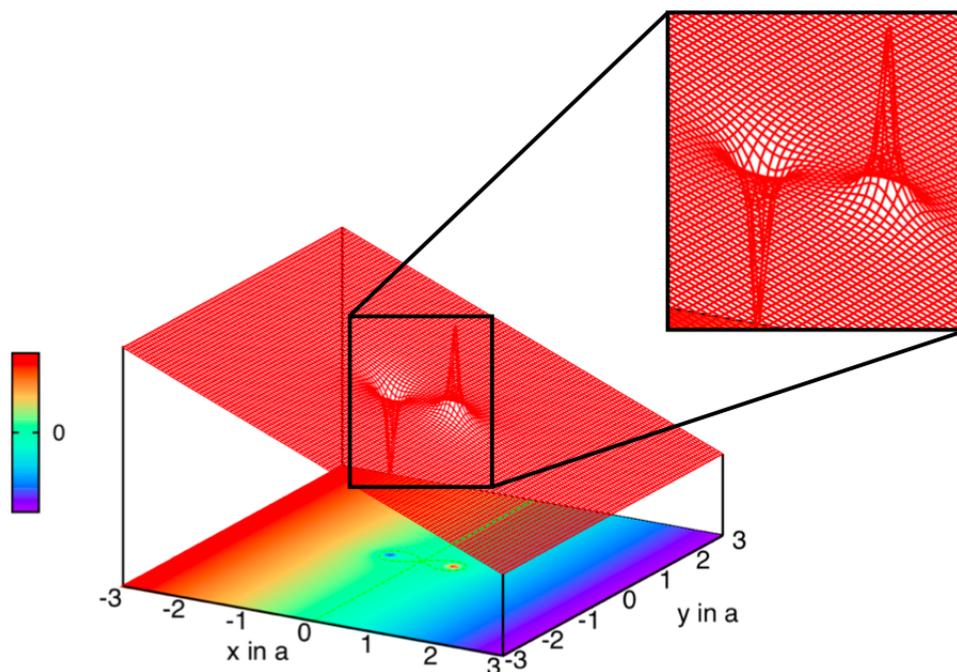
Figure 1.9.: Potential of a dipole in a homogeneous external field. The linear potential gives rise to the homogeneous field. The two divergences are due to the charges of the dipole. In-between both charges there is a relatively flat plateau. It leads to the depolarization. Similarly, close to the charges along their connection line we see the enhancement of the field due to an increased slope.
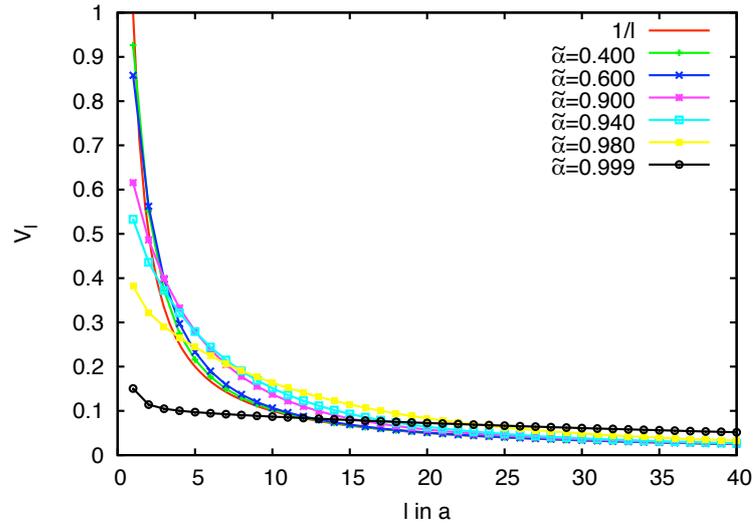
Figure 1.10.: Screened Coulomb matrix elements V_l for an infinitely long chain of polarizable point dipoles for different polarizabilities. The screened interaction decreases monotonously with the distance. Close to the ferroelectric instability the screened interaction becomes almost independent of the distance l (see black curve).
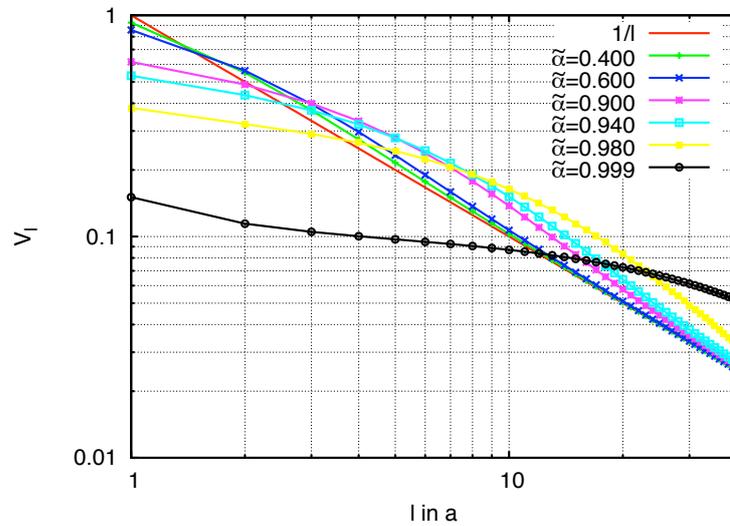
Figure 1.11.: Log-log plot of the fully screened Coulomb matrix elements V_l for an infinitely long chain of polarizable point dipoles. For large distances the microscopic dielectric function $\varepsilon \to 1$ or equivalently $V_l \propto 1/l$ (red line). The intersection of the curves with $1/l$ give the critical distance $l_c(\alpha)$, where the transition from screening to anti-screening takes place.

critical distance $l_c(\alpha)$, which depends on the polarizability, a transition from screening to anti-screening takes place, where V_l is larger than the bare Coulomb matrix element q^2/la. This transition is particularly evident in the log-log plot of figure 1.11. For asymptotically long distances the Coulomb interaction approaches the unscreened $V_l^{\text{ext}} \to q^2/l$. Where does this peculiar behavior stem from? With the energy correction (1.25) and the relation for the self-consistent dipoles (1.19) we obtain

$$\Delta V_l = -\langle p^{(0)}|E_l^{\text{pc}}\rangle = -\sum_i{}' p_i^{(0)} E_{i-l}^{\text{pc}} . \tag{1.52}$$

$|p^{(0)}\rangle$ denotes the dipole arrangement as induced by a point charge at the origin and $|E_l^{\text{pc}}\rangle$ the field of a point charge at site l. The prime shall indicate that the sites carrying the charges are omitted in the summation. The right-hand-side shows that a dipole makes a contribution to the screening if $-p_i^{(0)} E_{i-l}^{\text{pc}} < 0$, when the field E_{i-l}^{pc} and dipole $p_i^{(0)}$ are aligned. In contrast, opposing directions lead to a positive contribution to the sum and therefore to anti-screening. Hence, for a given l we may divide the lattice into two sets of dipoles – the screening and the anti-screening dipoles. Depending on the dominating set the Coulomb interaction is either screened or anti-screened.

In a one-dimensional chain with two charges the anti-screening contributions stem from the region between both charges – the anti-screening volume. It is illustrated for $l = 8$ in figure 1.12 (red color). We observe that the dipoles in the anti-screening volume are effectively reduced compared to the screening of a single charge. The ones of the screening volume (black arrows) are amplified instead.

Figure 1.12.: One-dimensional arrangement of screening dipoles induced by two point charges a distance $l = 8$ apart. Compared to the screening dipoles for an individual point charge, the induced dipoles in the space between the charges are strongly reduced since the fields of both charges weaken each other. We call this area the anti-screening volume (red area). It gives rise to the possibility of anti-screening.

Moderate Polarizabilities   For polarizabilities up to $\tilde{\alpha} \lesssim 0.88$, the critical distance is $l_c = 2$. In this regime the main contributions to the screening are caused by the very close neighbors of the charges because only these dipoles have an appreciable induced dipole moment (see figure 1.6). For $l = 2$ the anti-screening volume consists of a single site. Since it is the nearest-neighbor of both charges it has a strong induced dipole moment from the first charge as well as a strong field of the second charge in opposite direction. This gives the dominant anti-screening contribution according to (1.52). All remaining dipoles in the chain cannot make up for this positive contribution and V_2 is effectively anti-screened. The net dipole moment of this site is, of course, zero.
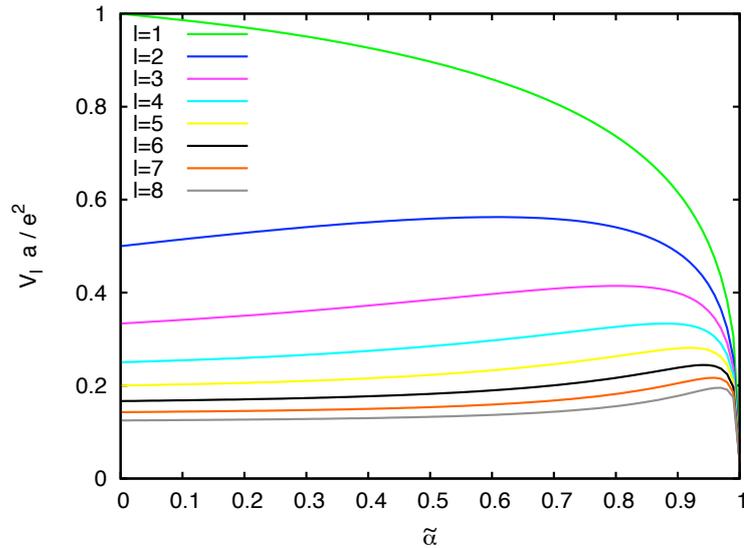
Figure 1.13.: Screened Coulomb matrix elements V_l for point charges on an infinitely long chain of polarizable point dipoles. The screened interaction decreases monotonously with the distance. Close to the ferroelectric instability the screened interaction becomes almost independent of the distance l. In the Hamiltonian the Coulomb energy essentially becomes a constant offset leading to a screening-induced loss of correlations.

The same explanation holds for longer-range Coulomb parameters. The dipoles inside the anti-screening volume are the closest to both charges and thus dominate, leading to anti-screening. However, the farther the charges are away from each other the more the dipole moments and field strength of the point charges decay. The effect of anti-screening becomes less pronounced. Asymptotically, the Coulomb interaction is unscreened.

The Coulomb integrals for $l = 0$ and for $l = 1$ are always screened (see figure 1.5). For two charges on the same and on adjacent sites there is no anti-screening volume and, therefore, no positive contribution to the sum (1.52). In addition, the strong induced dipoles and the high field strength of the point charge coincide at the same lattice sites, making this effect very pronounced.

Figure 1.5 shows the screening corrections for different distances as a function of $\tilde{\alpha}$. We find the strong screening for $l = 0, 1$ as well as the anti-screening for longer-ranges with the smaller distances being more pronounced. We could imagine that the more efficient screening for smaller distances l might lead to a confining potential. The distance-dependence of the bare Coulomb interaction is, however, even stronger at this range such that $V_{\text{bare}} + \Delta V$ remains a monotonously decaying function (cf. figure 1.11). It, however, becomes less distance-dependent.

High Polarizabilities and Ferroelectric Instability   For higher polarizabilites the induced dipoles become stronger and cover a larger area. Therefore, an increasing number of dipoles has a sizable contribution to the screening. For $\tilde{\alpha} \gtrsim 0.88$ they compensate and eventually overcompensate the anti-screening contribution for $l = 2$. Hence, $l_c(\alpha)$ increases. This is illustrated in the curves of figure 1.5. For even higher polarizabilities $\tilde{\alpha}$ $l_c(\alpha)$ increases further until a maximal critical distance l_c^{max} is reached. For larger $l > l_c^{\mathrm{max}}$ the anti-screening always prevails.

Very close to the ferroelectric instability ($\tilde{\alpha} \lesssim 1$) the strong screening for the short range $l < l_c^{\mathrm{max}}$ and the strong anti-screening for the long-range $l > l_c^{\mathrm{max}}$ effectively flatten the Coulomb interaction out (cf. black line in figure 1.10 and 1.11). This is because the anti-screening correction actually increases with distance. The screened Coulomb interaction becomes almost independent of the distance. This can be interpreted as a polarization-induced loss of electronic correlations, since all electron pair-interactions yield roughly the same Coulomb energy irrespective of their mutual distance. Hence, the Coulomb term just gives rise to a constant energy-offset in the Hamiltonian.

Screening of very long-range Coulomb matrix elements   Substituting the field of a point charge in equation (1.52) we obtain

$$\Delta V_l = {\sum_i}' \frac{p_i(l - i)}{a^2 |l - i|^3} \; . \tag{1.53}$$

With the self-consistent dipoles p_{0i} this sum yields the exact result and therefore is a recast of equation (1.49). The dipole moments are aligned with the local field and proportional in magnitude. With the asymptotic expression for the $E_i^{\mathrm{local}} = 1/\varepsilon_E E_i^{\mathrm{ext}}$ we can thus approximate

$$p_{0i} \approx p_i = \frac{\alpha}{\varepsilon_E} \frac{i}{a^2 |i|^3} \; , \tag{1.54}$$

effectively neglecting the complication caused by the local-field effects. Their contribution to the sum is small since finite-size effects are strongly localized to a small region around the charges. Moreover, they decay with $1/l^2$ (assuming not too large polarizabilities).

With this approximation the summation can be performed analytically yielding

$$\Delta \bar{V}_l = \frac{\alpha}{a^4 \varepsilon_E} \left\{ \frac{2}{l^3} \left(\sum_{i=1}^{l-1} \frac{4}{i} + \frac{2}{l} \right) + \frac{1}{l^2} \left(\sum_{i=1}^{l-1} \frac{4}{i^2} - 4\zeta(2) + \frac{2}{l^3} \right) \right\} \; . \tag{1.55}$$

From this we infer the asymptotic limit $\Delta \bar{V}_l \to \mathcal{O}(\ln(l)/l^3)$. Figure 1.14 shows the results (green line). We observe a posteriori that the approximation indeed is well justified. For small l we find a deviation due to local-field effects when comparing to the analytic solution. For large l, however, there is hardly any difference at all.

We briefly introduce the continuum approximation which can readily be generalized to higher dimensions. To that end, we smear the dipoles out along the line and substitute the summation with an integral which does not contain the line segments representing

the unit cells of the two charges, i.e. $[x - a/2, x + a/2]$ where x is either 0 or l. Carrying out the integration yields

$$\Delta \tilde{V}_l = \frac{4\alpha}{a^4 \varepsilon_E l^2} \left\{ \frac{1}{l} \ln \frac{l^2 - a^2/4}{a^2/4} - \frac{l}{l^2 - a^2/4} \right\} . \tag{1.56}$$

Inspection confirms that the same asymptotic behavior is retained (see blue curve in figure 1.14).

Figure 1.14 shows that this continuum approximation essentially differs from the sum only for short distances. Still it takes longer to converge to the analytic results than the sum (1.55). This is more obvious in the difference plot shown in figure 1.15. However, also this simple approximation yields good results and gives the proper asymptotics.

The Coulomb parameters decay with $\Delta V_l \to \mathcal{O}(\ln(l)/l^3)$ which is obviously faster than $1/l$. This shows that the Coulomb potential is unscreened for large distances as already observed in figure 1.11.

1.2.3.3. Relation between Electric Field and Screening Energy

In the previous section we used an approximation for the electric field to obtain the dipoles for the derivation of the asymptotic behavior. The field obviously seems to have a properly defined dielectric constant $\varepsilon_E \neq 1$, whereas for the Coulomb matrix element the dielectric constant ε_V always eventually assumes the value 1. This mismatch is surprising. From textbook continuum electrostatics we know that the electric field is

$$\boldsymbol{E}(\boldsymbol{r}) = -\boldsymbol{\nabla} V(\boldsymbol{r})/q = -\boldsymbol{\nabla} \frac{q}{\varepsilon |\boldsymbol{r}|} , \tag{1.57}$$

where obviously the constant $1/\varepsilon$ in V is the same for $\boldsymbol{E}$. Hence, $\varepsilon_E \equiv \varepsilon_V$.

This is not true for the dielectric constants defined in our one-dimensional model: $1/\varepsilon_E$ based on the electric field reads

$$1/\varepsilon_E = E_n^{\mathrm{local}} \cdot n^2 , \tag{1.58}$$

whereas

$$1/\varepsilon_V = V_l \cdot l . \tag{1.59}$$

Figure 1.16 illustrates an example for this discrepancy of the two different $1/\varepsilon$ constants. From the analytic solution for the Coulomb matrix elements we can formally derive the correction term relating both. Treating the discrete sites l as a continuous variable enables us to use equation (1.57). With a complicated but exact expression for the $1/l^2$ power law

$$\frac{q}{l^2} = \frac{2q}{\pi} \int_0^\pi \mathrm{d}\kappa \, \sin\left(\kappa n\right) \mathrm{Im}\left(\mathrm{Li}_2(e^{\mathrm{i}\kappa})\right) \tag{1.60}$$

we obtain

$$\mathcal{E}_n = -\boldsymbol{\nabla} \frac{V_n}{q} = -\frac{2q\zeta(3)}{\pi\tilde{\alpha}} \int_0^\pi \mathrm{d}\kappa \, \frac{\sin\left(\kappa n\right) \mathrm{Im}\left(\mathrm{Li}_2(e^{\mathrm{i}\kappa})\right)}{\zeta(3)/\tilde{\alpha} - \mathrm{Re}\left(\mathrm{Li}_3(e^{\mathrm{i}\kappa})\right)} \left(1 - \frac{\tilde{\alpha}}{\zeta(3)} \left(\frac{\kappa}{4} \frac{d}{d\kappa} + 1\right) \mathrm{Re}(\mathrm{Li}_3 e^{\mathrm{i}\kappa})\right) . \tag{1.61}$$
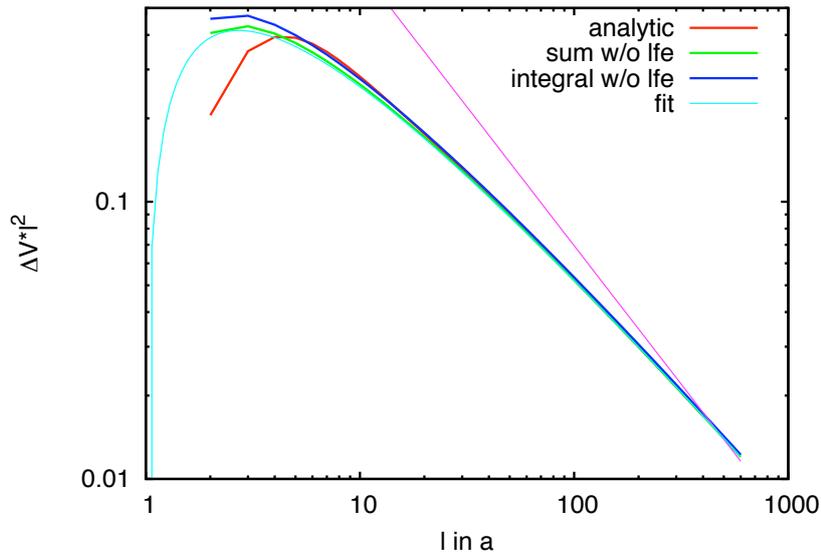
Figure 1.14.: Asymptotic behavior for $\tilde{\alpha} = 0.4$ of $\Delta V_l \cdot l^2$ for the analytic solution (red line), the sum (green line) and for the continuum limit (dark blue line) neglecting local-field effects. Theoretically, $\mathcal{O}(\ln(l)/l)$ is expected. The light blue line shows a fit for $c\ln(l)/l$ to the data of the sum calculation in the interval $l = [300 : 600]$ yielding $c \approx 1.128$. This is close to the theoretical constant $c^{\mathrm{exact}} \approx 1.120$ of equation (1.56). The magenta line represents a $1/l$ decay for comparison purposes.
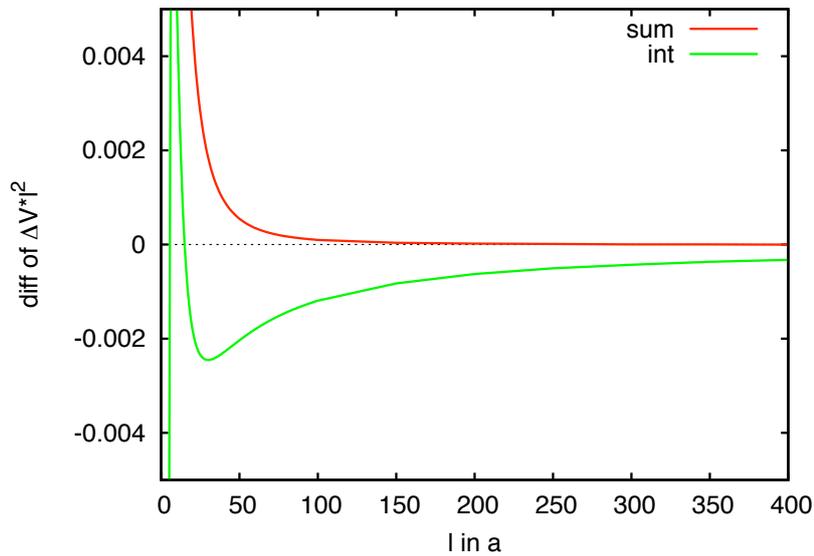
Figure 1.15.: Difference between the analytical solution and the sum (red) (1.55) and integral (green) (1.56). We observe local-field effects close to the charge. The sum gives a very good approximation to the analytic solution, whereas the integral converges only at much larger distances.
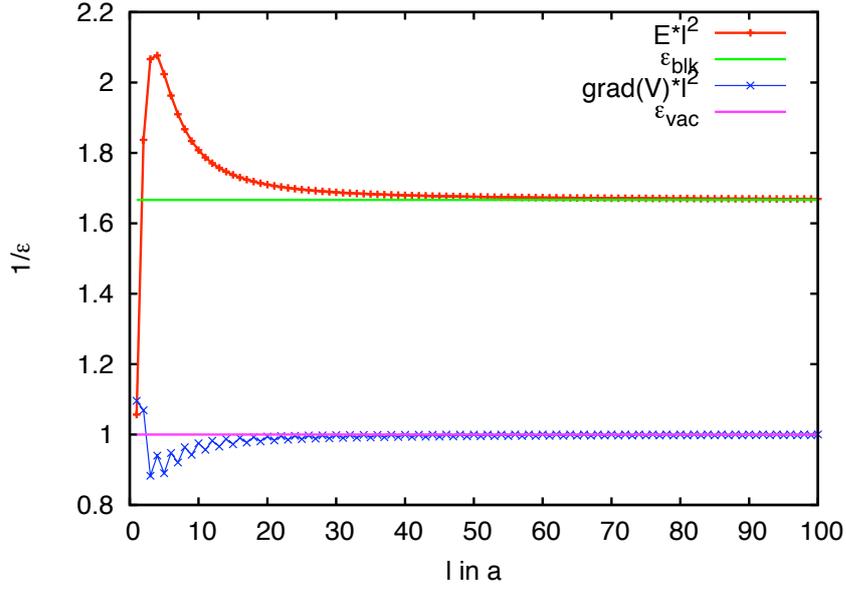
Figure 1.16.: $1/\varepsilon$ for analytically derived electric field E_l and $^d/_{dl} V_l/q$ for an infinite chain of polarizable point dipoles with polarizablility $\tilde{\alpha} = 0.4$. Whereas the electric field decays with a screening of $1/\varepsilon = 0.6$ for large distances, V_l is unscreened ($\varepsilon = 1$). This seeming inconsistency is removed by appropriate averaging (see text).

We identify the first summand as

$$E_n^{\text{local}} = -\frac{2q\zeta(3)}{\pi\tilde{\alpha}} \int_0^\pi \mathrm{d}\kappa \, \frac{\sin(\kappa n) \operatorname{Im}\left(\operatorname{Li}_2(e^{\mathrm{i}\kappa})\right)}{\zeta(3)/\tilde{\alpha} - \operatorname{Re}\left(\operatorname{Li}_3(e^{\mathrm{i}\kappa})\right)} \, , \tag{1.62}$$

which includes ε_E. Consequently, the latter two summands give the correction terms stemming from ε_V.

How does this seeming inconsistency come about? Neither $1/\varepsilon_E$ nor $1/\varepsilon_V$ are the usual macroscopic dielectric constants. Instead both are microscopic quantities and only defined *at the lattice sites*. In order to obtain the macroscopic dielectric constant ε and to put the derivative of V_l onto firm grounds we need to perform a suitable averaging procedure (see section 1.4.1).

Being a real physical system, the chain is embedded in three-dimensional space. Hence, the averaging has to take all three spatial dimensions into account. This poses the problem of finding the right averaging volume. It has to be chosen such that it is large compared to the lattice constant but small w.r.t. macroscopic dimensions. It is therefore not sensible to define a quasi-one-dimensional volume along the chain. Even though this would yield a finite result for the screening, i.e. $1/\varepsilon > 1$, it would directly depend on the extent of the

volume perpendicular to the chain. Consequently, it would not be well-defined. Using an appropriately large averaging volume in all spatial dimensions, the result of averaging inevitably leads to no screening, i.e. $1/\varepsilon = 1$, hence, removing the ostensible inconsistency.

1.2.4. Comparison to Cluster Calculations using the Real-Space MPDM Code

While we have an analytical solution for the one-dimensional case, in general, we need to resort to numerical solutions. Here, we discuss a real-space approach based on finite clusters. The analytical solution gives us the means to assess the convergence of this method as a function of the polarizability or cluster size.

To that end, we evaluate the dielectric-constant-like ε^{-1} numerically and compare to the analytic results. Figure 1.17 shows the results for a finite cluster of 201 sites. Agreement is perfect for not too large polarizabilities and not too close to the cluster boundary, where we can clearly identify finite-size effects. These stem from the missing dipoles outside the cluster. For a large range of polarizabilities the finite-size effects remain rather small and the real-space approach gives a very good approximation. We can even make the cluster the smaller the lower the polarizability.

The upper plot of figure 1.18 shows the electric field. For already quite high polarizabilities but below $\tilde{\alpha} < 0.99$ hardly any difference is observable. The lower plot gives the relative error to the exact solution. A noticeable error starts as far as $l = 80$ for the already quite large $\tilde{\alpha} = 0.90$.

However, very close to the instability, for instance for $\tilde{\alpha} = 0.999$, deviations from the analytical results are very pronounced and spread over the entire cluster. Of course we could significantly increase the cluster. But very soon this real-space approach becomes infeasible. Therefore, it is not suitable to study the instability. We will introduce a more efficient method to tackle systems close to the instability in section 1.4.3.
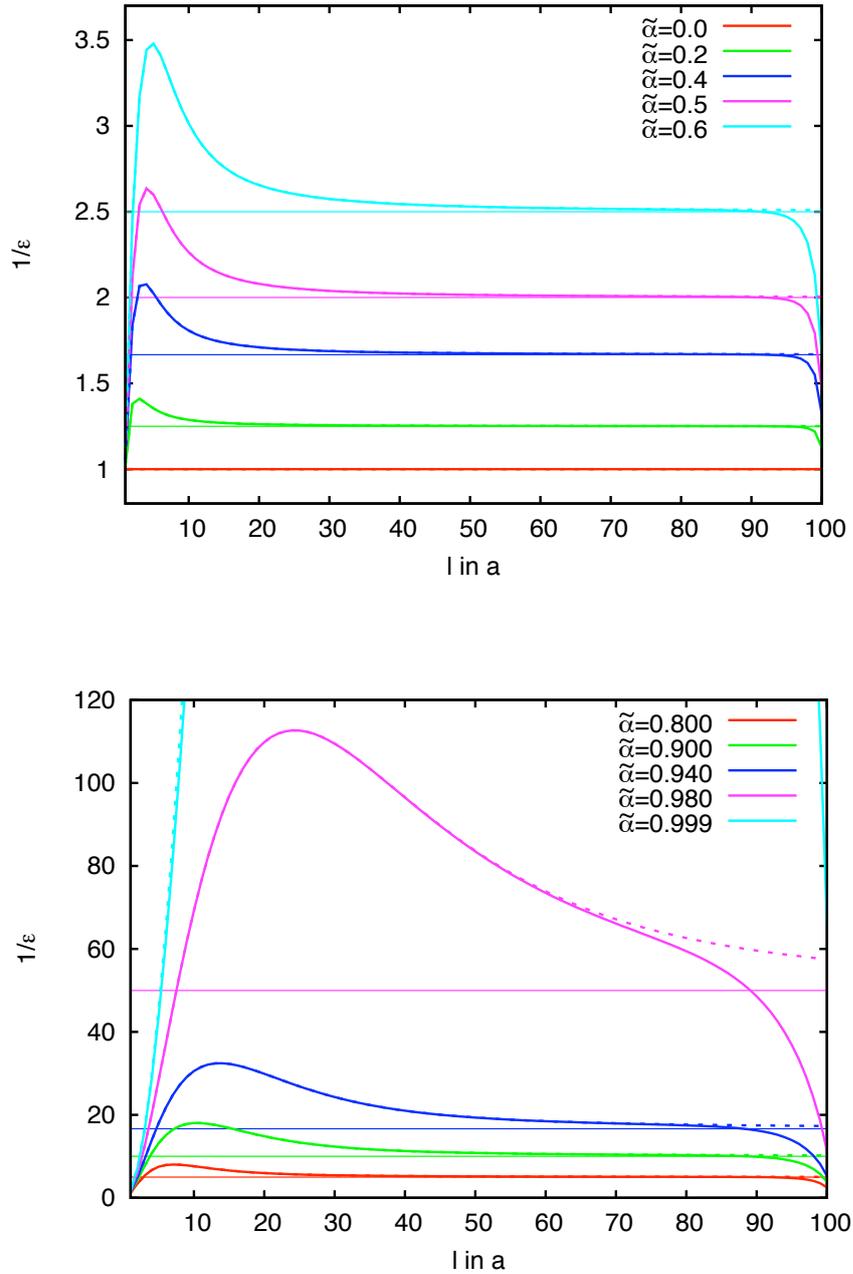
Figure 1.17.: $1/\varepsilon_l$ plot for a finite one-dimensional cluster with $N = 100$ (201 sites). The results directly correspond to analytical calculations (dashed lines in corresponding color) already shown in figure 1.7. Direct comparison shows hardly any deviation apart from finite-size effects at the cluster boundary. This effect becomes stronger for higher polarizabilities.
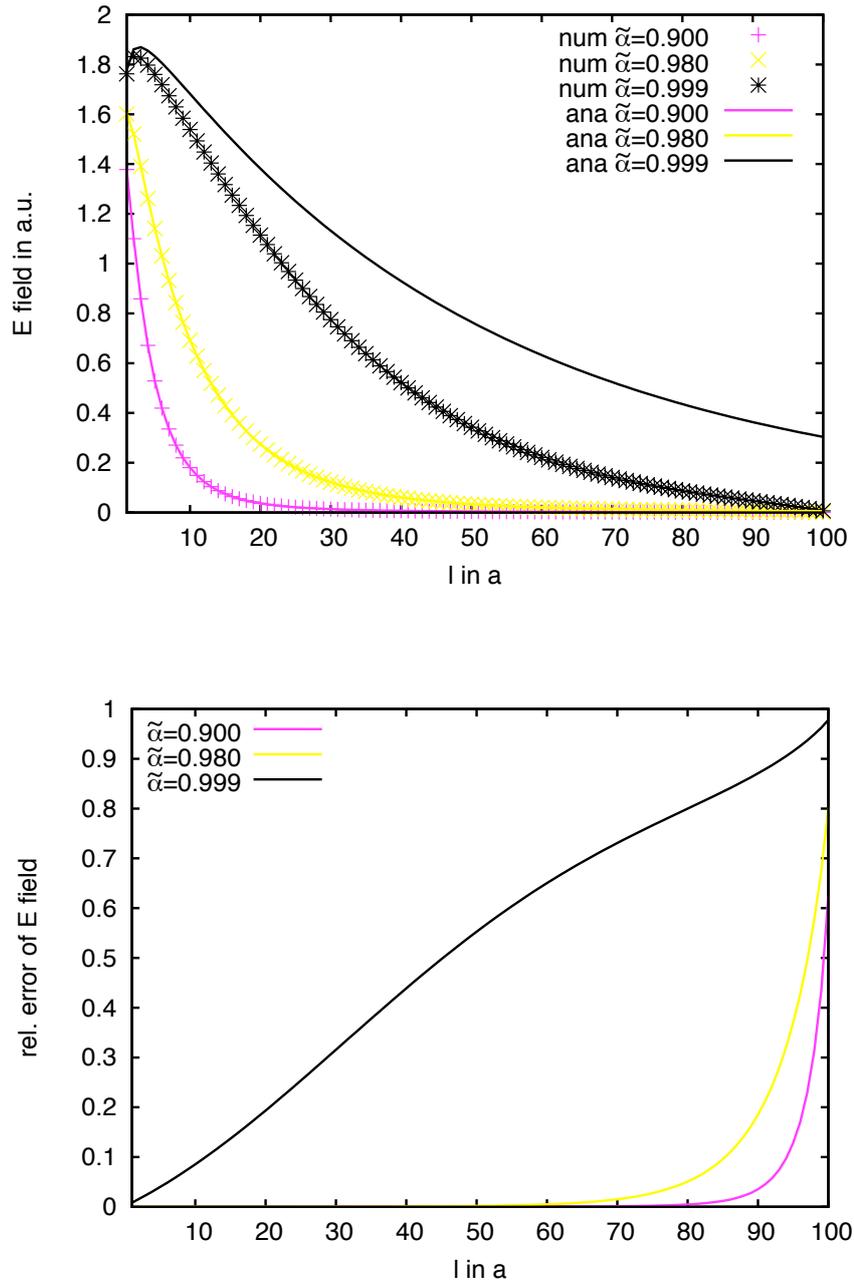
Figure 1.18.: Microscopic local field comparison of analytical calculation for an infinite system and numerical result for a cluster ($N = 100$) for different polarizabilities. The lower figure gives the relative deviation of the numerical simulation. For $\tilde{\alpha} = 0.999$ we observe a strong discrepancy over the entire cluster. For lower polarizabilities the solutions only deviate significantly in a small domain close to the cluster boundary. For $\tilde{\alpha}$ not too close to the instability the cluster method thus gives a good approximation.

1.3. Screening in a Two-Dimensional Square Lattice

In this section we turn our attention to a two-dimensional square lattice of point dipoles. Instead of giving an analytical solution we treat the system numerically, finding again a loss of screening for long distances similar to the one-dimensional case.

1.3.1. Confinement to Two Dimensions

Without loss of generality we define the coordinate system such that the two-dimensional lattice extends in $\boldsymbol{e}_x$ and $\boldsymbol{e}_y$ direction. A lattice vector thus becomes $\boldsymbol{R}_{ij} = a(i\boldsymbol{e}_x + j\boldsymbol{e}_y)$, where a is the lattice constant. Similarly, the dipole at $\boldsymbol{R}_{ij}$ shall be denoted by $\boldsymbol{p}_{ij} = p_{ix}\boldsymbol{e}_x + p_{iy}\boldsymbol{e}_y$, whose field is given by equation (1.11). At lattice site (m, n) the field due to a dipole at (i, j) reads

$$\boldsymbol{E}_{ij}^{\mathrm{dip}}(\boldsymbol{R}_{mn}) = \begin{cases} \dfrac{3\left(\boldsymbol{R}_{mnij} \cdot \boldsymbol{p}_{ij}\right) \cdot \boldsymbol{R}_{mnij} - R_{mnij}^2 \boldsymbol{p}_{ij}}{|\boldsymbol{R}_{mnij}|^5} & \boldsymbol{p}_{ij} \perp \boldsymbol{e}_z \quad \text{in plane} \\[2em] -\dfrac{p_{ijz}\boldsymbol{e}_z}{|\boldsymbol{R}_{mn} - \boldsymbol{R}_{ij}|^3} & \boldsymbol{p}_{ij} \parallel \boldsymbol{e}_z \quad \text{out of plane} \end{cases}, \qquad (1.63)$$

where $\boldsymbol{R}_{mnij} = \boldsymbol{R}_{mn} - \boldsymbol{R}_{ij} \neq \boldsymbol{0}$.

The case of a homogeneous external field $\boldsymbol{E}^{\mathrm{ext}}$ is solved easily. It leads to a translationally invariant system, since all dipoles point in the same direction with the same magnitude, i.e. $\boldsymbol{p}_{mn} = \boldsymbol{p}$ for all m, n. To obtain the total dipole field at a site it suffices to evaluate the sum over all dipoles seen from position $\boldsymbol{0}$. The field at the origin of a single dipole at $\boldsymbol{R}_{ij}$ is

$$\boldsymbol{E}_{ij}^{\mathrm{dip}}(\boldsymbol{0}) = \frac{a^2}{R_{ij}^5}\left\{\boldsymbol{e}_x\left(\left(2i^2 - j^2\right)p_x + 3ijp_y\right) + \boldsymbol{e}_y\left(\left(2j^2 - i^2\right)p_y + 3ijp_x\right)\right\} - \boldsymbol{e}_z\frac{p_z}{|\boldsymbol{R}_{ij}|^3}, \qquad (1.64)$$

where the first two terms give the in-plane and the last the out-of-plane contribution.

For $\boldsymbol{p}$ in the x-y-plane

$$\boldsymbol{E}^{\mathrm{local}}(\boldsymbol{R}) = \boldsymbol{E}^{\mathrm{ext}} + \sum_{ij \neq 0,0} \boldsymbol{E}_{ij}^{\mathrm{dip}}(\boldsymbol{0}), \qquad (1.65)$$

the cross terms ij vanish. For each fixed j the summations over $i > 0$ and $i < 0$ cancel. Due to symmetry the summations over i^2 and j^2 yield the same result. Thus,

$$\boldsymbol{E}_{ij}^{\mathrm{local}} = \boldsymbol{E}^{\mathrm{ext}} + \boldsymbol{p}\sum_{i,j \neq 0,0}\frac{a^2 i^2}{R_{ij}^5} = \boldsymbol{E}^{\mathrm{ext}} + \frac{\boldsymbol{p}}{2}\sum_{i,j \neq 0,0}\frac{1}{R_{ij}^3} = \boldsymbol{E}^{\mathrm{ext}} + \gamma\frac{\boldsymbol{p}}{2a^3}, \qquad (1.66)$$

for $\boldsymbol{p} \perp \boldsymbol{e}_z$. Similarly, the out-of-plane case may be evaluated giving a negative sign for the dipole summation and a factor of $1/2$. Hence,

$$\boldsymbol{E}_{ij}^{\mathrm{local}} = \boldsymbol{E}^{\mathrm{ext}} + \frac{\gamma}{2a^3}\left(\boldsymbol{e}_x\,p_x + \boldsymbol{e}_y\,p_y - \boldsymbol{e}_z\,2p_z\right), \qquad (1.67)$$

where γ denotes the lattice sum $\gamma = a^3 \sum_{i,j \neq 0,0} 1/R_{ij}^3$. In 1927 Topping [15] evaluated this lattice sum approximately using a modified Jones' and Ingham procedure (see [16]). Apparently, he was unaware of the fact that exactly this summation had already been calculated exactly by Lorenz [17] more than 50 years earlier. The exact solution is

$$\gamma = 4\zeta(3/2)\beta(3/2) \approx 9.03362 , \tag{1.68}$$

where ζ denotes Riemann's zeta function and β is Dirichlet's beta function

$$\beta(s) = \sum_{n=0}^{\infty} \frac{(-1)^n}{(2n+1)^s} . \tag{1.69}$$

Assuming an isotropic polarizability and using $\boldsymbol{p} = \alpha \boldsymbol{E}^{\text{local}}$ the local field can be rewritten as

$$\boldsymbol{E}^{\text{local}} = \frac{\boldsymbol{e}_x E_x^{\text{ext}} + \boldsymbol{e}_y E_y^{\text{ext}}}{1 - \gamma\alpha/2a^3} + \frac{\boldsymbol{e}_z E_z^{\text{ext}}}{1 + \gamma\alpha/a^3} . \tag{1.70}$$

For the evaluation of the Coulomb matrix elements we place charges on lattice sites. Thus, within the plane the only non-vanishing components are the in-plane components. Hence, we will restrict our discussion to this case.

The in-plane epsilon ε reads

$$1/\varepsilon = \frac{1}{1 - \gamma\alpha/2a^3} . \tag{1.71}$$

This equation also hints at a ferroelectric instability similar to the one-dimensional case. The critical polarizability for the Γ-point instability is $\alpha_{\text{CM}} = 2a^3/\gamma \approx 0.221a^3$; there could, of course, be instabilities at lower polarizabilities if the maximal eigenvalue of the dipole matrix is not at the Γ-point. Numerically we indeed find hints suggesting that the instability occurs earlier.

1.3.2. Numerical Solution

We handle the two-dimensional square lattice numerically using the self-consistency loop presented in scheme 1.2. For this real-space based method we again rely on finite clusters. To assess the convergence with system size and to rule out finite-size effects we treat two different cluster sizes: $N = 20$ with 1681 and $N = 56$ with 12769 sites.

From the self-consistent solution we plot the dipoles and study the fields and Coulomb matrix elements.

1.3.2.1. Dipoles and Electric Fields

Figure 1.19 shows the self-consistent dipole arrangement in the two-dimensional plane for a negative point charge in the center of the lattice. The polarizability is $\alpha = 0.05$ (upper
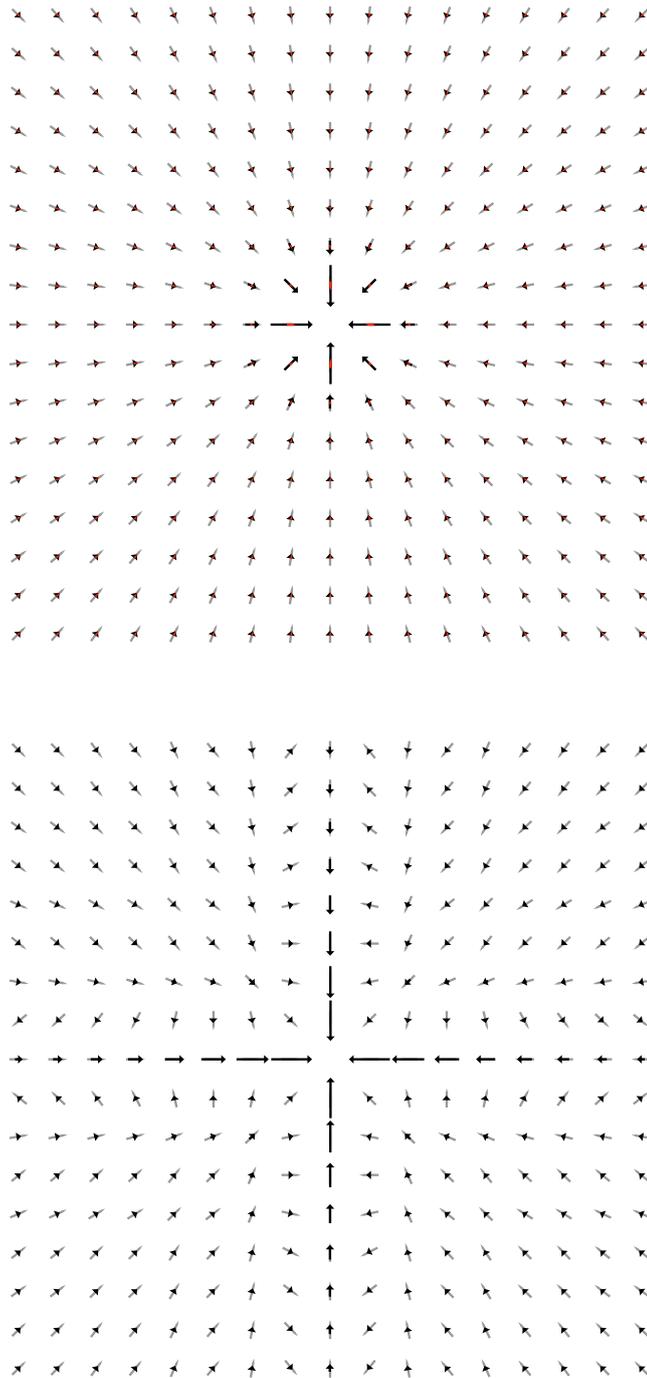
Figure 1.19.: Dipole arrangement induced by a negative point charge in the center of a two-dimensional square lattice of polarizable point dipoles with polarizability $\alpha = 0.05$ (upper picture) far from and $\alpha = 0.195$ (lower picture) close to the ferroelectric instability. The magnitude of the dipoles is proportional to the length of the corresponding arrows with different proportionality constants in the two plots, as close to the instability the dipole magnitudes are significantly larger.
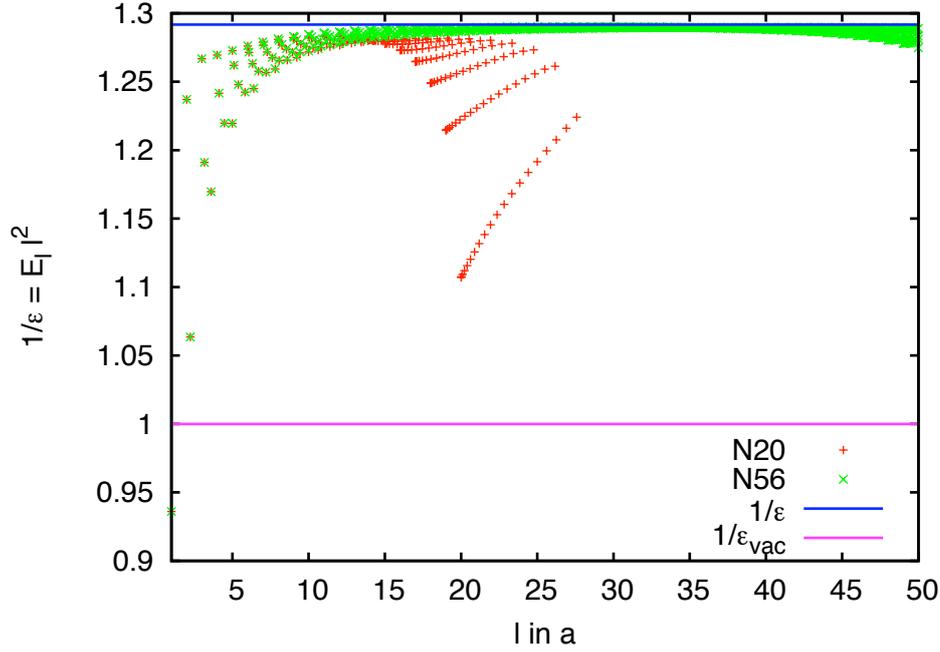
Figure 1.20.: $1/\varepsilon_E = \boldsymbol{e}_r \cdot \boldsymbol{E}_l^{\text{local}} l^2$ constructed from the radial component of the electric field of a two-dimensional square lattice of polarizable point dipoles with polarizability $\alpha = 0.05$. Red crosses are for a system size of $N = 20$ (21^2 number of dipoles), green crosses for a size of $N = 56$. The blue lines denotes ε given by equation (1.72). The magenta line gives the unscreened $\varepsilon_{\text{vac}} = 1$ of the vacuum. The strong scattering of values close to the charge and at the cluster boundary stems from different crystallographic directions.

plot), a value quite far away from the ferroelectric instability. For this case the real-space approach should yield reliable results – even for quite small clusters.

As expected the dipoles are aligned radially to the point charge, likewise are the local fields at the lattice sites. In contrast, the lower plot of figure 1.19 shows the result of a simulation for $\alpha = 0.195$ being quite close to the ferro-electric instability. We observe a strong deviation from the radial alignment. This is a strong hint that the ferroelectric instability does not occur at the Γ-point for $\alpha_{\text{CM}} = 2a^3/\gamma$ but already for smaller values. Instead, the $\boldsymbol{k}$-point giving rise to the instability determines this strange screening pattern.

For the system with low polarizability we again study the dielectric constant-like quantity $\varepsilon_E^{-1} = \boldsymbol{e}_r \cdot \boldsymbol{E}^{\text{local}}|\boldsymbol{l}|^2$ based on the electric field. Figure 1.20 shows the results for two different system sizes to assess the convergence – a small system with 1681 dipoles ($N = 20$, plotted in red) and a relatively large system with 12769 ($N = 56$, plotted in green).

We identify four distinct ranges in the larger cluster. The nearest-neighbor $l = 1$ of the charge is always screened, it is smaller than the vacuum $1/\varepsilon_{\mathrm{vac}} = 1$ (magenta line), whereas for all other distances we find anti-screening. This is very similar to the behavior found in the one-dimensional chain. It has been discussed in the previous section, where we also found anti-screening. The second range contains the dipoles close to the charge except for the first neighbor. This is the local-field domain. The scattering of the values is due to different crystallographic directions. This domain extends until about $l = 20$. The next range $l \approx 20$ to 40 shows constant behavior consistent with $1/\varepsilon$ (blue line) as derived above for the homogeneous system

$$\varepsilon^{-1} = \left(1 - \gamma\alpha/2a^3\right)^{-1} \approx 1.2917 \ . \tag{1.72}$$

Towards the boundary of the cluster $l \approx N$ we find finite-size effects. Fields and Coulomb integrals up to this range can thus be considered converged. The final range is the domain of finite-size effects which manifest themselves as a variation in the field towards weaker anti-screening. The scattering again stems from different crystallographic directions.

In the smaller system with $N = 20$ the domains of local-field and finite-size effects blend into each other seamlessly. We do not find the constant domain governed by ε^{-1}. Since we cannot separate the local-field from the finite-size regimes, this system is too small to draw general conclusions.

1.3.2.2. Coulomb Parameters

The Coulomb parameters V_l obtained for the same system are presented in the upper plot of figure 1.21 as a function of the distance between the two charges. Comparing to the unscreened interaction (blue curve) we observe screening for short distances just like in the one-dimensional chain. This is emphasized in the lower plot showing the screening correction energy ΔV_l. The explanation for this behavior is a direct generalization of that for the one-dimensional case (see section 1.2.3.2).

The screening correction of the Coulomb matrix element ΔV_l (generalization of (1.52)) is given by

$$
\begin{aligned}
\Delta V_l &= -\langle \boldsymbol{p}^{(0)} | \boldsymbol{E}_l^{\mathrm{pc}} \rangle = -{\sum_i}' \boldsymbol{p}^{(0)}\left(\boldsymbol{R}_i\right) \cdot \boldsymbol{E}^{\mathrm{pc}}\left(\boldsymbol{R}_i - \boldsymbol{l}\right) \\
&= -{\sum_i}' p^{(0)}\left(\boldsymbol{R}_i\right) E^{\mathrm{pc}}\left(\boldsymbol{R}_i - \boldsymbol{l}\right) \cos\left(\beta\left(\boldsymbol{R}_i\right)\right) ,
\end{aligned} \tag{1.73}
$$

where $\beta\left(\boldsymbol{R}_i\right)$ denotes the angle at site i between the field of the point charge at $\boldsymbol{l}$ and the dipole moment induced by the charge at $\boldsymbol{0}$. While in the one-dimensional case the relative sign determined whether the dipole at i contributes to the (anti-)screening the contribution, in higher dimensions is given by $\cos\left(\beta(\boldsymbol{R}_i)\right)$. If $\beta < \pi/2$, we therefore obtain a screening and otherwise an anti-screening contribution to the sum (1.73). Obviously, if the field vector is perpendicular to the dipole moment this dipole has no contribution at all. Hence, for radially aligned dipoles as we have for small polarizability α the anti-screening
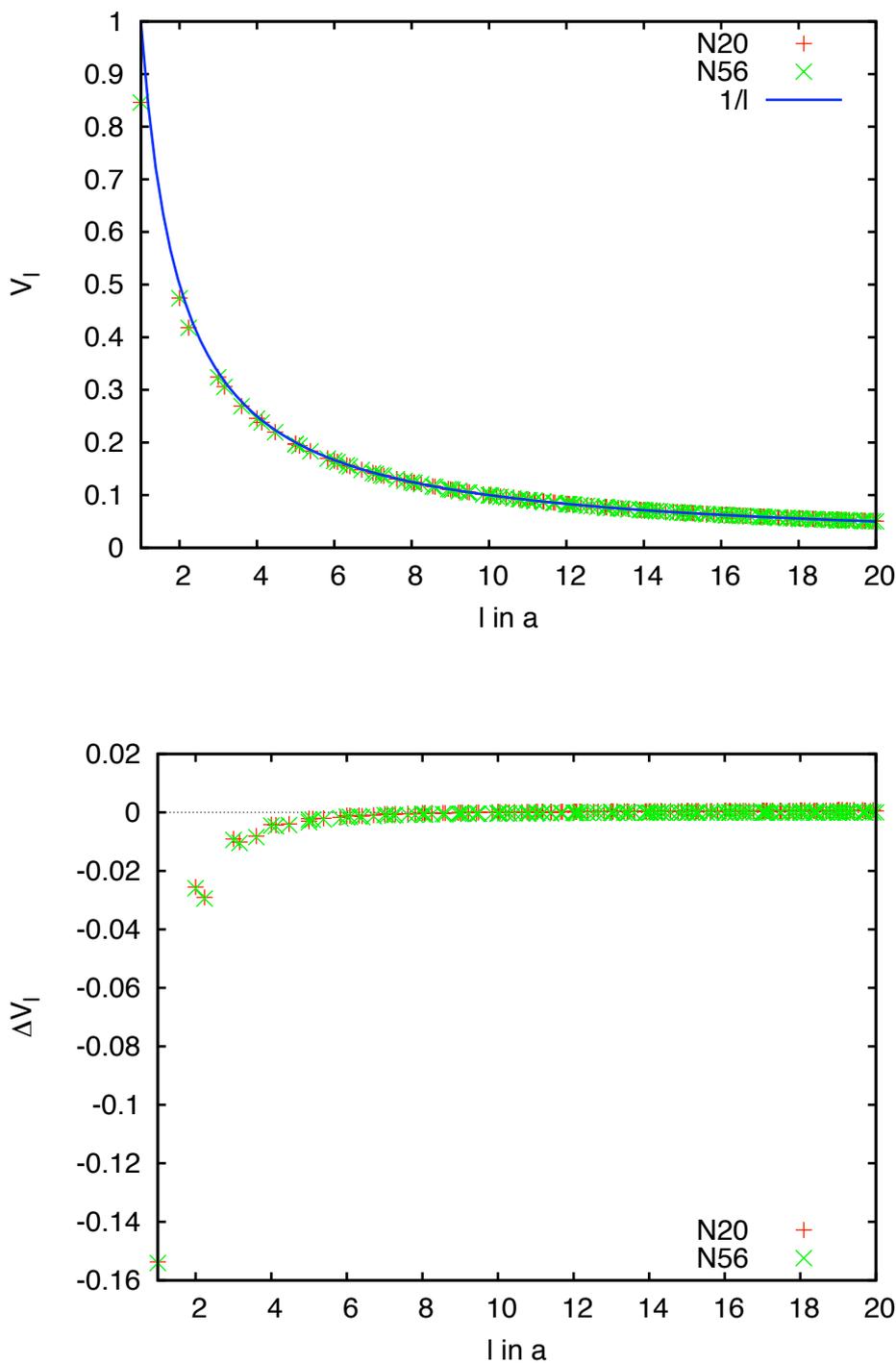
Figure 1.21.: Screened Coulomb parameters V_l (upper) and screening correction ΔV_l (lower) for a square lattice of polarizable point dipoles with polarizability $\alpha = 0.05$. Green crosses denote a system size of $N = 20$, red crosses a size of $N = 56$. The blue line in the left figure denotes the unscreened vacuum Coulomb interaction $1/|l|$. Apart from local-field effects for short distances $|l|$ the Coulomb interaction is not screened.

volume is given by a circle with a diameter determined by l. This is illustrated in figure 1.22, where the anti-screening volume is marked with red arrows.

The anti-screening contribution is the largest along the line between both charges, since the cosine functions assumes its maximum for 0°. This is why anti-screening is most pronounced in one dimension, where this line actually coincides with the chain. In two dimensions the anti-screening contributions do not seem to be strong enough to eventually lead to (pronounced) anti-screening. There are simply too many neighbors in the "screening" volume always outweighing the dipoles in the anti-screening volume.

For large α, where the dipoles are no longer radially aligned (cf. lower plot of figure 1.19), the shape of the anti-screening volume is no longer a circle. For $\alpha = 0.195$ close to the instability figure 1.23 provides an example of a non-trivial anti-screening volume for $l = 8$. We will not further study this system due to its proximity to the ferroelectric instability. A treatment in reciprocal space is more appropriate (see next section).

To check for finite-size effects we again plot $1/\varepsilon_V = V_l \cdot l$. The upper plot of figure 1.24 gives the results for the two sizes, $N = 20$ and $N = 56$, for all directions in the crystal. Being an integrated quantity the scattering of the values for different crystallographic directions is less pronounced than for the electric field. For simplicity we therefore restrict ourselves to a high-symmetry direction along the crystal and study more system sizes (lower plot).

As expected, the curves deviate from each other the larger l and the smaller the system. Based on the size dependence for each l we can extrapolate to an infinitely large system. Using a quadratic extrapolation we obtain the red curve in figure 1.24. This gives a good approximation to the infinitely large crystal in this range.

We find that the Coulomb interaction is unscreened, i.e. $1/\varepsilon_V \to 1$. This behavior is analogous to our findings in the one-dimensional chain for the same reason: since the plane is embedded in three-dimensional space and therefore the three-dimensional Coulomb law holds, the dipoles in the two-dimensional plane cannot make up for the loss of the electric field strength proportional to r^2.

For finite systems there are finite-size effects close to the cluster boundary which manifest themselves as anti-screening. They stem from the substantially unequal treatment of the screening and anti-screening volume. The latter is entirely accommodated within the simulation cluster, whereas only small parts of the screening volume are included. The loss of screening may also be calculated analytically using the continuum limit integral method we used for the one-dimensional system.

All in all we have a situation similar to the one-dimensional case: for very short distances both Coulomb interactions are screened due to local-field effects. For large distances both are unscreened. The difference is, however, that in one dimension there is a domain of anti-screening which is absent in the two-dimensional plane.
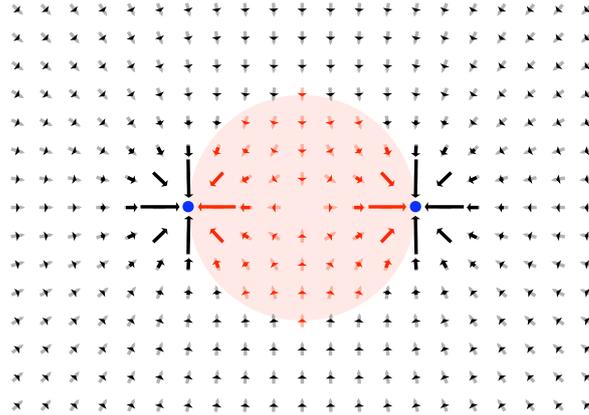
Figure 1.22.: Two-dimensional arrangement of screening dipoles induced by two point charges for a small polarizability ($\alpha = 0.02$). Compared to the screening dipoles for an individual point charge, the induced dipoles in the space between the charges is strongly reduced, since the fields of both charges shorten each other to a degree given by the angle β between the field vectors. This anti-screening volume (red circle) contains the lattice sites with $\beta < \pi/2$. On the line connecting the charges $\beta = 0$ and the anti-screening is strongest. That is why anti-screening is most pronounced in one-dimensional systems.
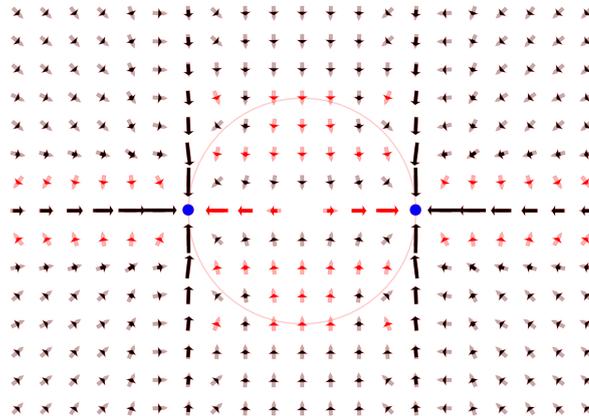
Figure 1.23.: Two-dimensional arrangement of screening dipoles induced by two point charges for a polarizability $\alpha = 0.195$ close to the instability. The anti-screening volume (red arrows) is considerably more complicated due to the complex dipole arrangement shown in the lower plot of figure 1.19. While equation (1.73) still yields the screening correction its summands do not solely determine the anti-screening volume. It is given by the total contribution of $\Delta V_l = -1/2 \left(\langle \boldsymbol{p}^{(0)} | \boldsymbol{E}_l^{\mathrm{pc}} \rangle + \langle \boldsymbol{p}^{(l)} | \boldsymbol{E}_0^{\mathrm{pc}} \rangle \right)$ at each lattice site. For comparison the light red circle denotes the anti-screening volume from figure 1.22.
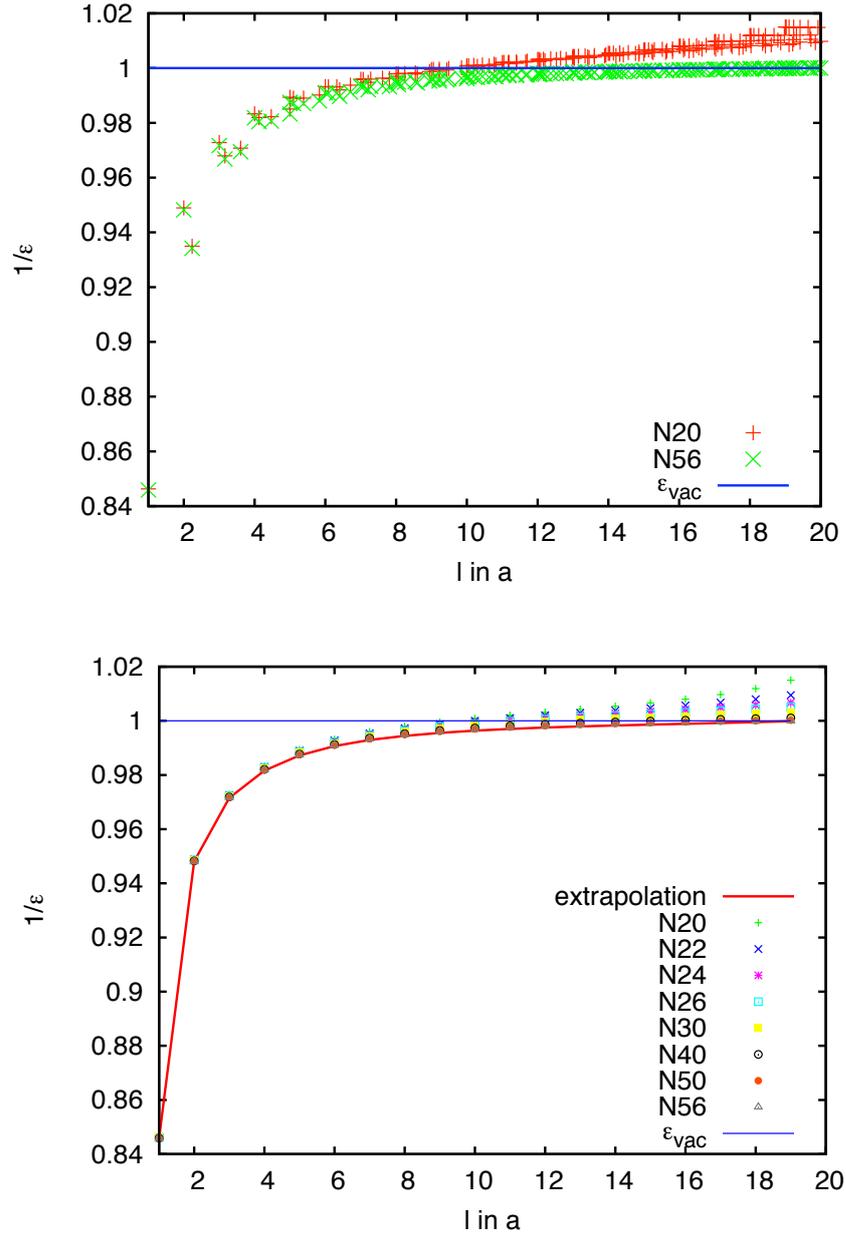
Figure 1.24.: $1/\varepsilon_V$ calculated from all Coulomb matrix elements $V_{\boldsymbol{l}}$ for finite systems with $N = 20, 56$ (red, green) (upper figure) and for more system sizes along crystallographic a-axis (lower figure) for a two-dimensional square lattice of polarizable point dipoles of polarizability $\alpha = 0.05$. In the domain of local-field effects (short distances) we observe screening in contrast to the one-dimensional chain. Finite-size artifacts, apparent at the cluster boundary, give rise to anti-screening. The reason is that the finite simulation cluster comprises the entire anti-screening volume but neglects most of the screening volume. With increasing system sizes the effect diminishes (lower figure). Using the cluster size dependence we can extrapolate to an infinitely large system (red curve). In analogy to the one-dimensional case the Coulomb integrals are unscreened for large distances in an infinite system.

1.3.3. Microscopic Field and Averaging

The actual microscopic field is given by

$$\boldsymbol{E}^{\text{micro}}(\boldsymbol{r}) = \boldsymbol{E}^{\text{ext}} + \sum_{\boldsymbol{R}_i} \boldsymbol{E}^{\text{dip}}(\boldsymbol{p}(\boldsymbol{R}_i), \boldsymbol{r} - \boldsymbol{R}_i) , \tag{1.74}$$

where $\boldsymbol{r}$ is a continuous coordinate in space. It has a considerably more complicated structure compared to the microscopic field at the lattice sites. For example, it diverges at the lattice sites because $\boldsymbol{r} \to \boldsymbol{R}_i$. The same is true for the potential which is easier to plot being a scalar field. The potential of a cutout of the planar system is depicted in figure 1.25. We observe the radial potential of the point charge at $(0,0)$ and the radially aligned (and diverging) dipole potentials at the different lattice sites.
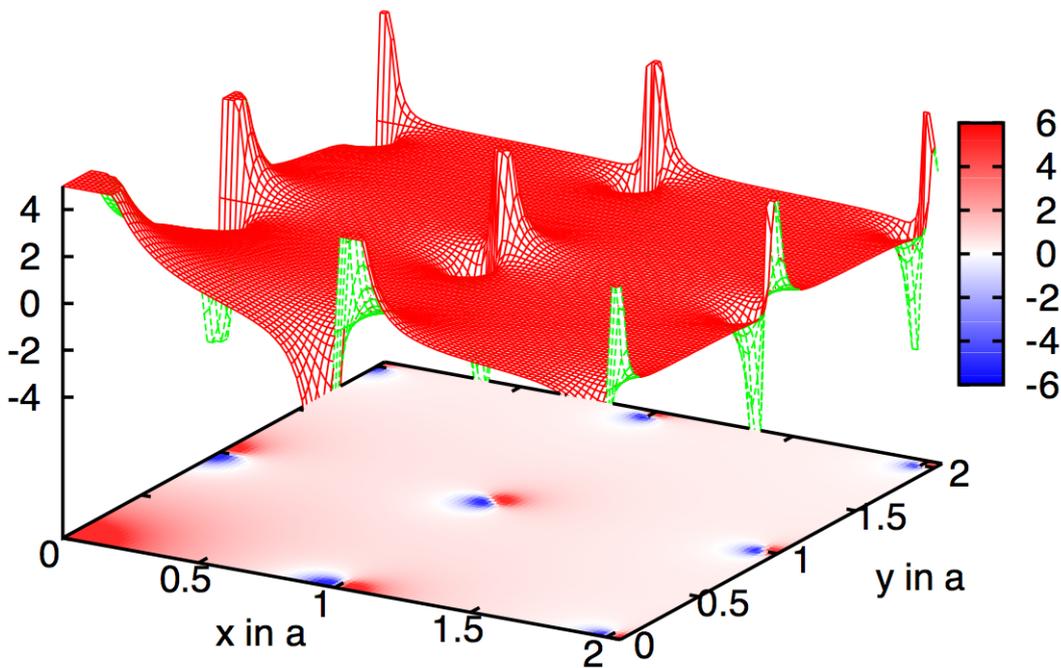
Figure 1.25.: Potential Φ of a two-dimensional square lattice ($a = 1$) of polarizable point dipoles ($\alpha = 0.05$) with a negative charge $q = -1$ at the origin. Divergencies have been cut at $\Phi = \pm 5$.

Let us briefly come back to the ostensible inconsistency of $1/\varepsilon_E \neq 1/\varepsilon_V = 1$. As in the one-dimensional case, for a macroscopic average of the microscopic electric field we need to use an averaging method which averages over regions large on the microscopic and small on the macroscopic scale expanding in three dimensions. Since the third dimension does not carry dipoles the average will eventually yield zero.

1.4. Screening in a Three-Dimensional Simple Cubic Lattice

In this section we study a three-dimensional simple cubic lattice of polarizable point dipoles. We find that the field $\boldsymbol{E}$ and Coulomb matrix elements are consistent with textbook electrostatics. Here, screening actually means a reduction in the strength of the fields and interactions. We use the Clausius-Mossotti relation to connect the microscopic polarizability and the macroscopic dielectric constant.

We start this section with a non-standard derivation of the Clausius-Mossotti relation, which is more suitable to our needs. This part is followed by the results obtained with the real-space code for a system with a relatively low polarizability. It is necessary to be sufficiently far away from the ferroelectric instability in order for the real-space MPDM to work properly – this is especially true for three dimensions where relatively small clusters can be treated. To study systems with high polarizability or even close to the instability we need to resort to the $\boldsymbol{k}$-space MPDM method, which we introduce at the end of this section.

1.4.1. Clausius-Mossotti Relation from the Microscopic Perspective

The Clausius-Mossotti relation, also known as Lorentz-Lorenz relation in refractivity, serves to establish a connection between the microscopic perspective of a solid and the macroscopic one. It is valid in the case of dielectrics in three dimensions without permanent polarization and assumes that the dielectric function is homogeneous. The standard derivation of the Clausius-Mossotti relation found in many standard textbooks [18, 19, 20] starts out from the macroscopic view and then constructs the connection to microscopic quantities of the lattice.

Since we gain results from a microscopic model, the opposite way seems more suitable. Following Aspnes [21] we first obtain the microscopic solution and then, in a second step, perform an appropriate averaging operation relating both perspectives.

Assume we have an infinitely large simple cubic lattice of polarizable point dipoles in a homogeneous external field $\boldsymbol{E}^{\mathrm{ext}}$ as well as the microscopic solution. Due to translational invariance all dipole moments are the same $\boldsymbol{p}(\boldsymbol{R}_i) = \boldsymbol{p}_i = \boldsymbol{p}$ for all sites i, as is the local field $\boldsymbol{E}^{\mathrm{local}}(\boldsymbol{R}_i) = \boldsymbol{E}^{\mathrm{local}}$, where

$$\boldsymbol{E}^{\mathrm{local}} = \boldsymbol{E}^{\mathrm{ext}} + \sum_{\boldsymbol{R}_i \neq \boldsymbol{0}} \boldsymbol{E}^{\mathrm{dip}}(\boldsymbol{p}, -\boldsymbol{R}_i) \tag{1.75}$$

according to equation (1.12). For a simple cubic system it is easy to see that the dipole summation term is identically zero due to symmetry [18]: the lattice vectors may be written as $\boldsymbol{x}_{ijk} = (ia, ja, ka)^t$, where a denotes the lattice constant and $i, j, k \in \mathbb{Z}$. Within

this notation the x component of the dipole summation term in (1.75) becomes

$$\boldsymbol{e}_x \cdot \boldsymbol{E}^{\text{dip}} = \sideset{}{'}\sum_{ijk} \frac{3\left(i^2 p_1 + ij p_2 + ik p_3\right) - \left(i^2 + j^2 + k^2\right) p_1}{a^3 \left(i^2 + j^2 + k^2\right)^{5/2}} \ . \tag{1.76}$$

The cross terms ij and ik vanish since i (or j) runs over all positive and negative numbers. In contrast the sums

$$\sideset{}{'}\sum_{ijk} \frac{i^2}{\left(i^2 + j^2 + k^2\right)^{5/2}} = \sideset{}{'}\sum_{ijk} \frac{j^2}{\left(i^2 + j^2 + k^2\right)^{5/2}} = \sideset{}{'}\sum_{ijk} \frac{k^2}{\left(i^2 + j^2 + k^2\right)^{5/2}} \ , \tag{1.77}$$

are non-zero but all equal. Hence, $\boldsymbol{e}_x \cdot \sum_{\boldsymbol{R}_i \neq \boldsymbol{0}} \boldsymbol{E}^{\text{dip}} = 0$. The same argument works for the y and z component and therefore, $\sum_{\boldsymbol{R}_i \neq \boldsymbol{0}} \boldsymbol{E}^{\text{dip}} = 0$ in a simple cubic crystal. Note that for other geometries this is generally not the case! For instance, for both low-dimensional systems treated above this does not hold (cf. equation (1.39) for one- and (1.67) for two-dimensional systems). However, for the simple cubic lattice the local field at each site is given by the external field applied to the system, i.e.

$$\boldsymbol{E}^{\text{local}} = \boldsymbol{E}^{\text{ext}} \ . \tag{1.78}$$

To establish the connection between the microscopic quantities and the macroscopic observable we perform a suitable averaging operation (see Kranendonk and Sipe [22]). For the dipoles

$$\boldsymbol{p}(\boldsymbol{r}) = \sum_i \alpha \boldsymbol{E}^{\text{micro}}(\boldsymbol{R}_i)\, \delta(\boldsymbol{r} - \boldsymbol{R}_i) \ . \tag{1.79}$$

and the microscopic field

$$\boldsymbol{E}^{\text{micro}}(\boldsymbol{r}) = \boldsymbol{E}^{\text{ext}} + \sum_{\boldsymbol{R}_i} \boldsymbol{E}^{\text{dip}}(\boldsymbol{p}(\boldsymbol{R}_i), \boldsymbol{r} - \boldsymbol{R}_i) \ , \tag{1.80}$$

this can be carried out straightforwardly since all unit cells are equivalent. Hence, we define the macroscopic dipole moment as

$$\boldsymbol{P} = \frac{1}{V} \int_V \mathrm{d}^3 r\ \boldsymbol{p}(\boldsymbol{r}) = \frac{1}{V} \sum_i \boldsymbol{p}_i = n\boldsymbol{p} = n\alpha \boldsymbol{E}^{\text{local}} \ . \tag{1.81}$$

V denotes the volume of the crystal and n the number of dipoles per unit volume. In the case of a simple cubic lattice we have $n = 1$. Similarly, we obtain the macroscopic electric field. The average of the first term of equation (1.80) being a constant is the term itself. To carry out the averaging operation on the second term we first calculate the average field of a single dipole. It is practical to represent the field in terms of the potential (see second term of equation (1.3)):

$$\langle \boldsymbol{E}^{\text{dip}}(\boldsymbol{p}) \rangle_V = -\int_V \mathrm{d}^3 r\ \boldsymbol{\nabla}\left(\frac{\boldsymbol{p} \cdot \boldsymbol{r}}{r^3}\right) = -\int_{\partial V} \mathrm{d}^r a\ \left(\frac{\boldsymbol{p} \cdot \boldsymbol{r}}{r^3}\right) = \begin{cases} -\dfrac{4\pi}{3}\boldsymbol{p} & \boldsymbol{p} \text{ inside } V \\ 0 & \boldsymbol{p} \text{ outside } V \end{cases} \ , \tag{1.82}$$

here V denotes an arbitrary volume. Similar to Gauss's theorem the integration does not depend on the choice of the volume V or its surface ∂V as long as the dipole is within V. For the averaging of equation (1.80) we again choose the entire crystal volume. With the aid of equation (1.82) we obtain

$$\boldsymbol{E}^{\text{macro}} = \boldsymbol{E}^{\text{ext}} - \frac{4\pi}{3}\boldsymbol{P} = \left(1 - \frac{4\pi}{3}n\alpha\right)\boldsymbol{E}^{\text{ext}} \tag{1.83}$$

for the macroscopic electric field.

In systems not exhibiting such a high level of symmetry we need to employ a more general averaging procedure. Therefore, we define the averaged macroscopic field as

$$\boldsymbol{E}^{\text{macro}}(\boldsymbol{r}) = \langle \boldsymbol{E}^{\text{micro}}(\boldsymbol{r})\rangle_{V(d)} = \frac{1}{V(d)}\int_{V(d)} \mathrm{d}^3\xi \ \boldsymbol{E}^{\text{micro}}\left(\boldsymbol{r} - \boldsymbol{\xi}\right) , \tag{1.84}$$

where d is a characteristic length of the averaging volume $V(d)$ and satisfies $a \ll d \ll \lambda$. λ characterizes the spatial variation of the macroscopic field. Thus, effectively the averaging is done over a volume which is large on the microscopic but small on the macroscopic scale – a mesoscopic volume. For the averaging to make sense, the enclosed number of dipoles should be proportional to the volume. To fulfil this criterion we take a simply connected convex volume $V(d)$. Usually a sphere or cube is taken for simplicity.

We define the macroscopic dielectric displacement

$$\boldsymbol{D} = \varepsilon\boldsymbol{E}^{\text{macro}} = \boldsymbol{E}^{\text{macro}} + 4\pi\boldsymbol{P} , \tag{1.85}$$

where ε is the macroscopic dielectric constant ε. With the the latter two parts of this definition and equation (1.83) we obtain the Clausius-Mossotti relation

$$n\alpha = \frac{3}{4\pi}\frac{\varepsilon - 1}{\varepsilon + 2} , \tag{1.86}$$

or equivalently,

$$\varepsilon = \frac{1 + 8\pi\alpha n/3}{1 - 4\pi\alpha n/3} . \tag{1.87}$$

It is important to note that the *macroscopic* external field $\boldsymbol{E}^{\text{macro}}$ is not equal to the *microscopic* external field. The latter is larger by $4\pi/3\boldsymbol{P}$ to compensate the field of the induced dipoles. We will observe a manifestation of this difference in the next section.

In low-dimensional systems we have seen that we cannot define macroscopic averages since at least one dimension does not carry dipoles and the three-dimensional average inevitably yields zero. In low-dimensional nano-devices, however, when the dimensions are large enough to properly accommodate an averaging volume the Clausius-Mossotti relation holds again. Interestingly, Mahan showed in 2006 that even though the dipole summations within this volume give rise to a generally non-vanishing term, $\boldsymbol{e}_i \cdot \sum_{\boldsymbol{R}_i \neq \boldsymbol{0}} \boldsymbol{E}^{\text{dip}} \neq 0$, $i \in \{x, y, z\}$, their effect is compensated by the surface charges of the nano-devices [23].

1.4.2. Numerical Solution for Moderate Polarizability in Real Space

With $a = 1$ for the lattice constant the Clausius-Mossotti relation predicts the ferroelectric instability to occur at $\alpha_{\mathrm{CM}} = 3/4\pi \approx 0.2387$. From figure 1.3 in section 1.1.4 we know that the lattice actually is unstable against spontaneous polarization for smaller $\alpha < \alpha_{\mathrm{CM}}$. The largest eigenvalue is found at the M-point $(\pi, \pi, 0)$. For the real-space simulations it is crucial to be sufficiently far away from the instability, since we can only treat small clusters. To that end, we choose $\varepsilon = 2.4$, which corresponds to a molecular polarizability of $\alpha \approx 0.076$. In order to obtain the dipoles, fields and the energy correction, we place a negative point charge $q = -1$ in the center of the cluster and employ the self-consistency scheme of figure 1.2.

1.4.2.1. The Electric Field

Figure 1.26 shows the self-consistent dipoles in the x-y-plane. Again, we obtain a mainly radial field. This reflects the fact that the system is indeed away from the instability.
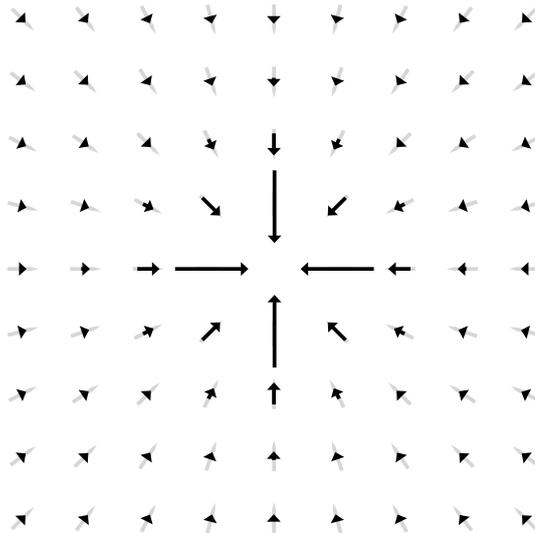
Figure 1.26.: Dipole arrangement in the x-y-plane ($z = 0$) induced by a negative point charge in the center of a three-dimensional cubic crystal of polarizable point dipoles with polarizability $\alpha \approx 0.076$ (cf. remarks of figure 1.19).

To study the screening behavior we study the dielectric-constant-like quantity $\varepsilon_E^{-1}(\boldsymbol{l}) = \boldsymbol{e}_r \cdot \boldsymbol{E}_l |l^2|$ as a function of the distance to the point charge. Figure 1.27 gives the results for three different system sizes $N = 16$, 20, and 22. The actual number of sites in the crystal is given by 35937, 68921, and 91125 ($\#\text{sites} = (2N + 1)^3$).
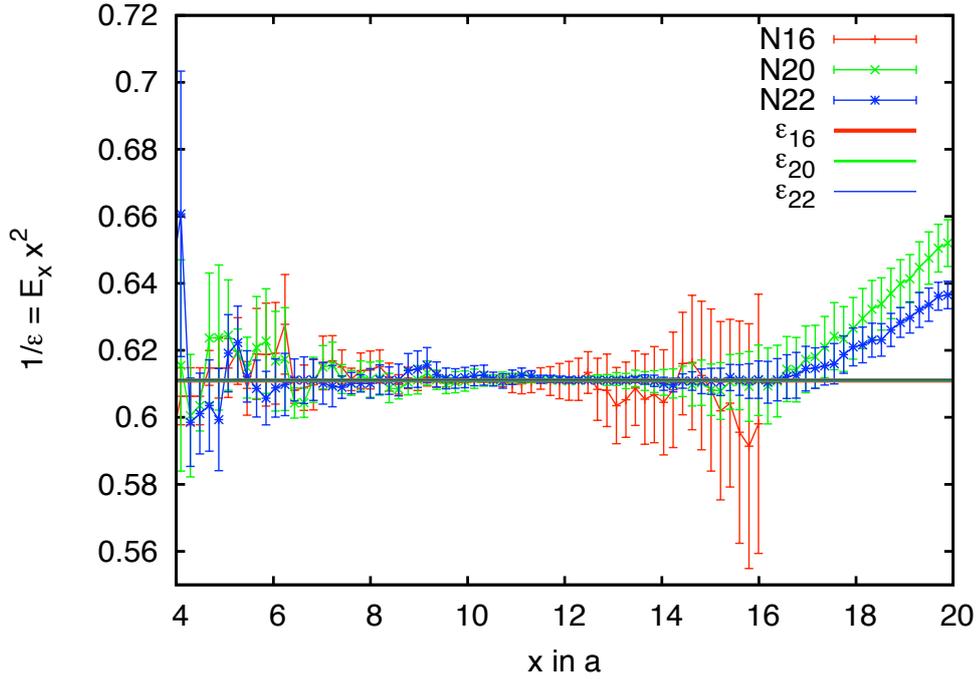
Figure 1.27.: $1/\varepsilon_E = \boldsymbol{e}_r \cdot \boldsymbol{E}_x^{\text{local}} x^2$ constructed from the radial component of the electric field of a three-dimensional cubic crystal of polarizable point dipoles with polarizability $\alpha \approx 0.076$. Red, green and blue denote system sizes of $N = 16$, 20, and 22, respectively. The horizontal multi-color line gives a weighted least-squares fit to obtain the "bulk" $1/\varepsilon_E$ (refer to text).

Already in the two-dimensional case (see figure 1.20) we observed a variation of the $\varepsilon_E^{-1}(|\boldsymbol{l}|)$ values for a given distance interval $|\boldsymbol{l} \pm \delta\boldsymbol{l}|$, where $\delta\boldsymbol{l}$ denotes a small region around l, due to different crystallographic directions in the square lattice. This is even more pronounced in three dimensions. In order to make the plot easier to interpret we define a binning for the results. The distances are discretized in bins of width w. For each bin we evaluate average value (solid lines) and standard deviation (error bar).

Close to the charge we observe local-field effects. From a distance of about 8 lattice constants the "bulk" domain starts, which gives an almost constant ε_E^{-1} and quite a small fluctuation. It is followed by a region towards the cluster boundary where finite-size effects become dominant. To obtain a good estimate for the "bulk" ε_E^{-1}, we perform a least-squares fitting in the region $[8, 16]$ weighted by the standard deviation. For all system sizes we obtain essentially the same result. It is plotted as the horizontal three-colored line in figure 1.27. The largest cluster of $N = 22$ yields $\varepsilon_E^{-1} = 0.61111 \pm 6.076 \cdot 10^{-5}$.

Obviously, the result does not agree with $\varepsilon^{-1} = 1/2.4 \approx 0.4167$, the reason being that ε

is a macroscopic, whereas ε_E by definition is a microscopic quantity. In the previous section we discussed how to perform the averaging operation. In three dimensions this averaging operation yields a result $\varepsilon^{-1} \neq 1$ in contrast to low-dimensional systems, where we found no screening at all for large distances seen from the macroscopic perspective. From (1.83) we know the connection between both perspectives, which is just a proportionality factor

$$\kappa = 1 - \frac{4\pi}{3} n\alpha \ . \tag{1.88}$$

Hence, for the actual macroscopic $1/\varepsilon$ we obtain

$$\frac{1}{\varepsilon} = \kappa \frac{1}{\varepsilon_E} \ . \tag{1.89}$$

For $\alpha \approx 0.0760$ we get $\kappa \approx 0.7614$ and as a result $1/\varepsilon \approx 0.4167$ which is exactly the inverse of the dielectric constant we started out with.

1.4.2.2. The Coulomb Parameters

For the evaluation of the Coulomb parameters we again use

$$\Delta V_{\boldsymbol{l}} = -\sum_{\boldsymbol{R}_i}{}' \boldsymbol{p}(\boldsymbol{R}_i) \cdot \boldsymbol{E}(\boldsymbol{R}_i - \boldsymbol{l}) \ , \tag{1.90}$$

where $\boldsymbol{E}(\boldsymbol{r})$ is the field of a point charge given by equation (1.10) and $\boldsymbol{p}(\boldsymbol{R}_i)$ denotes the dipole at lattice site $\boldsymbol{R}_i$ induced by a charge at the origin. The prime at the sum means that lattice sites $\boldsymbol{R} = \boldsymbol{0}$ and $\boldsymbol{R} = \boldsymbol{l}$ are skipped in the summation. This formula is especially suitable for the actual numerical calculation since the dipoles $\boldsymbol{p}(\boldsymbol{R}_i)$ can be reused from the calculation of the energy correction of the local Hubbard term $\Delta U = \Delta V_{\boldsymbol{0}}$. Consequently, we just need to have one computationally intensive run to obtain ΔU using the self-consistency scheme shown in figure 1.2. The other Coulomb elements follow from a cheap postprocessing step applying formula (1.90).

First, we plot the ε_V^{-1} of the Coulomb parameters $V_{\boldsymbol{l}}$ along a high-symmetry crystal axis, for instance $\boldsymbol{l} = l\boldsymbol{e}_x$, to understand the qualitative characteristics of this system. Figure 1.28 shows the result for three different system sizes $N = 16, 20$, and, 22. The self-consistency calculation is done for cubes of edge length $2N + 1$. We then evaluate the Coulomb matrix elements $V_{\boldsymbol{l}}$ according to equation (1.90) for a sphere cut out of the cubes.

Instead of obtaining an almost horizontal line with approximately $\varepsilon_{\text{bulk}}^{-1} = \varepsilon_V^{-1} = 1/2.4$ we observe an almost linear behavior up until about $|\boldsymbol{l}| = R$. At $|\boldsymbol{l}| > R$ the test charge giving rise to $\boldsymbol{E}$ in (1.90) does not overlap with the dipole cluster anymore. We find near-field effects which express themselves as a bend in the curve towards the far-field limit, the vacuum $\varepsilon_{\text{vac}}^{-1} = 1$. Here, the dipoles merely mediate the field of the point charge within the crystal to the outside and we can effectively treat the cluster as a point charge.

Looking at the slopes of the linear error in the dielectric constant we find that they decrease with system size. A more careful investigation shows that the slope decays proportional to $1/\lambda$, where λ is a characteristic length scale of the system, for instance, the radius R. Hence, it is an effect of finite size.
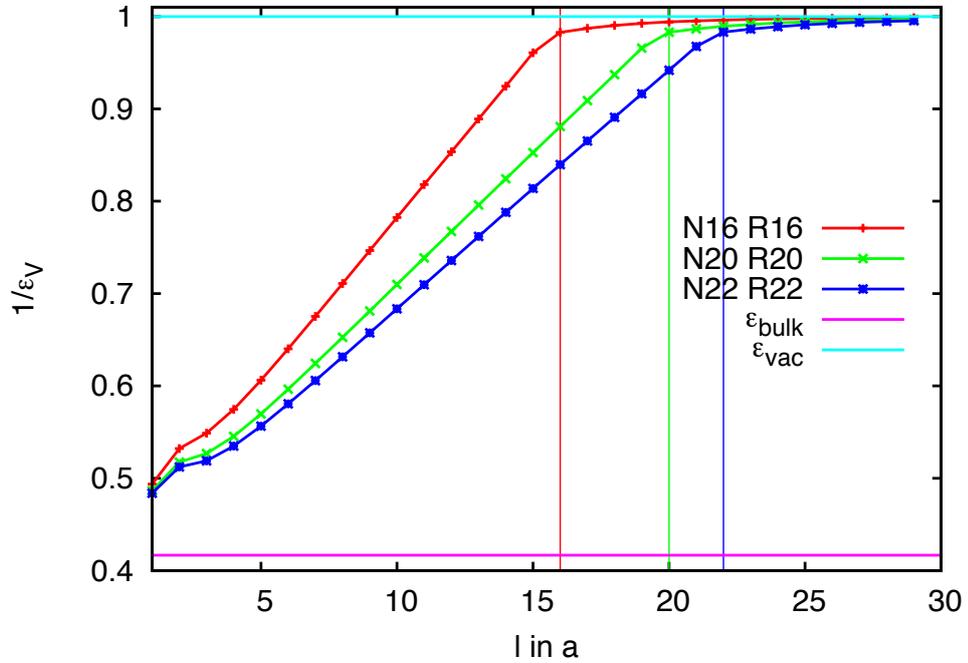
Figure 1.28.: $1/\varepsilon_V$ calculated from the Coulomb matrix elements $V_{\boldsymbol{l}}$ along a high-symmetry crystallographic axis for a sphere with radius $R = N$ embedded in finite systems with cube length $N = 16, 20, 22$ (red, green, blue). The crystal consists of polarizable point dipoles of polarizability $\alpha \approx 0.076$. Instead of the constant behavior with $1/\varepsilon_{\mathrm{bulk}}$ (magenta line) we observe a linear error in $1/\varepsilon_V$ which is due to the finite size of the system (see text). For $|\boldsymbol{l}| > R$ the test charge giving rise to $\boldsymbol{E}$ in (1.90) does not overlap with the dipoles anymore. Outside but close to the cluster we see near-field effects as a bend in the curve. The near field decays to the far field yielding the familiar vacuum behavior $1/\varepsilon_{\mathrm{vac}}$ (light blue line).

The Continuum Limit and the Finite-Size Error of the Real-Space Method
Neglecting local-field effects we can calculate the dipoles as

$$
\boldsymbol{p}\left(\boldsymbol{R}_i\right) = -\frac{q\alpha}{\varepsilon\kappa}\frac{\boldsymbol{R}_i}{\left|\boldsymbol{R}_i\right|^3} \; ,
\tag{1.91}
$$

where we used κ to obtain the microscopic local $\varepsilon_E = \varepsilon\kappa$ from the actual dielectric constant as given by equation (1.89). Inserting equations (1.10) and (1.91) in (1.90) yields

$$
\Delta\tilde{V}_{\boldsymbol{l}} = -\frac{q^2\alpha}{\varepsilon\kappa}\sum_{\boldsymbol{R}_i}{}'\frac{\boldsymbol{R}_i}{\left|\boldsymbol{R}_i\right|^3}\frac{\boldsymbol{R}_i - \boldsymbol{l}}{\left|\boldsymbol{R}_i - \boldsymbol{l}\right|^3} \; .
\tag{1.92}
$$

To actually evaluate equation (1.92) we use the continuum approximation introduced in section 1.2.3.2 for the one-dimensional system. $\boldsymbol{R}_i$ becomes a continuous vector $\boldsymbol{r} \in \mathbb{R}^3$ and we replace the sum with the integral

$$
\Delta\tilde{V}_{\boldsymbol{l}} = -\frac{q^2\alpha}{\varepsilon\kappa}\int_{S(R)}\mathrm{d}^3r\,\frac{\boldsymbol{r}}{\left|\boldsymbol{r}\right|^3}\frac{\boldsymbol{r} - \boldsymbol{l}}{\left|\boldsymbol{r} - \boldsymbol{l}\right|^3} \; ,
\tag{1.93}
$$

where $S(R)$ denotes a sphere with radius R encircling both charges. This integral may be evaluated analytically. Rewriting as

$$
\int_{S(R)}\mathrm{d}^3r\,\frac{\boldsymbol{r}}{\left|\boldsymbol{r}\right|^3}\frac{\boldsymbol{r} - \boldsymbol{l}}{\left|\boldsymbol{r} - \boldsymbol{l}\right|^3} = \int_{S(R)}\mathrm{d}^3r\,\left(-\boldsymbol{\nabla}\frac{1}{\left|\boldsymbol{r}\right|}\right)\left(-\boldsymbol{\nabla}\frac{1}{\left|\boldsymbol{r} - \boldsymbol{l}\right|}\right) \; ,
\tag{1.94}
$$

enables us to use Green's first identity

$$
\int_V\mathrm{d}V\,\left(\nabla\phi\right)\left(\nabla\psi\right) = \int_{\partial V}\mathrm{d}S\,\psi\left(\boldsymbol{\nabla}\phi\cdot\mathbf{n}\right) - \int_V\mathrm{d}V\,\left(\psi\Delta\phi\right) \; ,
\tag{1.95}
$$

where $\phi, \psi \in \mathcal{C}^2$ and $\boldsymbol{n}$ is the outward pointing surface-normal of dS. With the help of Poisson's equation, i.e. $\Delta 1/r = 4\pi\,\delta^3(r)$, we finally obtain

$$
\Delta\tilde{V}_{\boldsymbol{l}} = -\frac{4\pi q^2\alpha}{\varepsilon\kappa}\left(\frac{1}{\left|\boldsymbol{l}\right|} - \frac{1}{R}\right) \; .
\tag{1.96}
$$

For an infinitely large crystal, i.e. $R \to \infty$, the screening energy correction is

$$
\Delta\tilde{V}_{\boldsymbol{l}} = -\frac{4\pi q^2\alpha}{\varepsilon\kappa}\frac{1}{\left|\boldsymbol{l}\right|} \; .
\tag{1.97}
$$

Therefore the full Coulomb interaction follows

$$
\tilde{V}_{\boldsymbol{l}} = \frac{q^2}{\left|\boldsymbol{l}\right|} - \frac{4\pi q^2\alpha}{\varepsilon\kappa}\frac{1}{\left|\boldsymbol{l}\right|} = \frac{q^2}{\varepsilon\left|\boldsymbol{l}\right|} \; ,
\tag{1.98}
$$

which obviously is the expected statically screened Coulomb potential in a dielectric medium.
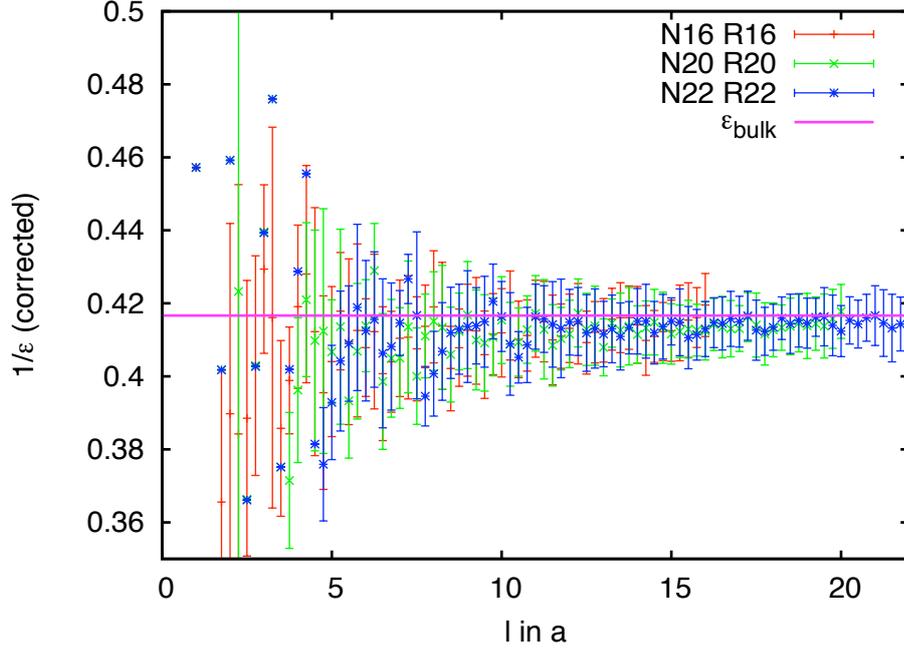
Figure 1.29.: $1/\varepsilon_V$ calculated from the Coulomb matrix elements V_l for all directions within a sphere with radius $R = N$ embedded in finite systems with cube length $N = 16, 20, 22$ (red, green, blue). The crystal consists of polarizable point dipoles of polarizability $\alpha \approx 0.076$. The correction (1.99) fixes the linear error and we obtain the proper bulk behavior $1/\varepsilon_{\mathrm{bulk}} = 1/2.4$.

However, in our real space MPDM code we can only treat finite systems and therefore, the second term in equation (1.96) has a non-vanishing contribution. Just as the linear error in our numerical results, it decays with a characteristic length $1/R$. Having done the calculation for a sphere of radius R cut out of the lattice we can correct the Coulomb parameter using

$$V_l = V_l^{\mathrm{num}}(R) - \frac{4\pi q^2 \alpha}{\varepsilon \kappa} \frac{1}{R} \,, \tag{1.99}$$

where $V_l^{\mathrm{num}}(R)$ denotes the numerically derived Coulomb parameter for the sphere cluster of radius R.

Figure 1.29 gives the result for all directions in the cluster. Just as in the case of electric fields we plot the average of all directions for a bin at a given distance with the standard deviations as the error bars (see previous section for details on the binning strategy). Apparently, we successfully corrected the constant error in the potential thanks to the correction term in equation (1.99). We again find local-field effects close to the charge

giving rise to strong fluctuations in the deviation and the average value. From about $l = 8a$ we observe that the bulk dielectric constant $\varepsilon_{\text{bulk}}^{-1} = 1/2.4$ is reproduced quite well. Surprisingly this also holds for the potential at the boundary of the cluster in contrast to the electric field shown in figure 1.27.

However, for more complicated crystal structures or higher polarizabilities th real-space approach quickly meets its limits due to finite-size effects.

1.4.3. Numerical Solution in Reciprocal Space

Therefore, we turn to $\boldsymbol{k}$-space (see section 1.1.4), where we effectively evade finite-size effects and directly treat infinitely large systems. We begin with a short introduction to the method and then evaluate the energy corrections for simple cubic systems of different polarizabilities – even α quite close to the ferroelectric instability. For the moderate $\alpha \approx 0.076$ we compare the $\boldsymbol{k}$-space results to those derived in real-space.

1.4.3.1. The method

The method is analogous to the one-dimensional case (see section 1.2), except that the diagonalization of the dipole-dipole matrix Γ is not as simple. We employ Ewald's method (see appendix A) to obtain the $\boldsymbol{k}$-space representation $\Gamma(\boldsymbol{k})$ that is directly diagonalizable.

With $\gamma_{\boldsymbol{k}n}$ being the eigenvalue and $\langle \boldsymbol{k}n | \boldsymbol{E_0} \rangle$ the eigenvector we can write the energy correction $\Delta V_{\boldsymbol{l}}$ as

$$\Delta V_{\boldsymbol{l}} = - \sum_{n, \boldsymbol{k} \in 1.\text{BZ}} e^{-\mathrm{i}\boldsymbol{k}\boldsymbol{l}} \, |\langle \boldsymbol{E_0} | \boldsymbol{k}n \rangle|^2 \left(\alpha^{-1} - \gamma_{\boldsymbol{k}n} \right)^{-1} \, . \tag{1.100}$$

For the actual evaluation we need the transform of the field of a point charge on a real-space grid to $\boldsymbol{k}$-space, $\boldsymbol{E}(\boldsymbol{k})$. The direct evaluation of the Fourier transform

$$\boldsymbol{E}(\boldsymbol{k}) = \sum_i e^{-\mathrm{i}\boldsymbol{k}\boldsymbol{r_i}} \frac{q}{|r_i|^2} \hat{\boldsymbol{r_i}} \tag{1.101}$$

converges but convergence slows down, when approaching the divergence at the Γ-point.

The continuous Fourier transform of the field of a point charge can be readily calculated analytically instead, giving

$$\boldsymbol{E}^{\text{cont}}(\boldsymbol{k}) = -\frac{4\pi\mathrm{i}}{|k|} \boldsymbol{e_k} \, , \tag{1.102}$$

where $\boldsymbol{e_k}$ is the unit vector in $\boldsymbol{k}$ direction.

The Poisson resummation (see appendix F) provides the connection between both, the continuous and the discrete Fourier transform. It is essentially a periodic extension of the continuous Fourier transform with respect to the reciprocal lattice vectors, i.e.

$$\boldsymbol{E}(\boldsymbol{k}) = \sum_{\boldsymbol{G}} \boldsymbol{E}^{\text{cont}}(\boldsymbol{k} + \boldsymbol{G}) = -4\pi\mathrm{i} \sum_{\boldsymbol{G}} \frac{\boldsymbol{k} + \boldsymbol{G}}{|\boldsymbol{k} + \boldsymbol{G}|^2} \, . \tag{1.103}$$
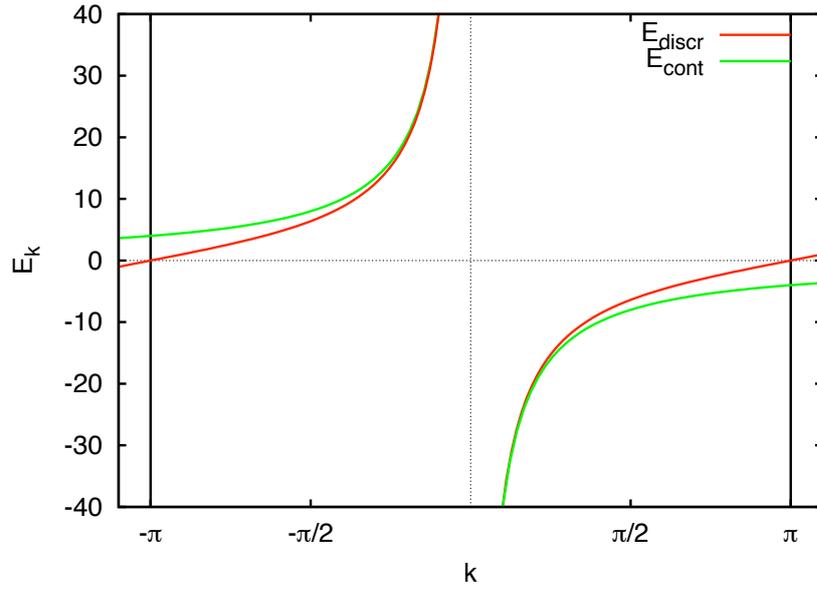
Figure 1.30.: Continuous (green) and discrete (red) Fourier transform for a simple cubic lattice of the field of a point charge. The Poisson resummation establishes the connection between both and effectively is a periodic extension of the continuous Fourier transform. Close to the Γ-point both fields agree very well.

For the numerical evaluation of the Fourier transform we can only sum over a finite number of Brillouin zones. Therefore, we insert an additional Gaussian convergence factor, $\exp(-\beta(\boldsymbol{k}+\boldsymbol{G}))$, to each term in the sum. β is chosen in such a way, that the numerical contribution of the term with the largest $\boldsymbol{G}_{\max}$ is below a threshold value ε, for instance $\varepsilon = 10^{-14}$. Thus, we effectively obtain the discrete Fourier transform of the Gaussian-shielded field,

$$\boldsymbol{E}_\beta(\boldsymbol{k}) = \sum_{\boldsymbol{G}} \boldsymbol{E}^{\mathrm{cont}}(\boldsymbol{k}+\boldsymbol{G})e^{-\beta(\boldsymbol{k}+\boldsymbol{G})} \ . \tag{1.104}$$

Performing this calculation for different values of small β and extrapolating to $\beta = 0$, we finally get $\boldsymbol{E}(\boldsymbol{k})$.

Figure 1.30 compares both Fourier transforms – the continuous and the discrete for a simple cubic lattice. We observe that close to the Γ-point both results match. They deviate, however, significantly at the border of the Brillouin zone due to the periodic extension.

Given the field $\boldsymbol{E}(\boldsymbol{k})$ we can now numerically evaluate the screening correction (1.100) for differently dense grids of the first Brillouin zone. Finally, we extrapolate to the infinitely dense $\boldsymbol{k}$-grid.

The Γ-point, if present in a sampling, needs special treatment. Since the Coulomb interaction diverges for $\boldsymbol{k} \to \boldsymbol{0}$ due to its long-range nature, we cannot directly evaluate the $\boldsymbol{k} = \boldsymbol{0}$ point. This applies also to the electric field. Still, an integral containing the Γ-point gives a finite value. We therefore replace the infinite contribution of $\boldsymbol{k} = \boldsymbol{0}$ in equation (1.100) by an integral over a sphere whose volume is equal to the volume of the $\boldsymbol{k}$-point in the sampling. For an equidistant grid with N_k^3 grid points in the Brillouin zone we have $V_k = V_{\mathrm{BZ}}/N_k^3$. Since close to the Γ-point the continuous and discrete fields are essentially equal we can safely use equation (1.102) as very good approximation for $\boldsymbol{E}(\boldsymbol{k})$ and obtain for the contribution of the Γ-point

$$V_{\boldsymbol{l}}^{(\Gamma)} = -\frac{8\pi K V_c}{3} \sum_n \left(\alpha^{-1} - \gamma_{\boldsymbol{0}n}\right)^{-1} \;, \tag{1.105}$$

where K is the radius of the sphere of volume $V_k = 4\pi/3K^3$, i.e. $K = (3V_k/4\pi)^{1/3}$. V_c denotes the volume of the unit cell in real-space.

1.4.3.2. Results

Using this $\boldsymbol{k}$-space approach we evaluate the Coulomb parameter $V_{\boldsymbol{l}}$ along a high-symmetry axis for different polarizabilities. At first we chose $\alpha \approx 0.076$ ($\varepsilon = 2.4$) to compare to the real-space results of the previous section. Figure 1.31 gives the extrapolation to the infinitely dense $\boldsymbol{k}$-space grid based on $N_k = 384^3$, 192^3, 96^3 (green line) as well as the real-space extrapolation (red line) for $l = 0, 1, 2, 3$ along a high symmetry axis. The results of both methods are in good agreement. However, we expect the $\boldsymbol{k}$-space approach to yield more accurate results. The real-space approach relies on small clusters and needs a finite-size error treatment. The $\boldsymbol{k}$-space code on the other hand just needs to handle small matrices for each $\boldsymbol{k}$-point in the Brillouin zone. Hence, we can easily afford very dense $\boldsymbol{k}$-grids yielding more reliable results.

For high polarizabilities the real-space approach is not applicable at all since finite-size effects become dominant. The $\boldsymbol{k}$-space approach avoids these problems by effectively treating infinitely large crystals. Figure 1.32 gives some results for high polarizabilites up to values very close to the instability (see magenta boxes). We see a very good agreement of the Clausius-Mossotti derived $1/\varepsilon$ and $1/\varepsilon_V$ for distances larger than the region of finite-size effects. Again we observe that these effects become more pronounced and extended the higher polarizabilities.

1.5. Summary

In this chapter we discussed how to effectively describe a non-polar molecular crystal (with localized charge distributions at the lattice sites) in terms of a microscopic (polarizable) point-dipole model (MPDM). Within this model we show how to obtain the arrangement of dipole moments and the energy corrections due to screening. We discuss two different
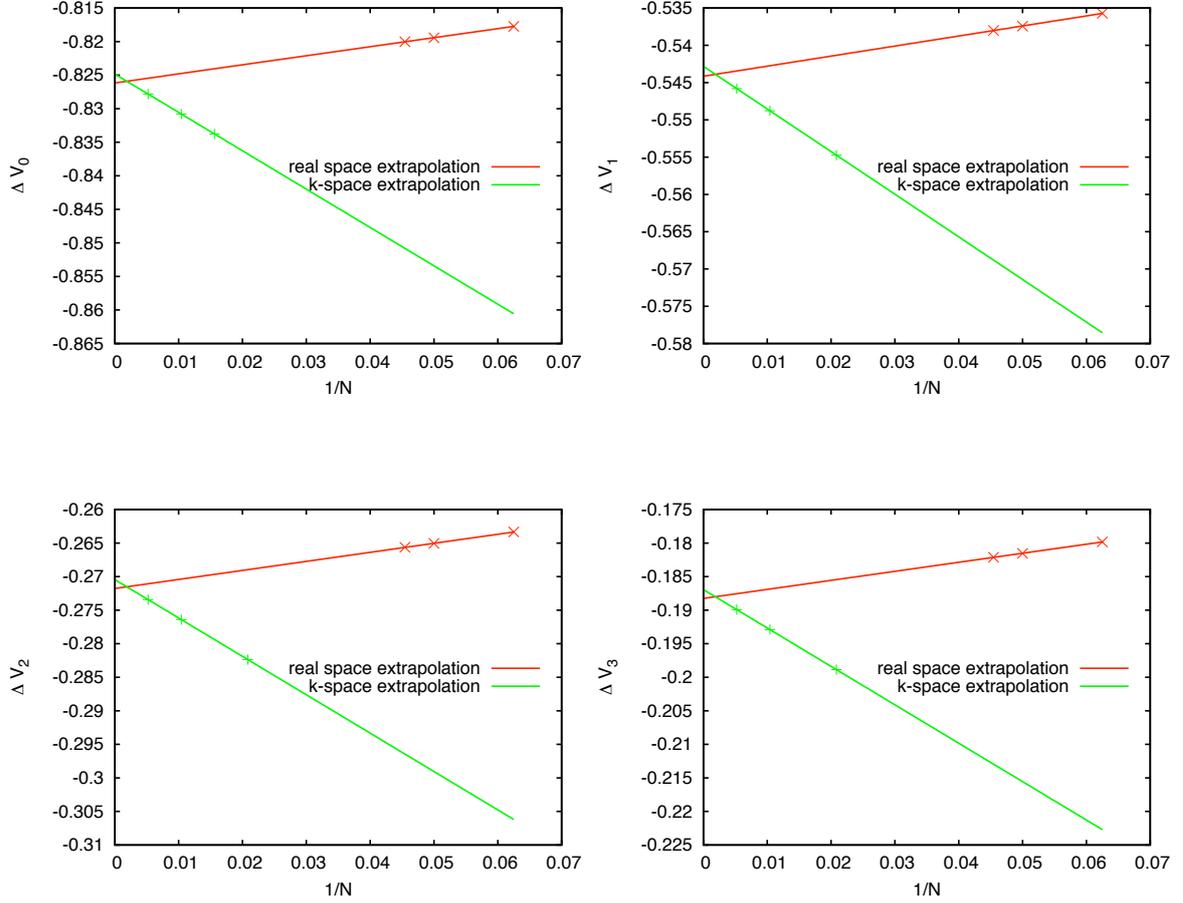
Figure 1.31.: V_l extrapolation for a simple cubic crystal with $\alpha \approx 0.076$ ($\varepsilon = 2.4$). The green lines represent the real-space extrapolation to infinitely large grids based on the results for $N = 16$, 20, 22. The red lines provide the extrapolation to the infinitely dense grid in **k**-space based on $N_k = 384^3$, 192^3, 96^3. The different plots denote different distances l along a high-symmetry axis, namely $l = 0$, 1, 2, 3. We observe good agreement for both methods. We expect the real-space approach to be less accurate due to small system sizes and the explicit finite-size correction.
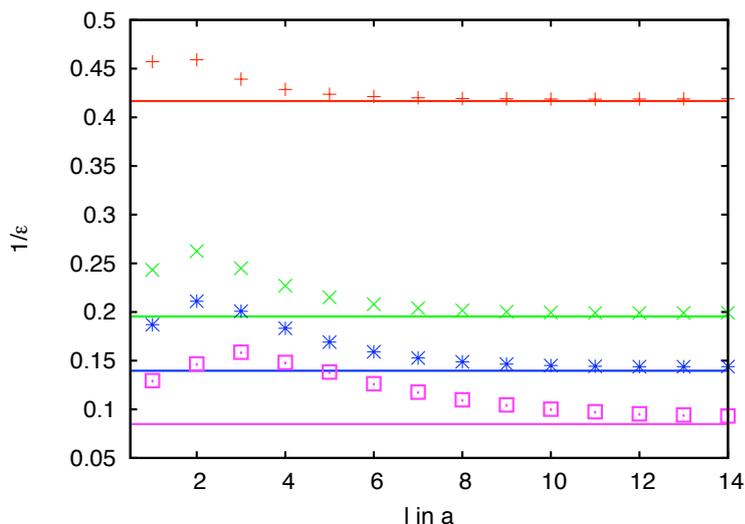
Figure 1.32.: V_l of a simple cubic crystal for $\alpha = 0.076, 0.138, 0.161$ and $\alpha \lessgtr \alpha_c$ calculated with the $\boldsymbol{k}$-space method and extrapolated to the infinitely dense Brillouin zone sampling. We observe good agreement with the Clausius-Mossotti relation (horizontal lines) outside the domain of finite-size effects.

treatments – a real-space and a $\boldsymbol{k}$-space approach. Except for the one-dimensional case, which is solvable analytically, we have to rely on numerical calculations for either method.

In one- and two-dimensional systems we find exotic screening and anti-screening effects, which we can understand in terms of an anti-screening volume argument. Asymptotically, the interaction is unscreened leading to results seemingly in contradiction with macroscopic electrostatics. This contradiction is, however, resolved by noting that the averaging procedures leading to macroscopic electrostatics are not appropriate for dipoles restricted to lower-dimensional manifolds.

For three-dimensional lattices the usual screening behavior is recovered. We can properly describe the screening for distances larger than the local-field effects with the Clausius-Mossotti relation relating the microscopic α to the macroscopic world. Still, unusual screening patterns appear for high-polarizabilities when the largest eigenvalue of the dipole-matrix is not situated at the Γ-point. In the asymptotic limit Coulomb matrix elements are screened with $1/\varepsilon$.

Our numerical codes to solve the MPDM provide us with means to study the inter-molecular screening corrections to Coulomb integrals in real organic crystals. Actual calculations for two compounds, TTF-TCNQ and (BEDT-TTF)$_2$I$_3$, will be presented in chapter 2. We find that the inter-molecular screening gives sizable contributions to the model parameters, which turn out to be important for a realistic description.

Organics

Molecules are the basic building blocks of organic crystals. Within those crystals molecules are held together by weak van der Waals or electrostatic interactions. We study two compounds, TTF-TCNQ and (BEDT-TTF)$_2$I$_3$. The constituents of both are non-polar molecules. Taken by themselves the molecules have closed shells and are quite stable. This suggests a two-step approach. We first deal with the constituents and study their

properties. Afterwards, we assemble the molecules into a solid and tackle the additional complications imposed by the full crystal. Interestingly, this approach is quite similar to the actual synthesis. For chemists these systems are of paramount importance since they allow for relatively easy molecular and crystal engineering. Hence, organic solids already bring us close to designing materials with desired physical properties – the common goal of chemists and physicists.

Both systems studied here are binary systems, i.e. the crystal is built from two different molecules. Constructing the crystal out of TTF and TCNQ or BEDT-TTF and I_3, respectively, leads to a charge-transfer, similar to salts – hence the name: charge-transfer salts. Unlike in ordinary salts the transfer of electrons leads to incompletely filled bands and might give rise to metallic behavior. Remarkably, TTF-TCNQ, for instance, is a good metal albeit containing not a single metal-atom – it is a metal-free metal. Due to their crystal structure the conductance of many organic solids is highly anisotropic. It can vary by several orders of magnitudes for different crystallographic directions. Hence, we have effectively low-dimensional metals, where TTF-TCNQ is a quasi one- and $(BEDT\text{-}TTF)_2I_3$ a quasi two-dimensional system.

Being weakly bound, the overlap between the molecular orbitals of adjacent molecules is rather small and so are the hopping-matrix elements relative to the Coulomb integrals. Hence, we deal with strongly correlated materials in low dimensions. This is a combination which potentially leads to striking many-body effects. A particularly exotic example is the spin-charge separation found in TTF-TCNQ.

In strongly correlated systems electrons loose their individuality. Consequently, standard methods based on single-particle mean-field pictures break down – even for qualitative statements. Instead, we have to deal with a full quantum-many body problem, whose solution is intractable. To that end, we replace the full Hamiltonian with an effective- or model-Hamiltonian, which only contains dominant effects and important single-particle orbitals. In this chapter we will show how to extract the model parameters for a realistic description of organic solids in terms of the Hubbard model using the examples of TTF-TCNQ and $(BEDT\text{-}TTF)_2I_3$.

Even though we cannot use density-functional theory (DFT) to describe the entire organic crystal, we can employ it for the building blocks. From DFT we obtain the hopping-matrix elements as well as the bare and intra-molecularly screened Coulomb parameters. With the crystal structure taken from X-ray scattering experiments we construct the full crystal and obtain the screening contributions caused by the electrons of all molecules using the distributed dipole approach. For its solution we employ the methods developed in chapter 1.

This chapter is structured in five parts. We start with a general introduction to density-functional theory. While the underlying theory is the same for all DFT codes, they differ significantly in their approaches. We therefore dedicate the second section to the code we employ: FHI-aims (Fritz-Haber Institut's Ab Initio Molecular Simulations). Afterwards, we sent how to actually extract the model parameters from DFT and our screening code presented in the previous chapter. In the final two sections we apply these methods to two organic systems – TTF-TCNQ and $(BEDT\text{-}TTF)_2I_3$.

2.1. Electronic Structure Theory

2.1.1. Density-Functional Theory

The most successful approach to electronic structure calculations so far is density-functional theory (DFT). In the Kohn-Sham framework with the current approximation to the exchange-correlation functional it is applicable to systems where a single-particle picture for the electrons can appropriately describe the electronic structure. This is the case when electronic correlations are not too strong.

Quantum chemical methods beyond Hartree-Fock theory [24, 25] such as Configuration Interaction [26], Coupled Cluster [27], Møller and Plesset [28] are wavefunction-based. They can give quite accurate results for the correlation energy. However, for large systems they are computationally very demanding.

In contrast, DFT offers a tremendous reduction in complexity since its fundamental variable is the electron density ρ, which is a function of three coordinates, whereas the wavefunction depends on $3N_e$ coordinates. The original idea to use the density instead of the wavefunction stems from 1927. Thomas [29] and Fermi [30] devised a method that considered (classically) interacting electrons in an external potential $v(r)$. The kinetic energy is approximated by the kinetic energy functional of the homogeneous electron gas. This theory, though giving some qualitative trends for total energies of atoms, did not even capture chemical bonding due to the overly simplistic kinetic energy lacking shell effects. However, it inspired Hohenberg and Kohn in the 1960s to think about the possibility of having a complete and exact description of the electronic structure based on the density alone. In 1964 they published their seminal Hohenberg-Kohn theorem [31], which forms the basis of DFT.

Hohenberg-Kohn Theorem It actually comes in two statements. The first being that the ground-state density $\rho(\boldsymbol{r})$ of a bound system of interacting electrons uniquely (up to some additive constant) determines the external potential V_{ext} giving rise to the ground-state density. The external potential V_{ext} determines the Hamiltonian, therewith the many-body wavefunction of the ground state and consequently all properties of the system.

In wavefunction based methods the ground-state energy is accessible by solving the eigenvalue problem $H\Psi = \epsilon\Psi$ or minimizing the energy expectation value

$$E = \min_{\tilde{\Psi}} \langle \tilde{\Psi} | H | \tilde{\Psi} \rangle \; , \tag{2.1}$$

where $\tilde{\Psi}$ is a normalized trial function for a given number of electrons. To generalize this concept to densities we define the set $S(\rho)$ of different trial wavefunctions, all giving the same density ρ. This leads to

$$E\left[\rho, V_{\text{ext}}\right] = F\left[\rho\right] + \int \mathrm{d}^3 r \; V_{\text{ext}}(\boldsymbol{r})\rho(\boldsymbol{r}) \; , \tag{2.2}$$

where $F\left[\rho\right]$ is determined by the constrained minimization

$$F\left[\rho\right] = \min_{\tilde{\Psi} \in S(\rho)} \langle \tilde{\Psi} | T + U | \tilde{\Psi} \rangle \; . \tag{2.3}$$

$F[\rho]$ is a universal functional of the density – in the sense, that it does not depend on V_{ext}, i.e. on the specific system. It contains the kinetic energy T as well as the interaction energy U of the electrons among each other.

Hence, minimizing (2.2) over all densities ρ yields the ground-state density ρ_0 as well as the ground-state energy $E_0 = E[\rho, V_{\text{ext}}]$ for a given $V_{\text{ext}}(\boldsymbol{r})$. This is the second statement of the Hohenberg-Kohn theorem. A succinct proof of both has been given by Levy [32] and Lieb [33].

Conceptually, we thus have means to *exactly* evaluate ground-state properties from the density as basic quantity alone. This is a significant formal progress. However, implicitly we still have a minimization with respect to the full Hilbert space in equation (2.3) and we do not know the universal functional $F[\rho]$ explicitly.

Kohn-Sham Density-Functional Theory   The most common ansatz to find a good approximate functional is the Kohn-Sham method published in 1965 [34]. It maps the system of interacting electrons onto a system of independent particles T_{ind} in a mean-field Hartree potential plus the exchange-correlation potential under the constraint that the ground-state density of both the interacting and the non-interacting system is the same. The exchange-correlation term E_{xc} describes the difference between the true $F[\rho]$ and the fictitious kinetic $T_{\text{ind}}+$ Hartree energy, i.e.

$$F[\rho] = T_{\text{ind}}[\rho] + \frac{e^2}{2} \int \mathrm{d}^3r \, \mathrm{d}^3r' \, \frac{\rho(\boldsymbol{r})\rho(\boldsymbol{r}')}{|\boldsymbol{r}-\boldsymbol{r}'|} + E_{\text{xc}}[\rho] \ . \tag{2.4}$$

Of course, the exact E_{xc} is not known either. However, it is usually relatively small and therefore a good quantity to be approximated.

To minimize the Kohn-Sham functional

$$E^{\text{KS}}[\rho] = \int \mathrm{d}^3r \, V_{\text{ext}}(\boldsymbol{r})\rho(\boldsymbol{r}) + T_{\text{ind}}[\rho] + \frac{e^2}{2} \int \mathrm{d}^3r \, \mathrm{d}^3r' \, \frac{\rho(\boldsymbol{r})\rho(\boldsymbol{r}')}{|\boldsymbol{r}-\boldsymbol{r}'|} + E_{\text{xc}}[\rho] + E_{\text{ions}} \tag{2.5}$$

the density needs to satisfy the variational equation

$$0 = \int \mathrm{d}^3r \, \delta\rho(\boldsymbol{r}) \left\{ V(\boldsymbol{r}) + e^2 \int \mathrm{d}^3r' \, \frac{\rho(\boldsymbol{r})}{|\boldsymbol{r}-\boldsymbol{r}'|} + \frac{\delta T_{\text{ind}}[\rho]}{\delta\rho(\boldsymbol{r})} + \frac{\delta E_{\text{xc}}[\rho]}{\delta\rho(\boldsymbol{r})} \right\} \ , \tag{2.6}$$

under the constraint that the number of electrons is conserved

$$\int \mathrm{d}^3r \, \delta\rho(\boldsymbol{r}) = 0 \ . \tag{2.7}$$

Equation (2.6) has the form of a non-interacting electron system whose electrons move in an effective external potential

$$V_{\text{eff}}(\boldsymbol{r}) = V(\boldsymbol{r}) + e^2 \int \mathrm{d}^3r' \, \frac{\rho(\boldsymbol{r}')}{|\boldsymbol{r}-\boldsymbol{r}'|} + V_{\text{xc}}(\boldsymbol{r}) \ , \tag{2.8}$$

where the exchange-correlation potential is given by

$$V_{\text{xc}} = \frac{\delta E_{\text{xc}}[\rho]}{\delta\rho(\boldsymbol{r})} \ . \tag{2.9}$$

Hence, we can obtain the ground-state density by first solving a single-particle Schrödinger equation

$$\left(-\frac{1}{2m}\nabla^2 + V_{\text{eff}}\left(\boldsymbol{r}\right)\right)\varphi_\alpha\left(\boldsymbol{r}\right) = \epsilon_\alpha\varphi_\alpha\left(\boldsymbol{r}\right) \tag{2.10}$$

and then evaluating the density by

$$\rho\left(\boldsymbol{r}\right) = \sum_{\alpha:\text{occ}} |\varphi_\alpha\left(\boldsymbol{r}\right)|^2 , \tag{2.11}$$

where the sum runs over the N lowest eigenvalues respecting the Pauli exclusion principle. Equations (2.10) and (2.11) are the Kohn-Sham equations, which have to be solved self-consistently since the effective potential V_{eff} depends on the density via (2.8).

A summation of the Kohn-Sham energies ϵ_α gives

$$2\sum_{\alpha:\text{occ}}\epsilon_\alpha = T_{\text{ind}}\left[\rho\right] + \int \mathrm{d}^3r \, V_{\text{eff}}\left(\boldsymbol{r}\right)\rho\left(\boldsymbol{r}\right) \tag{2.12}$$

by construction, where the factor 2 stems from the spin degeneracy in a paramagnetic system. Using (2.13), (2.8) and, (2.12) we obtain the total energy

$$E^{\text{KS}}\left[\rho\right] = 2\sum_{\alpha:\text{occ}}\epsilon_\alpha - \frac{e^2}{2}\int \mathrm{d}^3r\,\mathrm{d}^3r'\,\frac{\rho(\boldsymbol{r})\rho(\boldsymbol{r}')}{|\boldsymbol{r}-\boldsymbol{r}'|} - \int \mathrm{d}^3r\, V_{\text{xc}}\left(\boldsymbol{r}\right)\rho\left(\boldsymbol{r}\right) + E_{\text{xc}}\left[\rho\right] . \tag{2.13}$$

Local Density Approximation A simple yet very successful approximation to E_{xc} is the local density approximation (LDA). It approximates E_{xc} by

$$E_{\text{xc}}\left[\rho\right] = \int \mathrm{d}^3r\,\rho(\boldsymbol{r})\varepsilon_{\text{xc}}(\rho(\boldsymbol{r})) , \tag{2.14}$$

where $\varepsilon_{\text{xc}}(\rho(\boldsymbol{r}))$ is the exchange and correlation energy per electron of the homogeneous electron gas of density $\rho(\boldsymbol{r})$. It can be split into two parts

$$\varepsilon_{\text{xc}}(\rho(\boldsymbol{r})) = \varepsilon_{\text{x}}(\rho(\boldsymbol{r})) + \varepsilon_{\text{c}}(\rho(\boldsymbol{r})) , \tag{2.15}$$

the exchange $\varepsilon_{\text{x}}(\rho(\boldsymbol{r}))$ and the correlation energy $\varepsilon_{\text{c}}(\rho(\boldsymbol{r}))$. For the homogeneous electron gas we can express the former analytically [35]

$$\varepsilon_{\text{x}}(\rho(\boldsymbol{r})) = -\frac{3}{4}\left(\frac{3\rho\left(\boldsymbol{r}\right)}{\pi}\right)^{1/3} . \tag{2.16}$$

For the correlation energy no analytical form aside from its low- and high-density limit is known. Instead, it has been evaluated numerically by Ceperley and Alder with quantum Monte Carlo calculations [36]. These discrete results then have been interpolated by, for instance, Perdew and Wang, giving the PW-LDA (PW91) [37] exchange correlation potential.

In chemistry and solid state physics there is a plethora of exchange-correlation functionals. The LDA has been used extensively until the 1990s. Nowadays, functionals within the Generalized-Gradient Approximation (GGA) are preferred. In this work we will mainly use the popular GGA-functional PBE [38] proposed by Perdew, Burke and Ernzerhof in 1996.

Shortcomings In contrast, to the Thomas-Fermi method Kohn-Sham-DFT with the LDA and its generalizations describes the shell structure of bound electrons, which is e.g. at the heart of chemical bonding. Even though the LDA is a crude approximation to the real many-body correlation effects, it gives astonishingly good results for many material classes where it is meaningful to speak of single electrons.

However, LDA fails even qualitatively for systems with strongly correlated electrons, where the single-electron picture is lost. Mott insulators are, for instance, metallic within LDA. To treat these system we will have to resort to a model Hamiltonian description.

Standard DFT also fails [39] to properly describe long-range van der Waals interactions, in particular, the leading R^{-6} term originating from correlated spontaneous dipole fluctuations. This is, however, not entirely surprising since the Kohn-Sham ansatz is built around a static mean-field treatment and does not explicitly account for dynamic charge fluctuations. Interestingly, PBE seems to provide reasonable estimates for weakly bound systems. However, they actually are due to favorable errors or cancellations[40].

2.1.2. Density-Functional Practice with FHI-aims

While all DFT codes share the underlying principles, there are pronounced differences in the actual strategies chosen to tackle the Kohn-Sham problem.

2.1.2.1. Basis set

The most notable is the choice of the basis set $\{|\phi_i\rangle\}_i$ for the Kohn-Sham orbitals $\{|\varphi_\alpha\rangle\}_\alpha$. The expansion

$$|\varphi_\alpha\rangle = \sum_j c_{\alpha j}|\phi_j\rangle \tag{2.17}$$

transforms the Kohn-Sham problem from a continuous differential equation into a tractable linear algebra problem. Since we can only use a finite number of basis functions this expansion introduces an approximation. Different physical settings suggest different choices for the basis sets. In solid-state physics planewave-based basis sets are often used since they naturally accommodate the periodicity requirements of crystals. In contrast, localized basis functions, such as Slater-type orbitals or Gaussians, are a natural choice for finite systems such as molecules. The FHI-aims [41] code, we use in our studies of molecules, belongs to the latter group. It has been developed at the Fritz-Haber-Institute in Berlin under the supervision of Volker Blum. To obtain a highly efficient code without sacrificing accuracy FHI-aims relies on numeric atom-centered orbitals (NAO) basis functions of the form

$$\phi_i(\boldsymbol{r}) = \frac{u_i(r)}{r} Y_{lm}(\Theta, \Phi) \ , \tag{2.18}$$

where (r, Θ, Φ) are the spherical coordinates of $\boldsymbol{r}$ and $Y_{lm}(\Theta, \Phi)$ denote the spherical harmonics. The radial function $u_i(r)$ is numerically tabulated allowing for maximum flexibility. Exploiting this flexibility to obtain a compact, but still accurate set, is key to an efficient DFT code. FHI-aims comes with a highly optimized element-dependent
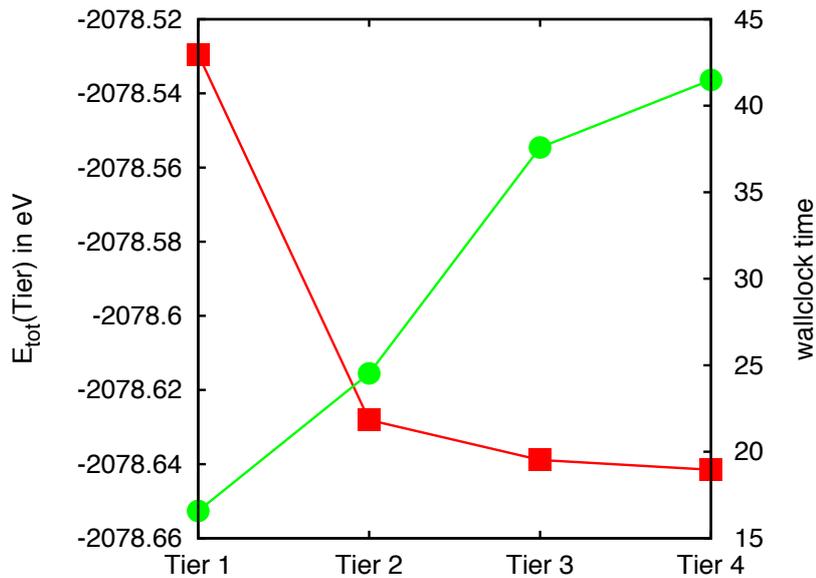
Figure 2.1.: Total energy (in eV) and wallclock time (in s) for a water molecule as a function of the tier. We observe that the energy converges at the expense of the runtime. Tier 4 only adds basis functions to the oxygen atom (see table 2.1). Time has been measured with the serial version on a 2.53 GHz Intel Core 2 Duo.

basis set which retains a high and transferable accuracy up to meV-level total energy convergence [42]. The radial functions are numerical solutions to the Schrödinger-like radial equation

$$\left[-\frac{1}{2}\frac{\mathrm{d}^2}{\mathrm{d}r^2} + \frac{l\,(l+1)}{r^2} + v_i\,(r) + v_{\mathrm{cut}}(r) \right] u_i\,(r) = \epsilon_i\,u_i(r) \,, \tag{2.19}$$

where r is discretized on a logarithmic grid. $v_i\,(r)$ denotes the physical potential and $v_{\mathrm{cut}}(r)$ is the cutoff potential. It ensures that each radial function is strictly localized within a sphere of given radius, i.e. $u_i(r) = 0$ outside the sphere. Hence, different non-overlapping spatial regions are separated from each other allowing for an almost linear scaling with the system size for sufficiently large clusters.

The basis sets per species are structured in a hierarchy of tiers. The minimal tier is constructed by setting $v_i\,(r)$ to the self-consistent radial potential of the free atom and taking the solutions for the core and valence electrons. Since the core electron wavefunctions hardly change in the case of chemical bonds and remain almost exactly described, this method significantly facilitates the all-electron treatment. To treat chemical bonds the minimal tier is, however, not sufficient. The construction and choice of the basis functions for the tiers beyond the minimal are given in [42].

Table 2.1.: Radial basis functions beyond the minimal tier used by FHI-aims for the water molecule (`aims_standard.pre-CPC`). H(nl, Z) denotes a hydrogen-like radial function for the bare Coulomb potential Z/r for quantum numbers n and l. ionic(nl, r) adds a free-ion like radial function, where n and l also give the quantum numbers and r the onset radius of the confining potential.

	H	O
tier 1	H($2s$, 2.1)	H($2p$, 1.8)
	H($2p$, 3.5)	H($3d$, 7.6)
		H($3s$, 6.4)
		H($4f$, 11.6)
tier 2	H($1s$, 0.85)	H($3p$, 6.2)
	H($2p$, 3.70)	H($3d$, 5.6)
	H($2s$, 1.20)	H($5g$, 17.6)
	H($3d$, 7.00)	H($1s$, 0.75)
tier 3	H($4f$, 11.20)	ionic($2p$, 9.4486)
	H($3p$, 4.80)	H($4f$, 10.8)
	H($4d$, 9.00)	H($4d$, 4.7)
	H($3s$, 3.20)	H($2s$, 6.8)
tier 4		H($3p$, 5.0)
		H($3s$, 3.3)
		H($5g$, 15.6)
		H($4f$, 17.6)
		H($4d$, 14.0)
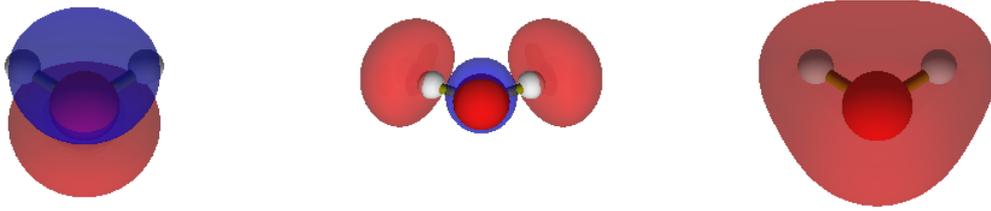
Figure 2.2.: $1b_1$ (HOMO) and $4a_1$ (LUMO) with isovalue 0.08 Å$^{-\frac{3}{2}}$ and total-electron density with isovalue 0.08 Å^{-3} of an H_2O molecule.

Obviously, low tiers mean fewer basis functions and therefore fast calculations at the expense of a loss in accuracy. This tier is practical for relaxation calculations. High tiers demand higher computational effort but provide more accurate results. It remains the task of the user to determine how many basis functions or tiers are actually needed. For the example of a water molecule the wallclock runtime and the energy as a function of the tier are plotted in figure 2.1. The basis set is compiled in table 2.1. The basis sets for all the atom species used in our work are given in appendix C.

2.1.2.2. Kohn-Sham Generalized Eigenvalue Problem

In each iteration of the self-consistency loop we need to solve the single-particle Kohn-Sham equations (2.10). Since the basis functions are not orthogonal, expanding the Hamiltonian with (2.17) gives the generalized Kohn-Sham eigenvalue problem

$$\sum_j h_{ij}\, c_{lj} = \epsilon_l \sum_j c_{lj}\, s_{ij}\ , \tag{2.20}$$

where

$$h_{ij} = \langle \phi_i | h^{\mathrm{KS}} | \phi_j \rangle = \int_{\mathbb{R}^3} \mathrm{d}^3 r\, \phi_i^*(\boldsymbol{r}) h^{\mathrm{KS}} \phi_j(\boldsymbol{r}) \tag{2.21}$$

and s_{ij} denotes the overlap matrix elements

$$s_{ij} = \langle \phi_i | \phi_j \rangle = \int_{\mathbb{R}^3} \mathrm{d}^3 r\, \phi_i^*(\boldsymbol{r}) \phi_j(\boldsymbol{r})\ . \tag{2.22}$$

Usually the numerical integrals for the overlap and Hamiltonian matrix are the dominant part of the computational effort. Formally, both scale as $\mathcal{O}(N^3)$ with the system size N. However, the locality of the basis functions allows for an almost $\mathcal{O}(N)$ scaling when the systems become large.

To solve the generalized eigenvalue problem a Cholesky decomposition is performed on the overlap matrix, yielding

$$s_{ij} = L_{il} L_{lj}^t\ . \tag{2.23}$$
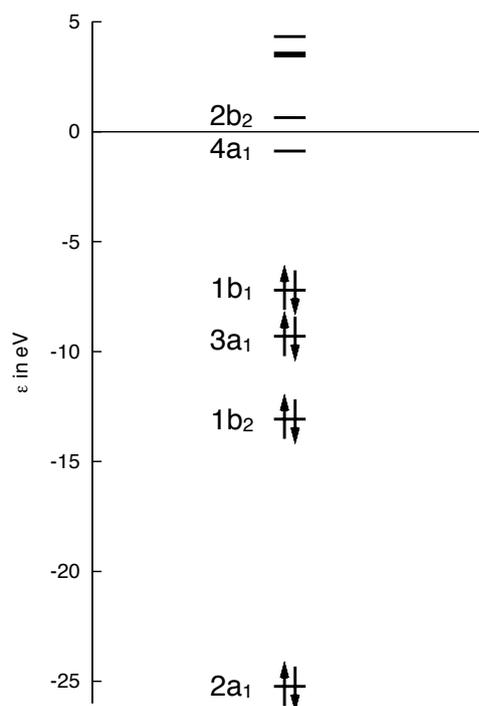
Figure 2.3.: Molecular energy levels of an isolated water molecule H_2O. The first
molecular orbital is not plotted for it has an eigenenergy of $-510\,\mathrm{eV}$.

The eigenvalues of (2.20) are those of the standard eigenvalue problem

$$\left(L^{-1}h^{\mathrm{KS}}L^{-t}\right)\left(L^{-t}c\right) = \epsilon\left(L^{-t}c\right) \; . \tag{2.24}$$

Its solution gives the Kohn-Sham orbitals and energies which we identify with the
molecular orbitals and energy levels. As an example figure 2.2 shows the molecular
orbitals for a H_2O molecule while figure 2.3 gives the molecular levels.

2.1.2.3. Dipole Moments

To treat organic crystals using the approach outlined in the introduction we need the
polarizabilites of their constituents. Within DFT codes with local basis sets such as
FHI-aims this is straightforward to do. We calculate the polarizability by extracting
the dipole moment as the self-consistent response of the electrons on the molecule to a
homogeneous external electric field $\boldsymbol{E}^{\mathrm{hom}}$.

To that end, we add a linear potential V^{hom} to the external potential V_{ext} such that
$\boldsymbol{E} = -\boldsymbol{\nabla}V^{\mathrm{hom}}$. Figure 2.4 gives an example for a linear potential with the radial potential
of a single atom. We see that the eigenvalue problem is now unbounded. The eigenstates
are superpositions of the continuum states and the bound states. This is, however, not
useful for our purpose. An electron fixed in a (metastable) bound state will eventually
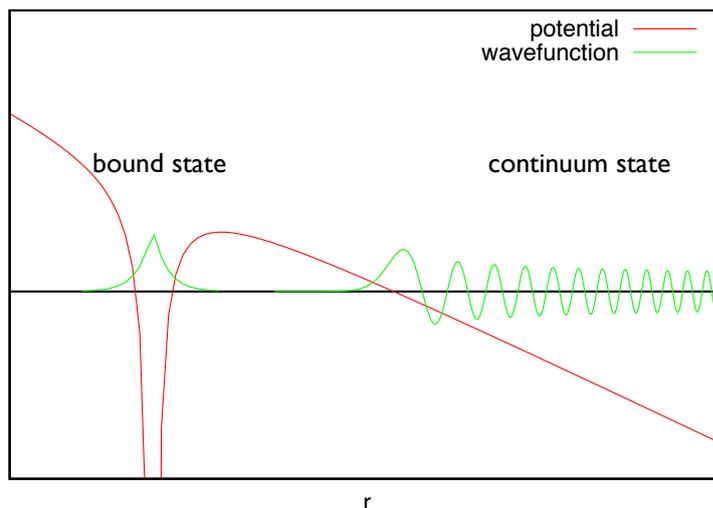
Figure 2.4.: Potential of an atom in an external homogeneous electric field. The real eigenstates are superpositions of the bound states and the continuum states. To evaluate polarizabilities we are, however, only interested in the response of the bound states to a linear potential. If the continuum states are spatially sufficiently far separated from the bound states we can fix the bound states by using a local basis.

(but after an astronomically large time) tunnel into the continuum states. The locality of the basis functions, however, confines the electrons to the region close to the molecule, i.e. to the bound states.

For non-polar systems the center of mass of the electrons and nuclii coincide. In the presence of the field they are, however, shifted with respect to each other and we obtain a non-vanishing dipole moment as response of the system

$$\boldsymbol{D} = \int \mathrm{d}^3 r \; \boldsymbol{r} \rho_{\mathrm{ion}}(\boldsymbol{r}) - \int \mathrm{d}^3 r \; \boldsymbol{r} \rho_{\mathrm{el}}(\boldsymbol{r}) \; , \tag{2.25}$$

where ρ_{ion} and ρ_{el} denote the ionic and electronic charge density, respectively. From $\boldsymbol{D}$ and $\boldsymbol{E}^{\mathrm{hom}}$ for sufficiently small fields and three directions we can directly obtain the polarizability tensor α

$$\boldsymbol{D} = \alpha \boldsymbol{E}^{\mathrm{hom}} \tag{2.26}$$

of the system.

2.1.2.4. Total-Energy Derivatives and Forces

Structure relaxations, vibrational properties, or ab-initio molecular dynamics require the derivatives of the total energy with respect to the atom positions $\boldsymbol{R}_i$ – the forces.

The simplest method to obtain the energy derivatives is to use the finite difference scheme which approximates the gradient by displacing the atomic positions. Even though

arbitrarily high accuracy is possible, this requires full total-energy calculations for each new displaced configuration and consequently leads to a high computational demand.

Using the Hellmann-Feynman theorem, i.e.

$$\boldsymbol{F}_i = -\boldsymbol{\nabla}_{\boldsymbol{R}_i}\langle E_{\text{tot}}\rangle = -\langle\boldsymbol{\nabla}_{\boldsymbol{R}_i}E_{\text{tot}}\rangle \ , \tag{2.27}$$

it suffices to perform only a single total-energy calculation. Once self-consistency is reached, we can directly evaluate the Hellmann-Feynman forces

$$\boldsymbol{F}_i^{\text{HF}} = e^2 \sum_{j,j\neq i} \frac{Z_i Z_j}{|\boldsymbol{R}_i - \boldsymbol{R}_j|^3}\left(\boldsymbol{R}_i - \boldsymbol{R}_j\right) - e\int \mathrm{d}^3 r \ \rho(\boldsymbol{r})\frac{Z_i}{|\boldsymbol{r} - \boldsymbol{R}_i|^3}\left(\boldsymbol{r} - \boldsymbol{R}_i\right) \ . \tag{2.28}$$

However, in the case of FHI-aims we have to consider two additional contributions to the force [42]. The Pulay forces stem from the basis dependence on the atom positions and vanish only in the limit of a complete basis set. An additional force originates from a multipole expansion of the density that is used within the Hartree potential evaluation. For an exact expansion up to infinite multipole order this contribution would be zero.

2.1.3. Hubbard model

Although there is a wide class of materials which can be sufficiently well described by Kohn-Sham DFT, it fails to capture the physics of systems with strong correlations. This is because no useful exchange-correlation functionals for these systems are known – let alone the exact one. Fortunately, there are other means of simplifying the full Schrödinger equation which lead to an understanding of these more exotic materials.

In organic solids the molecular orbitals are well localized at the molecules giving rise to narrow bands and thus small hopping parameters. Due to this weak hybridization we can use the molecular orbitals as basis set for a tight-binding description. The complexity of the many-body problem grows exponentially with increasing number of sites and basis functions. Hence, we restrict our calculation to the relevant electrons in the partly occupied molecular orbitals. In charge-transfer crystals this is the highest-occupied or lowest-unoccupied molecular orbital for electron donors or acceptors, respectively. The effect of the remaining occupied orbitals is a renormalization of the parameters of the model Hamiltonian.

The simplest model describing itinerant electrons with Coulomb repulsion among them is the Hubbard model. In this study we use the (extended) Hubbard model whose Hamiltonian in real space reads

$$H = -\sum_{\langle i,j\rangle,\sigma}(t_{ij}c_{i\sigma}^{\dagger}c_{j\sigma} + H.c.) + U\sum_i n_{i\uparrow}n_{i\downarrow} + V\sum_{\langle i,j\rangle}n_i n_j \ . \tag{2.29}$$

The first term denotes the kinetic energy in the tight-binding approximation. $c_i^{\dagger}$ creates and $c_i^{\dagger}$ annihilates an electron in the molecular orbital i. The first term thus describes the hopping of a single electron from site i to j and vice versa with the probability amplitude t_{ij}. t_{ij} is also called intermolecular-transfer integral or hopping parameter. The

second and third term represent the Coulomb energy, where $n_{i\sigma} = c_{i\sigma}^{\dagger} c_{i\sigma}$ is the occupation number of the molecular orbital at i with spin σ and $n_i = \sum_{\sigma} n_{i\sigma}$. Hence, the second term describes the local Coulomb repulsion of two electrons with opposite spin in one orbital and the third one the repulsion in neighboring orbitals.

This chapter deals with the evaluation of the Hubbard model parameters t_{ij}, U and V to define a Hubbard model which gives realistic results.

2.2. Organics

2.2.1. Building Blocks – Organic Molecules

Figure 2.5 gives an overview of some of the most important building blocks of organic crystals, showing the chemical structure formula along with the most commonly used names. It is remarkable that crystals built from these molecules can show metallic, superconducting, and magnetic behavior even though their electronic structure only stems from s- and p-electrons. These molecules have a mainly planar structure originating from the sp^2-hybridization between the atoms – most often carbon but also sulfur and oxygen. The σ-bonding orbitals are low in energy. Hence, they give a large contribution to the bonding.
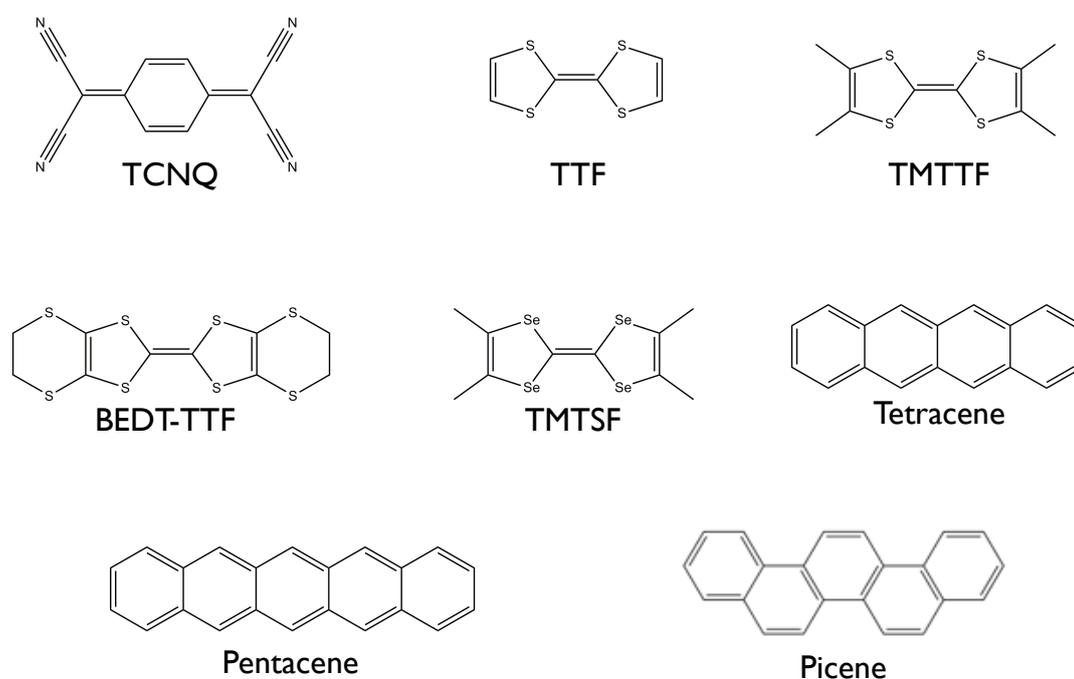
Figure 2.5.: Typical building blocks of organic crystals

The left part of figure 2.6 shows the highest few occupied and the lowest few unoccupied molecular levels of TCNQ. These orbitals have π-character. On the right side we see the highest-occupied molecular orbital (HOMO) and the lowest-unoccupied molecular orbital (LUMO). Being π-orbitals, they have a node in the molecular plane. There are the more nodes the higher the molecular level in energy.
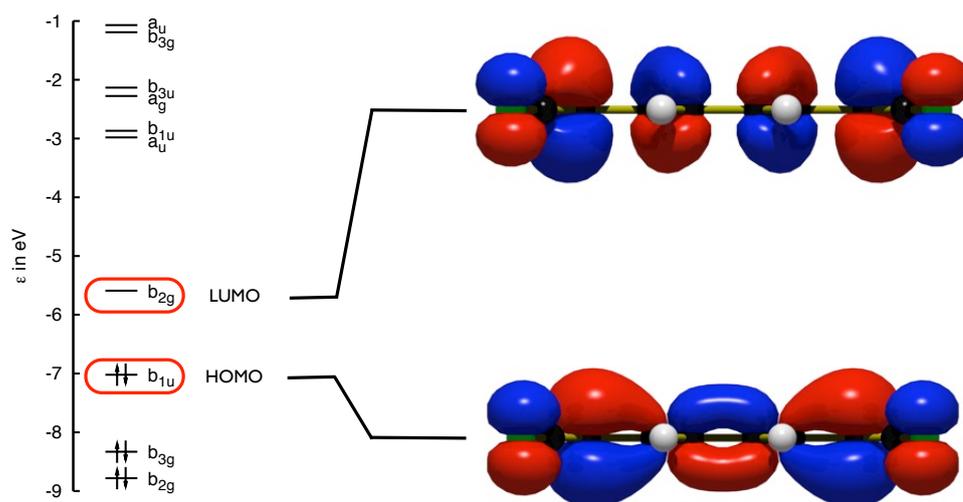
Figure 2.6.: Molecular levels (left) and wavefunctions (right) of the highest occupied/lowest unoccupied molecular orbital (HOMO/LUMO) of TCNQ. The π-character of both orbitals is evident from the node in the molecular plane. Moreover, we see that the higher orbital has an additional node.

Each molecular orbital $|\varphi_\nu\rangle$ comes with its Hartree or bare Coulomb integral

$$U_{\text{bare}}^\nu = \int \mathrm{d}^3 r \, \mathrm{d}^3 r' \, \frac{\rho_\nu(\boldsymbol{r})\rho_\nu(\boldsymbol{r}')}{|\boldsymbol{r} - \boldsymbol{r}'|} \, , \tag{2.30}$$

where $\rho_\nu(\boldsymbol{r}) = |\langle \boldsymbol{r}|\varphi_\nu\rangle|^2$. Figure 2.7 gives the U_{bare}^ν for TCNQ ($C_{12}N_4H_4$). For the $1s$ core states of carbon and nitrogen ($\nu \leq 16$) the Coulomb integral is large and close to the atomic bare Coulomb integrals. The delocalized π-bonds, however, spread throughout the entire molecule so that their bare Coulomb parameter are much smaller.

The polarizability of these molecules is highly anisotropic. This is due to the combination of their essentially linear shape and the π-bonds. Along the long molecular axis the polarizability is the largest, since the electrons can almost freely move within the extended π-orbitals. Perpendicular to this direction the extent of the molecules is significantly smaller. In general the smaller the extent in a direction the lower its polarizability, since the charges cannot move as far.

2.2.2. Molecular Crystals

The molecular packing of the building blocks results from a subtle balance between several intermolecular interactions with a typically close cohesive energy. That is why crystal engineering works so well in these compounds. Slightly different synthesis paths can lead to quite different crystal structures.

The interactions found between the molecules are of monopole-monopole, dipole-dipole, and π-overlap types. If there are molecules of different type within the system and the
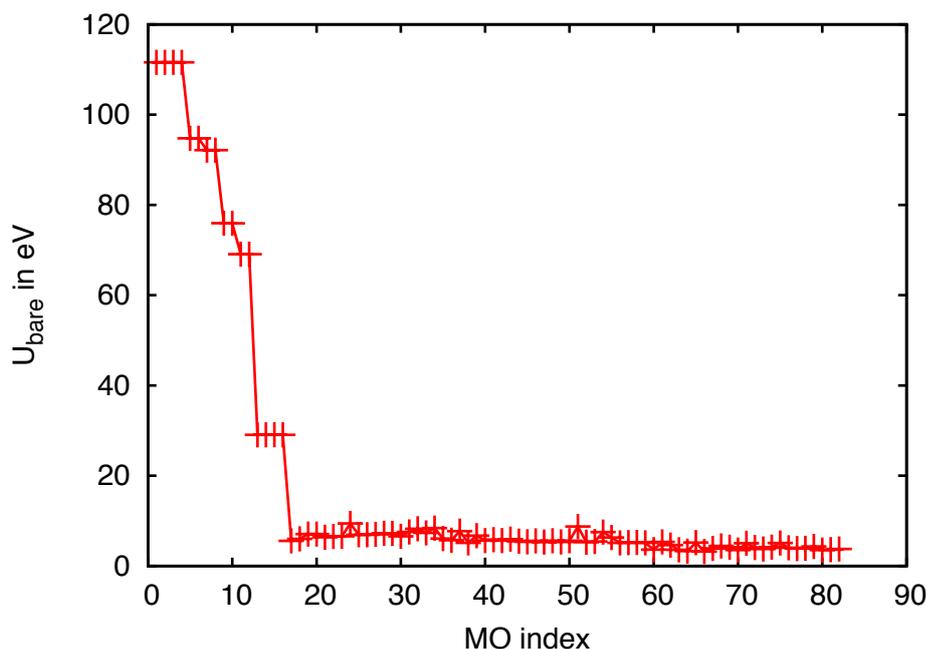
Figure 2.7.: U^{ν}_{bare} for the molecular orbitals of TCNQ. For the $1s$ core states of carbon
and nitrogen ($\nu \leq 16$) the Coulomb integral is large and close to the
atomic bare Coulomb integrals. The delocalized π-bonds, however, spread
throughout the entire molecule so that their bare Coulomb parameters
are much smaller.

HOMO energy of one is higher in energy than the LUMO of the other, a charge transfer
takes place. This leads to a net charge difference on the molecules and therefore to ionic-
like bonds. These compounds are known as charge-transfer salts. In TTF-TCNQ, for
instance, on average 0.6 electrons are transferred from the HOMO of TTF to the LUMO
of TCNQ. Dipole-Dipole interactions between two permanent dipoles are called Keeson
forces and their energies are typically of the order of $0.5\,\mathrm{eV/molecule}$. Van der Waals-
London dispersion forces describe the weak attractive interaction between a molecule with
either a permanent dipole moment or a charge fluctuation with a polarizable non-polar
molecule. The energies involved are usually smaller than $0.2\,\mathrm{eV/molecule}$. Finally, the
overlap between p_{π} orbitals leads to cohesion energies of often less then $0.4\,\mathrm{eV/molecule}$.

To determine the crystal structure X-ray diffraction experiments are employed. In
principle, they provide the complete crystal structure in terms of the unit cell and the
structure factor. While the former determines the periodicity of the crystal, the latter
provides the atom positions and types within the unit cell. The problem is, however,
that the organics usually have very many atoms in a large single unit cell. In the case of
(BEDT-TTF)$_2$I$_3$ there are, for example, 590 atoms of 4 different types (see figure 2.8).
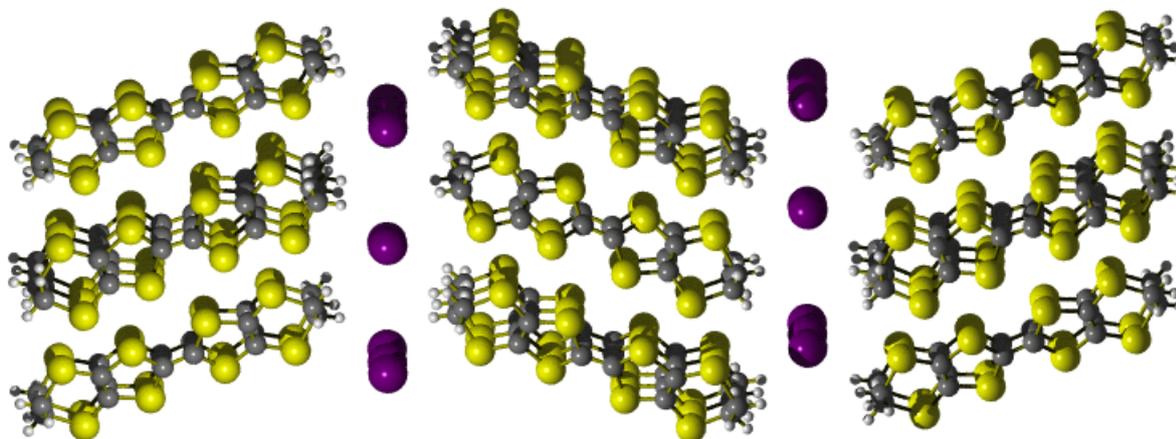
Figure 2.8.: (BEDT-TTF)$_2$I$_3$ unit cell which comprises 590 atoms of 4 different types making an analysis of the structure factor hard or impossible to do.

Therefore, the structure factor is very complicated. Consequently, it is hard to perform accurate experiments and get reliable results. Moreover, the position of the hydrogen atoms, 176 in the (BEDT-TTF)$_2$I$_3$ unit cell, is quite uncertain since having only a partial charge of less than an electron, they scatter very weakly.

Alternatively, we could perform DFT relaxation computations on the entire crystal to obtain a reliable crystal structure for our calculations. However, this approach is problematic since current DFT exchange-correlation potentials cannot reliably capture van der Waals bonding.

Instead, we strike a compromise. First, we relax the isolated molecules using DFT. Then we put these molecules into the crystal at positions and with orientations determined by X-ray diffraction experiments. That way we obtain a well-defined crystal structure.

2.2.2.1. Practical Approach

Crystal Construction Given the experimental data the first step is to isolate and identify the molecules within the unit cell. In a second step we calculate the center of mass

$$\boldsymbol{S}^G = \frac{\sum_i m_i \boldsymbol{r}_i^G}{\sum_i m_i} \tag{2.31}$$

for each molecule, where atom i has a mass m_i and is at position $\boldsymbol{r}_i^G$. G denotes the geometry. In order to determine the orientation we move the coordinate system such that it resides in the center of mass of the molecule and evaluate the moment-of-inertia tensor

$$\Theta_{\alpha\beta}^G = \sum_i m_i \left[(\boldsymbol{r}_i^G)^2 \delta_{\alpha\beta} - x_{i\alpha}^G x_{i\beta}^G \right], \tag{2.32}$$

DFT structures   experimental structure
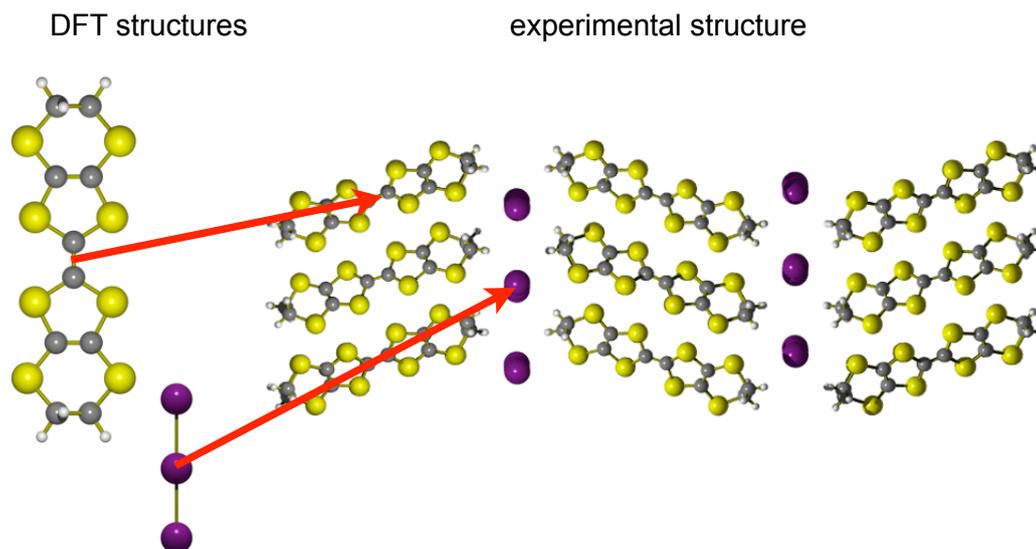
Figure 2.9.: Crystal Construction: Having the orientations and positions of the molecules in the experimental unit cell we replace these building blocks by DFT relaxed structures. The experimental molecules are not well-defined due to the inaccuracy of X-ray diffraction experiments while the DFT pendants are.

where the position of atom i is further decomposed in $\boldsymbol{r}_i^G = (x_{i0}^G, x_{i1}^G, x_{i2}^G)^t$. Diagonalizing $\Theta_{\alpha\beta}^G$ yields the principal moments as eigenvalues $\{\hat{\Theta}_\alpha^G\}_\alpha$ of $\Theta_{\alpha\beta}^G$ and the principal axes as eigenvectors $\{\boldsymbol{e}_\alpha^G\}$. Usually, all eigenvalues are distinct and thus the principal axes are unambiguously defined. Without loss of generality, we choose $\{\boldsymbol{e}_\alpha^G\}_\alpha$ to be a right-handed system.

For the DFT relaxed structures we follow the same procedure. Within the coordinate system of their principal axes both structures should agree quite well. As quantitative measure for their similarity we evaluate the root-mean-square deviation of the atomic coordinates $\sqrt{\sum_i (\boldsymbol{r}_i^{\mathrm{DFT}} - \boldsymbol{r}_i^{\mathrm{exp}})^2 / N}$ and compare the principal moments.

Having the orthogonal transformation matrices $T_G = (\boldsymbol{e}_1^G, \boldsymbol{e}_2^G, \boldsymbol{e}_3^G)$ of DFT-relaxed and experimental molecules as well as their orientation we can easily exchange the "experimental" molecules inside the unit cell by the DFT relaxed pendants (see figure 2.9). Hence, obtaining a well-defined structure.

Crystal Modification   The transformation matrices $T_G = (\boldsymbol{e}_1^G, \boldsymbol{e}_2^G, \boldsymbol{e}_3^G)$ are inconvenient to handle. While it is easy to obtain distances between two molecules by their center-of-mass vectors, the relative orientation is hard to see directly from the matrices. But as they describe an orientation in three dimensional space, there are only three independent degrees of freedom. To parametrize the orientation we use Euler angles. From the 12 equivalent definitions of the Euler angles we choose the (Z, Y', Z'') convention which is

commonly used in quantum mechanics. It is introduced in appendix B and depicted in figure B.1.

What we actually need here is to extract the Euler angles (α, β, γ) from a general rotation matrix – in our case the T^G matrices. The algorithm we use is given in listing B.1 of appendix B.

Having a description in terms of Euler angles and center-of-mass vectors we cannot only quantify the relative position and orientation but we can also easily modify the crystals. This provides us with the means to study for instance the effect of pressure on the crystals or reorientation of molecules close to the surface. We can do full theoretical crystal engineering.

2.3. Evaluation of Model Parameters

Having a well-defined crystal structure we can start evaluating the model parameters for a treatment in terms of generalized Hubbard models. They only explicitly consider the "relevant" valence electrons in the system. The effect of the others is a renormalization of the parameters. We start with the hopping parameters, which we can evaluate from DFT calculations alone.

We continue with the calculation of the bare and intra-molecularly screened Coulomb integrals also from DFT. With the electrostatic approach introduced in chapter 1 we obtain the additional inter-molecular screening contribution from all other molecules in the system.

2.3.1. Hopping Parameters

In the previous subsection we have already discussed the dominant form of interactions in organics. Compared to ordinary solids the overlap between adjacent molecules is relatively weak leading to a weak bonding and a small hybridization. This suggests to treat the kinetic energy in terms of a tight-binding description, where we assume that the molecular orbitals (MO) remain unchanged when forming bonds. Bonding is achieved by a linear combination of the MOs giving bonding and anti-bonding orbitals.

The tight-binding hopping parameters $t_{ij}^{\nu\nu'}$ between molecular levels ν and ν' of molecules at $\boldsymbol{R}_i$ and $\boldsymbol{R}_j$ respectively, are defined as

$$-t_{ij}^{\nu\nu'} = \left\langle \phi_{i\nu} \middle| v_j \middle| \phi_{j\nu'} \right\rangle , \qquad (2.33)$$

where v_j denotes the molecular potential of the molecule at $\boldsymbol{R}_j$. We can interpret the hopping as a perturbative correction to a single molecule placed within a crystal. Usually, only very close neighbors have to be treated. For the systems treated here we have only single-band models and hybridization between like molecules. Therefore, we have $t_{ij}^\nu = t_{ij}^{\nu\nu}$ where ν is either the highest occupied or lowest unoccupied molecular orbital. From these tight-binding parameters we can readily infer the band-structure

$$\epsilon_{\boldsymbol{k}\nu} = \varepsilon_\nu - \sum_{ij} t_{ij}^\nu e^{i\boldsymbol{k} \cdot (\boldsymbol{R_i} - \boldsymbol{R_j})} . \qquad (2.34)$$

To actually evaluate the hopping parameters we use a dimer approach [43]. Similar to the splitting of atomic energy levels in bonding and anti-bonding orbitals when forming diatomic homonuclear molecules, the molecular energy levels split when two molecules approach one another. From this bonding and anti-bonding splitting the modulus of the hopping integral is directly accessible.

To see this, let ν denote the molecular level and ε_ν its molecular energy. For a specific dimer with states $|\phi_\nu^x\rangle$, where $x = A, B$ distinguishes the two molecules, the tight-binding Hamiltonian reads

$$H_\nu^{\mathrm{TBA}} = \begin{pmatrix} \varepsilon_\nu & -t^\nu \\ -t^\nu & \varepsilon_\nu \end{pmatrix} . \qquad (2.35)$$
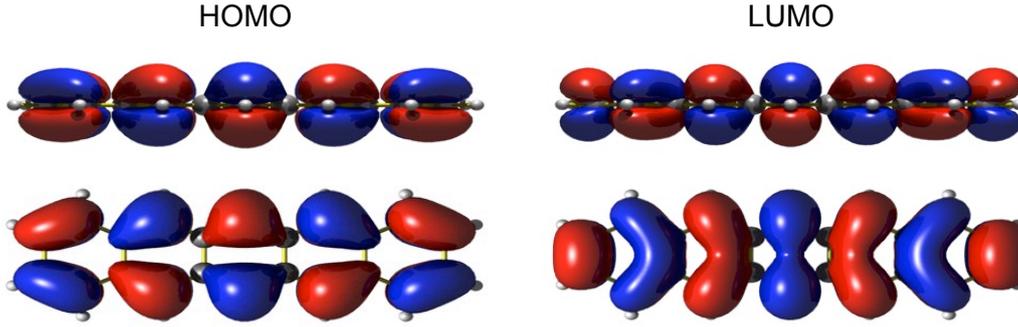
HOMO LUMO

Figure 2.10.: HOMO (left) and LUMO (right) of pentacene: side and top view. We observe the node in the molecular plane and the additional node in the LUMO compared to the HOMO.

Diagonalization yields the symmetric/anti-symmetric state, i.e.

$$|\varphi_\nu^{s/a}\rangle = \frac{1}{\sqrt{2}} \left(|\phi_\nu^A\rangle \pm |\phi_\nu^B\rangle \right) \tag{2.36}$$

with their corresponding eigenenergies, i.e.

$$|\epsilon_\nu^{s/a}\rangle = \varepsilon_\nu \mp t^\nu \; . \tag{2.37}$$

We perform DFT calculations for a dimer built from molecules a distance l apart and with a specified relative orientation determined by the rotation matrix T taken from the crystal data. The dimer energy levels of the HOMO and LUMO directly give the absolute value of the splitting $|\Delta\varepsilon^\nu| = 2|t^\nu|$. The sign of t^ν cannot directly be deduced from this method. It can, however, be inferred from the symmetry of the dimer wavefunction. If the bonding orbital, the lower one in energy, is symmetric ($|\varphi_\nu^{s/a}\rangle$) then t^ν is positive. To have this physically intuitive sign convention, we added the minus signs in front of the hopping parameters in the tight-binding Hamiltonian (2.35).

Correspondingly, if the lower molecular orbital is antisymmetric, t^ν is negative. Figure 2.11 gives an example for these symmetries of a pentacene crystal. We find that in this configuration the hopping parameter of the HOMOs is negative while it is positive for the LUMOs.

Doing theoretical molecular engineering we can modify the configuration, for instance, by changing the distance and the relative orientation. Or in a more physical picture we can assess the crystals response to a change of pressure. Since we chose a tight-binding description we have to make sure that its prerequisites are not violated. It is crucial to check that the molecular orbitals do not mix considerably and that the HOMO-LUMO gap is still larger than the splitting of the molecular levels.

HOMO   LUMO

anti-bonding

$2|t^\nu|$
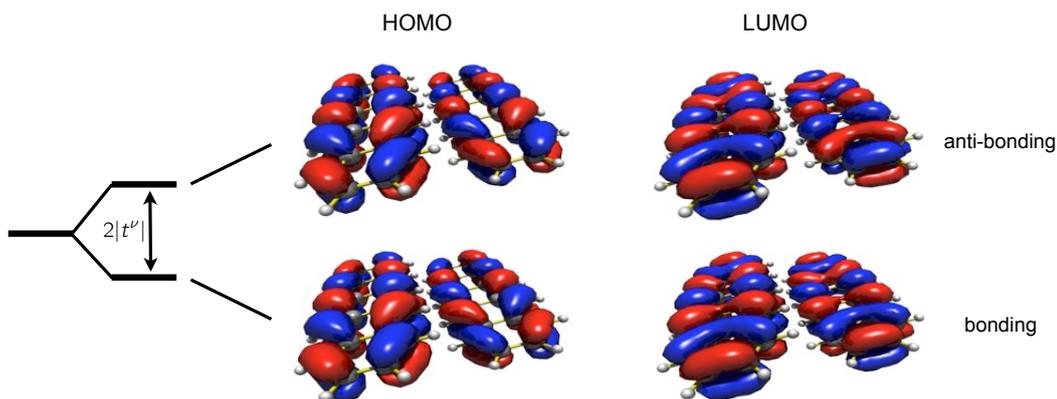
bonding

Figure 2.11.: Schematic bonding/anti-bonding splitting to derive the absolute value of the hopping-matrix elements t^ν. Their signs can be derived from the symmetry of the dimer wavefunction. The bonding dimer orbitals are an antisymmetric and a symmetric linear combination of the molecular orbitals for HOMO and LUMO of pentacene (cf. figure 2.10), respectively. Hence, $t_{\mathrm{HOMO}} < 0$, while $t_{\mathrm{LUMO}} > 0$. The dimer configuration is the a-direction of pentacene at 293 K as published in [44, 45].

The tight-binding approach works the better the larger the distance between the molecules. Figure 2.11 shows the dimer model with the distance and orientation realized in the crystal. We observe that the molecular orbitals are hardly changed with respect to the isolated molecule. When we, however, move the molecules closer to one another they will eventually come too close and the tight-binding picture breaks down. The total energy as a function of the configuration, be it distance or orientation, is a very good indicator for this break down. When it shows a steep change, physics beyond the tight-binding description becomes relevant.

Figure 2.12 gives the distance dependence along the cyrstallographic a-direction of the total energy for pentacene (see [44, 45]). We find a Lennard-Jones-like behavior. For short distances the total energy increases steeply indicating the break down of the tight-binding ansatz. The molecular orbitals distort and we observe a strong increase in energy due to the repulsion of the electrons and nuclei confined to a small spatial area. At large distances we obtain the energy of two isolated molecules. In between, there is a bonding region, where the mininum yields the equilibrium distance for a pure dimer. The distance realized in a-direction of the crystal is slightly smaller due to the long-range tails of the other molecules in the crystal. Moreover, van-der Waals bonds are not accurately treated within PBE. The corresponding hopping parameters for HOMO and LUMO are shown in figure 2.13. We observe that the second-nearest neighbors along this direction have hardly any hopping amplitude left. Consequently, it is sufficient to treat only nearest-neighbors.

The hopping-matrix elements as a function of orientation have more structure. As an example we give them and the total energy for a rotation of both molecules about their
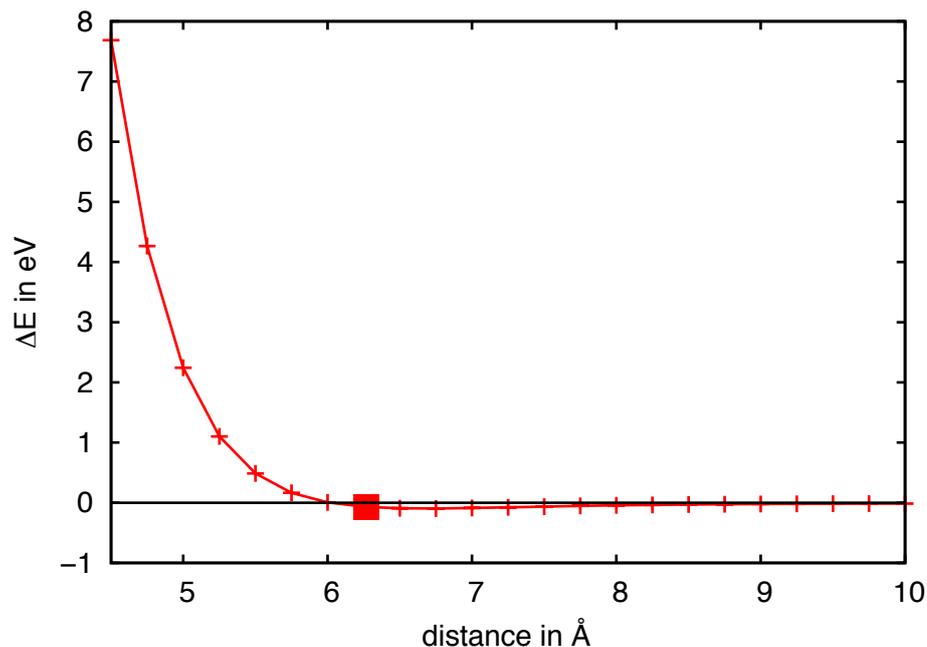
Figure 2.12.: Total energy difference between a dimer of two pentacene molecules at a distance d and two isolated molecules. For small distances there is a strong repulsion leading to a steep increase in the energy. For large distances the total energy is twice the energy of an isolated molecule. In between, there is a shallow "bonding" range. The square denotes the distance realized in the crystal. It is at a slightly smaller distance than for the dimer.
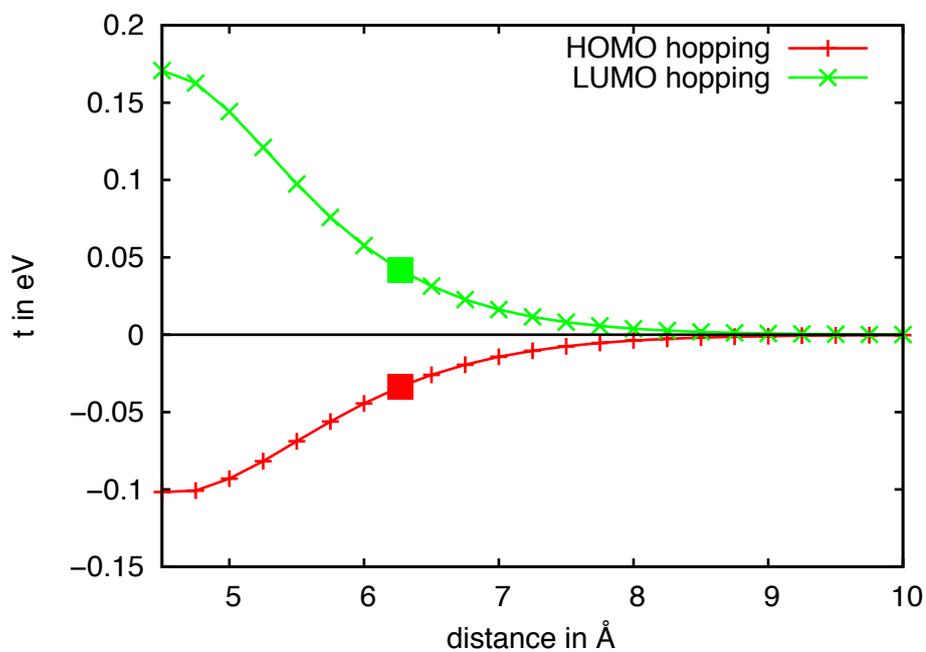
Figure 2.13.: Hopping-matrix element of HOMO and LUMO for pentacene as a function of the distance d along the crystallographic a-direction. The signs are consistent with figure 2.11.
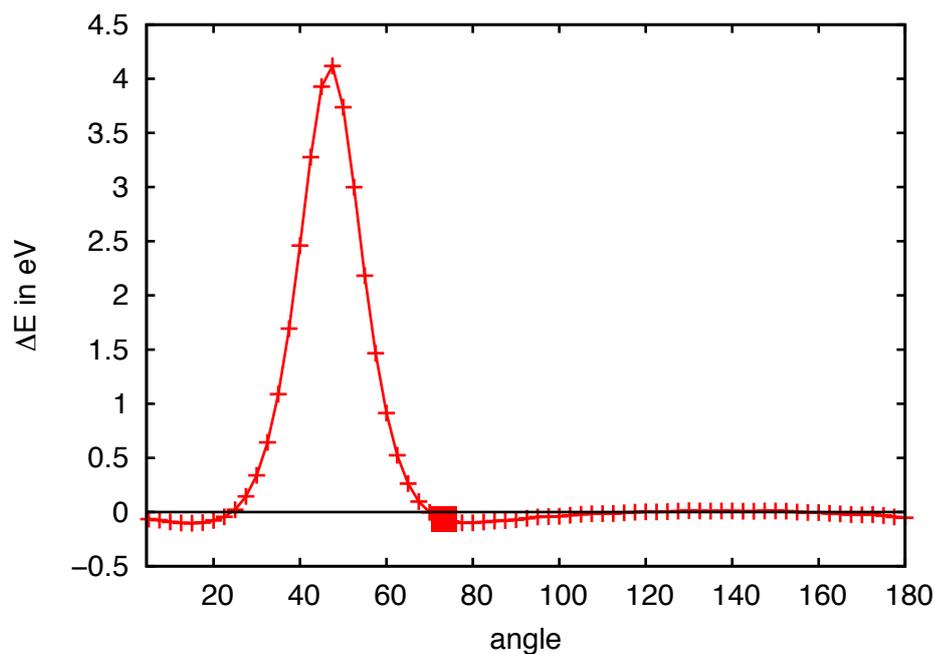
Figure 2.14.: Total energy difference between a dimer of two pentacene molecules at different angles and two isolated molecules. We observe a significant increase in the total energy at about 30° to 70° indicating that the tight-binding ansatz breaks down. The square denotes the relative orientation found in the molecular crystal.
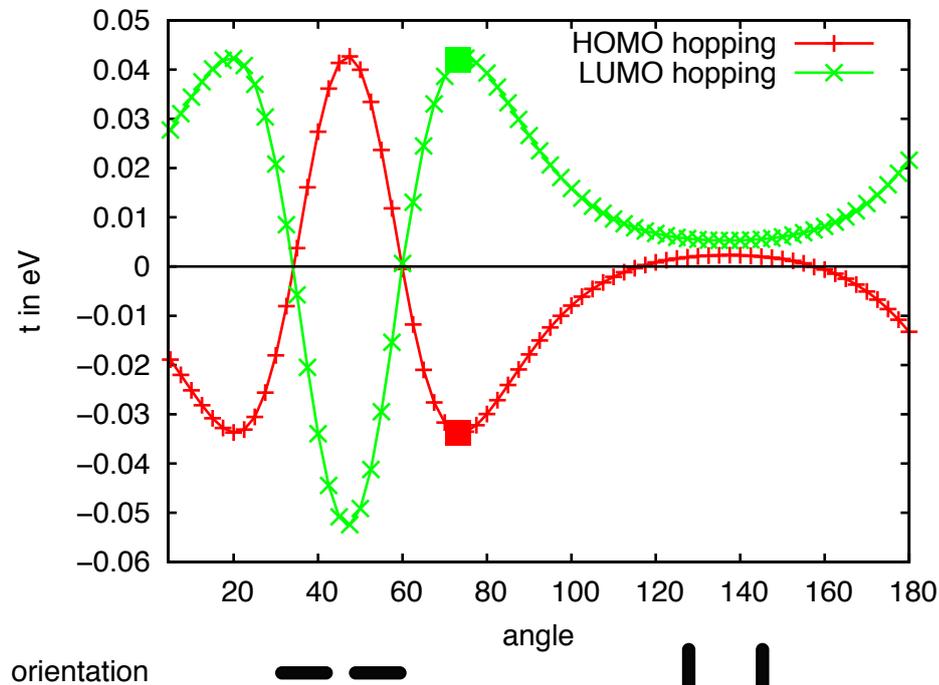
Figure 2.15.: Hopping-matrix elements at different angles for the HOMO and LUMO of a pentacene crystal along the a-direction. The crystal configuration is marked by the squares ($\angle\gamma \approx 76°$). Between 30° and 70° the tight-binding ansatz may not be well defined (see 2.14). For a discussion of the zeros see text.

116.25°   140.00°   157.50°
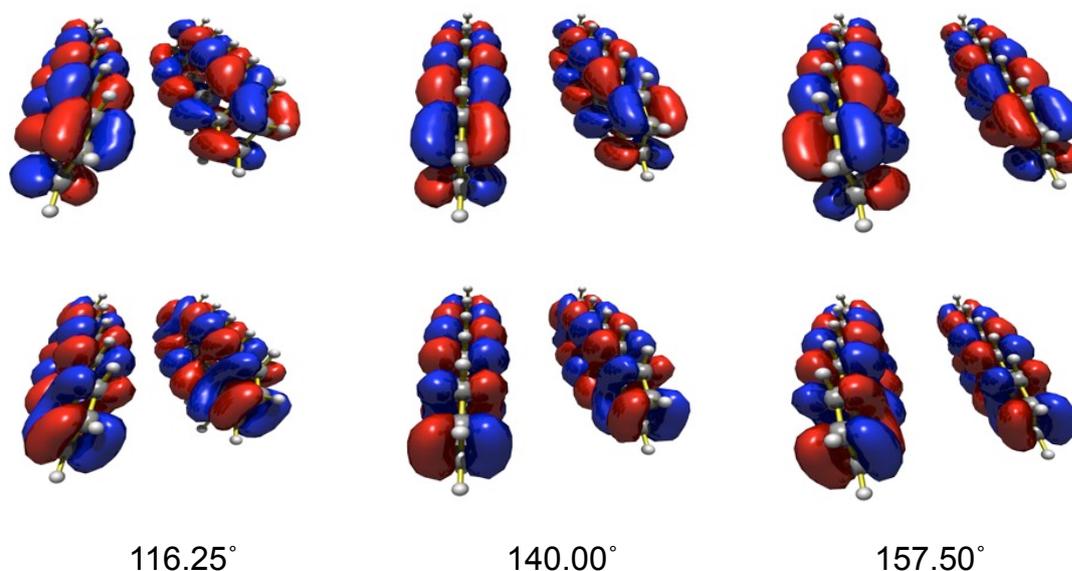
Figure 2.16.: Dimer wavefunctions for pentacene at different angles. First/Second row gives the HOMO/LUMO-based dimer. The node along the long molecular axis in the HOMO gives rise to the sign changes in the hopping-matrix elements.

long molecular axis at the distance realized within the crystal. Figure 2.14 shows the total energy which is periodic with periodicity π due to the symmetry of the configuration. Between 30° and 70° we observe a sharp increase in total energy, which indicates that the tight-binding approach breaks down. These configurations correspond to the molecules almost lying in the same plane. At about 50° their effective distance is minimized and their orbitals overlap and distort one another the most.

Figure 2.15 provides the hopping-matrix elements. At first we notice that the general shape of both functions for HOMO- and LUMO-based hopping is quite similar, however, flipped. At about 76° the configuration of the molecular crystal is assumed and we obtain the matrix elements $t_{\text{HOMO}} \approx -0.03\,\text{eV}$ and $t_{\text{LUMO}} \approx 0.04\,\text{eV}$.

A more detailed study, however, reveals some important differences. For about 136° the molecules are oriented such that the molecular planes of the molecules face each other (see 140° configuration in figure 2.16). In the LUMO-based hopping (green line) we see that the hopping-matrix elements increase in size when tilting around that angle. This is because the molecules effectively come closer to one another increasing the overlap. In contrast, the HOMO-based matrix elements become smaller. They even become zero at angles 116.5° and 155.0° and change sign. The reason for the different behavior becomes apparent when we take the shape of the molecular orbitals into consideration (cf. figure 2.10). The configuration and the dimer orbitals are shown in figure 2.16. The LUMOs

have lobes along the middle molecular axis and therefore do not change sign when tilting along the long axis. The HOMOs have an additional node along the long axis. Even though the molecules effectively come closer, the lobes on one molecule hybridize with lobes of different sign, leading first to a diminishing of the matrix elements, eventually to zero, and even a sign change.

2.3.2. Coulomb Parameters

Compared to the hopping-matrix elements the Coulomb parameters are significantly harder to determine. If we could treat all electrons in our Hubbard model Hamiltonian, the correct Coulomb parameter would be given by the bare Hartree integrals. They are readily evaluated. The complexity comes from the screening that describes the effect of all the electrons that we have not explicitly included in the Hubbard model. Thus, we start by evaluating the bare Coulomb integrals. Then we take the screening of the electrons on the molecules themselves into account – the intra-molecular screening. In the final step we also include the effect of all other lattice molecules using the electrostatic approach described in the previous chapter.

2.3.2.1. Bare Coulomb integrals

The bare Coulomb integral for the molecular orbital ν on two molecules a relative distance of $\boldsymbol{l}$ apart and rotated relative to each other by matrix T is given by

$$V_{\mathrm{bare}}^{\nu,\boldsymbol{l},T} = \int \mathrm{d}^3 r \, \mathrm{d}^3 r' \, \frac{\rho_\nu^{0,\mathbb{1}}(\boldsymbol{r}) \rho_\nu^{\boldsymbol{l},T}(\boldsymbol{r}')}{|\boldsymbol{r} - \boldsymbol{r}'|} \,, \tag{2.38}$$

where $\rho_\nu^{\boldsymbol{l},T}(\boldsymbol{r}) = |\varphi_\nu^{\boldsymbol{l},T}(\boldsymbol{r})|^2$ and $\varphi_\nu^{\boldsymbol{l},T}(\boldsymbol{r})$ is the densities of orbital ν. The local Coulomb integral, the Hubbard-U_{bare}, is given by $V_{\mathrm{bare}}^{\nu,0,\mathbb{1}} = U_{\mathrm{bare}}$. Technically, we perform the integrations over the wavefunctions evaluated on real-space grids. For grids of different step sizes we extrapolate to an infinitely dense grid (cf. figure 2.17).

For distances larger than $2R$, where R denotes the radius of the sphere which encompasses all nuclei, we can, to a very good approximation, regard the electron densities at both molecules as point charges and obtain the standard Coulomb law $V_{\mathrm{bare}}^{\nu\boldsymbol{l}T} = 1/|\boldsymbol{l}|$. Small deviations for $|\boldsymbol{l}| \approx 2R$ are due to the near field, where higher-order terms also contribute. Figure 2.18 shows the bare Coulomb integrals for two TTF (blue), TCNQ (magenta) and BEDT-TTF (red) molecules a distance d apart. We observe that for $d \gtrsim 2R$ (colored thin lines per molecule) the bare matrix elements are indeed well described by the $1/d$ Coulomb law (green curve).

2.3.2.2. Intra-molecular screening

As a first step towards renormalized parameters for realistic simulations we consider the effect of the additional electrons within the charged molecule – the intra-molecular screening. We again employ all-electron Kohn-Sham DFT.
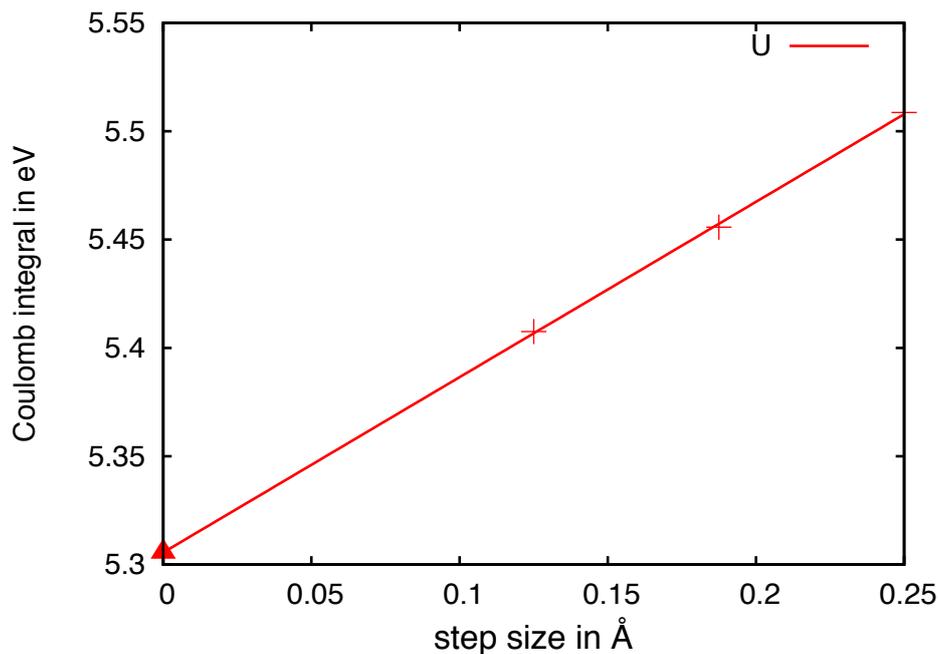
Figure 2.17.: Extrapolation of the bare Coulomb integral U for BEDT-TTF. Integration is performed on real-space grids with different step sizes to extrapolate to an infinitely dense grid.
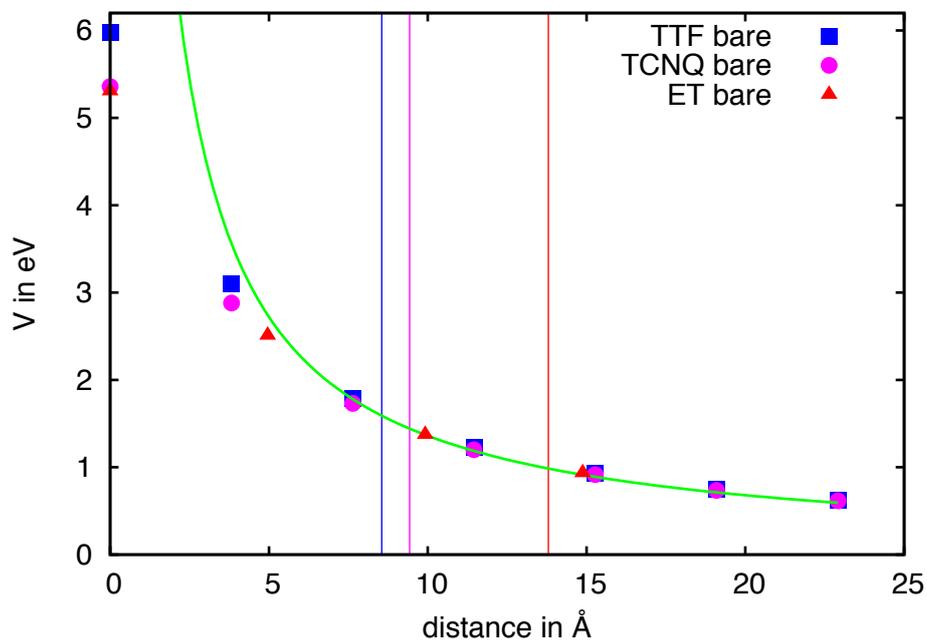
Figure 2.18.: Bare Coulomb integrals for different distances between two TTF (blue), TCNQ (magenta) or BEDT-TTF (red) molecules. For large distances $|\boldsymbol{l}| > 2R$, where R denotes the geometric radius (radius of sphere encompassing all nuclei), the Coulomb integral is given by the standard Coulomb law (green line) between two point charges (apart from negligible near-field effects for $|\boldsymbol{l}| \gtrapprox 2R$). These radii for TTF (blue), TCNQ (magenta) and BEDT-TTF (red) are shown as thin perpendicular lines.

Janak's theorem [46] states that the derivative of the total energy with respect to the occupation number n_ν of state ν directly relates via

$$\frac{\partial E^{\text{tot}}}{\partial n_\nu} = \epsilon_\nu \tag{2.39}$$

to the corresponding eigenvalue ϵ_ν. Here, E^{tot} is the total Kohn-Sham energy given by

$$E^{\text{tot}}[\rho] = T[\rho] + \int \mathrm{d}^3 r \, V_{\text{ext}} \rho(\boldsymbol{r}) + \frac{e^2}{2} \int \mathrm{d}^3 r \, \mathrm{d}^3 r' \, \frac{\rho(\boldsymbol{r})\rho(\boldsymbol{r}')}{|\boldsymbol{r} - \boldsymbol{r}'|} + E_{\text{xc}}[\rho] + E_{\text{ions}} , \tag{2.40}$$

where $T[\rho]$ denotes the kinetic energy, E_{ions} the ion-ion Coulomb energy and $E_{\text{xc}}[\rho]$ the exchange-correlation functional. Starting from this theorem, von Barth [47], Springer and Aryasetiawan [48] showed that

$$\frac{\partial \epsilon_\nu}{\partial n_\mu} = \frac{\partial^2 E^{\text{tot}}[\rho]}{\partial n_\nu \, \partial n_\mu} = \langle \mu\nu | \left(V + f_{\text{xc}} \right) \varepsilon^{-1} | \mu\nu \rangle \tag{2.41}$$

$$= \int \mathrm{d}^3 r \, \mathrm{d}^3 r' \, |\varphi_\nu(\boldsymbol{r})|^2 |\varphi_\mu(\boldsymbol{r}')|^2 \left(V(\boldsymbol{r}, \boldsymbol{r}') + f_{\text{xc}}(\boldsymbol{r}, \boldsymbol{r}') \right) \varepsilon^{-1}(\boldsymbol{r}, \boldsymbol{r}') \tag{2.42}$$

holds, where $V(\boldsymbol{r}, \boldsymbol{r}')$ is the bare Coulomb interaction and $\varepsilon^{-1}(\boldsymbol{r}, \boldsymbol{r}')$ the inverse dielectric function, which describes the screening effect. $f_{\text{xc}}(\boldsymbol{r}, \boldsymbol{r}')$ is defined by

$$f_{\text{xc}}(\boldsymbol{r}, \boldsymbol{r}') = \frac{\partial^2 E_{\text{xc}}[\rho]}{\partial \rho(\boldsymbol{r}) \, \partial \rho(\boldsymbol{r}')} = \frac{\partial V_{\text{xc}}(r)}{\partial \rho(\boldsymbol{r}')} . \tag{2.43}$$

It is much smaller than $V(\boldsymbol{r}, \boldsymbol{r}')$. Hence, to a good approximation we may assume that $f_{\text{xc}} = 0$ giving the screened Coulomb interaction $W = \varepsilon^{-1} V$ only, i.e.

$$\frac{\partial^2 E^{\text{tot}}[\rho]}{\partial n_\nu \, \partial n_\mu} \approx \langle \mu\nu | W | \mu\nu \rangle . \tag{2.44}$$

Hence, we theoretically obtain the intra-molecularly screened Coulomb integrals by the second derivative of the Kohn-Sham total energy with respect to the orbital occupation.

In practice, we vary the orbital occupation by artificially changing the charge of the molecule. Let us first discuss the evaluation of the local Hubbard-U_0. If we want to calculate the screening of the LUMO we add fractional charges q from $q = 0$ to $q = 2$ electrons to the molecule. In the case of the HOMO we obviously need to take electrons out.

For these systems we perform Kohn-Sham DFT total energy calculations, where the self-consistency leads to a relaxation of the orbitals – the screening. The total energy (2.40) can be fitted very well by a parabola (cf. figure 2.19)

$$E_{U_0^\nu}(q) = a_0 + a_1 q + U_0^\nu \frac{q^2}{2} , \tag{2.45}$$

from which according to (2.44) we obtain the intra-molecularly screened Hubbard U_0.
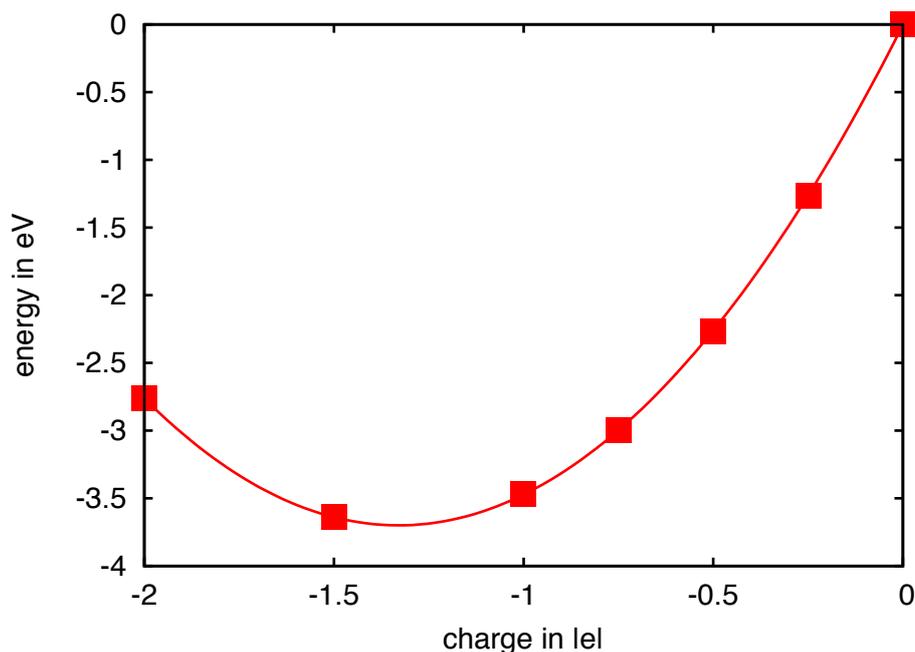
Figure 2.19.: Determination of the intra-molecularly screened Coulomb parameter U_0 of TCNQ (for data see table 2.3 on page 98) with the tier 2 basis set. The parabolic fit agrees perfectly with the data points giving a reliable U_0 according to (2.45).

The evaluation of $V_0^{\nu,\boldsymbol{l}}$ is done similarly. We consider two molecules with an additional charge of $q/2$ put on each. Now, q can range from zero to 4 electrons. The total energy for different q is fitted to

$$E_{V_0^{\nu,l,T}}(q) = 2E_{U_0^\nu}(q/2) + b_0 + b_1 q + V_0^{\nu,\boldsymbol{l},T}\left(\frac{q}{2}\right)^2 , \qquad (2.46)$$

yielding $V_0^{\nu,\boldsymbol{l},T}$. The first term accounts for the screening effects for individual molecules not to be captured in V_0.

2.3.2.3. Inter-molecular screening or full screening

In the previous section we merely treated the electrons within the molecules themselves. For the determination of the inter-molecular screening we have to take the entire crystal built from infinitely many molecules into account. We obtain their contribution to the Coulomb integrals $\Delta V_{\boldsymbol{l}}$ by constraining charges q to single molecules a distance $\boldsymbol{l}$ apart and calculating the reduction in energy due to polarization.
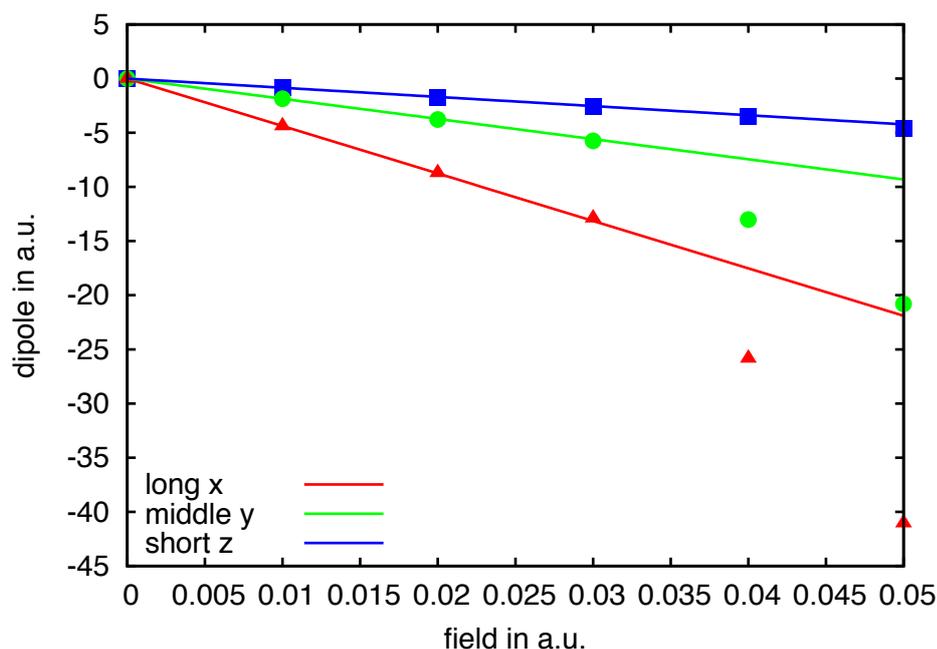
Figure 2.20.: Example fits for TCNQ to obtain polarizabilities along the principal moment of inertia axes. $x/y/z$ represents the long/middle/short axis. The fitting is based on the first three fields. For too large fields the response is no longer linear.

In principle, we could do these calculations within constrained-DFT, which is however infeasible even for relatively small systems. Instead, we resort to the electrostatic approach developed in chapter 1 to reach the infinite-system size limit. To this end, we need the polarizability tensor of each molecule in the crystal. According to section 2.1.2.3 we take an isolated molecule and apply a weak homogeneous external field along the principal axes. The linear response along all three principal directions determines the polarizability tensor, which we obtain by linear fits. An example is shown in figure 2.20. We follow the convention that the x-, y-, z-axis denotes the long, middle, and short axis of the molecule. Therefore, the z-axis is perpendicular to the molecular plane for planar molecules.

The simplest approach for an electrostatic treatment is to represent each molecule by a single polarizable point dipole. This approach works well, e.g. in the case of C_{60} as shown by Pederson and Quong [49]. In general, however, it is too crude – especially for closely packed stacks of planar molecules with high polarizabilities. Let us assess why. In TTF-TCNQ, for instance, we find stacks of TCNQ which show a mainly quasi one-dimensional behavior. The direction of minimal polarizability $\alpha_{zz} = 82\,a_0^3$ roughly points along the stack. From chapter 1 we know that the critical polarizability for a
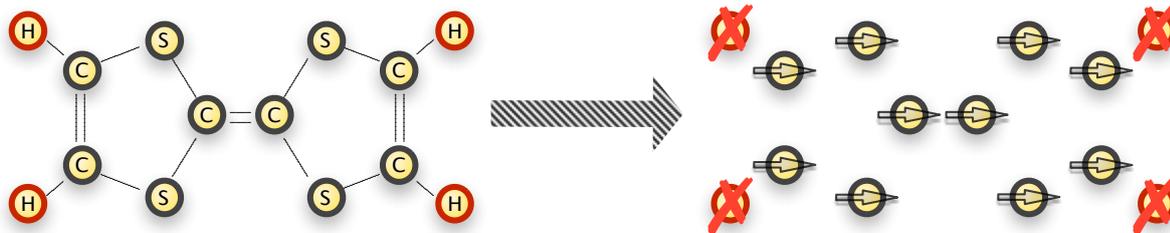
Figure 2.21.: Illustration of the Distributed Dipole Approach using a TTF molecule. Within the DDA all non-hydrogen atoms are replaced by polarizable point dipoles.

one-dimensional system is

$$\alpha_c = \frac{b^3}{4\zeta(3)}, \tag{2.47}$$

where b is the distance between the center-of-masses of two adjacent TCNQ molecules, here: $7.21\,a_0$. Thus, we find the critical polarizability $\alpha_c \approx 77.95\,a_0^3$ which is obviously smaller than α_{zz} of an isolated TCNQ molecule rendering this ansatz too crude. Moreover, the approximation by a single polarizable dipole is also problematic since the molecules inside the stack are so close to one another that they are inside the convergence radius of the dipole expansion making near-field effects important.

As a remedy we use the distributed dipole approach (DDA) where we distribute the molecular polarizability over all non-hydrogen atoms [50, 51] – effectively describing a molecule by a set of polarizable point dipoles (cf. figure 2.21). There are several distribution recipes. We can, for instance, use a weighted distribution over the atoms by Mulliken [52] or Hirshfeld [53] charges or use bonds instead of atoms. For the results presented in this work we use a uniform distribution over all non-hydrogen atoms and solve the system in real space.

Figure 2.22 gives an example calculation for the inter-molecular screening contribution ΔU for a charged TCNQ molecule. Even though the energy range on the y-axis is quite large, the extrapolation works well and we obtain reliable results.
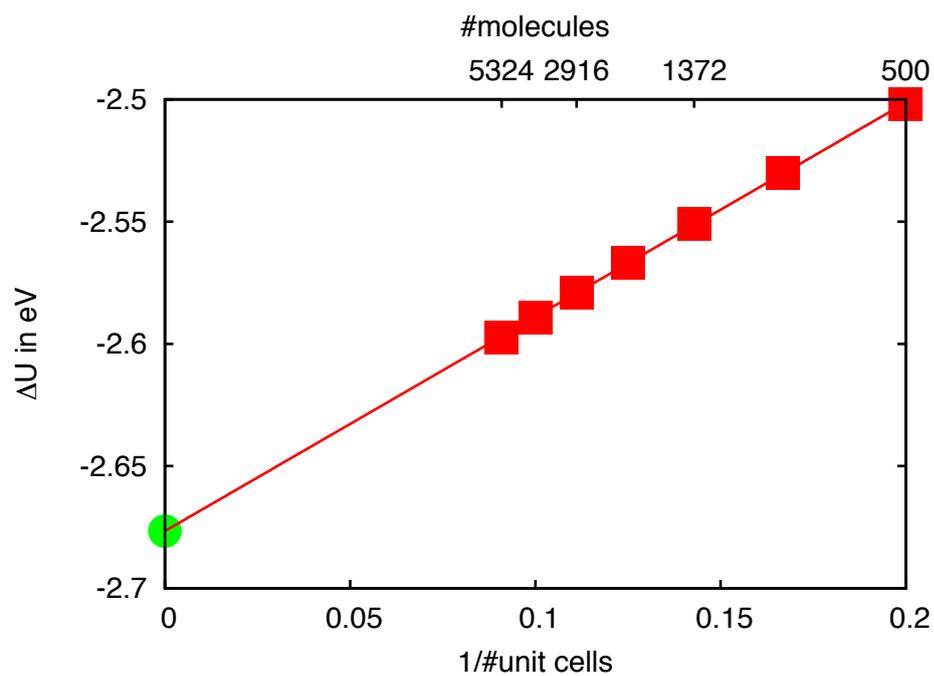
Figure 2.22.: Inter-molecular screening contribution ΔU for a charged TCNQ molecule. The energy range is rather large (black arrowed line). The extrapolation, however, works fine (red line) and we obtain a quite reliable result of about $\Delta U = -2.68$ (green circle) for the infinitely large crystal.

2.4. Application to TTF-TCNQ

In 1973 Alan Heeger and colleagues at the University of Pennsylvania synthesized the first organic conductor. It shows such unusual properties that even today it is still extensively studied [57, 58]. It is a charge-transfer salt consisting of two organic compounds – tetrathiafulvalene $C_6S_4H_4$ (TTF) and tetracyanoquinodimethane $C_{12}N_4H_4$ (TCNQ). Their chemical structure is shown in figure 2.23.

Figure 2.23.: Structural formulæ of TTF (left) and TCNQ (right).

Containing only carbon, hydrogen, sulfur, and nitrogen the salt made out of those two compounds has at $-220°$ C a conductivity comparable to copper at room temperature. Hence, it is a metal that does not contain a single metal atom. Moreover, it turns out that electron hopping in these materials happens only along stacks of like molecules giving rise to nearly one-dimensional bands. This low dimensionality in tandem with strong Coulomb repulsion compared to the kinetic energy leads to many-body effects, which can be observed in angular-resolved photoemission spectroscopy experiments (ARPES) [59, 60] and lead to an enhancement of the magnetic susceptibility [61]. TTF-TCNQ is one of the very few systems where signatures of exotic physics such as spin-charge separation has been clearly seen experimentally [62, 63, 64].

In order to interpret these experimental results, realistic estimates for the Coulomb integrals are necessary. Until recently, attempts to understand the exotic physics shown by TTF-TCNQ relied on the t-U Hubbard model. This description, however, runs into severe problems. To map the solution for the t-U model on ARPES data the hopping-matrix element along the molecular stacks has to be about twice of what has been estimated from band structure calculations [65] and experiment [66]. Using these ad-hoc parameters it is, however, impossible to understand the temperature dependence of the spectra. The reason for these shortcomings is the neglect of the inter-molecular Coulomb integrals [67]. This had already been suspected by Hubbard and others [68, 69].

With the methods described in the previous section we derive realistic model parameters. We find that the effect of the next-neighbor interaction V, being approximately $U/2$, indeed is to broaden the spectrum similar to enlarging t. Solving the corresponding generalized t-U-V Hubbard model we find that the addition of V does not lead to a Hubbard-Wigner-lattice as anticipated by Hubbard [68, 67].

2.4.1. The Crystal

Isolated TTF and TCNQ molecules are neutral, closed-shell systems and therefore stable. Figure 2.24 shows the energy levels in the vicinity of the HOMO and LUMO for both molecules.
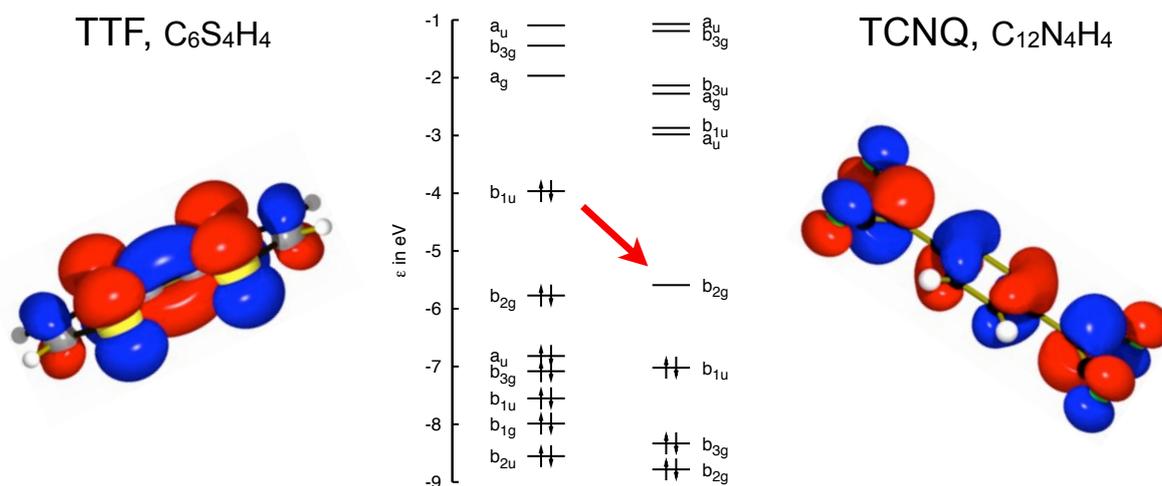
Figure 2.24.: Molecular-energy levels of isolated TTF with its HOMO (left) and TCNQ with its LUMO (right). The HOMO of TTF is significantly higher in energy than the LUMO of TCNQ. Hence, a charge transfer takes place. Due to the interplay between the HOMO-LUMO energy difference and charging energy about 0.6 electrons move from TTF to TCNQ. Isovalues for isosurfaces of wavefunctions are $d = \pm 0.08 \text{Å}^{-3/2}$.

When forming a crystal out of TTF and TCNQ molecules a charge transfer takes place, since the HOMO of TTF is significantly higher in energy than the LUMO of TCNQ. The interplay between the HOMO-LUMO gap and the charging energy leads to a transfer of on average about 0.6 electrons from TTF to TCNQ.

TTF-TCNQ crystallizes in a monoclinic structure of space group symmetry $P2_1/c$. Figure 2.25 shows this structure for views along the [010] and [100] direction. The lattice parameters are $a = 12.298(6)$ Å, $b = 3.819(2)$ Å, $c = 18.468(8)$ Å and $\beta = 104.46°$ [70]. Within the crystal there are stacks of like molecules, either the TTF cations or TCNQ anions, which run along the short crystallographic b axis through the entire crystal. The π-type HOMOs and LUMOs of adjacent molecules in the stacks overlap, hence forming a quasi one-dimensional band since the overlap between different stacks is negligible (the orbitals are shown in figure 2.24). Due to the charge transfer these quasi one-dimensional
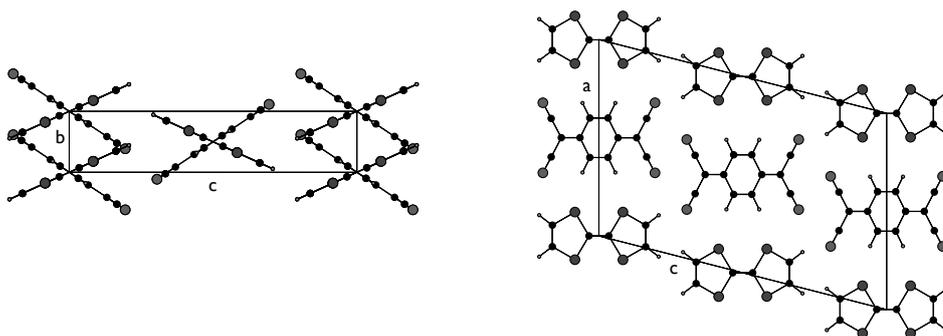
Figure 2.25.: Monoclinic crystal structure of TTF-TCNQ, with $P2_1/c$ symmetry and lattice parameters $a = 12.298(6)$ Å, $b = 3.819(2)$ Å, $c = 18.468(8)$ Å and $\beta = 104.46°$ [70]. Left/right figure provides the view along the [010]/[100] direction.

bands are partially filled and the system is metallic.

Assuming rigid molecules they can be described by their relative position and orientation of two molecules and thus a stack, i.e. the distance of the centers of gravity and the relative tilting angle. Obviously, these parameters are chosen in such a way as to minimize the total energy. There are two competing effects to be balanced. A gain in van der Waals-like bonding energy for approaching molecules and a strong repulsion when the molecules come too close. Figure 2.27 depicts this behavior.

Another aspect to consider is the packing density. To achieve high packing densities it is practical for the molecules to have a very similar footprint and commensurate inter-planar stacking distances within the stacks. When allowing the molecules to tilt, we can achieve both goals. Tilting changes the effective distance between the molecules for fixed center
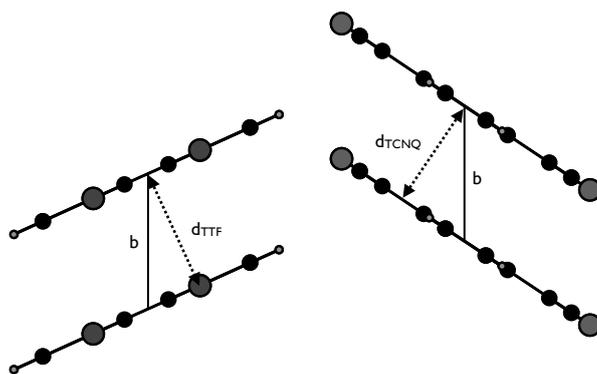
Figure 2.26.: Two adjacent molecules of a TTF (left) and TCNQ (right) stack. $b = 3.819(2)$ Å denotes the lattice vector. The tilting of the molecules effectively reduces the inter-planar distance $d_{TTF} = 3.48$ Å, $d_{TCNQ} = 3.17$ Å (for comparison: graphite $d_{graphite} = 3.35$ Å).

of mass distances (see figure 2.26) and can also lead to a similar footprint. The latter can be observed in the unit cell shown in figure 2.25. The left figure shows different stacks along the a-direction which have the same projection on the c-axis. Along the c- and b-axes there are only stacks of like molecules.

In TTF and TCNQ the molecules are tilted about the a-axis by an angle of $\theta_{\mathrm{TTF}}^{\pm} = \pm 24.5°$ and $\theta_{\mathrm{TCNQ}}^{\pm} = \pm 34.0°$, respectively. Between adjacent stacks the angle changes sign. This is shown in figure 2.26. The inter-planar distance $d_i = b \cos(\theta_i^{\pm})$ between adjacent TTF cations is $d_{\mathrm{TTF}} = 3.48\,\text{Å}$, whereas the one between TCNQ anions is given by $d_{\mathrm{TCNQ}} = 3.17\,\text{Å}$. For comparison the inter-planar distance in graphite of $3.32\,\text{Å}$ lies in between.

2.4.2. Model Parameters

2.4.2.1. Hopping parameters t_{TTF}, t_{TCNQ}

We study the hopping parameters as a function of the center-of-mass distance and the stacking angle as described in section 2.3.1.

Hopping for different angles First we fix the center-of-mass distance to the experimental value of b and evaluate the dependence on the relative angle about the axis a of the crystal. Figure 2.27 gives the total energy for TTF- (blue) and TCNQ-dimers (magenta). The circles indicate the experimentally observed angles. The configuration for $0°$ describes a parallel alignment of the two molecules, where their center-of-mass difference vector is perpendicular to the molecular plane. At this position the molecules have the largest effective distance from one another.

For larger angles starting at about $30°$ the inter-planar distances become so small that there is a steep increase in energy indicating a breakdown of the tight-binding description. Therefore, we restrict our discussion of the hopping-matrix elements to the interval $[0°, 50°]$.

Figure 2.28 presents the corresponding hopping integrals t. From the symmetry of the dimer wavefunction (figure 2.29) we infer that the hopping-matrix elements are negative for TTF. At parallel alignment ($\theta = 0°$) the molecular lobes directly face their counterpart of the opposite molecule. Therefore, we find a relatively large overlap and hence a large absolute value for the hopping-matrix element. An increase of the angle up to about $30°$ reduces $|t_{\mathrm{TTF}}|$ even though the effective distance of the molecules becomes smaller. This is due to the nodal structure of the HOMO of TTF. We find mainly two kinds of lobes – the central double bond between the carbon atoms and the localized lobes of the sulfur atoms. It is the loss in overlap of the sulfur lobes that leads to the diminishing, while the hopping contribution due to the central lobe remains relatively stable. From $\theta = 30°$ on we observe a steep increase in $|t_{\mathrm{TTF}}|$ arising from the central bond and the diminishing inter-planar distance. This gain in energy is, however, overcompensated by the Coulomb
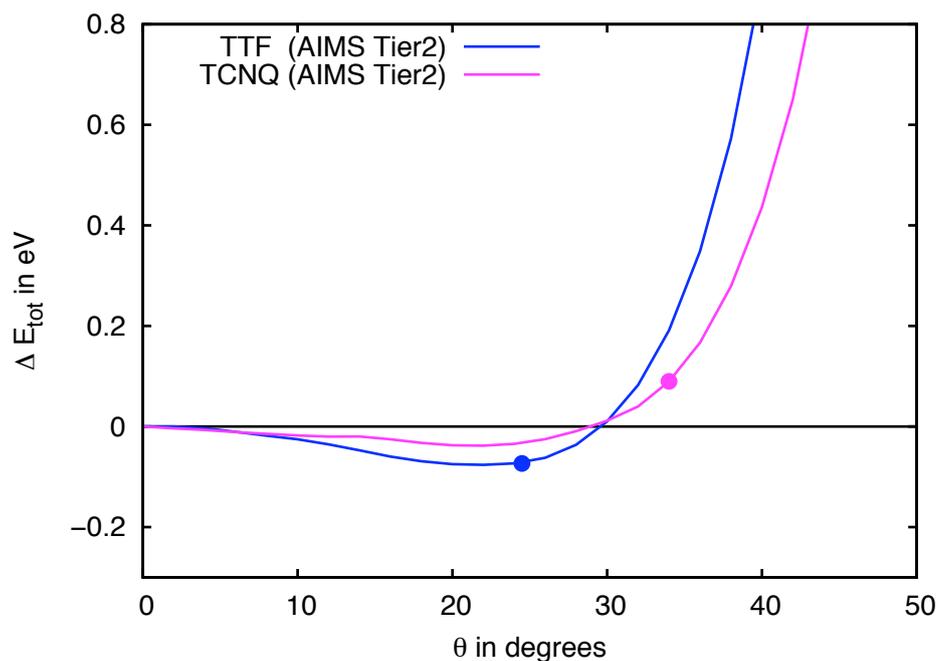
Figure 2.27.: Total energies for pairs of adjacent molecules relative to the total energy of angle 0° for different angles at the distance realized in the crystal. The inter-planar distance and therefore the effective distance of two molecules decreases with increasing θ as $\cos\theta$. Calculations were performed with the tier 2 basis set and the PBE functional. Circles denote the experimentally observed configuration.
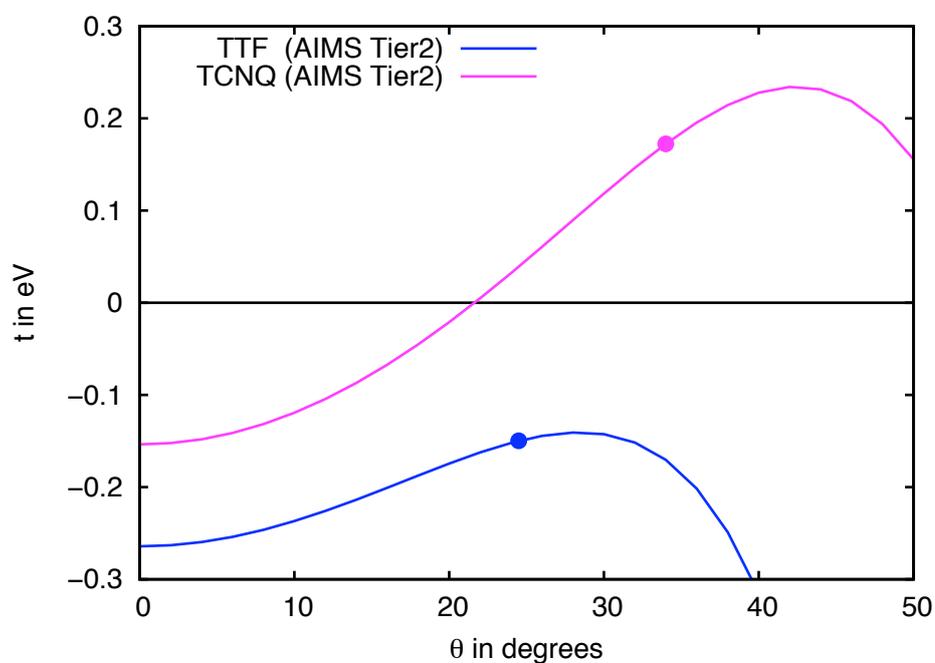
Figure 2.28.: Hopping-matrix elements for different angles at the distance realized in the crystal. Calculations were performed with the tier 2 basis set and with the PBE functional. Circles denote the experimentally observed structure.
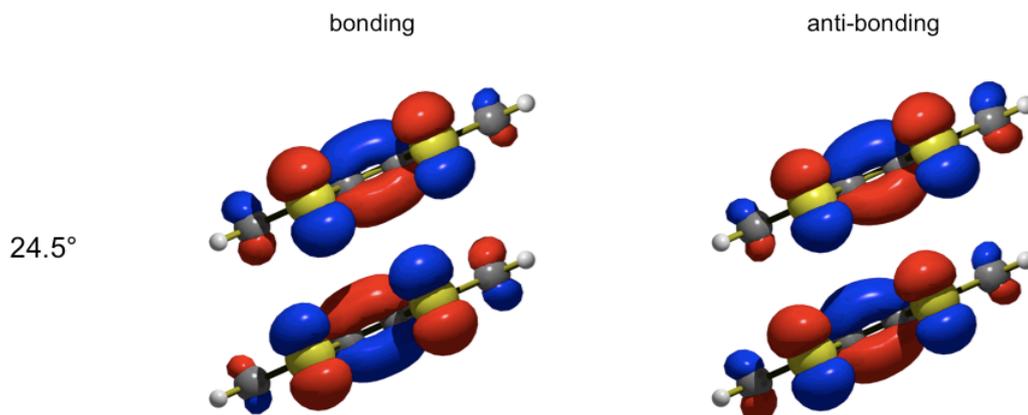
Figure 2.29.: TTF molecule 'dimer' to deduce the sign of the hopping parameter. It is negative since the bonding wavefunction is anti-symmetric. Since the main lobes run parallel to the long axis we do not expect a sign change in the hopping-matrix element when rotating about the middle axis. Isovalues for isosurfaces of wavefunctions are $d = \pm 0.08 \text{Å}^{-3/2}$.

repulsion as seen in the total energy plot.

The hopping integrals for TCNQ show an even more interesting behavior. Again, for $\theta = 0°$ the hopping-matrix element is negative and relatively strong. The lobes of the LUMO of TCNQ run along the y-axis, parallel to the rotation axis. Therefore, when leaving the parallel alignment, the overlap of the lobes with their partner ones decreases while the overlap with the neighboring lobes (of opposite sign) increases. Hence, $|t_{\text{TCNQ}}|$ decreases. Examples for some angles are shown in figure 2.30. At about 21° the lobes face the nodes of the partner molecule overlapping with lobes of both sign with equal weight. The matrix element becomes $t_{\text{TCNQ}} = 0$. For larger angles the hopping becomes positive. It increases further and reaches its maximum $|t_{\text{TCNQ}}| = t_{\text{TCNQ}}$ at about 41° due to a decrease in the effective distance and the more direct overlap. For even larger angles the overlap decreases again leading to a diminishing of t_{TCNQ} as before.

Hopping Parameters For Different Distances   To study the distance dependence we fix the angle to the experimental values. Since we know the sign of the hopping parameters at the experimental settings and there are no zeros in the hopping function for different distances we can directly take the sign from the previous section.

For small distances we find strong hopping; here, the application of the tight-binding ansatz is, however, not appropriate as indicated by the total energy (right plot of figure 2.31). For the experimental distance we recover the hopping-matrix elements calculated before. Further increasing the dimer distance leads to a rapid decay in the hopping amplitudes. For the second-nearest neighbor distance we find hardly any hopping
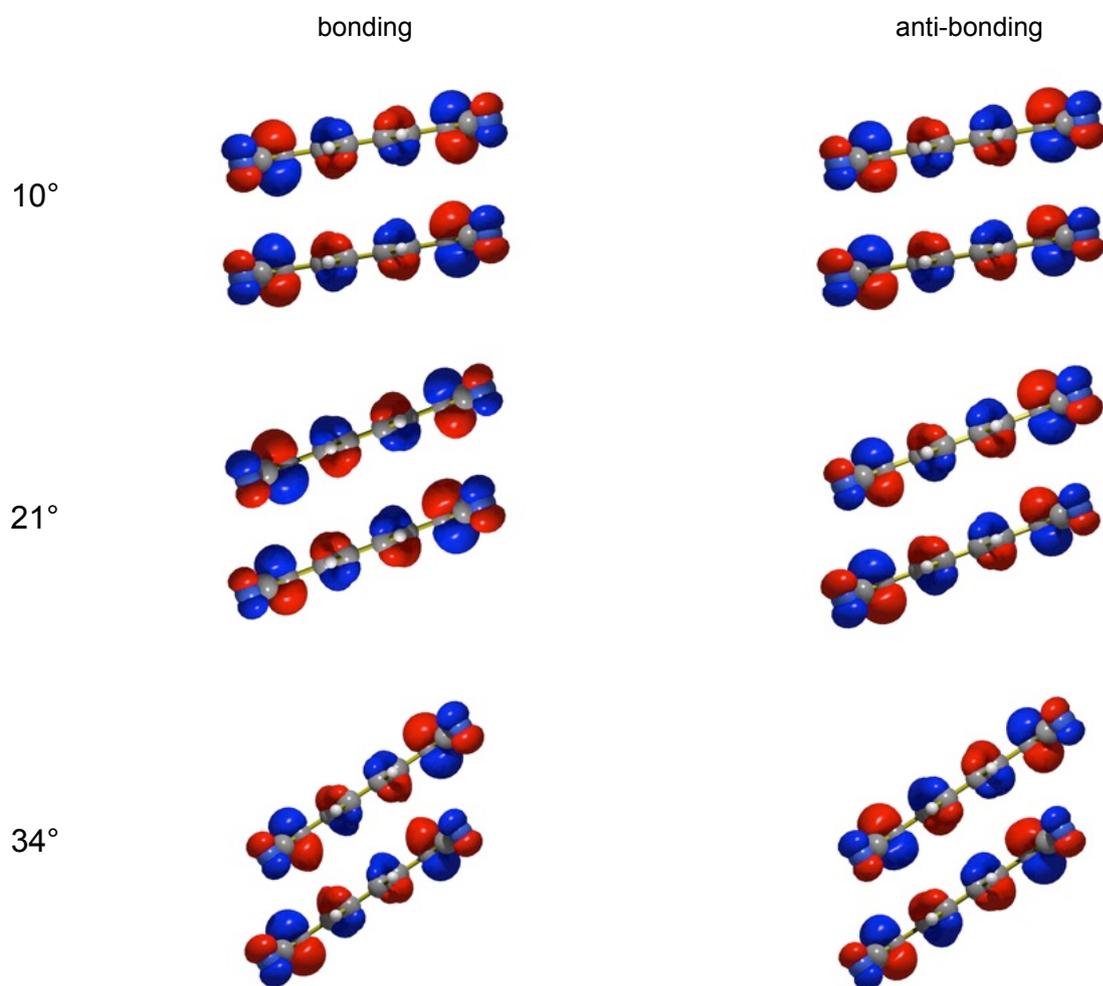
Figure 2.30.: TCNQ molecule 'dimer' to deduce the sign of the hopping integral for different angles. The first row shows molecules at experimental distance but rotated by an relative angle of $10°$. Since the wavefunction of the bonding orbital is anti-symmetric, $t_{\mathrm{TCNQ}} < 0$. For an angle of $34°$ it is symmetric and thus $t_{\mathrm{TCNQ}} > 0$. For $21°$ we are very close to $t_{\mathrm{TCNQ}} = 0$. Isovalues for isosurfaces of wavefunctions are $d = \pm 0.08 \mathrm{\mathring{A}}^{-3/2}$.
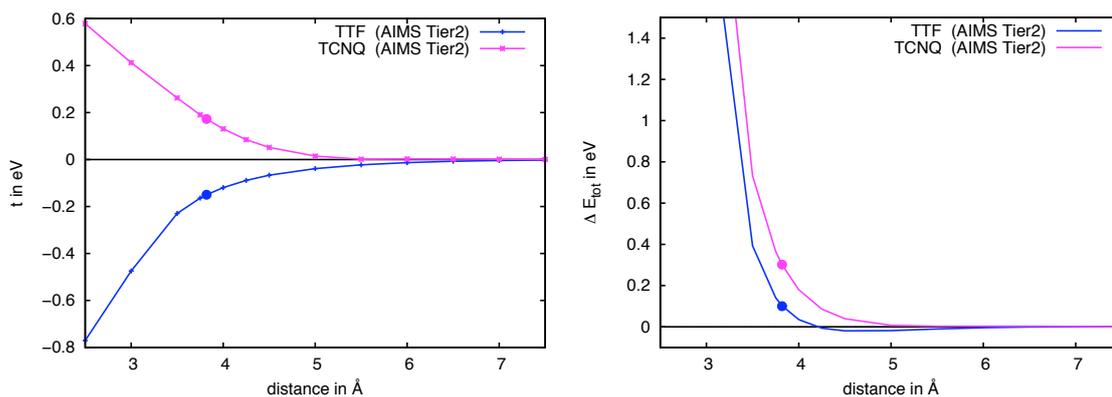
Figure 2.31.: Hopping-matrix elements for different distances at the relative angle
realized in the crystal. Calculations were performed with the tier 2 basis
set and the PBE exchange-correlation functional. Circles denote the
distance from the experimental structure. The hopping-matrix elements
decay fast. There is no long-range hopping and we thus obtain simple
cosine bands.

anymore. For even larger distances we asymptotically get the results of two isolated
molecules. Therefore, we can restrict the description to nearest-neighbor hopping only.

Thus, for TTF and TCNQ stacks we find effectively one-dimensional single-orbital
bands, well described a nearest-neighbor tight-binding ansatz. Hence, the dispersion
relation (2.34) becomes

$$\epsilon_{k\nu} = \varepsilon_\nu - 2t^\nu \cos(ka) , \tag{2.48}$$

where $t_{\text{TTF}} = -0.15\,\text{eV}$ and $t_{\text{TCNQ}} = 0.17\,\text{eV}$.

2.4.2.2. Coulomb parameter

Bare Coulomb integrals   From the molecular orbitals of an isolated molecule we
evaluate the bare Coulomb integrals (2.38) according to the method given in section
2.3.2.1. The results for the LUMO of TCNQ and HOMO of TTF are summarized in table

Table 2.2.: Bare Coulomb parameters of TCNQ and TTF for near neighbors in the
stacks derived by the method given in section 2.3.2.1. All-electron DFT
calculations were performed with PBE and the tier 2 basis set. All energies
are given in eV.

	U_{bare}	V_{bare}	V'_{bare}	V''_{bare}
TTF	5.98	3.10	1.79	1.23
TCNQ	5.36	2.88	1.73	1.20
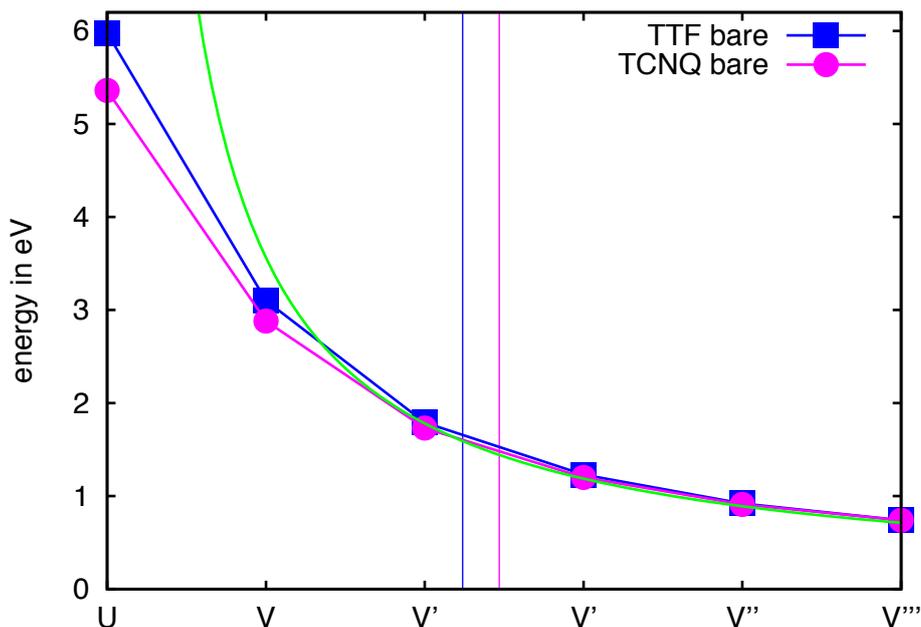
Figure 2.32.: Bare Coulomb integrals for the HOMO of TTF (blue) and the LUMO
of TCNQ (magenta). For large distances the bare Coulomb integrals
seamlessly pass into the $1/r$ Coulomb repulsion (green).

2.2 and visualized in figure 2.32.

For large distances we find the $1/r$ Coulomb law (green) as discussed in section 2.3.2.1. In this regime the Coulomb integrals for the HOMO of TTF and the LUMO of TCNQ are the same. For the onsite U_{bare} and next-neighbor matrix element V_{bare} there are, however, pronounced differences. The main charge density of the HOMO of TTF resides on the four sulfur atoms and is therefore quite localized. A compact charge density obviously leads to a large U_{bare}. These sulfur lobes also significantly protrude from the molecular plane explaining the strong effect on V_{bare}.

The LUMO of TCNQ, in contrast, is more extended giving a smaller U_{bare}. Since there are no lobes sticking as far out of the molecular plane, this is also true for V_{bare}.

Intra-Molecularly Screened Coulomb Integrals   For the intra-molecularly screened Coulomb integrals we follow the recipe of section 2.3.2.2.

Starting with the local Hubbard-U we add electrons to TCNQ which will occupy the LUMO. From the change in the total energy we gain the Coulomb parameters via fitting. The results are collected in table 2.3 and plotted in figure 2.33.

For comparison, we give the results for different tiers and the PW-LDA exchange-correlation functional in tier 3. The total energies with LDA are about 140 eV higher in

Table 2.3.: U_0 of TCNQ with different functionals and basis sets. All energies are given in eV. The LDA and PBE exchange-correlation functionals and the basis sets give roughly similar results for U_0, although the total energies differ significantly between LDA and PBE with an offset of about $140\,\text{eV}$. The difference is mainly due to different energies of the core levels and therefore irrelevant for the charging energy. Some results are shown in figure 2.33.

charge $q/|e|$	E_{tot} in eV			
	PBE tier 1	PBE tier 2	PBE tier 3	LDA tier 3
0.00	-18450.79	-18451.17	-18451.22	-18311.90
-0.25	-18452.07	-18452.45	-18452.48	-18313.23
-0.50	-18453.07	-18453.43	-18453.48	-18314.30
-0.75	-18453.81	-18454.16	-18454.22	-18315.08
-1.00	-18454.30	-18454.65	-18454.71	-18315.60
-1.50	-18454.46	-18454.82	-18454.87	-18315.87
-2.00	-18453.56	-18453.94	-18454.00	-18315.11
U_0/eV	4.240	4.180	4.161	4.196
$\Delta U_0^{\text{fit}}/\text{eV}$	±0.003	±0.007	±0.009	±0.004

Table 2.4.: U_0 of TTF with different basis sets. The results for both basis sets agree very well. All energies are given in eV.

charge $q/|e|$	E_{tot} in eV	
	PBE tier 2	PBE tier 3
0.00	-49606.82	-49606.84
0.25	-49605.67	-49605.70
0.50	-49604.26	-49604.29
0.75	-49602.54	-49602.57
1.00	-49600.53	-49600.59
1.50	-49595.66	-49595.69
2.00	-49589.56	-49589.62
U_0/eV	4.709	4.703
$\Delta U_0^{\text{fit}}/\text{eV}$	±0.003	±0.003

Table 2.5.: Intra-molecularly screened Coulomb integrals for near-neighbor distances. Calculations performed with the PBE functional and the tier 2 basis set. The results from tables 2.4 and 2.3 have been fitted to function (2.46) to gain the parameters (cf. figure 2.35). All energies are given in eV.

	V_0	V_0'	V_0''
TTF	2.91	1.69	1.20
TCNQ	2.73	1.63	1.19
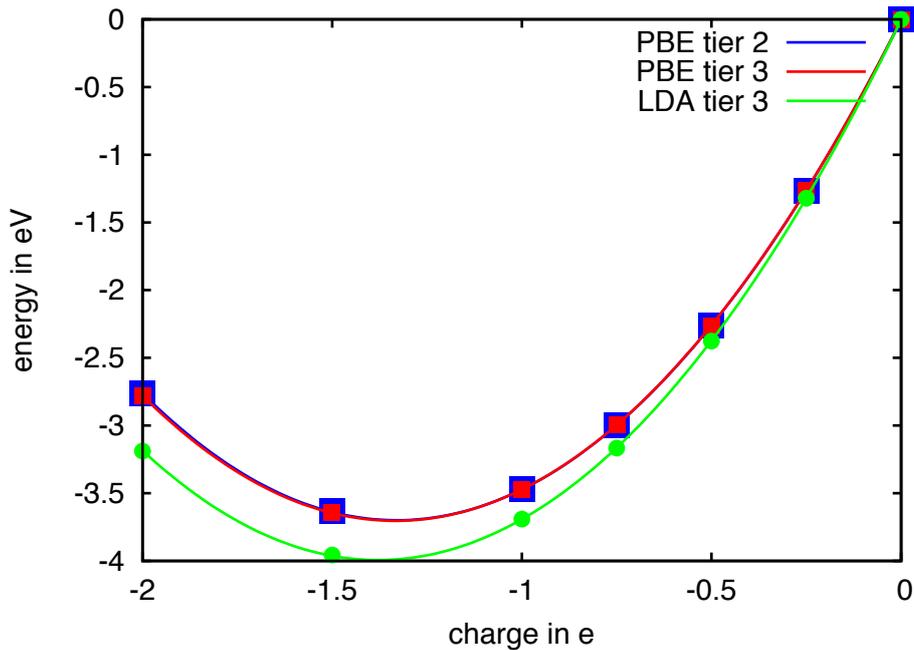
Figure 2.33.: Determination of the intra-molecularly screened Coulomb parameter U_0 of TCNQ from the data shown in table 2.3. Tier 2 (blue) and tier 3 (red) basis sets for the PBE functional show hardly any difference. LDA energies change slightly faster with increasing numbers of electrons (green).

energy. This difference is mainly due to the different energies of the core levels. Therefore, we obtain quite similar results which are just slightly larger than the ones from the corresponding PBE tier 3 calculation.

Within PBE and different basis sets we also find consistent results. The difference between the first and second tier are about 60 meV, while between second and third it is about 20 meV. Hence, for these quantities tier 1 would already suffice.

We evaluate the local Hubbard U_0 for TTF, accordingly. Table 2.4 provides the results for tier 2 and tier 3. Both agree very well.

The near-neighbor Coulomb matrix elements V_{bare} are accessible by charging molecular dimers. Figure 2.34 gives our findings for both types of molecules and shows the least-squares fit to actually obtain the parameters. Table 2.5 gives the final results.

Comparing the intra-molecularly screened and bare Coulomb matrix elements we can study the effect of screening within the molecules. Figure 2.35 provides this comparison of both integrals. For the local Hubbard-U the screening is pronounced. For both molecules the value of U_{bare} is reduced by more than 1 eV, i.e. more than 20%. For near-neighbors we hardly find any screening. Intra-molecular screening mainly acts locally.
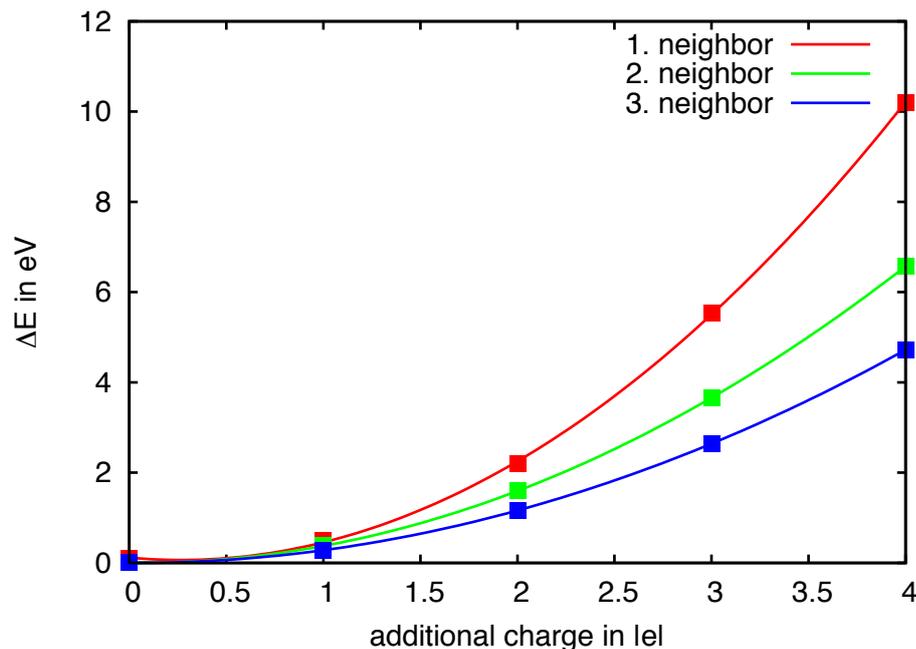
Figure 2.34.: Determination of intra-molecularly screened Coulomb parameters for near neighbors V_0, V_0' and V_0'' of TTF. ΔE denotes $\Delta E = E_{V_0^\nu, I, T}(q) - 2E_{U_0^\nu}(q/2)$. Calculations performed with the PBE functional and the tier 2 basis set.
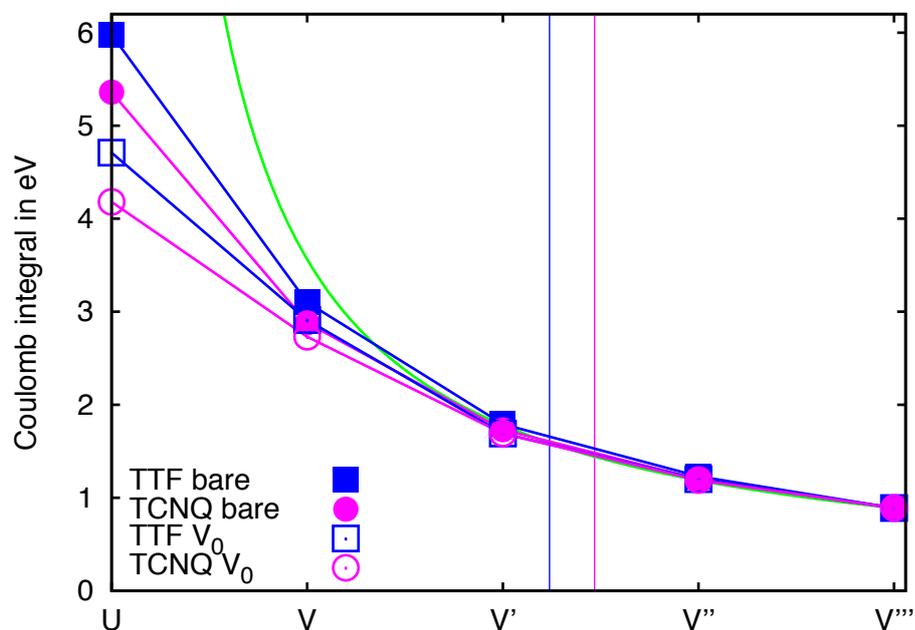
Figure 2.35.: Bare (filled symbols) and intra-molecularly screened (unfilled symbols) Coulomb integrals for the HOMO of TTF (blue) and the LUMO of TCNQ (magenta). For large distances the Coulomb integrals seamlessly pass into the $1/r$ Coulomb repulsion (green). Intra-molecular screening mostly screens the local Coulomb integral ($> 1\,\text{eV}$). Neighbors are hardly screened.
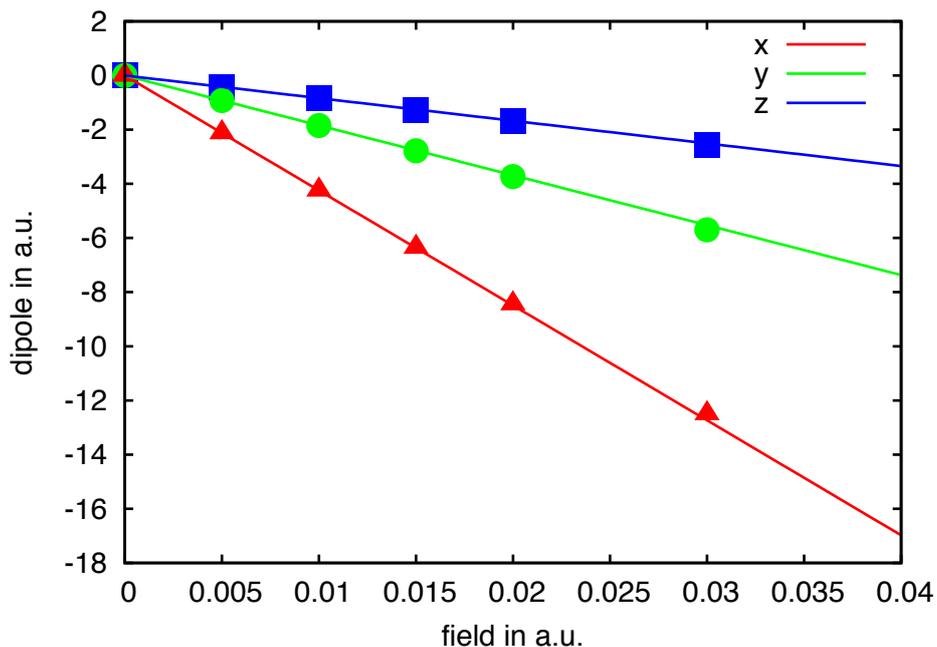
Figure 2.36.: TCNQ polarizabilities along the principal moment of inertia axes. x/y represents the long/short axis. Results are shown in table 2.6. The fit is based on the four weakest fields. For larger fields the response becomes non-linear.

Inter-Molecular Screening As an ingredient for the DDA we need the polarizabilities of the molecules. Figure 2.36 shows the dipole response of the molecules to a small external electric field along with the fit to determine the polarizability tensor α. x, y, and z represent the (red) long, middle (green) and short (blue) axis of the molecules.

The numerical results are compiled in table 2.6 for both molecules. Comparing PBE tier 1 calculations with the corresponding higher tiers (only TCNQ case) shows that the polarization is significantly more sensitive to the basis set than the intra-molecular screening parameters. An electric field distorts and shifts the orbitals making more basis functions necessary. The second last column of table 2.6 gives the result for a calculation with the LDA exchange-correlation functional using the tier 3 basis set. Both polarizabilities agree within a few percent.

We use the polarizabilities obtained from the tier 2 PBE DFT runs to perform the DDA calculations using our electrostatic real-space screening code to evaluate the inter-molecular screening contribution. The results are summarized in table 2.7.

We notice that for TTF-TCNQ the screening is very efficient. $U = U_0 + \Delta U$, for instance, is reduced by more than $2.5\,\mathrm{eV}$. $V = V_0 + \Delta V$ is still reduced by almost $2\,\mathrm{eV}$.

Table 2.6.: Polarizabilities of TTF and TCNQ with different functionals and basis sets. x/y represent the long/short axis of the molecules. Polarizabilites are in atomic units, i.e. a_B^3.

direction	TTF		TCNQ			
	PBE tier 2	PBE tier 3	PBE tier 1	PBE tier 2	PBE tier 3	LDA tier 3
α_{xx}	227.74	231.71	427.81	435.85	437.95	424.48
α_{yy}	159.69	161.58	177.33	183.65	186.22	184.23
α_{zz}	86.29	90.04	67.94	78.38	84.56	83.61

Table 2.7.: Inter-molecularly screened Coulomb contributions. We use the real-space distributed dipole approach (DDA) up to 5324 molecules and extrapolate to infinitely many (cf. 2.22). All energies are given in eV.

	ΔU	ΔV	$\Delta V'$	$\Delta V''$
TTF	-2.83	-1.80	-1.30	-0.94
TCNQ	-2.68	-1.73	-1.34	-0.95

And even the second-nearest neighbor Coulomb matrix elements are diminished by more than 1 eV.

2.4.2.3. Parameter Summary

For quick reference we summarize the parameters for constructing a realistic generalized Hubbard model for TTF-TCNQ. All relevant values are compiled in table 2.8.

Table 2.8.: All relevant results for TTF-TCNQ obtained by FHI-aims (PBE, tier 2) and the DDA solved with our real-space code. All results in eV.

	t	U	V	V'	V''
TTF bare	0.15	5.98	3.10	1.79	1.23
TTF intra-mol. scr.		4.71	2.91	1.69	1.20
TTF full screening		1.87	1.11	0.39	0.26
TCNQ bare	0.17	5.36	2.88	1.73	1.20
TCNQ intra-mol. scr.		4.18	2.73	1.63	1.19
TCNQ full screening		1.50	1.00	0.29	0.24

We find that indeed the on-site *and* longer-range Coulomb matrix elements are important in TTF-TCNQ. Compared to the band-width W of about 0.6 eV and 0.7 eV for TTF and TCNQ, respectively, the ratio U/W is larger than 2. The nearest-neighbor interaction V is still about $U/3$. Hence, it must be included in a realistic model. In principle, even the third-nearest neighbors should be included.

We also find a sizable coupling between neighboring stacks, which after taking screening into account is about 0.4 eV.

2.4.3. Realistic Description

Hence, in principle for a realistic description of TTF-TCNQ we require a three-dimensional generalized Hubbard model, where we take both inter-stack as well as long-range Coulomb interactions into account. Previous calculations used simple t-U Hubbard models [64]. To make contact to these calculations we also restrict ourselves to a single stack of TTF or TCNQ. First, we study the t-U model. In a second step, we analyze what happens when including V.

2.4.3.1. t-U Model

We use a 20 sites system with 6 electrons of either spin to model a stack of TCNQ. To match angular-resolved photo emission experiments (ARPES) with a simple t-U Hubbard model, we have to choose $U = 1.96$ eV and $t_{\mathrm{fit}} = 0.4$ eV, a hopping value twice as large as our result from the previous section. With our massively parallel Lanczos solver (see appendix E) and Cluster Perturbation Theory [71] we obtain the spectral function plotted in figure 2.37. We observe that the tight-binding cosine band (green line) is mainly retained in the many-body picture with the bandwidth being slightly reduced. However, the Coulomb interaction leads to striking changes due to correlation effects. In the interval
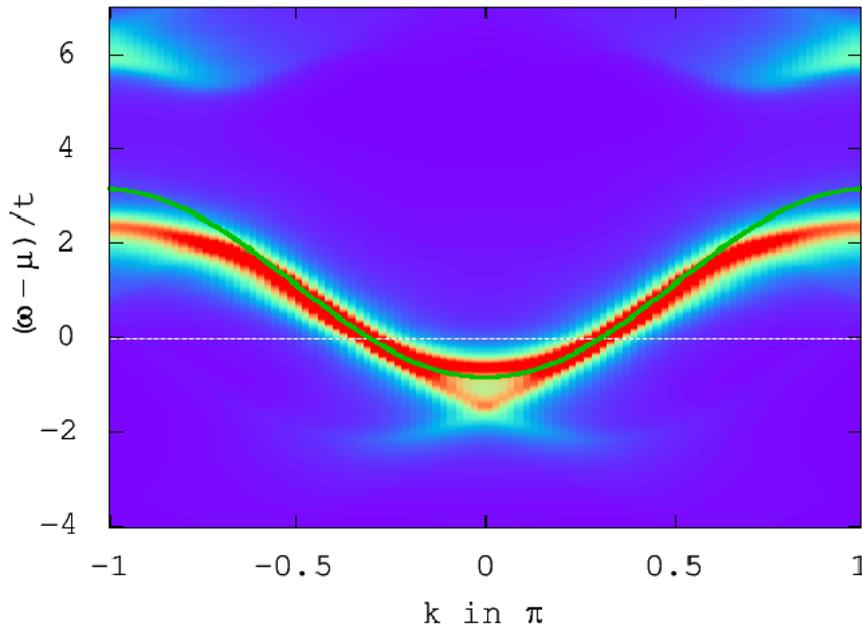
Figure 2.37.: Angular-resolved spectral function obtained by CPT for a 20 sites TCNQ system with 6 electrons of either spin ($U = 1.96$ eV, $t = 0.4$ eV). The white line shows the chemical potential, the green cosine represents the independent-particle band. Signatures of spin-charge separation can be observed around the Γ-point. For a discussion refer to text.
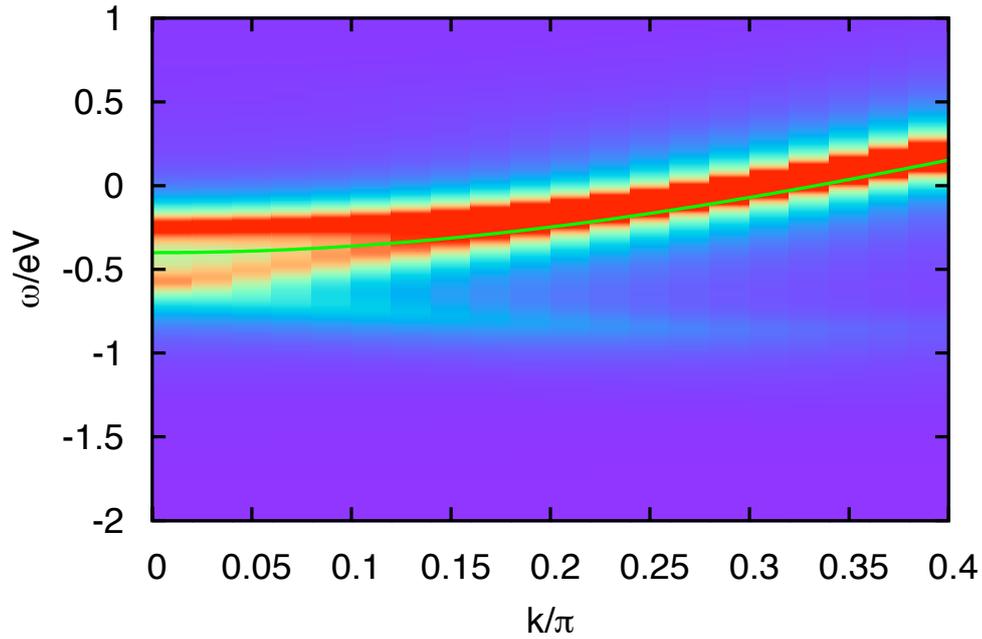
Figure 2.38.: Magnification of $A_k(\omega)$ in interval $0 < k < k_F$ of the TCNQ calculation
shown in figure 2.37.

$-k_F < k < k_F$, with $k_F/\pi = 0.3$ we find three dispersing features. Figure 2.38 shows a
blowup of this region. Exploiting $A_{-k}(\omega) = A_k(\omega)$ we only present the spectral function
for $k_F > 0$.

Close to the Fermi level (white line) at $\omega - \mu = 0$ there are peaks with high weight
ranging from $\omega \approx -0.5t$ at $k = 0$ to $\omega \approx 0t$ at $k = k_F$, showing a rather narrow dispersion.
According to Luttinger liquid theory these spectral weights correspond to the spinon
branch. In figure 2.37 we see that there is only a single spinon branch, since the partial
branches for $k < 0$ and $k > 0$ join at the Γ-point with zero slope. At higher binding
energies, i.e. lower values of ω, there seem to start two branches. Figure 2.37 suggests
that the lower branch, labelled shadow branch, is the continuation of the upper branch for
$k < 0$. This is known from the Bethe ansatz solution [72]. This shadow band runs from
$k = 0$ and $\omega \approx -1.5t$ to $k = k_F$ from $\omega \approx -2.2t$ quickly losing weight with increasing
$|k|$. The actual holon band extends from $k = 0$ and $\omega \approx -1.5t$ to $\omega \approx -0t$ at $k = k_F$. It
appears to join the spinon branch at k_F. The holon and spinon branches have almost
constant weight in this region with the spinon branch being considerably more pronounced.
These results indeed agree very well with experimental data.

2.4.3.2. *t-U-V* Model

While the *t-U* Hubbard model derived spectral function agrees well with ARPES experiments, the temperature dependence does not agree at all. Moreover, doubling the hopping parameter in this ad-hoc manner is very unsatisfactory.

Hubbard-Wigner Lattice   Hence, we resort to a *t-U-V* Hubbard model description. From table 2.8 we see that U and V are larger than the bandwidth $W = 4t$. As a first approximation Hubbard [68] suggested to use the zero-bandwidth limit ($t = 0$) and to assume $U \to \infty$ for $U > V$. In the following we only consider TCNQ. The argument also holds for TTF when regarding holes instead of electrons.

   The filling of a TCNQ stack is 0.6. With $U \to \infty$ all double occupancies are suppressed. Due to V the electrons also try not to be next neighbors. The corresponding many-body ground state can be described in terms of a generalized Wigner lattice [35] with periodicity of 5 sites. The electrons arrange in a pattern [68] $\cdots \bullet \circ | \bullet \bullet \circ \bullet \circ | \bullet \bullet \circ \bullet \circ | \bullet \bullet \circ \bullet \circ | \bullet \bullet \circ \cdots$, where $\bullet$ or $\circ$ denote an occupied or unoccupied orbital, respectively. The spectral function for this state is easy to interpret. Even when including t [71]. This approach, however, fails to properly describe the experimental results. Clearly, the approximation $U \to \infty$ and therefore double-occupancy $d = 0$ is not approximate.

The Effect of V   Evidently, double-occupancies are essential for explaining the failure of the Hubbard-Wigner lattice approach. In an uncorrelated system the probability of double occupations is given by $d = n_\uparrow \cdot n_\downarrow$ – hence, $d = 0.09$ for TCNQ filling. Using $U = 1.7$ eV, $t = 0.18$ eV in a 20 site model and the Lanczos method we already find about $d = 0.01$. Increasing V leads to an increase in d. For $V = 0.9$ eV we find $d = 0.027$.

   In order to obtain the same concentration of doubly occupied sites d in a *t-U* model we have to increase the hopping parameter to $t = 0.37$, close to t_{fit}. Hence, increasing V seems to encourage hopping which leads to a broadening of the spectrum. Consider two electrons passing each other. When being neighbors they pay V. Then, occupying the same orbital costs U but they "gain" V. After passing each other they again pay V. Thus, this process requires the energy $U - V$, instead of U to happen.

   Figure 2.39 shows the spectral function for TCNQ with $U = 1.7$ eV, $t = 0.18$ eV and varying values of V. We see that the main effect of V is to broaden the spectrum around the Fermi level. Remarkably, we can understand the broadening in first-order Rayleigh-Schrödinger perturbation theory [67, 71] (red lines). Surprisingly, perturbation theory gives a remarkably good description for the effect of V up to $U/2$, the area of interest.

Spectral Functions   Using CPT to evaluate the spectral function for the *t-U-V* model is not straightforward, as we have to decide how to deal with the V-term between different clusters. We can, e.g., include the next-neighbor interaction V in periodic boundary conditions. Figure 2.40 shows the high-resolution spectral function. Figure 2.41 presents
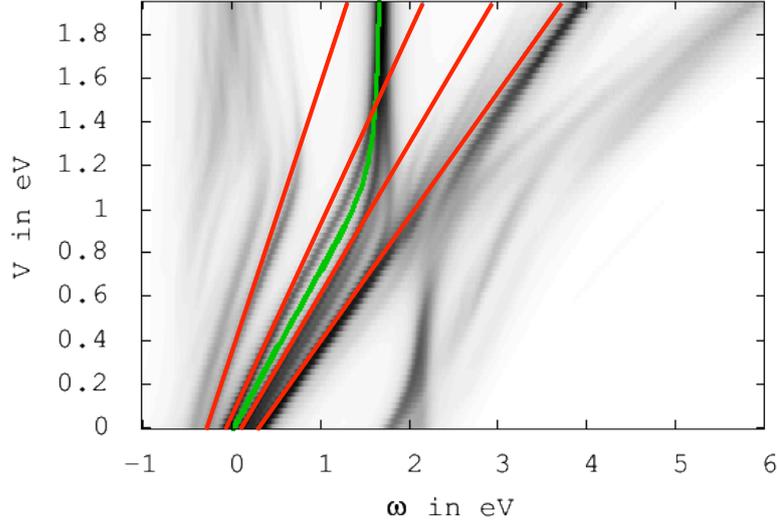
Figure 2.39.: Density plot of spectral function for TCNQ ($U = 1.7$, $t = 0.18$) as a function of V of a 10 sites chain, with 3 electrons of either spin type. The green curve denotes the chemical potential. The four blue lines show the shift in the peaks with the largest spectral weight in first-order perturbation theory.

the results for an alternative method, kCPT: Performing Lanczos calculations for a periodic cluster of L sites where the next neighbor hopping is renormalized by a factor of $\sin(\pi/L)/(\pi/L)$ we evaluate the cluster Green's function $\mathcal{G}_c(K,\omega)$. In a CPT-like calculation we obtain the full Green's function by

$$\mathcal{G}^{-1}(K + \tilde{k}, \omega) = \mathcal{G}_c^{-1}(K, \omega) - \Sigma(K, \tilde{k}, \omega) \, \alpha \,, \tag{2.49}$$

where

$$\Sigma(K, \tilde{k}, \omega) = \epsilon(K + \tilde{k}) - \bar{\epsilon}(K) \,. \tag{2.50}$$

ϵ is the usual tight-binding energy $\epsilon(k) = -2t \cos(k)$ and $\bar{\epsilon}(K)$ is defined as

$$\bar{\epsilon}(K) = \frac{L}{2\pi} \int\limits_{K-\pi/L}^{K+\pi/L} \mathrm{d}\tilde{k} \, \epsilon(\tilde{k}) = -\frac{tL}{\pi} \, \sin(k) \bigg|_{K-\pi/L}^{K+\pi/L} \,. \tag{2.51}$$

It can be regarded as a coarse grained version of ϵ.

Unfortunately both methods show strange finite-size effects making a detailed analysis hard. The two quasi-particle branches split below the Fermi level which originates mainly from the approximate treatment of the long-range interaction across the cluster boundary. For an accurate study we would need larger clusters.
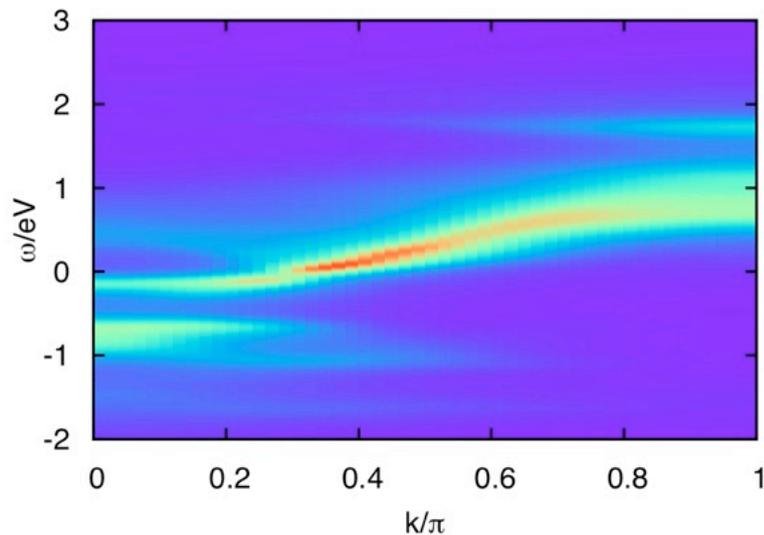
Figure 2.40.: CPT calculation of spectral function $A_k(\omega)$ with next-neighbor interaction $V = 0.9$ in PBC ($t = 0.18$, $U = 1.7$) for TCNQ filling ($n = 0.6$) on 20 sites.
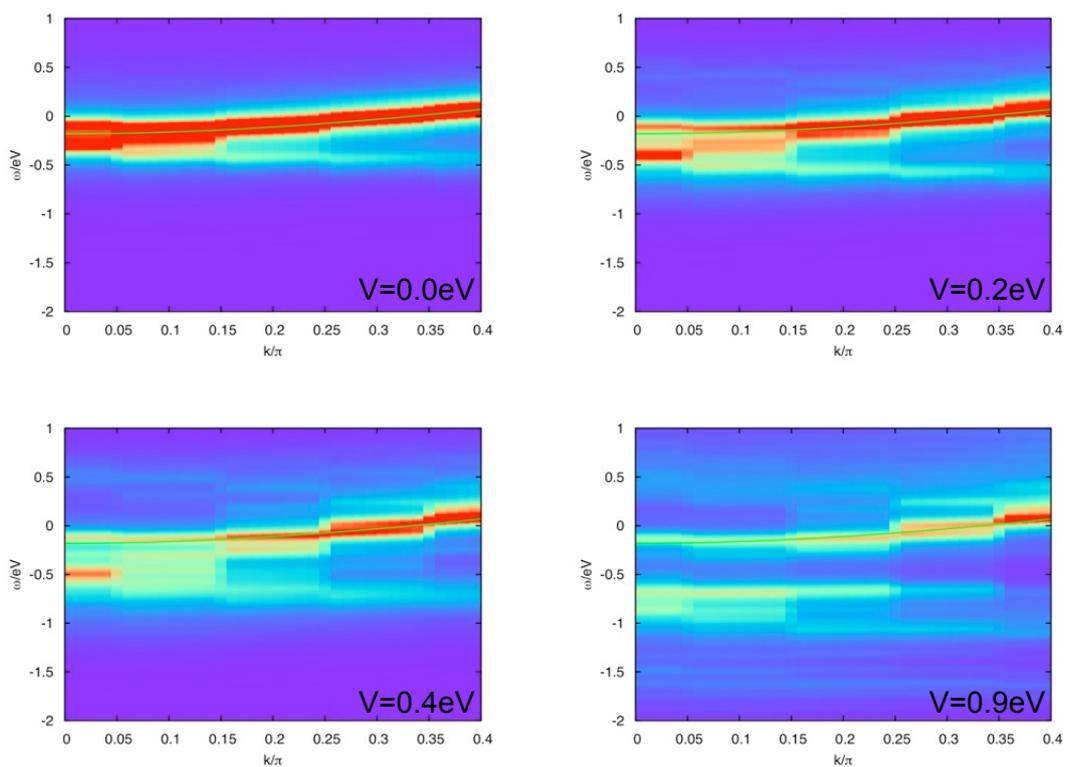
Figure 2.41.: kCPT calculation of spectral function $A_k(\omega)$ with next-neighbor interaction $V = 0.9$ ($t = 0.18$, $U = 1.7$) for TCNQ filling ($n = 0.6$) on 10 sites.

2.5. Application to (BEDT-TTF)$_2$I$_3$

Bis(ethylenedithio)tetrathiafulvalene (BEDT-TTF), often abbreviated as ET, is a very good electron donor with an extended π-electron system. With oxidants such as iodine it forms charge transfer compounds which have been shown to exhibit a wide range of properties. They can be insulators, semiconductors, metals, or even superconductors. It is characteristic of BEDT-TTF that it forms a variety of different phases with various oxidants.

Organic molecular crystals of (BEDT-TTF)$_2$X, where X denotes a tri-halide anion, are effectively low-dimensional systems. Here, we will study ET with the linear anion tri-iodide I$_3$, giving rise to the crystal (BEDT-TTF)$_2$I$_3$. There exist several crystal structures of this compound with identical stoichiometry. When synthesizing the predominant structures are the α- and β-phases. The α-phase is metallic at room temperature but exhibits a metal-to-insulator transition when cooled below 135 K [73, 74]. The β-phase, on the other hand, was the first quasi two-dimensional organic superconductor found at ambient pressure [75, 76]. In addition, the molecules can also condense in the κ- and Θ-phase. These two phases are only formed with iodine anions unlike the α- and β-phases where X denotes several possible tri-halide anions. Originally κ- and Θ-phases were first synthesized in 1986 as mixed-anion salts. Among them was, for instance, Θ-(BEDT-TTF)$_2$(I$_3$)$_{1-x}$(AuI$_2$)$_x$, where $x < 0.02$. Recently neat crystals of Θ-(BEDT-TTF)$_2$I$_3$ have been discovered [77]. 30% of these as well as the mixed-anion salts become superconducting below 3.6 K. There exist two slightly modified unit cells of Θ-(BEDT-TTF)$_2$I$_3$. The main difference is the positions of the I$_2$ anions which can be shifted by half the short lattice vector. In the crystal both unit cells are statistically distributed. After tempering only a single configuration occurs. The rest of the structure hardly changes. This structure is called Θ_T phase and has a slightly higher transition temperature of $T_c \approx 5\,K$.

Having several different phases allows for systematic investigations of the relation between structure and physical properties in these organic materials. A genealogy of the BEDT-TTF-based organic conductors was compiled by Mori [78, 79, 80]. An analysis of experimental results is given in the review [81] by Shibaeva and Yagubskii. We will study the Θ_T-(BEDT-TTF)$_2$I$_3$ structure.

2.5.1. The Crystal

2.5.1.1. The Building Blocks

As the name suggests BEDT-TTF [bis-(ethylenedithio)tetrathiafulvalene] is related to TTF by replacing the four hydrogen atoms with an additional sulphur atom and a methylene group. The chemical structure formula is shown in figure 2.42.

Figure 2.43 shows different conformation isomers, i.e. symmetry constrained minima of the total energy, of ET along with their HOMOs sorted by their total energy. The upper-most structure is obtained when imposing D_{2h} symmetry. It is planar (p) and has
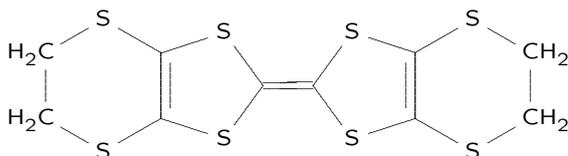
Figure 2.42.: Structure formula of bis-(ethylenedithio)tetrathiafulvalene (BEDT-TTF)

the highest total energy of $-97141.796\,\text{eV}$ (tier 2, PBE). When allowing the methylene-groups along with their accompanying sulphur atoms to move out of the molecular plane, the energy can be reduced significantly. There are two configurations. Nearest-neighbor methylene-groups at the respective long end of the molecule always point in opposite direction along the short axis. Their relative position across the molecule can be either eclipsed (ep) with symmetry D_{2h} or staggered (sp) with symmetry D_2. Both conformers have essentially the same total energy.

These planar structures are still unstable. It is energetically more favourable to allow for a further reduction in symmetry. This leads to a z-shape structure with either staggered or eclipsed methylene groups or a slightly lower w-shaped structure. The energy differences and their symmetry group are compiled in table 2.9. The subgroup relations between the different symmetry groups originating from D_{2h} are shown in figure 2.44.

Figure 2.45 gives the energy levels of the molecular orbitals for the different conformers sorted with decreasing energy from left to right. Going to the right we find an increase in the HOMO-LUMO gap. The occupied energy levels are shifted to lower energies, whereas the unoccupied ones are shifted to higher energies.

Table 2.9.: Energies relative to the lowest structure w eclipsed ($E = -97142.945\,\text{eV}$) of different conformers of ET obtained by DFT calculations with the PBE exchange correlations functional and the tier 2 basis set. Second last column gives the results of DFT calculations using NRLMOL by Brake and coworkers [82]. There is a significant difference in the results. We repeated the calculations with NRLMOL obtaining the last column. It agrees much better with our FHI-aims results.

conformer	symmetry group	$\Delta E_{\text{tot}}/\text{eV}$	$\Delta E_{\text{tot}}/\text{eV}$ [82]	$\Delta E_{\text{tot}}/\text{eV}$
planar	D_{2h}	1.150	1.76	1.215
planar eclipsed	C_{2h}	0.145		0.175
planar staggered	D_2	0.145		0.175
z eclipsed	C_2	0.113	0.07	0.115
z staggered	C_i	0.116	0.07	0.105
w eclipsed	C_s	0.000	0.00	0.000
w staggered	C_2	0.001	0.00	0.000

strictly planar (p), D$_{2h}$
$\Delta E = 1.150\,\text{eV}$

eclipsed planar (ep), C$_{2h}$
$\Delta E = 0.145\,\text{eV}$

staggered planar (sp), D$_2$
$\Delta E = 0.145\,\text{eV}$

eclipsed Z (ez), C$_2$
$\Delta E = 0.113\,\text{eV}$

staggered Z (sz), C$_i$
$\Delta E = 0.116\,\text{eV}$

eclipsed W (ew), C$_s$
$\Delta E = 0.000\,\text{eV}$

staggered W (sw), C$_2$
$\Delta E = 0.001\,\text{eV}$
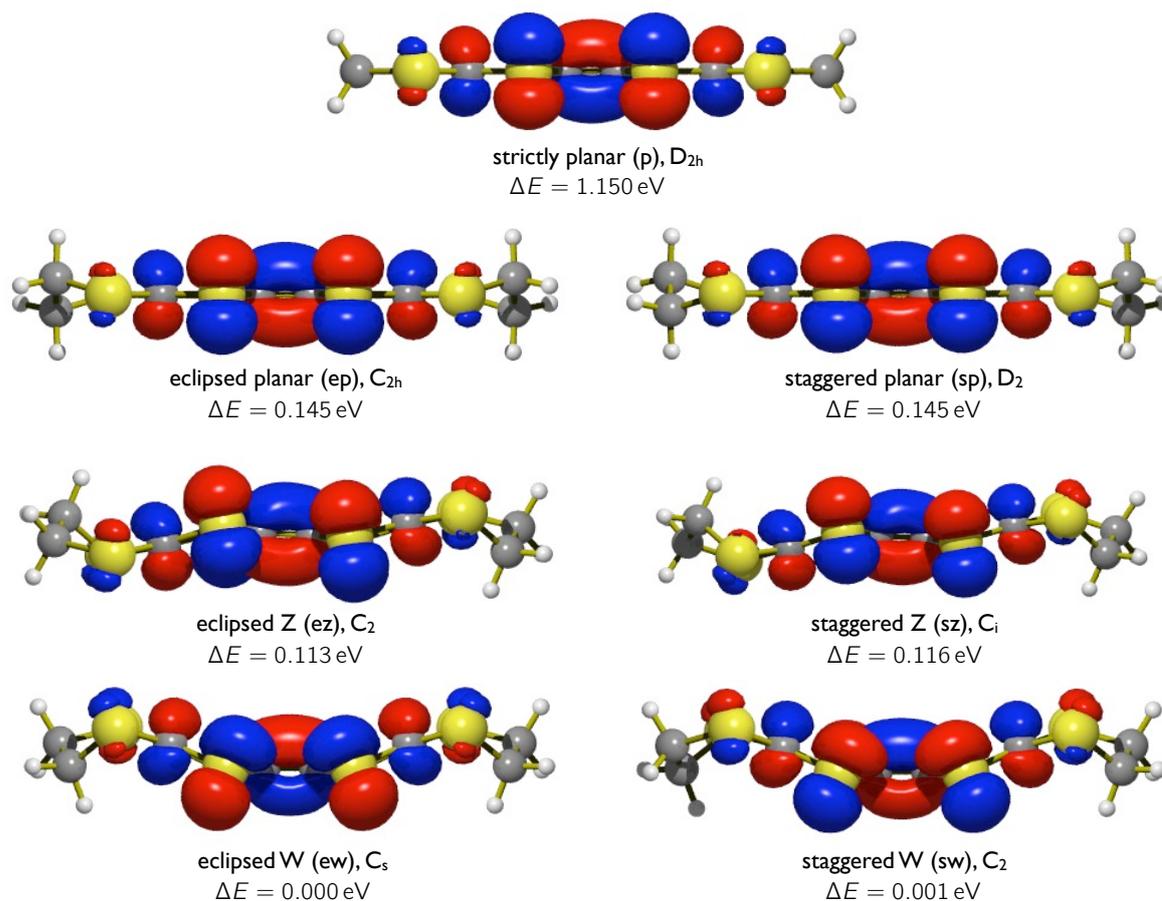
Figure 2.43.: Different conformers of ET with their HOMOs. The most stable structures are the W-shape conformers (last row). The eclipsed and staggered structures essentially have the same energy. Going upwards the energy increases. ΔE is defined as the energy difference with respect to the ground-state conformer. Isovalues for isosurfaces of wavefunctions are $d = \pm 0.08 \text{Å}^{-3/2}$.
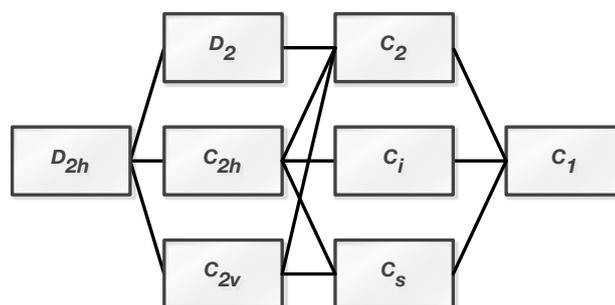
Figure 2.44.: Symmetry subgroups of D_{2h}.
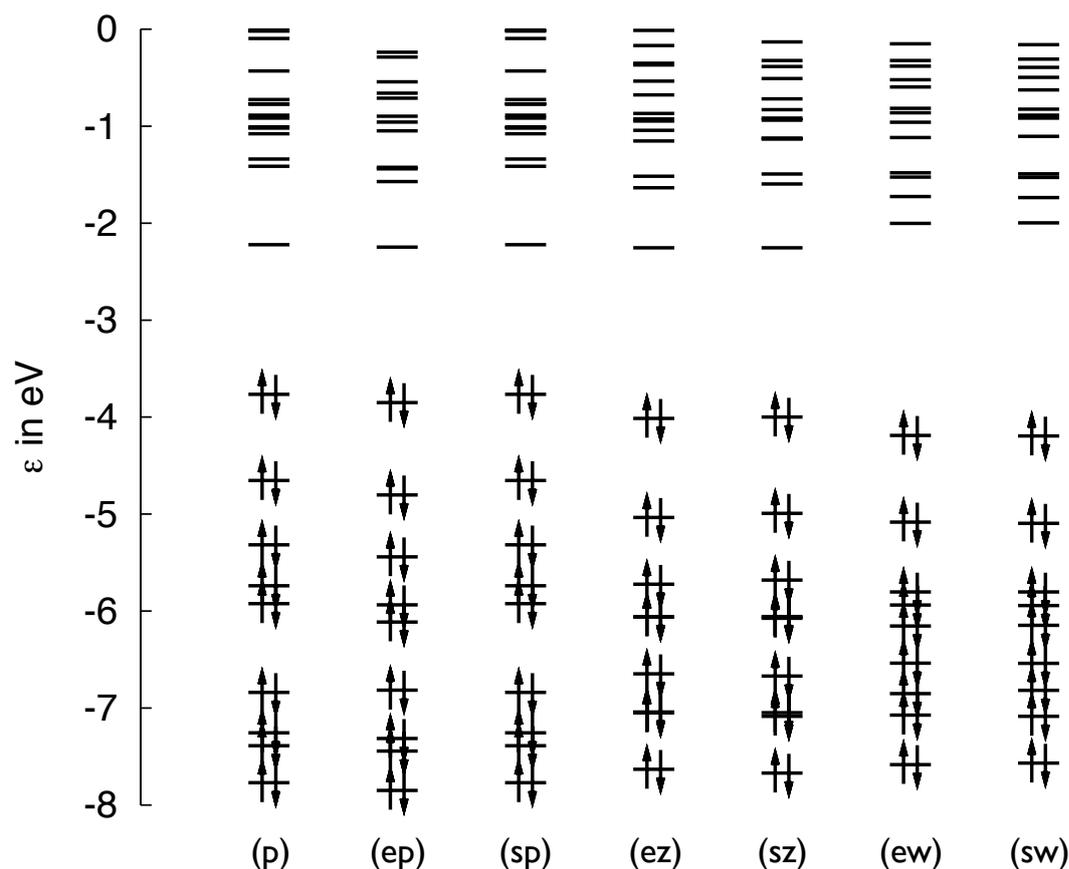
Figure 2.45.: Molecular energy levels for different conformers. From left to right: strictly planar (p), eclipsed planar (ep), staggered planar (sp), eclipsed (z), staggered (z), eclipsed (w), and, staggered (w). We observe that with decreasing total energy, HOMO/LUMO gap increases.

For these calculations we used the PBE exchange correlation functional and the tier 2 basis set in FHI-aims. Demiralp and Goddard [83] performed similar calculations using Hartree-Fock. Brake and coworkers [82] studied the energy differences of different conformers with DFT using the NRLMOL code, presumably with the PBE exchange correlation functional. The second last column in table 2.9 gives their results which differ from ours significantly. To check the reliability of our data we also performed NRLMOL calculations with the largest basis set available and obtained results (last column) very close to ours.

Figure 2.46 gives the ground-state conformer (ew) for different exchange-correlation functionals calculated in Gaussian03 with the 6-31G basis set. Interestingly, we find a visible change in the structure. While the W-shape conformers still remain the ground-state structures the banana-shape becomes flatter the higher the amount of exact exchange in comparison to correlation energy. For Hartree-Fock we thus get the straightest – an

almost planar structure. For PBE and LSDA we find a quite pronounced w-shape.

LSDA
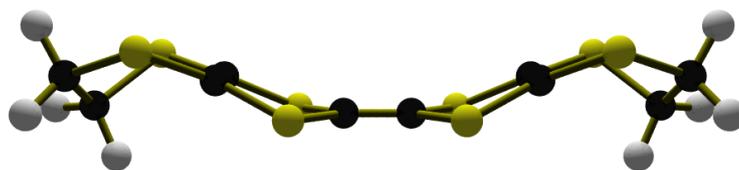
PBE
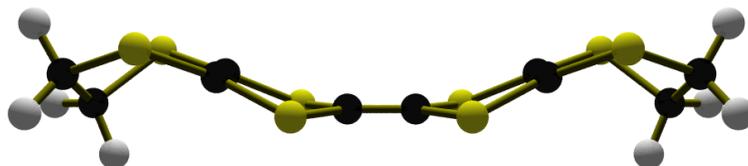
B3LYP
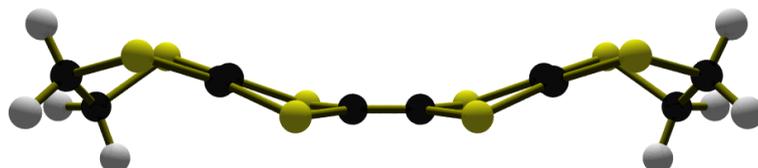
HF
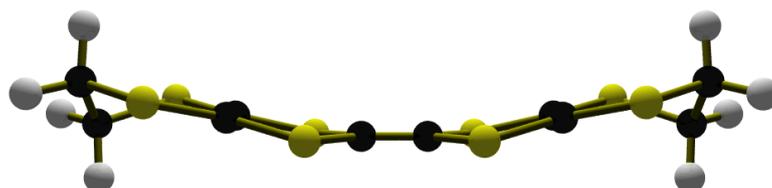
Figure 2.46.: Ground-state structures of ET for different exchange-correlation poten-
tials in Gaussian03 using the 6-31G basis set. Interestingly, increasing
the amount of exact exchange leads to flatter molecules.

2.5.1.2. The Crystal Structure Θ_T-(BEDT-TTF)$_2$I$_3$

Within the Θ_T-(BEDT-TTF)$_2$I$_3$ crystal the planar eclipsed and staggered structures are realized. Due to the similarity of their energies and the shape of their HOMOs we choose one of them, the eclipsed conformer, for our calculations. Figure 2.47 shows the HOMOs of ET and iodine. For the former we see that there is hardly any amplitude on the methylen groups.

When synthesizing a crystal out of ET and iodine molecules, a charge transfer takes place. The HOMO of ET is more than $3\,\mathrm{eV}$ higher than the partially filled iodine HOMO (cf. figure 2.47). On average, half an electron is therefore transferred from BEDT-TTF to iodine giving rise to a quarter-filled band derived from the HOMOs of BEDT-TTF.

The crystal structure of this charge-transfer salt belongs to the monoclinic space group with $P2_1/c$ symmetry. The experimentally determined lattice parameters are $a = 9.964\,\text{Å}$, $b = 10.088\,\text{Å}$, and $c = 34.419\,\text{Å}$ with the angle $\beta = 97.98°$ [84]. Figure 2.48 gives different views on the unit cell of Θ_T-(BEDT-TTF)$_2$I$_3$.
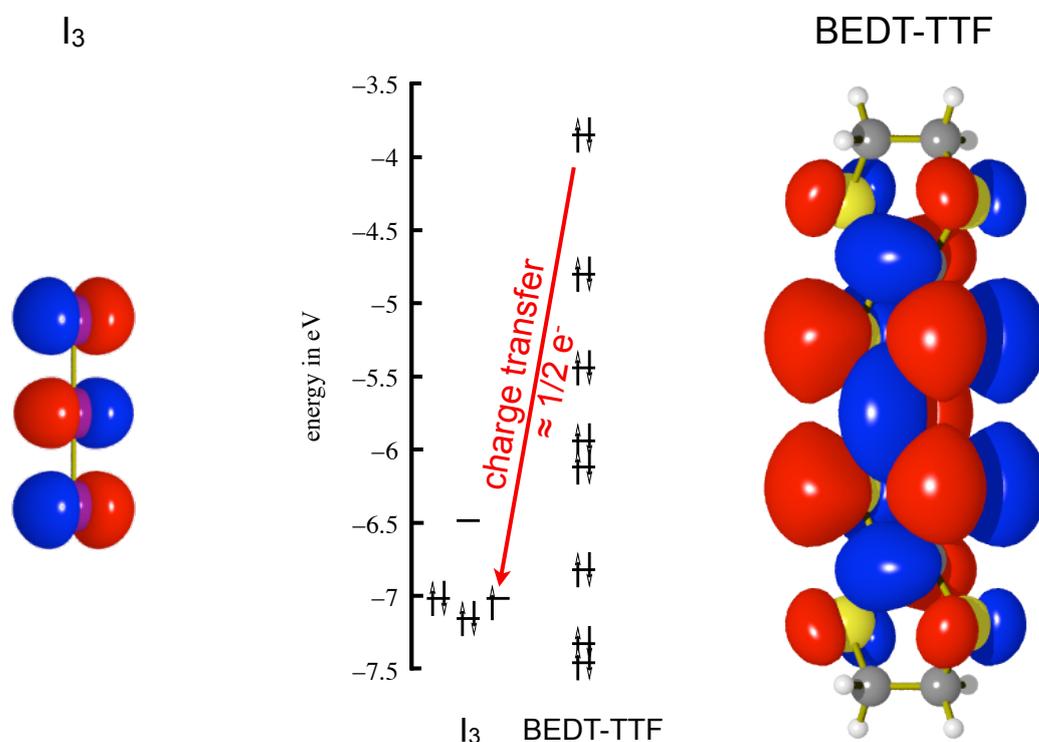
Figure 2.47.: Molecular energy levels of ET and I$_3$ center of figure and the corresponding HOMOs at the left and right side, respectively. The energy of the HOMO of ET is higher in energy than the partially filled HOMO of I$_3$. On average, half an electron is transferred from ET to I$_3$ giving a quarter-filled band derived from the HOMOs of ET. Isovalue $0.06\,\text{Å}^{-3/2}$.
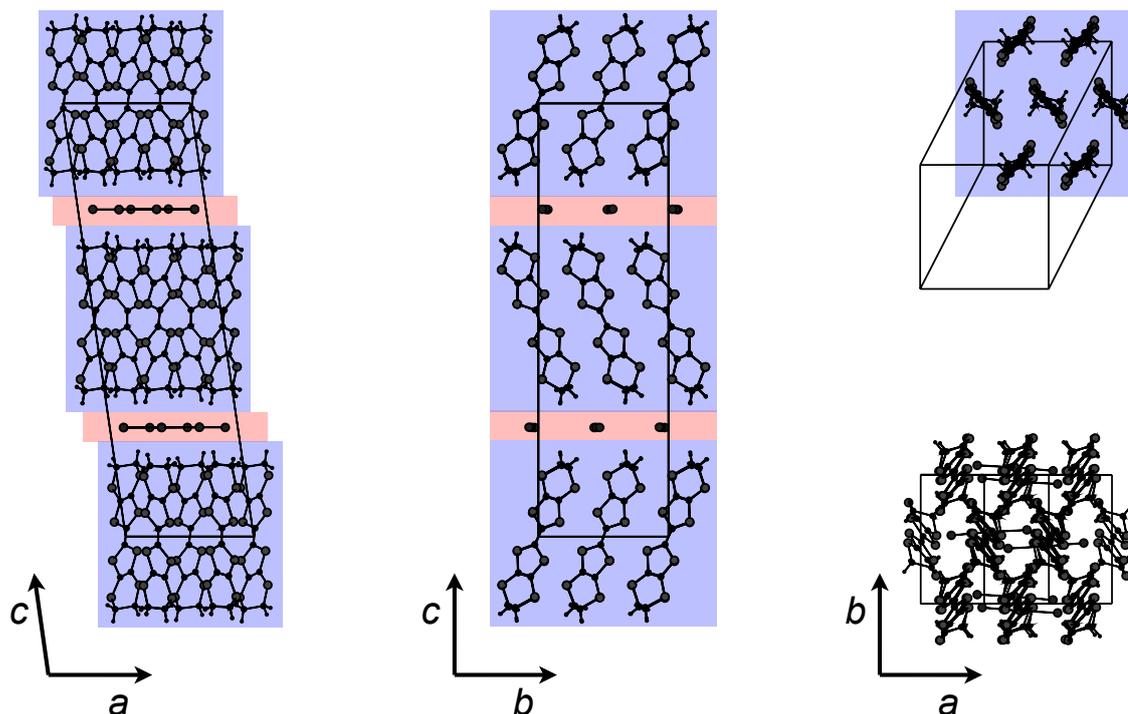
Figure 2.48.: Different views on the unit cell of Θ_T-(BEDT-TTF)$_2$I$_3$: along the c-axis
we find a sandwich structure of donor and acceptor layers. In the a-b
planes we find the acceptor iodine molecules and the highly-conducting
BEDT-TTF planes.

We observe a sandwich like structure (two outer-left views). The donor layers of BEDT-TTF alternate with the acceptor iodine layers along the c-axis. The a-b BEDT-TTF planes show metallic behavior from room- down to low temperatures. The experimentally observed ratio of the resistivity in these planes and perpendicular to them is $\rho_\perp/\rho_\parallel \approx 500$ [84], i.e. we find a quasi two-dimensional metal. The right-most column of figure 2.48 shows two different perspectives on these planes. Within the BEDT-TTF a-b-planes the molecules are tilted such that the sulfur atoms show a staggered arrangement.

The key to understanding the Θ_T-(BEDT-TTF)$_2$I$_3$ molecular crystal are the highly-conducting planes. We model these planes in terms of a two-dimensional Hubbard model. To fix the notation we provide a view on the plane parallel to the long axis of the molecules in figure 2.49. We label the two important direction: the a-direction along the nearest-neighbors and the diagonal d-direction. In the former, the center-of-mass distance between the molecules is $4.96\,\text{Å}$, while in the latter it is $5.61\,\text{Å}$.
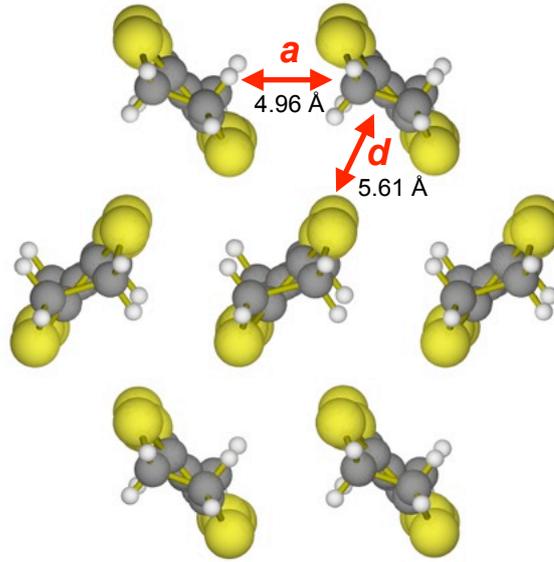
Figure 2.49.: Structure of Θ_T-(BEDT-TTF)$_2$I$_3$: the highly conducting a-b-plane built from BEDT-TTF. We define the a-bond along the a-direction where we find the nearest neighbors. The d-bond runs along the diagonal direction.

2.5.2. Model Parameters

2.5.2.1. Hopping parameter

The a-bond   We start with the a-bond and its hopping parameter t_a evaluated for different angles using FHI-aims with PBE and the tier 2 basis set. Figure 2.50 gives the results for t_a as well as the total energy. We deduce the sign of the hopping-matrix element from figure 2.51. For the angle of 49.36°, being realized in the crystal, we find the hopping-matrix element $t_a = -0.04$ eV.

Interestingly, we observe quite a strong dependence on the angle. In the interval [40.0°, 60.0°], an interval of only 20°, t_a ranges from -0.18 eV to practically zero. This strong sensitivity is due to the pronounced lobes at the sulfur atoms (cf. figure 2.52). Their overlap with the partner sulfur lobes on the opposite molecule changes strongly as illustrated in figure 2.51. Moreover, we deduce from the total energy as well as the dimer wavefunction at 40° that already at this angle the tight-binding approach is no longer applicable.

The distance dependence shows a sign change in the hopping-matrix element at about 4.2 Å. This is again an effect of the complex structure of the HOMOs. The sign-change, however, occurs at a distance, where the molecular orbitals are already distorted.
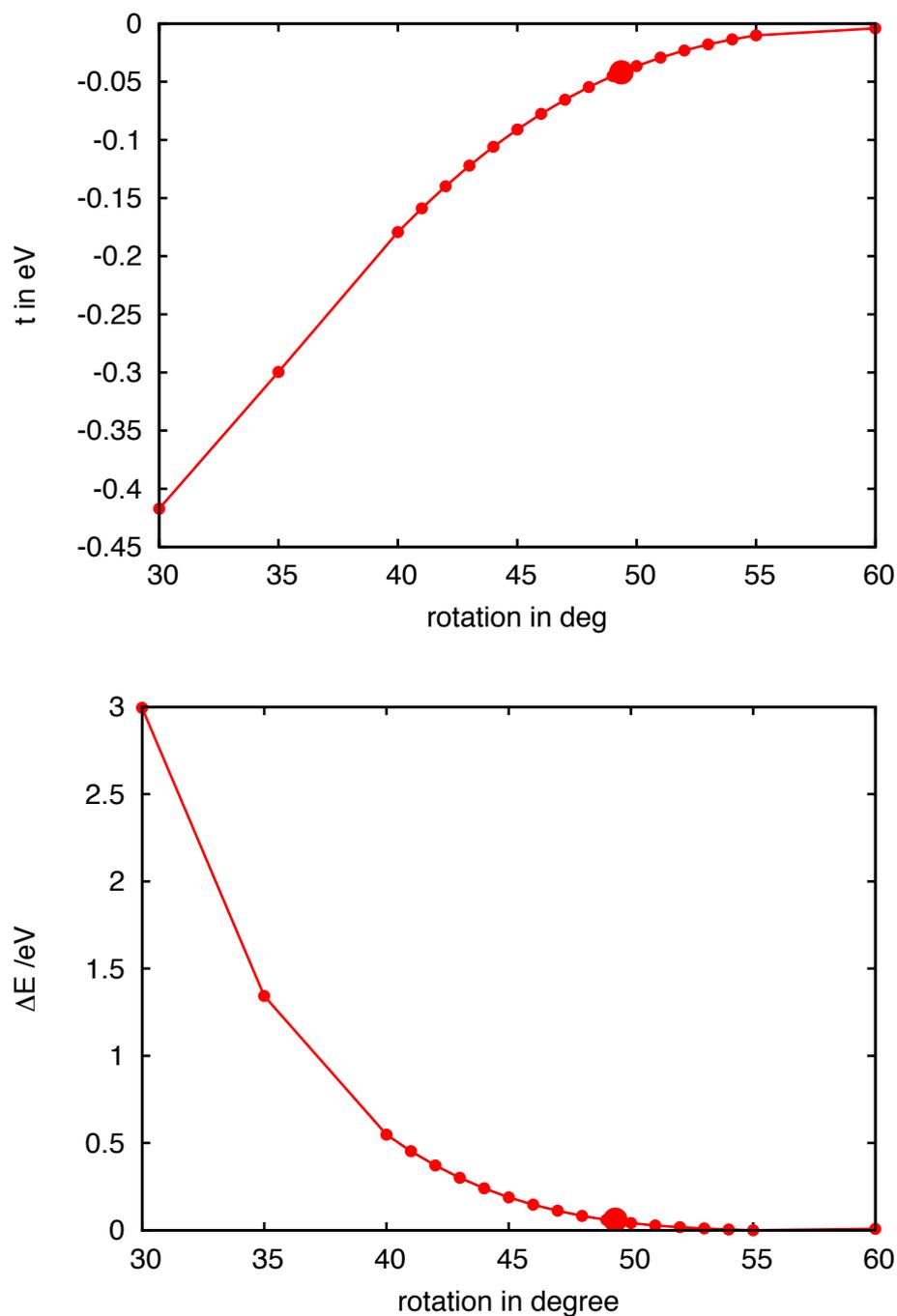
Figure 2.50.: Hopping (upper) and total energy (lower) for different angles along the
a-bond for (BEDT-TTF)$_2$I$_3$. The energy increases steeply for angles
smaller than 45°, the HOMOs start to distort (see figure 2.51), and the
tight-binding ansatz breaks down. The larger red circle shows the angle
realized in the crystal.
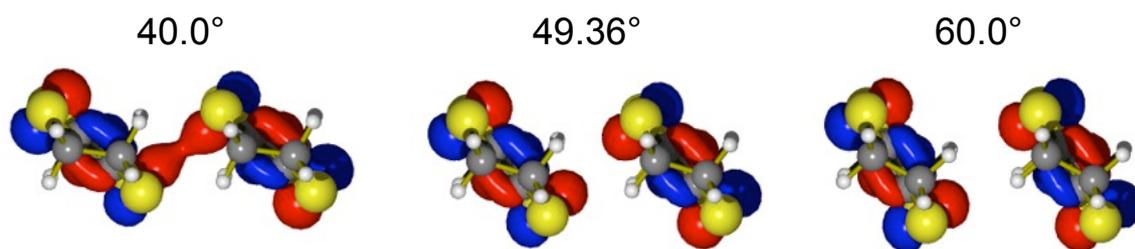
Figure 2.51.: Dimer bonding wavefunction for the a-bond at different angles (isovalue $0.08\,\text{Å}^{-3/2}$). The hopping-matrix element $t_a < 0$ is negative due to the anti-symmetry of the wavefunction. For $40°$ we already observe a distortion of the molecular orbital. The tight-binding ansatz breaks down.
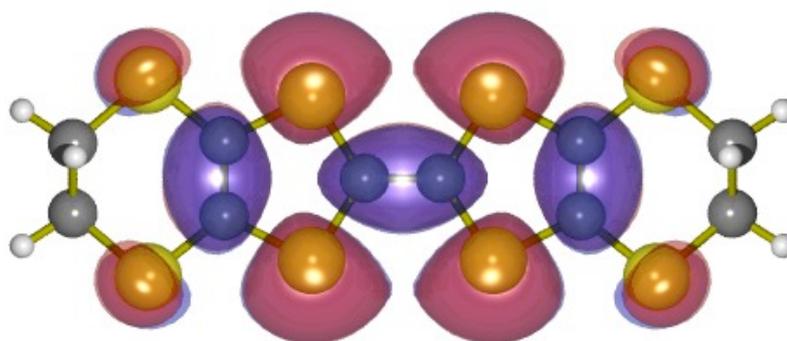
Figure 2.52.: HOMO wavefunction of BEDT-TTF. The pronounced lobes at the sulfur atoms (yellow) are responsible for the strong sensitivity of the hopping-matrix element t_a in a-direction (isovalue $0.04\,\text{Å}^{-3/2}$).
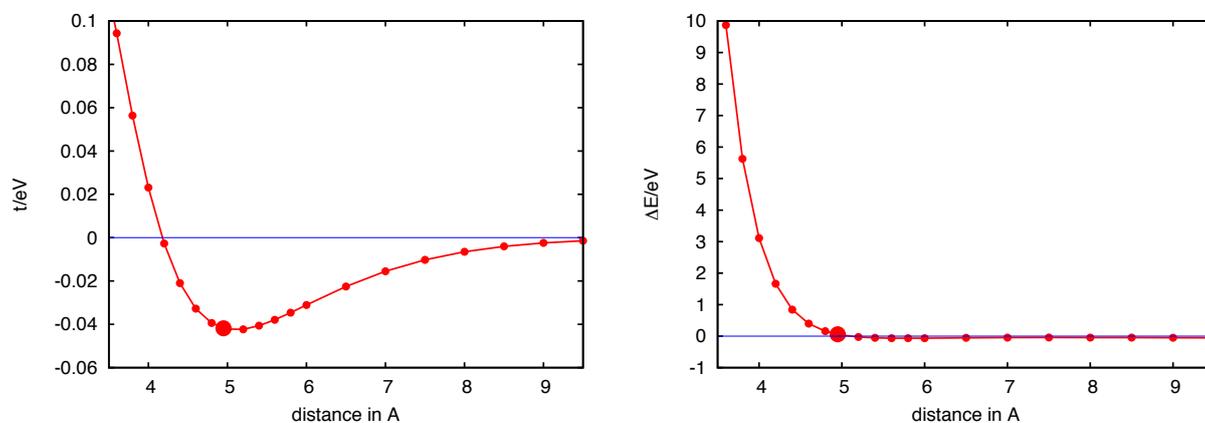
Figure 2.53.: Hopping and total energy for different distances of the a-bond for (BEDT-TTF)$_2$I$_3$. There is an appreciable hopping amplitude only for the first neighbor.

From the distance-dependence we see that similar to the TTF-TCNQ crystal we need not consider second-nearest neighbor hopping as the hopping amplitude is almost zero for this distance.

The d-bond   When performing the dimer calculation for the d-bond a charge transfer takes place. Figure 2.54 shows the two molecular orbitals where the lower one has obviously more amplitude than the upper one. A Mullikan analysis provides a quantitative perspective. Whereas the a-bond dimer has an exactly equal distribution of electrons on both molecules, we find that for the d-bond about 5% of an electron is transferred from one to the other molecule – more precisely about 195.952 electrons are on the upper and consequently 196.048 are on the lower molecule.

To understand how this charge transfer comes about, we construct a simple tight-binding model, where the molecules are represented by two sites with a relatively strong bond t. The inter-molecular bond is described by a smaller hopping parameter $t' \ll t$.
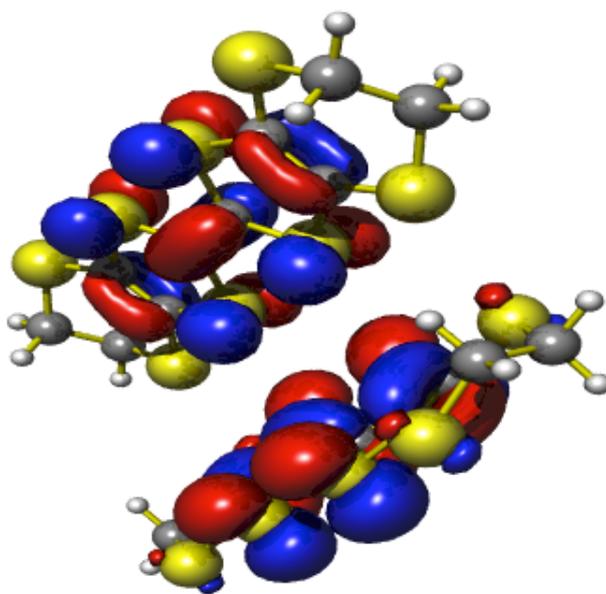
Figure 2.54.: d-bond dimer with bonding wavefunction for $(BEDT\text{-}TTF)_2I_3$ for the distance and configuration realized in the crystal. In contrast, to the crystal a charge transfer of about 5% of an electron takes place. It shows in a reduced amplitude on the upper molecule. The charge transfer can already be understood in second order perturbation theory.
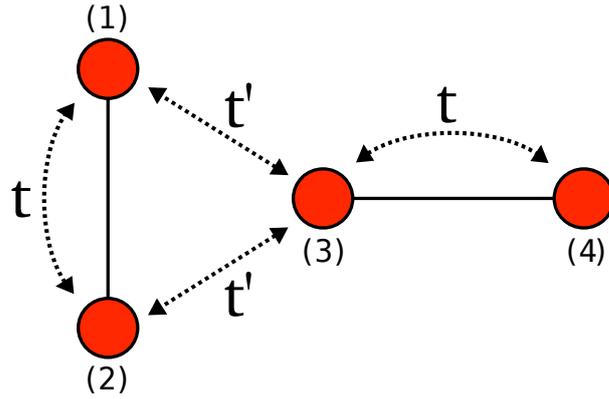
Figure 2.55.: Tight-binding model to study charge transfer found for the non-parallel dimer. By symmetry the first two sites will carry the same charge.

Figure 2.55 shows a sketch of the system and labels the sites.

The associated Hamiltonian for this model reads

$$H = \begin{pmatrix} 0 & t & t' & 0 \\ t & 0 & t' & 0 \\ t' & t' & 0 & t \\ 0 & 0 & t & 0 \end{pmatrix}. \qquad (2.52)$$

By diagonalization we obtain the eigenenergies and wavefunctions as function of the ratio t'/t. The solid lines in figure 2.56 show the lowest two eigenenergies for the half-filled system. To study the charge transfer we plot the occupation per site in figure 2.57. For $t'/t = 0$ we observe a uniform occupation as both molecules are isolated. Symmetry dictates that sites 1 and 2 always carry the same charge. For finite ratios t'/t, there is less charge on site 4. It is redistributed to site 3 on the same molecule and equally to sites 1 and 2 on the other. This redistribution corresponds to the inter-molecular charge transfer. We can already understand it in second-order Brillouin-Wigner perturbation theory as shown in figures 2.56 and 2.57.

Among all the dimer configurations studied in this work this T-shape dimer is the only one which exhibits a charge transfer. The other dimers have an inversion center, i.e. a point group symmetry, which maps both molecules onto each other. Hence, no charge transfer can occur.

From experimental data [84] we know that there are three inequivalent BEDT-TTF molecules per unit cell and inside a highly-conducting plane. A charge transfer between those might therefore occur in the crystal. A close look at 2.49 shows, however, that the highly-conducting a-b plane itself is almost inversion symmetric about the center of a molecule, i.e. it is an almost-symmetry. Therefore there should be hardly any charge transfer, if there was an almost-symmetry operation which maps the two molecules of the
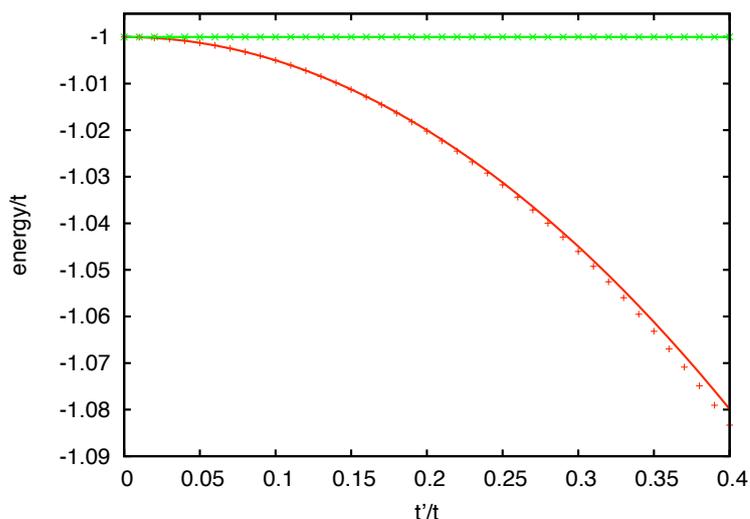
Figure 2.56.: Lowest two eigenenergies of dimer toy model to understand the charge
transfer along the d-bond in $(BEDT\text{-}TTF)_2I_3$. The solid lines denote
the exact result, whereas the symbols denote the results in second order
perturbation theory. Both agree the better the smaller the ratio t'/t.
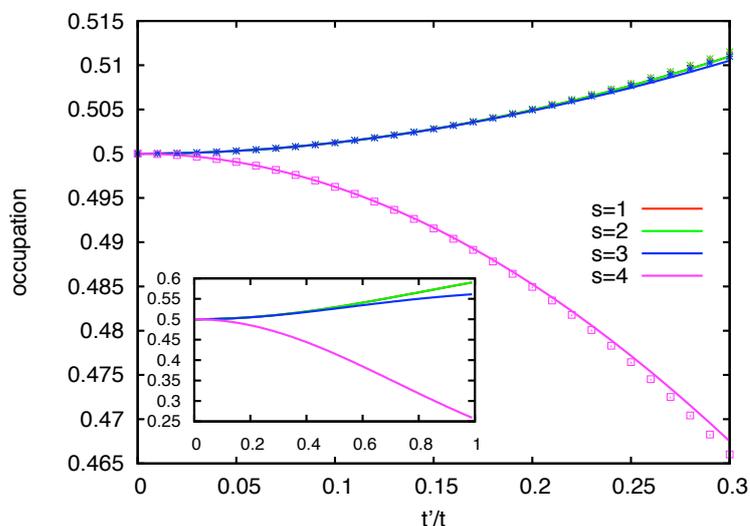
Figure 2.57.: Site occupation of dimer toy model to understand the charge transfer
along the d-bond in $(BEDT\text{-}TTF)_2I_3$. For $t'/t = 0$ we find an even
distribution among all sites. By symmetry sites 1 and 2 always have
the same occupation. Interestingly, for $t'/t > 0$ site 3 has approximately
the same occupation. Charge is transferred from site 4 almost evenly
to 1 to 3. The symbols denote the results in second order perturbation
theory.

d-bond onto each other. Indeed, we find a glide-mirror-rotation symmetry that practically maps both molecules onto each other. Its mirror plane is parallel to the *a*-bond and cutting the *d*-bond in half. The mirror operation is followed by a $1/4\boldsymbol{a}$ shift and a 180° rotation about the *z*-axis (parallel to the long molecular axis).

To see whether this practical symmetry is "strong" enough we perform periodic DFT calculations (tier 1, PBE) for a two-dimensional *a*-*b*-plane. A unit cell of this *a*-*b*-plane comprises four BEDT-TTF molecules. For the self-consistent solution we perform a Mulliken analysis [52]. Indeed, we find that all molecules carry the same Mulliken-integrated charge (accuracy $\approx 0.1\%$ electrons).

Since we cannot construct a finite cluster exhibiting the same symmetry, we need to resort to the two-dimensional calculations to obtain the diagonal hopping-matrix elements.

2.5.2.2. Coulomb parameters

The bare Coulomb integrals for the *a*-bond are given in table 2.10 along with the corresponding intra-molecularly screened values. For U_0, we also provide the intermediate data in table 2.11 for tiers 2 and 2 basis set. We find good agreement for both basis sets just like in the TTF-TCNQ case. Intra-molecular screening mostly affects U and to a smaller extend V. For larger distances the effect is negligible. The largest contribution of the local Hubbard-U amounts to about 1.6 eV.

Table 2.10.: BEDT-TTF results for bare and intra-molecularly screened Coulomb integrals (along the *a*-bond). We again find that only U and V are appreciably screened by the molecules inside the molecule. For U, the contribution is about 1.6 eV. All energies are given in eV.

	U	V	V'	V''
bare	5.3	2.5	1.4	0.9
intra-mol.	3.7	2.0	1.3	0.9

Since small rotations of the molecule strangely affect the hopping-matrix elements along this bond, we also study their effect on V_0. We hardly find any change (see figure 2.58). This means that the ratio t over U and V can change drastically upon pressure. This would therefore be an interesting experiment to perform.

The comparable distance between the molecules in the dimer of the *a*- and the *d*-bond leads to similar results for the bare Coulomb integral. Since the distance for the *d*-bond is a bit larger, the Coulomb integral is reduced by about 0.1 eV to $V_{\text{bare}}^d = 2.4$ eV.

To overcome the charge transfer in the *d*-bond, we rely on constraint-DFT calculations where we fix the number of electrons on each molecule of the *d*-dimer to keep their respective charges equal. We obtain $V_0^d = 2.1$ eV which is a bit larger than V_0^a despite V_{bare}^d being smaller. Hence, the intra-molecular screening is not as efficient as in the *a*-bond. We find two competing effects. The first being the higher polarizability along the

Table 2.11.: U_0 of planar eclipsed BEDT with the tier 1 and tier 2 basis set. All geometries are relaxed with respect to their basis set. Energies are given in eV.

	E_{tot}/eV	
charge $q/|e|$	PBE tier 2	PBE tier 3
0.00	-3569.932	-3569.935
0.25	-3569.893	-3569.895
0.50	-3569.844	-3569.846
0.75	-3569.787	-3569.789
1.00	-3569.721	-3569.723
1.50	-3569.564	-3569.566
2.00	-3569.373	-3569.375
U_0/eV	4.214	4.250

middle axis which tends to make the screening more efficient, i.e. decreases V_0^d. This effect is, however, overcompensated by the reduction in screening due to the larger distance.

Inter-Molecular Screening In contrast, to TTF and TCNQ we find small but finite off-diagonal elements in the polarizability tensor for electric fields in the principal directions of the inertia tensor of BEDT-TTF. For the two compounds of the crystal the calculation outlined in section 2.3.2.3 give the polarizability tensors

$$\alpha_{\text{ET}} = \begin{pmatrix} 170 & 0 & 0 \\ 0 & 286 & 3 \\ 0 & 3 & 512 \end{pmatrix} /a_0^3 \qquad \alpha_{\text{I}_3^-} = \begin{pmatrix} 80 & 0 & 0 \\ 0 & 80 & 0 \\ 0 & 0 & 316 \end{pmatrix} /a_0^3 . \qquad (2.53)$$

Using the DDA we obtain the screening correction for the Hubbard-U and the first neighbors along the a- and d-bond. All relevant Coulomb integrals are given in table 2.12.

Table 2.12.: BEDT-TTF results for the relevant Coulomb integrals. By almost-symmetry all local Coulomb parameters U are essentially identical (see 2.5.2.1). The Vs along different directions give slightly different results.

	U	V_a	V_d
bare	5.3	2.5	2.4
intra-mol.	3.7	2.0	2.1
ΔV - inter-mol.	-2.2	-1.5	-1.4
full screening	1.5	0.5	0.7
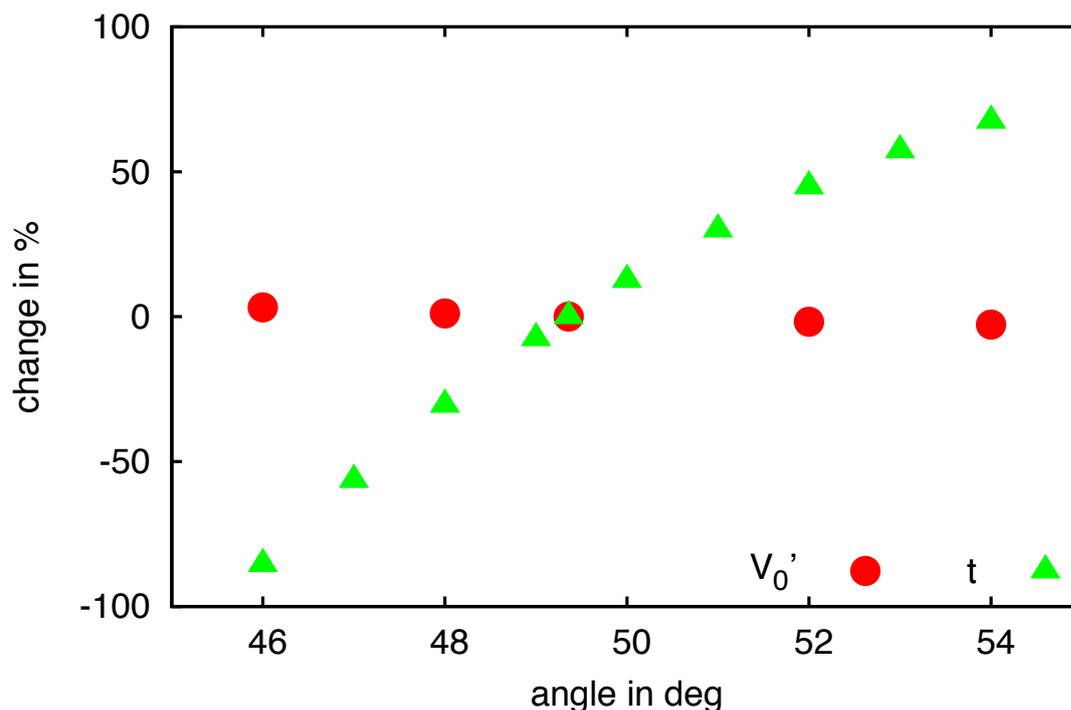
Figure 2.58.: Sensitivity comparison of hopping-matrix element t_a (green triangles) to intra-molecularly screened V_0 (red squares). Whereas the $V_0 = -2.04\,\text{eV}$ remains very stable the t_a vary strongly even for small angles $\pm 4°$.

2.6. Summary

In this chapter we devised a technique to reliably calculate realistic parameters to treat organic crystals in terms of an extended Hubbard model. To that end, we construct a model crystal from unit cells determined by X-ray diffraction experiments. Replacing the molecules in the experimental unit cell by well-defined DFT relaxed structures we obtain an idealized clean crystal. Using FHI-aims, a density-function theory code package based on numerically tabulated atom-centered orbitals, we evaluate the hopping parameters, bare- and intra-molecularly screened Hubbard parameters.

Using a dimer approach the hopping-matrix elements can be directly evaluated from the bonding/anti-bonding splitting of the highest-occupied (donor molecule) or lowest-unoccupied (acceptor molecule) molecular orbital. The bare Coulomb integrals readily follow from density integrations of the molecular orbital. To take the Coulomb parameter renormalization due to the electrons inside the molecules into account we charge a system of a single molecule (for U_0) or a dimer (for V_0), where the energetic response due to the relaxation of the orbitals gives the screening.

In order to also include the screening contribution of all the other molecules in the system we have to take a different approach. Quantum mechanical calculations for large enough systems are not feasible, even with the largest supercomputers at hand. Therefore,

we resort to the classical electrostatic approach developed in chapter 1. We find that it does not suffice to replace each molecule by a *single* polarizability, as the molecules are too close to each other. As a remedy, we describe a molecule as a set of point polarizabilities that are derived from uniform distribution of the DFT polarizability tensor of the molecule.

We apply this procedure to two compounds, TTF-TCNQ and $(BEDT\text{-}TTF)_2I_3$ obtaining a realistic set of model parameters for a Hubbard model description. Typical of organics, we find relatively small hopping matrix elements in comparison to the screened Coulomb integrals. For the local Hubbard-U screening is most pronounced, reducing the value to about 30% of the bare integral. Our results for TTF-TCNQ put early estimates given by Hubbard on a solid footing. For both materials we find that the next-neighbor interaction, which is usually neglected in Hubbard model calculations, has a sizable contribution. In $(BEDT\text{-}TTF)_2I_3$ its values are roughly 40% of the effective Hubbard-U, whereas in TTF-TCNQ it even is about 65%. Evidently, for both, but especially for the latter, their contribution should not be neglected.

As an example we show that the inclusion of V in TTF-TCNQ reveals important physics. It is key to solving a long-standing questions in the understanding of this interesting exotic material. In former treatments of TTF-TCNQ in terms of the t-U Hubbard model the estimated hopping matrix element t had to be doubled in order to match experiments. Including V, we showed that its effect is a simple broadening of the spectrum, mimicking the doubling of $2t$. We could also exclude the presence of Hubbard-Wigner-type states suggested by Hubbard. Moreover, using the correct t puts the temperature scale T_J, below which signatures of spin-charge separation are found, into ranges consistent with experiment.

For both systems, $(BEDT\text{-}TTF)_2I_3$ and TTF-TCNQ, we find that sufficient pressure should lead to interesting phenomena. In the former uniaxial pressure might significantly change the t/V-ratio due to its strong dependence on molecular orientations. In TTF-TCNQ hydrostatic pressure should drive the system even closer or over ferroelectric instability.

Dynamical Lattice Susceptibilities from DMFT

3.1. Dynamical Correlation and Green's functions

There is a broad variety of experimental techniques in condensed matter physics. Almost all of them can be classified into one of the three categories: spectroscopy, responses to external fields and probing of thermodynamical coefficients. We will focus on the former two categories only, since they allow for an analysis of the dynamical features of the system. These dynamics depend on the dominant intrinsic excitations. Even though there is a huge diversity in experimental techniques the general idea of the setup is almost always the same. A specimen is subjected to a (usually electromagnetic) external perturbation, for instance photons impinging on the surface or an influx of neutrons with their magnetic moments or – for transport – a voltage drop. From the theoretical point of view this perturbation manifests itself as an additional time-dependent term $H^{\mathrm{pert}}(t)$ to the Hamiltonian H_0

$$H^{\mathrm{pert}} = \int_{\mathbb{R}^d} \mathrm{d}^d r\, \boldsymbol{F}_X(\boldsymbol{r}, t) X(\boldsymbol{r}) \,, \tag{3.1}$$

where $\boldsymbol{F}_X$ and X are conjugate fields in terms of Legendre transforms. As an example $\boldsymbol{F}_X$ could be the magnetic field $\boldsymbol{H}$ and X the conjugated magnetization $\boldsymbol{M}$. Intuitively $\boldsymbol{F}_X$ denotes the force that couples to the system via the operator X. The effect of the perturbation is that expectation values of some operators, $\langle \mathcal{O} \rangle$, show a finite response $\langle \delta \mathcal{O} \rangle$. It is our goal to understand and predict the behavior of this change $\langle \delta \mathcal{O} \rangle$ under changes of $\boldsymbol{F}_X$, i.e. the functional dependence $\langle \delta \mathcal{O} \rangle [\boldsymbol{F}_X]$.

Usually the generalized 'force' $\boldsymbol{F}_X$ is very weak in comparison to the internal forces in the system. Hence, we can expand the response $\langle \delta \mathcal{O} \rangle [\boldsymbol{F}_X]$ to first order. This gives

$$\langle \delta \mathcal{O}_i^{\mathrm{LR}}(\boldsymbol{r}, t) \rangle = \int_{\mathbb{R}^d} \int_{\mathbb{R}} \mathrm{d}^d r\, \mathrm{d}t'\, \chi_{ij}^{\mathrm{LR}}(\boldsymbol{r}, \boldsymbol{r}'; t, t') F_{Xj}(\boldsymbol{r}', t') \,, \tag{3.2}$$

where χ^{LR} denotes the linear response function (or correlation function), which is the aim of this chapter. The components of $\mathcal{O}$ and $\boldsymbol{F}_X$ are given by either the experimental or theoretical setup (external parameter). To shorten the notation we will drop the superscript LR (linear response) and additionally assume that the expectation values $\langle \mathcal{O} \rangle$ and $\langle X \rangle$ vanish in the absence of the perturbation, i.e. they become $\langle \delta \mathcal{O} \rangle$, $\langle \delta X \rangle$, respectively.

In the following we will describe the response functions microscopically making them accessible to actual calculations. To that end, we start by briefly introducing some important concepts.

3.1.1. Concepts For A Microscopic Description

The physical models, we describe, are governed by a time-independent, particle-conserving Hamiltonian H with $[H, N] = 0$ in the Grand Canonical Ensemble. As an abbreviation we define

$$\mathcal{H} = H - \mu N \,, \tag{3.3}$$

with μ being the chemical potential and N the total particle number operator.

The (thermal) expectation value $\langle \mathcal{O} \rangle$ of any operator $\mathcal{O}$ can be evaluated by tracing over the entire Fock space

$$\langle \mathcal{O} \rangle = \frac{1}{\mathcal{Z}} \mathrm{Tr} \left(e^{-\beta \mathcal{H}} \mathcal{O} \right) \ , \tag{3.4}$$

where $\mathcal{Z} = \mathrm{Tr} \left(\exp \left(-\beta \mathcal{H} \right) \right)$ defines the partition function. In this notation a general operator $\mathcal{O}$ in the Schrödinger picture is transformed to the Heisenberg picture by

$$\mathcal{O}\left(t \right) = \exp(\mathrm{i}\mathcal{H}t)\mathcal{O} \, \exp(-\mathrm{i}\mathcal{H}t) \tag{3.5a}$$

$$\mathcal{O}^{\dagger}(t) = \exp(\mathrm{i}\mathcal{H}t)\mathcal{O}^{\dagger} \exp(-\mathrm{i}\mathcal{H}t) \ . \tag{3.5b}$$

Most often $\mathcal{O}$ is either an annihilator c or creator $c^{\dagger}$, or a single particle Hermitian operator, an observable, of the form

$$\mathcal{O} = \sum_{ij} c_i^{\dagger} O_{ij} c_j \ . \tag{3.6}$$

Then both equations (3.5) are identical.

For calculations at finite temperature it is beneficial to treat time and temperature on equal footing. To that end, we introduce the fictitious *imaginary time* τ [86]. We consider t as a complex variable and restrict it along the imaginary axis $-\mathrm{i}t \to \tau$. This rotation in the complex plane is called Wick rotation. For imaginary times analytical continuation of the transforms from Schrödinger to Heisenberg picture (3.5) gives

$$\mathcal{O}(\tau) \ = \ \exp(\mathcal{H}\tau)\,\mathcal{O}\,\exp(-\mathcal{H}\tau) \ , \tag{3.7a}$$

$$\bar{\mathcal{O}}(\tau) \ = \ \exp(\mathcal{H}\tau)\,\mathcal{O}^{\dagger} \exp(-\mathcal{H}\tau) \ . \tag{3.7b}$$

It is important to note that unlike in the real-time case, $\mathcal{O}(\tau)$ and $\bar{\mathcal{O}}(\tau)$ are not Hermitian conjugates. As we will discuss in section 3.1.6, τ can be restricted to the interval $\tau \in [0, \beta]$. We can think of the partition function as the time evolution operator in imaginary time evaluated at the end of the interval $\tau = \beta$ or $t = -\mathrm{i}\beta$ showing the formal equivalence of time and temperature.

Within the field integral formalism, which also holds for time-dependent Hamiltonians, we rewrite the expectation value (3.4) of a single-particle operator like (3.6) in the Heisenberg picture as

$$\langle \mathcal{O}\left(\tau \right) \rangle = \left\langle \sum_{ij} \phi_i^*\left(\tau \right) O_{ij} \phi_j\left(\tau \right) \right\rangle \tag{3.8}$$

$$= \frac{1}{\mathcal{Z}_S} \int \mathcal{D}\left[\phi \right] \mathcal{D}\left[\phi^* \right] \left(\sum_{ij} \phi_i^* O_{ij} \phi_j \right) \exp\left(-S\left[\phi, \phi^* \right] \right) \ , \tag{3.9}$$

with the partition function

$$\mathcal{Z}_S = \int \mathcal{D}\left[\phi \right] \mathcal{D}\left[\phi^* \right] \exp\left(-S\left[\phi, \phi^* \right] \right) \ , \tag{3.10}$$

and the action

$$S\left[\phi, \phi^* \right] = \int_0^{\beta} \mathrm{d}\tau \ \left[\phi^* \partial_{\tau} \phi + \mathcal{H} \right] \ . \tag{3.11}$$

3.1.2. Microscopic Response Theory

To relate (3.2) to the microscopic theory (for an extensive discussion see [87] or [88]) we define the action S_0 of the unperturbed Hamiltonian H_0. The action

$$\delta S\left[\phi, \phi^*, \boldsymbol{F}_X\right] = \int_0^\beta \mathrm{d}\tau\, H^{\mathrm{pert}} = \int_0^\beta \mathrm{d}\tau \int_{\mathbb{R}^d} \mathrm{d}^d r\, \boldsymbol{F}_X(\boldsymbol{r}, t) X(\boldsymbol{r}) \tag{3.12}$$

shall denote the perturbation effect on S_0. In addition, we formally couple the response operator $\mathcal{O}$ to the action via its conjugate pair $\boldsymbol{F}_{\mathcal{O}}$ giving

$$\delta S'\left[\phi, \phi^*, \boldsymbol{F}_{\mathcal{O}}\right] = \int_0^\beta \mathrm{d}\tau\, \boldsymbol{F}_{\mathcal{O}}\left(\tau\right) \mathcal{O}\left(\tau\right) \tag{3.13}$$

such that

$$S\left[\phi, \phi^*, \boldsymbol{F}_X, \boldsymbol{F}_{\mathcal{O}}\right] = S_0\left[\phi, \phi^*\right] + \delta S\left[\phi, \phi^*, \boldsymbol{F}_X\right] + \delta S'\left[\phi, \phi^*, \boldsymbol{F}_{\mathcal{O}}\right]. \tag{3.14}$$

Then, $\langle \mathcal{O}\left(\tau\right)\rangle$ (3.8) is accessible by the functional derivative

$$\langle \mathcal{O}\left(\tau\right)\rangle = \left.\frac{\delta}{\delta \boldsymbol{F}_{\mathcal{O}}\left(\tau\right)}\right|_{\boldsymbol{F}_{\mathcal{O}}=0} \ln \mathcal{Z}_S = \left.\frac{1}{\mathcal{Z}_S}\frac{\delta}{\delta \boldsymbol{F}_{\mathcal{O}}}\right|_{\boldsymbol{F}_{\mathcal{O}}=0} \mathcal{Z}_S. \tag{3.15}$$

In the absence of the perturbation $\langle \mathcal{O}\left(\tau\right)\rangle$ vanishes according to the assumption above (otherwise we could replace $\mathcal{O}$ by $(\mathcal{O} - \langle\mathcal{O}\rangle)$). When the driving force $\boldsymbol{F}_X$ of the perturbation is weak enough we replace the right-hand-side of (3.15) with its first-order expansion in $\boldsymbol{F}_X$ giving

$$\langle \mathcal{O}\left(\tau\right)\rangle \approx \int_0^\beta \mathrm{d}\tau' \left(\left.\frac{\delta^2}{\delta \boldsymbol{F}_{\mathcal{O}}\left(\tau\right)\,\delta \boldsymbol{F}_X\left(\tau'\right)}\right|_{\boldsymbol{F}_X=\boldsymbol{F}_{\mathcal{O}}=0} \ln \mathcal{Z}_S\right) \boldsymbol{F}_X\left(\tau\right). \tag{3.16}$$

Comparing to (3.2) yields

$$\chi\left(\tau, \tau'\right) = \left.\frac{\delta^2}{\delta \boldsymbol{F}_{\mathcal{O}}\left(\tau\right)\,\delta \boldsymbol{F}_X\left(\tau'\right)}\right|_{\boldsymbol{F}_X=\boldsymbol{F}_{\mathcal{O}}=0} \ln \mathcal{Z}_S. \tag{3.17}$$

With the product rule we can readily perform the functional derivatives

$$\chi\left(\tau, \tau'\right) = -\left(\left.\frac{1}{\mathcal{Z}_S}\frac{\delta}{\delta \boldsymbol{F}_{\mathcal{O}}}\right|_{\boldsymbol{F}_{\mathcal{O}}=0} \mathcal{Z}_S\bigg|_{\boldsymbol{F}_X=0}\right)\left(\left.\frac{1}{\mathcal{Z}_S}\frac{\delta}{\delta \boldsymbol{F}_X}\right|_{\boldsymbol{F}_X=0} \mathcal{Z}_S\bigg|_{\boldsymbol{F}_{\mathcal{O}}=0}\right) \tag{3.18}$$

$$+ \left.\frac{1}{\mathcal{Z}_S}\frac{\delta^2}{\delta \boldsymbol{F}_{\mathcal{O}}\left(\tau\right)\,\delta \boldsymbol{F}_X\left(\tau'\right)}\right|_{\boldsymbol{F}_X=\boldsymbol{F}_{\mathcal{O}}=0} \mathcal{Z}_S. \tag{3.19}$$

According to equation (3.15) the two functional derivatives in the parentheses give the expectation values of the unperturbed system $\langle X \rangle_{S_0}$ and $\langle \mathcal{O} \rangle_{S_0}$ which we assumed to be zero. Hence,

$$\chi\left(\tau, \tau'\right) = \frac{1}{\mathcal{Z}_S} \left. \frac{\delta^2}{\delta \boldsymbol{F}_{\mathcal{O}}\left(\tau\right) \, \delta \boldsymbol{F}_X\left(\tau'\right)} \right|_{\boldsymbol{F}_X = \boldsymbol{F}_{\mathcal{O}} = 0} \mathcal{Z}_S \, . \tag{3.20}$$

It now has the form of an expectation value (3.15) of a product of operators

$$\chi_{\mathcal{O}, X}(\tau, \tau') = \langle \mathcal{O}(\tau') X(\tau) \rangle \, . \tag{3.21}$$

For $\mathcal{O} = X$, we obtain a relation between two apparently different physical phenomena. In this case the response function is equal to the expectation value of $\mathcal{O}^2$. For the general case of $\langle \mathcal{O}(t) \rangle \neq 0$ we obtain

$$\chi_{\mathcal{O}, \mathcal{O}}(t, t') = \langle \left(\mathcal{O}(t') - \langle \mathcal{O}(t') \rangle\right) \left(\mathcal{O}(t) - \langle \mathcal{O}(t) \rangle\right) \rangle \, . \tag{3.22}$$

This relation is the *fluctuation-dissipation theorem*. On the left hand side we see the response function, which describes the dissipation in a system. If, for instance, $X = \boldsymbol{j}$, χ gives the conductivity, that describes how the kinetic energy of charge carriers is distributed among the excitations of the sample. The right hand side represents quantum-thermal fluctuations.

Operators   The operator $\mathcal{O}$ is some single particle operator of the form (3.6) where in general c, $c^\dagger$, can be either bosonic or fermionic. We will use Greek, Latin indices as subscripts on operators that act on eigenstates or real space sites, respectively. An exception to this rule are the indices q, k and Q, K which shall denote operators acting in reciprocal space. To better distinguish the corresponding particle operators we denote them by the letter a instead of c, i.e.

$$a_{\boldsymbol{k}\sigma} = \frac{1}{\sqrt{N}} \sum_i e^{\mathrm{i}\boldsymbol{k}\boldsymbol{r}_i} c_{i\sigma} \tag{3.23}$$

$$a_{\boldsymbol{k}\sigma}^\dagger = \frac{1}{\sqrt{N}} \sum_i e^{-\mathrm{i}\boldsymbol{k}\boldsymbol{r}_i} c_{i\sigma}^\dagger \, . \tag{3.24}$$

Common single-particle operators are the charge operator

$$C(\boldsymbol{R}_i) = \sum_\sigma c_{i\sigma}^\dagger c_{i\sigma} \tag{3.25}$$

for the charge susceptibility $\chi_{C,C}$ and the spin operators

$$S^a(\boldsymbol{R}_i) = \frac{1}{2} \sum_{\sigma\sigma'} c_{i\sigma}^\dagger \sigma_{\sigma\sigma'}^a c_{i\sigma'} \tag{3.26}$$

for the spin susceptibilities $\chi_{S^a, S^b} = \chi^{ab}$, where $a, b = \{x, y, z\}$ and $\boldsymbol{\sigma}^a$ is the corresponding Pauli matrix.

In a translation-invariant system these expressions can be Fourier transformed to yield

$$\mathcal{O}(\boldsymbol{Q}) = \sum_\sigma \int_{\mathrm{BZ}} \frac{\mathrm{d}^d k}{V_{\mathrm{BZ}}} \, v_{\boldsymbol{k}\sigma} a^\dagger_{\boldsymbol{k}\sigma} a_{\boldsymbol{k}+\boldsymbol{Q}\sigma} \,, \tag{3.27}$$

where $v_{\boldsymbol{k}\sigma} = 1$ for the charge-charge and $v_{\boldsymbol{k}\sigma} = \mathrm{sgn}(\sigma)$ for the spin-spin response function.

Inserting $\mathcal{O}$ into equation (3.21) we obtain a four-point correlation function which can readily be expanded in two-body Green's functions

$$\chi_{\mathcal{O}',\mathcal{O}}(t', t) = \left\langle \left(\sum_{ij} c_i^\dagger(t') O'_{ij} c_j(t') \right) \left(\sum_{lm} c_l^\dagger(t) O_{lm} c_m(t) \right) \right\rangle \tag{3.28}$$

$$= \sum_{ijlm} O'_{ij} O_{lm} \left\langle c_i^\dagger(t') c_j(t') c_l^\dagger(t) c_m(t) \right\rangle \,. \tag{3.29}$$

For the translation invariant system in $\boldsymbol{k}$-space we obtain with (3.27)

$$\chi_{\mathcal{O}',\mathcal{O}}(\boldsymbol{Q}, t', t) = \sum_{\sigma\sigma'} \int_{\mathrm{BZ}} \frac{\mathrm{d}^d k}{V_{\mathrm{BZ}}} \int_{\mathrm{BZ}} \frac{\mathrm{d}^d k'}{V_{\mathrm{BZ}}} \, v_{\boldsymbol{k}'\sigma'}^{\mathcal{O}'} v_{\boldsymbol{k}\sigma}^{\mathcal{O}} \left\langle a^\dagger_{\boldsymbol{k}'\sigma'}(t') a_{\boldsymbol{k}'+\boldsymbol{Q}\sigma'}(t') a^\dagger_{\boldsymbol{k}\sigma}(t) a_{\boldsymbol{k}+\boldsymbol{Q}\sigma}(t) \right\rangle \,. \tag{3.30}$$

If $v_{\boldsymbol{k}\sigma}$ is independent of $\boldsymbol{k}$ as it is for the aforementioned examples, this simplifies to

$$\chi_{\mathcal{O}',\mathcal{O}}(\boldsymbol{Q}, t', t) = \sum_{\sigma\sigma'} v_{\sigma'}^{\mathcal{O}'} v_\sigma^{\mathcal{O}} \int_{\mathrm{BZ}} \frac{\mathrm{d}^d k}{V_{\mathrm{BZ}}} \int_{\mathrm{BZ}} \frac{\mathrm{d}^d k'}{V_{\mathrm{BZ}}} \left\langle a^\dagger_{\boldsymbol{k}'\sigma'}(t') a_{\boldsymbol{k}'+\boldsymbol{Q}\sigma'}(t') a^\dagger_{\boldsymbol{k}\sigma}(t) a_{\boldsymbol{k}+\boldsymbol{Q}\sigma}(t) \right\rangle \,. \tag{3.31}$$

3.1.3. n-body Green's Function

In the following we generalize the correlation functions and introduce the concept of Green's functions. We define the n-body real-time Green's function as the expectation value

$$G^{(n)}(\alpha_1 t_1, \dots, \alpha_n t_n | \alpha'_1 t'_1, \dots, \alpha'_n t'_n) =$$
$$(-\mathrm{i})^n \left\langle \mathcal{T}_t \left[c_{\alpha_1}(t_1) \dots c_{\alpha_n}(t_n) c^\dagger_{\alpha'_n}(t'_n) \dots c^\dagger_{\alpha'_1}(t'_1) \right] \right\rangle \,, \tag{3.32}$$

where $\mathcal{T}_t$ denotes the time-ordering operator, that arranges the particle operators according to time. The operator with the largest t is positioned at the very left. For Fermions each permutation yields a minus sign. Real-time Green's functions have an obvious interpretation. They describe the propagation of a perturbation caused by injecting particles at space-time-spin points (α_i, t_i) and removing them at (α'_i, t'_i).

The zero-temperature Green's function follows from the real-time Green's function by replacing the thermal trace over all states in Fock space with just the ground-state expectation value $|\Psi_0\rangle$, i.e. $\langle x \rangle \to \langle \Psi_0 | x | \Psi_0 \rangle$ giving

$$G^{(n)}(\alpha_1 t_1, \dots, \alpha_n t_n | \alpha'_1 t'_1, \dots, \alpha'_n t'_n) =$$
$$(-i)^n \left\langle \Psi_0 \middle| \mathcal{T}_t \left[c_{\alpha_1}(t_1) \dots c_{\alpha_n}(t_n) c^\dagger_{\alpha'_n}(t'_n) \dots c^\dagger_{\alpha'_1}(t'_1) \right] \middle| \Psi_0 \right\rangle \tag{3.33}$$

for the real-time Green's function.

The imaginary time Green's function is defined in a similarly manner. It follows from a Wick rotation as described in section 3.1.1. We also need to define the imaginary time-ordering operator $\mathcal{T}_\tau$ which just like $\mathcal{T}_t$ arranges the imaginary times in ascending order from right to left. Hence,

$$
\begin{aligned}
G^{(n)}(\alpha_1\tau_1, \ldots, \alpha_n\tau_n | \alpha_1'\tau_1', \ldots, \alpha_n'\tau_n') = \\
-\left\langle \mathcal{T}_\tau \left[c_{\alpha_1}(\tau_1) \ldots c_{\alpha_n}(\tau_n) \bar{c}_{\alpha_n'}(\tau_n') \ldots \bar{c}_{\alpha_1'}(\tau_1') \right] \right\rangle .
\end{aligned}
\tag{3.34}
$$

Note, that the prefactors also differ in both definitions. They are a matter of convention and different authors make different choices. In our case the factors stem from the construction of Green's functions in terms of generating functions. Our convention agrees, for instance, with the textbooks of Abrikosov, Gorkov, Dzyaloshinski [89] and Fetter and Walecka [90] as well as many others. It, however, differs from Negele and Orland [87] where there is no minus sign in the definition of the imaginary-time Green's function.

3.1.4. Single-Particle Green's Function

The Green's function most often encountered is the single-particle Green's function. Specializing equations (3.34) and (3.32) to the single-particle case gives

$$
G_{\alpha\beta}(t, t') = -\mathrm{i} \left\langle \mathcal{T}_t \, c_\alpha(t) c_\beta^\dagger(t') \right\rangle
\tag{3.35}
$$

and

$$
G_{\alpha\beta}(\tau, \tau') = -\left\langle \mathcal{T}_\tau \, c_\alpha(\tau) \bar{c}_\beta(\tau') \right\rangle ,
\tag{3.36}
$$

respectively. For $t > t'$ it describes the propagation of an additional particle and for $t < t'$ of an additional hole in the system.

Having these Green's function gives us direct access to the single-particle expectation values (simple case of equation (3.29)) when choosing the time arguments appropriately,

$$
\langle \mathcal{O} \rangle = -i \int_{\mathbb{R}^d} \mathrm{d}^d r \, \mathrm{d}^d r' \mathcal{O}(\boldsymbol{r}, \boldsymbol{r}') G(\boldsymbol{r}, t; \boldsymbol{r}, t + 0^+)
\tag{3.37}
$$

$$
\langle \mathcal{O} \rangle = -\int_{\mathbb{R}^d} \mathrm{d}^d r \, \mathrm{d}^d r' \mathcal{O}(\boldsymbol{r}, \boldsymbol{r}') G(\boldsymbol{r}, \tau; \boldsymbol{r}', \tau + 0^+) ,
\tag{3.38}
$$

where $t^\pm = t \pm \eta$ with $\eta > 0$ and $\eta \to 0$. For imaginary times we have the analogous definition.

3.1.5. Two-Particle Green's Function

For the response functions the two-particle Green's functions play a crucial role. They are given by

$$
G_{\boldsymbol{\alpha}}^{(2)}(\tau_1, \tau_2, \tau_3, \tau_4) = \left\langle \mathcal{T}_\tau \, c_{\alpha_1}(\tau_1) \bar{c}_{\alpha_2}(\tau_2) c_{\alpha_3}(\tau_3) \bar{c}_{\alpha_4}(\tau_4) \right\rangle
\tag{3.39}
$$

or in real time

$$G_{\boldsymbol{\alpha}}^{(2)}\left(t_1, t_2, t_3, t_4\right) = \left\langle \mathcal{T}_t\, c_{\alpha_1}(t_1) c_{\alpha_2}^\dagger(t_2) c_{\alpha_3}(t_3) c_{\alpha_4}^\dagger(t_4) \right\rangle, \tag{3.40}$$

where we slightly deviate from the notation in (3.32) and (3.34) by renaming times $2 \leftrightarrow 3$ to be consistent with the implementation part below. For the standard notation for real-frequency two-particle Green's functions see [91].

Here we exclusively treat Fermions. The Greek letters denote multi-indices comprising at least a spin index σ_i and an orbital index. In a system where the total spin is a conserved quantity

$$\sigma_1 + \sigma_3 = \sigma_2 + \sigma_4 \tag{3.41}$$

is obviously fulfilled, otherwise the Green's function would be zero. In addition, if the system is paramagnetic, i.e. the system is invariant under a flip of all spins, we only need to treat two different spin-components of the two-particle Green's function. Namely, $\sigma_1 = \pm \sigma_3$ (also see section 3.3). Taking the spin quantum numbers out of the multi-index we thus can write

$$G_{\boldsymbol{\alpha}\sigma\sigma'}^{(2)}\left(\tau_1, \tau_2, \tau_3, \tau_4\right) = \left\langle \mathcal{T}_\tau\, c_{\alpha_1\sigma}(\tau_1) \bar{c}_{\alpha_2\sigma}(\tau_2) c_{\alpha_3\sigma'}(\tau_3) \bar{c}_{\alpha_4\sigma'}(\tau_4) \right\rangle \tag{3.42}$$

and similarly for the real-time case.

In the following we will treat real times to make the discussion more concrete, but the relations can be easily generalized to imaginary times. There are only three independent time orderings with distinct physical interpretations. For instance, if the two creators act first, i.e. t_2, $t_4 < t_1$, t_3, we describe the propagation of two additional particles in the system and therefore probe the energy spectrum of two-particle excitations ($N + 2$ or particle-particle spectrum). For t_2, $t_4 > t_1$, t_3 we study the analogous situation for two holes ($N - 2$ or hole-hole spectrum). For the other cases we study the particle-hole propagation which describes the excitation energies for an N-particle system. All other possible time orderings follow by permutation just giving a factor of ± 1, since

$$G^{(2)}\left(1, 2, 3, 4\right) = -G^{(2)}\left(2, 1, 3, 4\right) = G^{(2)}\left(2, 1, 4, 3\right) = -G^{(2)}\left(1, 2, 4, 3\right), \tag{3.43}$$

where an integer i denotes (α_i, t_i).

The two-particle Green's function has discontinuities for equal times, which originate from the single-particle Green's function. Let, for instance, $t_4 = t_3^- = 0$. We obtain

$$\begin{aligned}
G_{\boldsymbol{\alpha}}^{(2)}\left(t_1, t_2, 0^+, 0\right) &- G_{\boldsymbol{\alpha}}^{(2)}\left(t_1, t_2, 0^-, 0\right) \\
&= \langle \mathcal{T}_t\, c_{\alpha_1}(t_1) c_{\alpha_2}^\dagger(t_2) \left[c_{\alpha_3}, c_{\alpha_4}^\dagger\right]_+ \rangle = \mathrm{i} G_{\alpha_1\alpha_2}\left(t_1, t_2\right) \delta_{\alpha_3\alpha_4},
\end{aligned} \tag{3.44}$$

where $\left[\cdot, \cdot\right]_+$ denotes the anticommutator.

It is therefore practical to decompose $G_{\boldsymbol{\alpha}}^{(2)}$ in a "free" or unconnected part $G_{\boldsymbol{\alpha}}^{0\,(2)}$ and an interaction part $G_{\boldsymbol{\alpha}}^{\mathrm{int}\,(2)}$, such that

$$G^{(2)}(1, 2, 3, 4) = G^{0\,(2)}(1, 2, 3, 4) + G^{\mathrm{int}\,(2)}(1, 2, 3, 4). \tag{3.45}$$

The free part describes the propagation of a pair of excitations totally independent of one another. It gives rise to the discontinuities and is given by

$$G^{0\,(2)}(1,2,3,4) = G(1,2)G(3,4) - G(1,4)G(3,2) \; . \tag{3.46}$$

These single-particle Green's functions are, of course, usually fully dressed propagators, i.e. they have a non-vanishing self-energy.

The interaction part $G^{\text{int}\,(2)}(1,2,3,4)$ represents the interaction of these two excitations and contains the additional information of the two-particle Green's function. It is continuous (cf. (3.44)).

3.1.6. Analytical Structure and Properties of Correlation Functions

Comparing the single-particle Green's functions (3.35) with the dynamical correlation functions from the introduction (see for instance (3.21)) we see that both are two-point functions, i.e. depend on two points in space-time (among other possible dependencies like orbitals, spins). Both have the same analytical structure and we can treat them formally on equal footing. In fact, the single particle Green's function is nothing but the response function for removing a single particle at time t/τ and adding a particle at time t'/τ'. In this part we therefore treat a general correlation function, i.e.

$$\mathcal{C}_{\mathcal{O}_1\mathcal{O}_2}(\tau_1, \tau_2) = - \left\langle \mathcal{T}_\tau \, \mathcal{O}_1(\tau_1)\mathcal{O}_2(\tau_2) \right\rangle \; . \tag{3.47}$$

For $\mathcal{O}_1 = c$ and $\mathcal{O}_2 = c^\dagger$ it obviously gives the single particle Green's function. Exploiting that the Hamiltonian is time-independent we find, using the cyclic invariance of the trace, that the correlation functions do only depend on (real and imaginary) time differences $\tau = \tau_1 - \tau_2$, i.e. $\mathcal{C}(\tau_1, \tau_2) = \mathcal{C}(\tau_1 - \tau_2, 0) = \mathcal{C}(0, \tau_2 - \tau_1) = \mathcal{C}(\tau)$.

With Heaviside functions we can make the time-ordering operator explicit

$$\mathcal{C}_{\mathcal{O}_1\mathcal{O}_2}(\tau) = -\Theta(\tau) \left\langle \mathcal{O}_1(\tau)\mathcal{O}_2(0) \right\rangle - \xi_\mathcal{O}\Theta(-\tau) \left\langle \mathcal{O}_2(0)\mathcal{O}_1(\tau) \right\rangle \; . \tag{3.48}$$

The sign factor $\xi_\mathcal{O} = \pm 1$ depends on the statistics of $\mathcal{O}$: for fermionic operators it is $\xi_\mathcal{O} = 1$, for bosonic $\xi_\mathcal{O} = -1$. Evaluating the trace in an exact eigenbasis $\{|\Psi_n\rangle\}_n$ of the generalized Hamiltonian $\mathcal{H} = H - \mu N$ and inserting a partition of unity in the Fock space $\{|\Psi_m\rangle\}_m$ between the two operators we obtain the Lehmann or spectral representation

$$\mathcal{C}_{\mathcal{O}_1\mathcal{O}_2}(\tau) = -\frac{1}{\mathcal{Z}} \sum_{mn} \mathcal{O}_1^{nm}\mathcal{O}_2^{mn} \, e^{\mathcal{E}_{nm}\tau} \left(\Theta(\tau)e^{-\beta\mathcal{E}_n} - \xi_\mathcal{O}\Theta(-\tau)e^{-\beta\mathcal{E}_m} \right) \; . \tag{3.49}$$

Here, we introduced the abbreviating notation $\mathcal{E}_n = E_n - \mu N_n$ with E_n being the eigenenergy of H, N_n the number of particles in that state (note $[H, N] = 0$), $\mathcal{E}_{nm} = \mathcal{E}_n - \mathcal{E}_m$ and $\mathcal{O}^{mn}$ the matrix elements $\mathcal{O}^{mn} = \langle \Psi_m | \mathcal{O} | \Psi_n \rangle$.

For $\tau > 0$, (3.49) has the following τ-dependence: $\exp(\mathcal{E}_n(\tau - \beta)) \exp(-\tau\mathcal{E}_m)$. In infinite systems the spectrum of $\mathcal{H}$ is not bounded from above. Hence, the energies $\mathcal{E}_n$
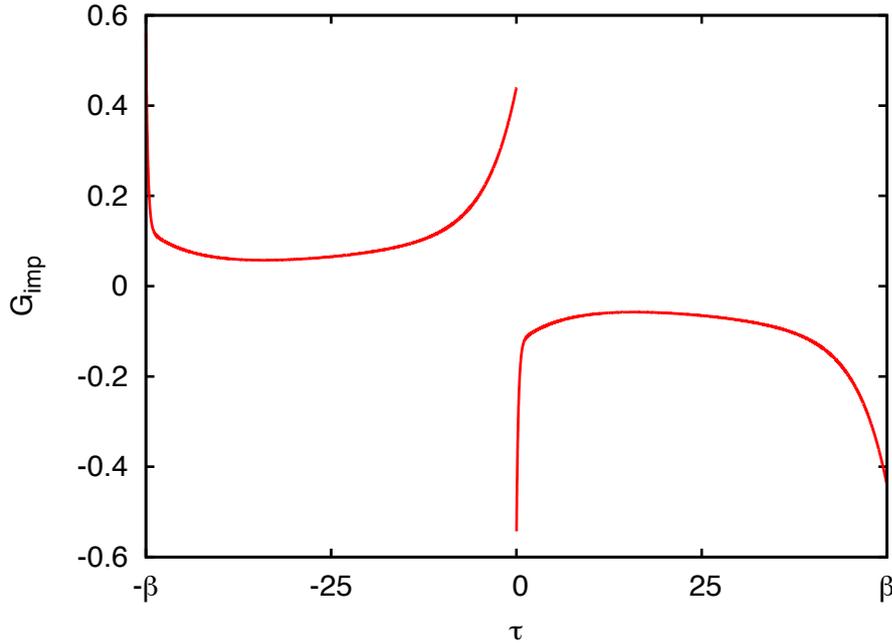
Figure 3.1.: τ-dependent impurity Green's function for a 5-dimensional Periodic Anderson Model ($t = 1/\sqrt{2d}$, $V = 0.2$, $U = 4$, $\epsilon_f = -0.3$ $\mu = -0.15$) at $\beta = 50$. From $G(0^-) = \langle n_\sigma \rangle$ we read off the impurity density $\langle n_\sigma \rangle = 0.44$. To 0^+ $G(\tau)$ undergoes a jump of size 1 to $\langle n_\sigma \rangle - 1$ due to the commutation relation. The fermionic anti-periodicity is apparent.

can and will become infinitely large. We therefore need to make sure that the factor $\tau - \beta$ in the former exponential remains negative. Therefore, $\tau < \beta$. Analogously for the $\tau < 0$ we get $\tau > -\beta$. Hence, $-\beta \leq \tau \leq \beta$.[1] Since the regions outside are clearly unphysical we restrict τ to the 2β interval and periodically extend the correlation function $\mathcal{C}$. That makes a Fourier expansion possible which yields only a discrete set of frequencies. A tremendous reduction in complexity and another advantage of the Matsubara method [92, 93]. Further inspection of equation (3.49) for $-\beta < \tau < 0$ shows

$$\mathcal{C}(\tau) = -\xi_\mathcal{O}\mathcal{C}(\tau + \beta) \ . \tag{3.50}$$

Consequently, the range $\tau \in [0, \beta]$ already contains all information. That justifies the integration boundaries we used in the introduction.

Figure 3.1 shows a typical fermionic imaginary time Green's function. The symmetry/antisymmetry (3.50) implies that the Fourier components of $\mathcal{C}(\tau)$ are only nonzero for

---

[1]Also for finite systems this restriction of τ is crucial. Even though $\mathcal{E}_n$ remains finite for $|\tau| > \beta$, the system would be highly unstable under an increase in system size: practically all weight is put in the high-energy states.

"even"/"odd" frequencies in the case of Bosons/Fermions, i.e.

$$
\omega_n = \begin{cases} \frac{\pi}{\beta} \, 2 \cdot n & \text{for Bosons ,} \\ \frac{\pi}{\beta} \, (2 \cdot n + 1) & \text{for Fermions .} \end{cases} \tag{3.51}
$$

For the Fourier series we have

$$
\mathcal{C}_{\mathcal{O}_1 \mathcal{O}_2}(\mathrm{i}\omega_n) = \int_0^\beta \mathrm{d}\tau \; e^{\mathrm{i}\omega_n \tau} \, \mathcal{C}_{\mathcal{O}_1 \mathcal{O}_2}(\tau) \tag{3.52}
$$

and

$$
\mathcal{C}_{\mathcal{O}_1 \mathcal{O}_2}(\tau) = \frac{1}{\beta} \sum_{\mathrm{i}\omega_n} e^{-\mathrm{i}\omega_n \tau} \, \mathcal{C}_{\mathcal{O}_1 \mathcal{O}_2}(\mathrm{i}\omega_n) \; . \tag{3.53}
$$

Expanding the series for (3.49) yields

$$
\mathcal{C}_{\mathcal{O}_1 \mathcal{O}_2}(\mathrm{i}\omega_n) = \int_0^\beta \mathrm{d}\tau \, \mathcal{C}_{\mathcal{O}_1 \mathcal{O}_2}(\tau) e^{\mathrm{i}\omega_n \tau} = \frac{1}{\mathcal{Z}} \sum_{mn} \frac{\mathcal{O}_1^{nm} \mathcal{O}_2^{mn}}{\mathrm{i}\omega_n + \mathcal{E}_{nm}} \left[e^{-\beta \mathcal{E}_n} + \xi_{\mathcal{O}} e^{-\beta \mathcal{E}_m} \right] \; . \tag{3.54}
$$

The characteristic denominator which we will often encounter stems from the $\Theta\,(\tau)$ functions.

Note that

$$
\mathcal{C}(\mathrm{i}\omega) = \mathcal{C}^*(-\mathrm{i}\omega) \tag{3.55}
$$

follows from equation (3.54). For numerical calculations it is useful to recast equation (3.54). Separating both summands in the brackets and renaming $m \leftrightarrow n$ in one of them we can rewrite (3.54) as a sum over (partial) correlation functions $C_{\mathcal{O}_1 \mathcal{O}_2}(n, z)$, i.e.

$$
\mathcal{C}_{\mathcal{O}_1 \mathcal{O}_2}(z) = \frac{1}{\mathcal{Z}} \sum_n e^{-\beta \mathcal{E}_n} C_{\mathcal{O}_1 \mathcal{O}_2}(n, z) \; , \tag{3.56}
$$

where the partial correlation functions are defined as

$$
C_{\mathcal{O}_1 \mathcal{O}_1}(n, z) = \sum_m \frac{\mathcal{O}_1^{nm} \mathcal{O}_2^{mn}}{z + (\mathcal{E}_m - \mathcal{E}_n)} + \xi_{\mathcal{O}} \sum_m \frac{\mathcal{O}_2^{nm} \mathcal{O}_1^{mn}}{z - (\mathcal{E}_m - \mathcal{E}_n)} \; . \tag{3.57}
$$

$C_{\mathcal{O}_1 \mathcal{O}_1}(n = 0, z)$ obviously gives the zero temperature correlation function. The finite-T function can thus be interpreted as the sum of $T = 0$ correlation functions based on the excited states weighted by their Boltzmann factor. As we will see later in this chapter the correlation functions satisfy sum rules. The contribution to these sum rules and consequently to the full correlation functions depends on the Boltzmann factor. Hence, in numerical calculations we can impose a Boltzmann cutoff to neglect these small contributions, leading to a significant reduction in computational cost. This evidently works the better the lower the temperature.

In the real-time domain things are similar but a little more involved. We employ the same prefactor convention we already used for the Green's functions. To go from

imaginary to real time we therefore replace $\tau \to \mathrm{i}t$ and multiply with i and obtain the causal or time-ordered response function

$$
\begin{align}
\mathcal{C}^{\mathrm{c}}_{\mathcal{O}_1 \mathcal{O}_2}(t) &= -\mathrm{i} \, \langle \mathcal{T}_t \, \mathcal{O}_1(t) \mathcal{O}_2(0) \rangle \tag{3.58}\\
&= -\mathrm{i} \, \Theta(t) \langle \mathcal{O}_1(t) \mathcal{O}_2(0) \rangle - \mathrm{i}\xi_{\mathcal{O}} \Theta(-t) \langle \mathcal{O}_2(0) \mathcal{O}_1(t) \rangle \tag{3.59}\\
&= -\frac{\mathrm{i}}{\mathcal{Z}} \sum_{mn} \mathcal{O}_1^{nm} \mathcal{O}_2^{mn} \, e^{\mathrm{i}\mathcal{E}_{nm}t} \, \left(\Theta(t)e^{-\beta\mathcal{E}_n} + \xi_{\mathcal{O}} \Theta(-t)e^{-\beta\mathcal{E}_m} \right) . \tag{3.60}
\end{align}
$$

According to (3.21) the right operator at time 0 is connected to the cause whereas the left operator describes the response of the system. Therefore, the latter term in (3.60) describes a response for (real) times $t < 0$, i.e. there is an (un)physical response prior to the cause. Therefore, we also define the physically more sensible *retarded* correlation function, which is non-zero only for $t > 0$,

$$
\mathcal{C}^{\mathrm{ret}}_{\mathcal{O}_1 \mathcal{O}_2}(t) = -\mathrm{i}\Theta\left(t\right) \left\langle \left[\mathcal{O}_1(t)\mathcal{O}_2(0) \right]_{\xi_{\mathcal{O}}} \right\rangle \tag{3.61}
$$

and the complementary *advanced* correlation function

$$
\mathcal{C}^{\mathrm{adv}}_{\mathcal{O}_1 \mathcal{O}_2}(t) = +\mathrm{i}\Theta\left(-t\right) \left\langle \left[\mathcal{O}_1(t)\mathcal{O}_2(0) \right]_{\xi_{\mathcal{O}}} \right\rangle , \tag{3.62}
$$

also containing both orderings of the two operators.

It is practical to study these functions in Fourier space. In the transform the Θ functions restrict the integration domain to positive or negative times. For $t > 0$, we have integrals of the type $\int_0^\infty \mathrm{d}t \, \exp(\mathrm{i}(\omega + \Delta E)t)$, which are not well-defined, since they oscillate at the integration boundary $t \to \infty$. We therefore introduce a convergence generating factor $\mathrm{i}\eta$ such that the resulting integral

$$
\int_0^\infty \mathrm{d}\omega \, e^{\mathrm{i}(\omega + \mathrm{i}\eta + \Delta E)t} = \frac{\mathrm{i}}{\omega + \mathrm{i}\eta + \Delta E} , \tag{3.63}
$$

is well-defined and can be readily evaluated. η effectively shifts the pole at $-\Delta E$ away from the real-frequency axis to $-\Delta E - \mathrm{i}\eta$ into the lower complex half plane and damps the oscillatory behavior at $t \to \infty$. For the Fourier expansion of the imaginary time correlation functions in (3.54) η was not neccessary since τ already absorbs the i at the energy difference and therefore ΔE accounts for the damping. Similarly, to make the integral for negative times well-defined, η changes its sign and we obtain the complex conjugate of the right hand side of (3.63). A straightforward calculation gives

$$
\mathcal{C}^{\mathrm{X}}(\omega) = \frac{1}{\mathcal{Z}} \sum_{mn} \mathcal{O}_1^{nm} \mathcal{O}_2^{mn} \left[\frac{e^{-\beta\mathcal{E}_n}}{\omega + \mathrm{i}s_1^X \eta + \mathcal{E}_{nm}} + \xi_{\mathcal{O}} \frac{e^{-\beta E_m}}{\omega + s_2^X \mathrm{i}\eta + \mathcal{E}_{nm}} \right] , \tag{3.64}
$$

where $\eta = 0^+$ and X can either be the causal, retarded or advanced correlation function with $s_1^{\mathrm{c}} = -s_2^{\mathrm{c}} = 1$, $s_1^{\mathrm{ret}} = s_2^{\mathrm{ret}} = +1$ and $s_1^{\mathrm{adv}} = s_2^{\mathrm{adv}} = -1$, respectively.

The poles of (3.64) carry physical meaning. They are at differences of eigenenergies of the system. In the case of single-particle Green's functions the energy differences stem
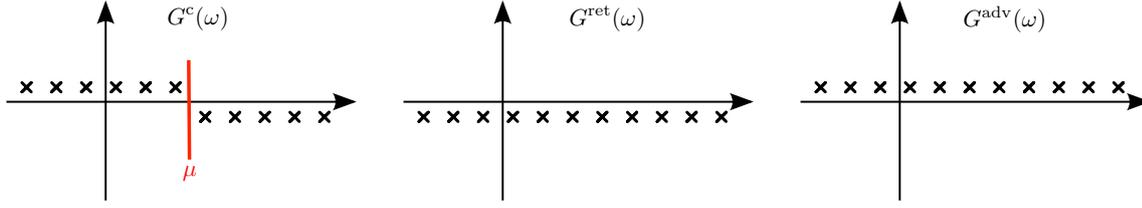
Figure 3.2.: Poles of the real-frequency Green's functions $G^{\mathrm{c}}(\omega)$, $G^{\mathrm{ret}}(\omega)$, and $G^{\mathrm{adv}}(\omega)$ in the complex plane.

from Hilbert spaces with one particle more or less, i.e. giving the single-particle spectrum. Similarly for two-particle operators (creator and annihilator) the energy spectrum for two particle excitations at fixed particle number is analyzed. In the absence of interactions we obtain the exact single/two particle energies.

The term $\pm\mathrm{i}\eta$ in the retarded/advanced correlation function shifts the poles to $z = -\mathcal{E}_{nm} \mp \mathrm{i}\eta$ slightly below/above the real axis. Both functions are related by complex conjugation, i.e. $\mathcal{C}^{\mathrm{ret}}(\omega) = \left[\mathcal{C}^{\mathrm{adv}}(\omega)\right]^{*}$. The retarded/advanced correlation function is analytic in the entire upper/lower half plane. Hence, we can obtain the Matsubara correlation functions for positive/negative frequencies by analytical continuation.

Formally, we write the analytic continuation as

$$\mathcal{C}_{\mathcal{O}_1\mathcal{O}_2}(z) = \frac{1}{\mathcal{Z}}\sum_{mn}\frac{\mathcal{O}_1^{nm}\mathcal{O}_2^{mn}}{z+\mathcal{E}_{nm}}\left[e^{-\beta\mathcal{E}_n} + \xi_{\mathcal{O}}e^{-\beta\mathcal{E}_m}\right]\,, \tag{3.65}$$

where for $z = \mathrm{i}\omega_n$ we obtain the Matsubara and for $z = \omega \pm \mathrm{i}\eta$ the retarded/advanced Green's function. However, the causal correlation function is obviously not accessible from this generalized function.

The causal correlation function has poles above and below the axis and therewith carries explicit information about the chemical potential μ. This makes it considerably harder to analyze. An analytical continuation is, for instance, not possible. The situation for all three real-frequency Green's functions is depicted in figure 3.2. Still, introducing the spectral function

$$\rho_{\mathcal{O}_1\mathcal{O}_2}(\omega) = -\frac{1}{\pi}\mathrm{Im}\,\mathcal{C}^{\mathrm{ret}}_{\mathcal{O}_1\mathcal{O}_2}(\omega) = +\frac{1}{\pi}\mathrm{Im}\,\mathcal{C}^{\mathrm{adv}}_{\mathcal{O}_1\mathcal{O}_2}(\omega)\,, \tag{3.66}$$

the three correlation functions can be related to one another. Using Dirac's identity

$$\lim_{\eta\to 0}\frac{1}{x\pm\mathrm{i}\eta} = \mp\mathrm{i}\pi\delta(x) + \mathcal{P}\frac{1}{x}\,, \tag{3.67}$$

where $\mathcal{P}$ denotes taking the principal part of an integral we obtain

$$\rho_{\mathcal{O}_1\mathcal{O}_2}(\omega) = \frac{1}{\mathcal{Z}}\sum_{mn}\mathcal{O}_1^{nm}\mathcal{O}_2^{mn}\,e^{-\beta\mathcal{E}_n}\left(1 + \xi_{\mathcal{O}}e^{\beta\omega}\right)\delta\left(\omega + \mathcal{E}_{nm}\right)\,. \tag{3.68}$$

Using the spectral representation and the identity

$$\tanh\left(\frac{\beta\omega}{2}\right)^{\xi_\mathcal{O}} = \frac{1 + \xi_\mathcal{O}\exp\left(-\beta\omega\right)}{1 - \xi_\mathcal{O}\exp\left(-\beta\omega\right)} \tag{3.69}$$

we get the following relations

$$\mathrm{Re}\left\{\begin{array}{c}\mathcal{C}^{\mathrm{c}}\\\mathcal{C}^{\mathrm{ret}}\\\mathcal{C}^{\mathrm{adv}}\end{array}\right\}(\omega) = \mathcal{P}\int_{-\infty}^{\infty}\mathrm{d}\omega'\frac{\rho(\omega')}{\omega - \omega'} \tag{3.70}$$

$$\mathrm{Im}\left\{\begin{array}{c}\mathcal{C}^{\mathrm{c}}\\\mathcal{C}^{\mathrm{ret}}\\\mathcal{C}^{\mathrm{adv}}\end{array}\right\}(\omega) = \left\{\begin{array}{c}-\tanh\left(\frac{\beta\omega}{2}\right)^{\xi_\mathcal{O}}\\-\\+\end{array}\right\}\pi\rho(\omega) . \tag{3.71}$$

Hence, the real part is the same for the three real frequency correlation functions whereas the imaginary parts differ due to the different positions of the poles.

Equation (3.70) is one of the two Kramers-Kronig relations which relate the imaginary part to the real part for functions which are analytic in either the upper or lower complex half-plane and decay faster than $1/|z|$ for $|z| \to \infty$. This is the case for $\mathrm{C}^{\mathrm{ret}}$ and $\mathrm{C}^{\mathrm{adv}}$ but not for C^{c}.

The spectral function obeys the following sum rule

$$\int_{-\infty}^{\infty}\mathrm{d}\omega\rho_{\mathcal{O}_1\mathcal{O}_2}(\omega) = \frac{1}{\mathcal{Z}}\sum_{mn}\mathcal{O}_1^{nm}\mathcal{O}_2^{mn}\left(e^{-\beta\mathcal{E}_n} + \xi_\mathcal{O}e^{-\beta\mathcal{E}_m}\right) \tag{3.72}$$

$$= \frac{1}{\mathcal{Z}}\sum_{n}e^{-\beta\mathcal{E}_n}\langle\Psi_n|\left[\mathcal{O}_1,\mathcal{O}_2\right]_{\xi_\mathcal{O}}|\Psi_n\rangle = \langle\left[\mathcal{O}_1,\mathcal{O}_2\right]_{\xi_\mathcal{O}}\rangle . \tag{3.73}$$

Thus, for the important example of the (diagonal) single-particle Green's function ($\mathcal{O}_1 = c$ and $\mathcal{O}_2 = c^\dagger$) with $\left[c_\alpha, c_\beta^\dagger\right]_\xi = \delta_{\alpha\beta}$, the spectral function is normalized to unity, irrespective of Bosons or Fermions. Similarly it can be shown that

$$\int_{-\infty}^{\infty}\mathrm{d}\omega\rho_{c_\alpha,c_\alpha^\dagger}(\omega)f_{\xi_c}(\omega) = \langle n_\alpha\rangle , \tag{3.74}$$

where $f_{\xi_c}(\omega)$ is the Fermi-Dirac or Bose function depending on the statistics of the particle operators and $\langle n_\alpha\rangle$ is the occupation number of state α.

Using the sum rule we can approximate equation (3.65) for large z by

$$\mathcal{C}_{\mathcal{O}_1\mathcal{O}_2}(z) \to \frac{\langle\left[\mathcal{O}_1,\mathcal{O}_2\right]_{\xi_\mathcal{O}}\rangle}{z} + \mathcal{O}\left(1/z^2\right) , \tag{3.75}$$

since the spectrum of H is bounded from below and above for the systems we treat here. For infinite systems the system is just bounded from below, however, high energy contributions are suppressed by Boltzmann factors.

Hence, the Green's functions asymptotically behaves according to $G(z) = 1/z$. Correlation functions with $[\mathcal{O}, \mathcal{O}]_{\xi_\mathcal{O}} = 0$ decay faster.

3.1.7. (Non-)Interacting Green's Functions and Self-Energy

3.1.7.1. Single-Particle Green's Function

The most important example for a correlation function is the single-particle Green's function. It provides the single-particle energy spectrum which describes the energy and lifetime of the perturbation caused by adding or removing a particle and reads $G(z) = \mathcal{C}_{c_\alpha, c_\alpha^\dagger}$.

In this section we mainly focus on non-interacting particles. Let $\{|\varphi_\alpha\rangle\}_\alpha$ denote the eigenbasis of the single-particle Hamiltonian with the corresponding eigenvalues ε_α. The eigenstates of the many-body Hamiltonian are Slater determinants $\Psi_\mu = |\varphi_{\mu_1}\varphi_{\mu_2}\cdots\rangle$ with the energy $E_\mu = \sum_{\text{occ}\alpha} \varepsilon_{\mu_\alpha}$.

We start from expression (3.56) with the sign-factors s_i^X as in (3.64) giving

$$\mathcal{G}_\alpha(z) = \frac{1}{\mathcal{Z}} \sum_n e^{-\beta E_n} \left\{ \sum_m \frac{|\langle m|c_\alpha^\dagger|n\rangle|^2}{z + is_1^X \eta - (E_m^{N+1} - E_n^N)} + \sum_m \frac{|\langle m|c_\alpha|n\rangle|^2}{z + is_2^X \eta + (E_m^{N-1} - E_n^N)} \right\} . \tag{3.76}$$

For arbitrary complex z and especially Matsubara frequencies we use $s_1^\text{M} = s_2^\text{M} = 0$.

For a fixed n the matrix element in the numerator of the first fraction is only non-zero if $|m\rangle = c_\alpha^\dagger|n\rangle$. In that case the energy difference in the denominator is the single-particle energy ε_α. The second fraction is only non-zero if $|m\rangle = c_\alpha|n\rangle$ with energy difference $-\varepsilon_\alpha$. Hence, we have

$$G_\alpha(z) = \frac{1}{\mathcal{Z}} \sum_n e^{-\beta E_n} \left\{ \frac{1 - \langle n|c_\alpha^\dagger c_\alpha|n\rangle}{z + is_1^X \eta - \varepsilon_\alpha} + \frac{\langle n|c_\alpha^\dagger c_\alpha|n\rangle}{z + is_2^X \eta - \varepsilon_\alpha} \right\} \tag{3.77}$$

$$= \frac{1 - f_F(\varepsilon_\alpha)}{z + is_1^X \eta - \varepsilon_\alpha} + \frac{f_F(\varepsilon_\alpha)}{z + is_2^X \eta - \varepsilon_\alpha} , \tag{3.78}$$

where f_F denotes the Fermi-Dirac distribution.

For the Green's functions with $s_1^X = s_2^X$, i.e. Matsubara, advanced, and retarded, this can be further simplified to

$$G_\alpha^0(z) = \frac{1}{z - \varepsilon_\alpha} . \tag{3.79}$$

While for the Matsubara Green's function the temperature information is retained in the choice of the frequencies ω_n, the temperature dependence cancels in the real-frequency Green's functions. This is not the case for the causal Green's function, where $s_1^\text{adv} = +1 = -s_2^\text{adv}$, i.e.

$$G_\alpha^0(\omega) = \frac{1 - f_F(\varepsilon_\alpha)}{\omega + i\eta - \varepsilon_\alpha} + \frac{f_F(\varepsilon_\alpha)}{\omega - i\eta - \varepsilon_\alpha} . \tag{3.80}$$

Comparing with the real-frequency version of (3.79) we see that each pole is split into two, one above and one below the real frequency axis with their weight given by f_F, $1 - f_F$, respectively. The weight distribution of the poles captures the temperature effects.

Generalizations In general, single-particle Green's functions are matrices in some orbital basis. The non-interacting Green's function, for instance, is

$$G^0(z) = \left(z - H^0\right)^{-1} , \tag{3.81}$$

where H^0 is the non-interacting single-particle Hamiltonian. In its eigenbasis $G^0(z)$ is obviously also diagonal with the eigenvalues being the z-dependent Green's functions $G^0_\alpha(z)$ from above.

In the case of interactions we can bring the full-interacting Green's function in a similar form introducing a (complex) electronic self-energy Σ which captures all many-body effects,

$$G(z) = \left(z - H^0 - \Sigma(z)\right)^{-1} . \tag{3.82}$$

An alternative form of (3.82) is the Dyson equation

$$\Sigma_\alpha(z) = \left[G^0_\alpha(z)\right]^{-1} - G^{-1}_\alpha(z) . \tag{3.83}$$

Many-body effects cause an energy dependent shift in the poles (real parts of Σ) and thus in the excitation energies as well as finite lifetimes which are inversely proportional to the imaginary parts of Σ.

3.1.7.2. Two-particle Green's Function

In the non-interacting case all higher-order Green's functions can be solely expressed in single-particle Green's functions by using using Wick's theorem. For the two-particle Green's function we find

$$
\begin{aligned}
G^{0\,(2)}_{\sigma\sigma'}(\tau_1, \tau_2, \tau_3, 0) &= \left\langle \mathcal{T}_\tau\, c_\sigma(\tau_1)\bar{c}_\sigma(\tau_2)c_{\sigma'}(\tau_3)\bar{c}_{\sigma'}(0)\right\rangle \\
&= \left\langle \mathcal{T}_\tau\, c_\sigma(\tau_1)\bar{c}_\sigma(\tau_2)\right\rangle\left\langle \mathcal{T}_\tau\, c_\sigma(\tau_3)\bar{c}_\sigma(0)\right\rangle - \left\langle \mathcal{T}_\tau\, c_\sigma(\tau_1)\bar{c}_{\sigma'}(0)\right\rangle\left\langle \mathcal{T}_\tau\, c_{\sigma'}(\tau_3)\bar{c}_\sigma(\tau_2)\right\rangle \\
&= G^{0\,(1)}(\tau_1, \tau_2)G^{0\,(1)}(\tau_3, 0) - \delta_{\sigma\sigma'}G^{0\,(1)}(\tau_1, 0)G^{0\,(1)}(\tau_3, \tau_2) ,
\end{aligned}
\tag{3.84}
$$

where we again exploit (imaginary) time translation invariance. Obviously this is a special case of (3.45) where (a) the interaction part $G^{\text{int}\,(2)}$ vanishes and (b) the propagators in the unconnected part (3.46) are the bare non-interacting particle propagators.

Fourier transforming of (3.84) to Matsubara frequencies yields

$$
\begin{aligned}
G^{0\,(2)}_{\sigma\sigma'}(\omega_1, \omega_2, \omega_3) &= \int_0^\beta \mathrm{d}\tau_1\, \mathrm{d}\tau_2\, \mathrm{d}\tau_3 \; e^{\mathrm{i}(\omega_1\tau_1 - \omega_2\tau_2 + \omega_3\tau_3)}\, G^{0\,(2)}_{\sigma\sigma'}(\tau_1, \tau_2, \tau_3, 0) \\
&= \beta\left(\delta_{\omega_1,\omega_2} - \delta_{\omega_3,\omega_2}\delta_{\sigma\sigma'}\right)G^{0\,(1)}(\mathrm{i}\omega_1)G^{0\,(1)}(\mathrm{i}\omega_3) .
\end{aligned}
\tag{3.85}
$$

3.1.8. From Green's to Dynamical Correlations Functions

General dynamical correlation functions based on single-particle operators and one-body Green's functions can be formally treated on equal footing. In this section we discuss how to obtain dynamical correlation functions from Green's functions. For non-interacting

particles only the single-particle Green's function is needed due to Wick's theorem. In general, however, the two-body Green's function is necessary.

As an example we calculate the imaginary time $\mathcal{C}_{S^z S^z}$ correlation function of the spin-operator

$$S^z = \frac{1}{2} (n_\uparrow - n_\downarrow) = \frac{1}{2} \left(c_\uparrow^\dagger c_\uparrow - c_\downarrow^\dagger c_\downarrow \right) \ . \tag{3.86}$$

According to equation (3.47) $\mathcal{C}_{S^z S^z}(\tau)$ is given by

$$\mathcal{C}_{S^z S^z}(\tau) = \left\langle \mathcal{T}_\tau \, S^z(\tau) S^z(0) \right\rangle = \frac{1}{4} \left\langle \mathcal{T}_\tau \, (n_\uparrow(\tau) - n_\downarrow(\tau)) (n_\uparrow(0) - n_\downarrow(0)) \right\rangle . \tag{3.87}$$

Expanding (3.87) in particle operators c, $c^\dagger$ and taking into account that the system is paramagnetic, which means that the terms are invariant under a flip of all spins, we obtain

$$\mathcal{C}_{S^z S^z}(\tau) = \frac{1}{2} \left(\left\langle \mathcal{T}_\tau \, \bar{c}_\uparrow(\tau^+) c_\uparrow(\tau) \bar{c}_\uparrow(0^+) c_\uparrow(0) \right\rangle - \left\langle \mathcal{T}_\tau \, \bar{c}_\uparrow(\tau^+) c_\uparrow(\tau) \bar{c}_\downarrow(0^+) c_\downarrow(0) \right\rangle \right) \ , \tag{3.88}$$

or in terms of the two-particle Green's functions from section 3.1.5

$$\mathcal{C}_{S^z S^z}(\tau) = \frac{1}{2} \left(G^{(2)}_{\uparrow\uparrow} \left(\tau, \tau^+, 0, 0^+ \right) - G^{(2)}_{\uparrow\downarrow} \left(\tau, \tau^+, 0, 0^+ \right) \right) \ . \tag{3.89}$$

Two-Particle Green's function Hence, with the two-particle Green's function we have direct access to the susceptibility. Numerically, we usually have $G^{(2)}_{\sigma\sigma'}(\omega_1, \omega_2, \omega_3)$ in Matsubara space which follows from a Fourier transform

$$G^{(2)}_{\sigma\sigma'}(i\omega_1, i\omega_2, i\omega_3) = \int_0^\beta d\tau_1 \, d\tau_2 \, d\tau_3 \ e^{i(\omega_1\tau_1 - \omega_2\tau_2 + \omega_3\tau_3)} \, G^{(2)}_{\sigma\sigma'} \left(\tau_1, \tau_2, \tau_3, 0 \right) \ . \tag{3.90}$$

The fourth frequency ω_4 follows implicitly by energy conservation. In order to calculate the Fourier transform of equation (3.89) using $G^{(2)}_{\sigma\sigma'}(i\omega_1, i\omega_2, i\omega_3)$, we need a partial Fourier transform. Since $\tau_4 = 0$ we need an adjusted time ordering where $\tau_3 = 0^-$ to ensure the correct ordering, i.e.

$$\mathcal{C}_{S^z S^z}(\tau) = \frac{1}{2} \left(G^{(2)}_{\uparrow\uparrow} \left(\tau, \tau^+, 0^-, 0 \right) - G^{(2)}_{\uparrow\downarrow} \left(\tau, \tau^+, 0^-, 0 \right) \right) \ . \tag{3.91}$$

Carrying out the transform we get

$$\begin{aligned}
G^{\text{pFT}}_{\sigma\sigma'}(i\Omega_n) &= \int_0^\beta d\tau \, e^{i\Omega_n\tau} \frac{1}{\beta^3} \sum_{i\omega_1 \, i\omega_2 \, i\omega_3} G^{(2)}_{\sigma\sigma'}(i\omega_1 \, i\omega_2 \, i\omega_3) e^{-i\omega_1\tau} e^{+i\omega_2\tau^+} e^{-i\omega_3 0^-} & (3.92) \\
&= \frac{1}{\beta^2} \sum_{i\omega_1 \, i\omega_2 \, i\omega_3} \delta_{\Omega_n, \omega_1 - \omega_2} G^{(2)}_{\sigma\sigma'}(i\omega_1, i\omega_2, i\omega_3) & (3.93) \\
&= \frac{1}{\beta^2} \sum_{i\omega_2 \, i\omega_3} G^{(2)}_{\sigma\sigma'}(i\Omega_n + i\omega_2, i\omega_2, i\omega_3) \ , & (3.94)
\end{aligned}$$

since $\delta_{\Omega_n, \omega_1 - \omega_2}$, Ω_n must be a bosonic Matsubara frequency.

All dynamical correlation functions based on single-particle operators are thus accessible in a similar way. All we have to adjust is the time ordering and the matrix elements $v^{\mathcal{O}}_{\boldsymbol{k}\sigma}$.

Non-Interacting Case Exploiting Wick's theorem we can decompose equation (3.94) into single-particle Green's functions for non-interacting particles. Using equation (3.85) only the term with $-\delta_{\sigma\sigma'} = -1$ survives giving

$$\mathcal{C}_{S^z S^z}(\mathrm{i}\Omega_n) \;=\; -\frac{1}{2\beta} \sum_{\mathrm{i}\omega_2\,\mathrm{i}\omega_3} \delta_{\omega_2,\omega_3}\, G\left(\mathrm{i}\Omega_n + \mathrm{i}\omega_2\right) G\left(\mathrm{i}\omega_3\right) \tag{3.95}$$

$$\;=\; -\frac{1}{2\beta} \sum_{\mathrm{i}\omega_m} G(\mathrm{i}\omega_m + \mathrm{i}\Omega_n) G(\mathrm{i}\omega_m) \;. \tag{3.96}$$

Equivalently, we can also start from (3.88) and use Wick's theorem in imaginary time

$$\mathcal{C}_{S^z S^z}(\tau) \;=\; \frac{1}{2}\Bigg\{ \left(G^{(1)}(\tau,\tau^+)G^{(1)}(0^-,0) - G^{(1)}(\tau,0)G^{(1)}(0,\tau^+)\right)$$

$$-G^{(1)}(\tau,\tau^+)G^{(1)}(0^-,0)\Bigg\} \tag{3.97}$$

$$\;=\; -\frac{1}{2}G(\tau,0)G(0,\tau) = -\frac{1}{2}G(\tau)G(-\tau) \;. \tag{3.98}$$

With a convolution/autocorrelation-like theorem (see appendix F) we can readily perform the Fourier transform of this expression to Matsubara frequencies $\mathrm{i}\Omega_n$ also yielding equation (3.96).

This calculation can also be done in the real-time case when using the causal Green's function, i.e.

$$\mathcal{C}^{\mathrm{c}}_{S^z S^z}(t) = -\frac{1}{2}G^{\mathrm{c}}(t)G^{\mathrm{c}}(-t) \;. \tag{3.99}$$

That is no surprise, since we could have also used Wick's rotation (and time ordering operator redefinition) for the continuation.

With an autocorrelation-like theorem (see appendix F) we now perform a frequency integral instead of the summation, i.e.

$$\mathcal{C}^{\mathrm{c}}_{S^z S^z}(\Omega) = -\frac{1}{2} \int_{-\infty}^{\infty} \mathrm{d}\omega\, G^{\mathrm{c}}(\omega + \Omega)G^{\mathrm{c}}(\omega) \;. \tag{3.100}$$

For reasons which we will discuss below we need to take the causal Green's functions.

3.1.8.1. Matsubara Summation

Summations of the type (3.96) often occur in condensed matter physics, e.g. for polarization bubbles. We briefly review their evaluation.

Let $g(z)$ be some function of the complex variable $z \in \mathbb{C}$ and ω_n bosonic or fermionic Matsubara frequencies. To calculate $\mathcal{S} = \sum_{\omega_n} g(\mathrm{i}\omega_n)$ we introduce a complex auxiliary pole-generating function $f_x(z)$ with simple poles at $z = \mathrm{i}\omega_n$. Any function with such poles
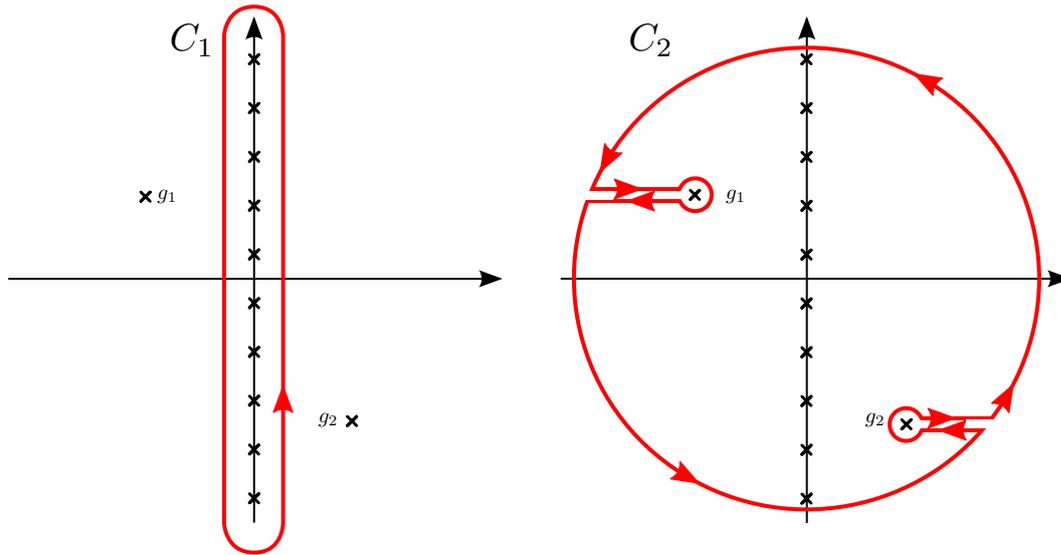
Figure 3.3.: Integration contours in complex plane: (left) straightforward contour to calculate Matsubara summation, when poles not on imaginary axis; (right) inflated contour excluding the poles of F which are encircled in clockwise manner.

could be used. However, it is practical to use the Fermi-Dirac or Bose-Einstein functions, i.e.

$$f_F(z) = \frac{1}{\exp(\beta z) + 1} \tag{3.101}$$

or

$$f_B(z) = \frac{1}{\exp(\beta z) - 1} \,, \tag{3.102}$$

since their singularities have the same residues $-\xi\beta^{-1}$ for all poles, where $\xi = 1$ for Fermions and $\xi = -1$ for Bosons. To evaluate the sum we reformulate the expression in terms of a contour integral encircling the poles of f_x only. The situation is depicted in the left plot of figure 3.3, where the crosses on the imaginary axis denote the (here fermionic) Matsubara frequencies and the other two poles stem from $g(z)$. Integration over the contour C_1 yields

$$\frac{\beta}{2\pi i} \oint_{C_1} dz\, f_x(z)\, g(z) = \beta \sum_{i\omega_n} \operatorname*{res}_{z = i\omega_n} (f_x(z)g(z)) = -\xi\mathcal{S} \,, \tag{3.103}$$

as long as there is no pole of g on the imaginary axis.

However, we are free to vary the contour as long as we do not include any pole of $g(z)$. If the integrand $|f_x(z)\, g(z)|$ decays faster than $1/z$ for $|z| \to \infty$ we can inflate the contour

to an infinitely large circle but excluding the poles of $g(z)$ as shown in the right plot of figure 3.3. The perimeter part of C_2 vanishes and we only retain g_i, the poles of $g(z)$, which are encircled in clockwise manner. Thus,

$$\mathcal{S} = \frac{\xi\beta}{2\pi\mathrm{i}} \oint_{C_2} \mathrm{d}z \, f_x(z) \, g(z) = \beta\xi \sum_i \operatorname*{res}_{z=g_i} f_x(z) \, g(z) \, . \tag{3.104}$$

Effectively, we replaced the summation over infinitely many Matsubara frequencies by a sum over a finite number of poles.

The product of two Green's functions obviously fulfills the decay requirement for the deformation. Hence, we can evaluate summation (3.96) using (3.104). To that end, we transform the particle operators in the Green's function into the eigenbasis of the Hamiltonian, i.e.

$$c_i^{(\dagger)} = \sum_\alpha \varphi_\alpha(\boldsymbol{R}_i) c_\alpha^{(\dagger)} \, . \tag{3.105}$$

Inserting this expansion into (3.56) and proceeding like in section 3.1.7, we obtain

$$G(z) = \sum_\alpha \frac{|\varphi_\alpha(\boldsymbol{R}_i)|^2}{z - \epsilon_\alpha} \, . \tag{3.106}$$

For the correlation function $\mathcal{C}_{S^z S^z}(\mathrm{i}\Omega_n)$ follows

$$\mathcal{C}_{S^z S^z}(\mathrm{i}\Omega_n) = \frac{1}{2} \sum_{\alpha\alpha'} |\varphi_\alpha|^2 |\varphi_{\alpha'}|^2 \chi_{\alpha,\alpha'}(\mathrm{i}\Omega_n), \tag{3.107}$$

where a typical form of $\chi_{\alpha\alpha'}(\mathrm{i}\Omega_n)$ is

$$\chi_{\alpha\alpha'}(\mathrm{i}\Omega_n) = -\frac{1}{\beta} \sum_{\mathrm{i}\omega_m} \frac{1}{\mathrm{i}\omega_m + \mathrm{i}\Omega_n - \varepsilon_\alpha} \frac{1}{\mathrm{i}\omega_m - \varepsilon_{\alpha'}} \, . \tag{3.108}$$

To evaluate $\chi_{\alpha\alpha'}(\mathrm{i}\Omega_n)$ we apply (3.104) and get

$$\chi_{\alpha\alpha'}(\mathrm{i}\Omega_n) = \frac{f_F(\varepsilon_\alpha - \mathrm{i}\Omega_n) - f_F(\varepsilon_{\alpha'})}{\mathrm{i}\Omega_n + \varepsilon_{\alpha'} - \varepsilon_\alpha} \, . \tag{3.109}$$

With Ω_n being a bosonic Matsubara frequency, i.e. $\exp(\beta\mathrm{i}\Omega) = 1$, the $\mathrm{i}\Omega$-dependence in the Fermi function can be dropped, $f_F(z + \mathrm{i}\Omega) = f_F(z)$ (see also below for a more detailed discussion). Hence, we obtain

$$\chi_{\alpha\alpha'}(\mathrm{i}\Omega_n) = \frac{f_F(\varepsilon_\alpha) - f_F(\varepsilon_{\alpha'})}{\mathrm{i}\Omega_n + \varepsilon_{\alpha'} - \varepsilon_\alpha} \, , \tag{3.110}$$

which is identical to (3.109) on the Matsubara axis. Its analytical continuation to real Ω gives the correct non-interacting susceptibility. Note, that this is not true for (3.109).

3.1.8.2. The Real Frequency Integral for the Susceptibility

The autocorrelation-like real frequency integral (3.100) is built from expressions corresponding to (3.108) but requires the causal Green's function, i.e.

$$
\chi^{\mathrm{c}}_{\alpha\alpha'}(\Omega) = -\frac{1}{2\pi} \int \mathrm{d}\omega \left(\frac{1 - f_F(\varepsilon_\alpha)}{\omega + \Omega + \mathrm{i}\eta - \varepsilon_\alpha} \frac{1 - f_F(\varepsilon_{\alpha'})}{\omega + \mathrm{i}\eta - \varepsilon_{\alpha'}} + \frac{1 - f_F(\varepsilon_\alpha)}{\omega + \Omega + \mathrm{i}\eta - \varepsilon_\alpha} \frac{f_F(\varepsilon_{\alpha'})}{\omega - \mathrm{i}\eta - \varepsilon_{\alpha'}} \right.
$$
$$
\left. + \frac{f_F(\varepsilon_\alpha)}{\omega + \Omega - \mathrm{i}\eta - \varepsilon_\alpha} \frac{f_F(\varepsilon_{\alpha'})}{\omega - \mathrm{i}\eta - \varepsilon_{\alpha'}} + \frac{f_F(\varepsilon_\alpha)}{\omega + \Omega - \mathrm{i}\eta - \varepsilon_\alpha} \frac{1 - f_F(\varepsilon_{\alpha'})}{\omega + \mathrm{i}\eta - \varepsilon_{\alpha'}} \right) . \tag{3.111}
$$
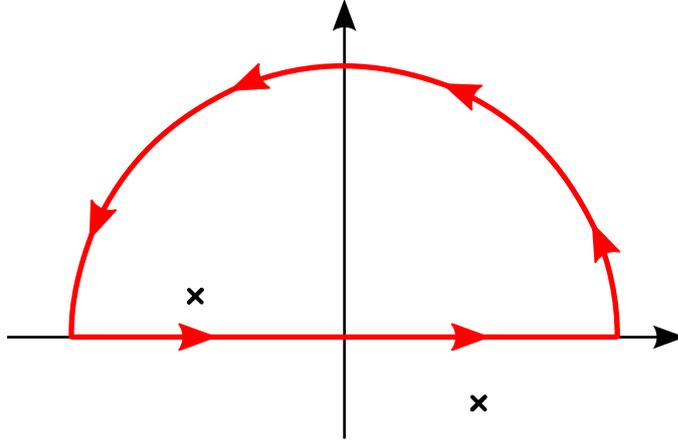
These integrals may be evaluated by closing the integrals with an additional semi-circle contour in the upper or lower complex plane and then exploiting the residue theorem (see figure 3.4). The semi-circle itself vanishes for the same reason the perimeter of the inflated contour vanishes above. Thus, if two poles are situated in the same half-plane we can close the contour in the other obtaining zero. Thus, only the terms with poles in both planes contribute. This is the reason why we need to take the causal Green's function to obtain a non-zero real-frequency susceptibility. Physically we can interpret the terms as the scattering of particles (poles in upper plane) with holes (poles in lower plane).

A simple calculation yields,

$$
\chi^{\mathrm{c}}_{\alpha\alpha'}(\Omega) = -\mathrm{i} \left\{ \frac{(1 - f_F(\varepsilon_\alpha)) f_F(\varepsilon_{\alpha'})}{\Omega + 2\mathrm{i}\eta - (\varepsilon_\alpha - \varepsilon_{\alpha'})} - \frac{(1 - f_F(\varepsilon_{\alpha'})) f_F(\varepsilon_\alpha)}{\Omega - 2\mathrm{i}\eta - (\varepsilon_\alpha - \varepsilon_{\alpha'})} \right\} . \tag{3.112}
$$

This is a causal susceptibility. If we flip the sign in front of $\eta = 0^+$ in the second/first term we obtain the retarded/advanced susceptibility

$$
\chi^{\mathrm{ret/adv}}_{\alpha\alpha'}(\Omega) = \mathrm{i} \frac{f_F(\varepsilon_\alpha) - f_F(\varepsilon_{\alpha'})}{\Omega \pm \mathrm{i}\eta - (\varepsilon_\alpha - \varepsilon_{\alpha'})} , \tag{3.113}
$$

which is directly related to (3.110) via analytic continuation (except for the prefactor convention). Inserting (3.112) into (3.107) for real frequencies we obtain the causal z-spin susceptibility.

3.1.9. Analytic Continuation and Padé Approximants

We would like to briefly dwell on the topic of analytic continuation. Formally, dealing with the Matsubara formalism is easier and considerably more convenient compared to directly dealing with real-frequency quantities. In the end, however, experiments describe dynamics in real time and real frequencies and we therefore need to extract the real- from the Matsubara frequency-dependent functions.

   Let us suppose we have a correlation function $\mathcal{C}^{\mathrm{M}}(\mathrm{i}\omega_n)$ for all positive Matsubara frequencies. How do we obtain the corresponding real-frequency retarded correlation function $\mathcal{C}^{\mathrm{ret}}(\omega)$? From complex analysis we know that if we succeed in constructing a function $\mathcal{F}(\mathrm{i}\omega_n)$ which is analytic in the upper half-plane and satisfies

$$\mathcal{C}^{\mathrm{M}}(\mathrm{i}\omega_n) = \mathcal{F}(\mathrm{i}\omega_n) \qquad \forall \, \mathrm{Im}\,(\mathrm{i}\omega_n) > 0 \ , \tag{3.114}$$

i.e. coincides with $\mathcal{C}^{\mathrm{M}}$ on infinitely many points (limit point is infinity), both functions are identical in the upper half-plane

$$\mathcal{C}^{\mathrm{ret}}(\omega) = \mathcal{F}(\omega) \ . \tag{3.115}$$

In particular they coincide on the real-frequency axis.

   With this in mind let us revisit the different forms of the bubble (3.109), (3.110), and, the retarded (3.113). Obviously (3.110) is connected to (3.113) via analytic continuation, whereas (3.109)

$$-\frac{1}{\beta} \sum_{\mathrm{i}\omega_n} \frac{1}{\mathrm{i}\omega_n + z - \varepsilon_\alpha} \frac{1}{\mathrm{i}\omega_n - \varepsilon_{\alpha'}} = \frac{f_F(\varepsilon_\alpha - z) - f_F(\varepsilon_{\alpha'})}{z + \varepsilon_{\alpha'} - \varepsilon_\alpha} \ , \tag{3.116}$$

being the direct result of our calculation is not. This function has simple poles at $z = \varepsilon_\alpha - \varepsilon_{\alpha'}$, denoting the physical excitations, as well as spurious poles at $z = \varepsilon_\alpha - \mathrm{i}\pi\,(2n+1)\,/\beta$. These additional poles are encoded in the z-dependent Fermi function on the right-hand side. This cannot be a proper candidate for $\mathcal{F}(z)$.

   With z restricted to bosonic Matsubara frequencies $f_F(\varepsilon_\alpha - z) = f_F(\varepsilon_\alpha)$ holds. Now (3.110) coincides with (3.109) on all bosonic frequencies but, in addition, has no poles in the upper half-plane. Hence, it is the proper $\mathcal{F}(z)$ for analytic continuation. Therewith the problem is formally solved.

   However, suppose we have Green's functions as black boxes and would like to perform the Matsubara summation to obtain dynamical correlation functions. This is exactly the problem we face in numerical calculations. Let us first perform a partial fraction decomposition on the left hand side of (3.116). In general, we have

$$\frac{1}{(z-\alpha)(z-\beta)} = \frac{1/\alpha - \beta}{z-\alpha} + \frac{1/\beta - \alpha}{z-\beta} = \frac{1}{\alpha - \beta}\left(\frac{1}{z-\alpha} - \frac{1}{z-\beta}\right) \tag{3.117}$$

and in our non-interacting case

$$-\frac{1}{\beta}\sum_{\mathrm{i}\omega_m}\frac{1}{\mathrm{i}\omega_m+\mathrm{i}\Omega_n-\varepsilon_\alpha}\frac{1}{\mathrm{i}\omega_m-\varepsilon_{\alpha'}}$$

$$=-\frac{1}{\varepsilon_\alpha-\varepsilon_\beta-\mathrm{i}\Omega_n}\frac{1}{\beta}\sum_{\mathrm{i}\omega_m}\left(G_\alpha\left(\mathrm{i}\omega_m+\mathrm{i}\Omega_n\right)-G_\beta\left(\mathrm{i}\omega_m\right)\right)\quad(3.118)$$

$$=-\frac{1}{\varepsilon_\alpha-\varepsilon_\beta-\mathrm{i}\Omega_n}\frac{1}{\beta}\sum_{\mathrm{i}\omega_m}\left(G_\alpha\left(\mathrm{i}\omega_m\right)-G_\beta\left(\mathrm{i}\omega_m\right)\right)\;,\qquad(3.119)$$

where in the last line we shifted the summation index of the first Green's function. Evidently, this gives (3.113). In this form the calculation can be evaluated numerically and yields the desired results on the real axis.

For general Green's functions that suggests the ansatz

$$-\frac{1}{\beta}\sum_{\mathrm{i}\omega_m}\frac{1}{G_\alpha^{-1}\left(\mathrm{i}\omega_m\right)G_\beta^{-1}\left(\mathrm{i}\omega_m+\mathrm{i}\Omega_n\right)}=-\frac{1}{\beta}\sum_{\mathrm{i}\omega_m}\frac{G_\beta\left(\mathrm{i}\omega_m+\mathrm{i}\Omega_n\right)-G_\alpha\left(\mathrm{i}\omega_m\right)}{G_\alpha^{-1}\left(\mathrm{i}\omega_m\right)-G_\beta^{-1}\left(\mathrm{i}\omega_m+\mathrm{i}\Omega_n\right)}\quad(3.120)$$

$$=\frac{1}{\beta}\sum_{\mathrm{i}\omega_m}\frac{G_\alpha\left(\mathrm{i}\omega_m\right)}{G_\alpha^{-1}\left(\mathrm{i}\omega_m\right)-G_\beta^{-1}\left(\mathrm{i}\omega_m+\mathrm{i}\Omega_n\right)}-\frac{1}{\beta}\sum_{\mathrm{i}\omega_m}\frac{G_\beta\left(\mathrm{i}\omega_m\right)}{G_\alpha^{-1}\left(\mathrm{i}\omega_m-\mathrm{i}\Omega_n\right)-G_\beta^{-1}\left(\mathrm{i}\omega_m\right)}\;.$$

$$(3.121)$$

The first Green's function in the numerator in (3.120) gives rise to the spurious poles. We can remove them by shifting the summation just like in (3.119). The denominator of the result (3.121) still depends on $\mathrm{i}\omega_m$ – albeit only via self-energy and hybridization. Numerical tests for the shifted expressions, however, still show poles in the upper complex plane. Therefore, we have to resort to the Padé approximant method.

3.1.9.1. Padé Approximants

Instead of trying to repair the expressions to make them analytic in the upper half-plane we construct a function $\mathcal{F}_N^{\mathcal{P}}(z)$ which is analytic in this half-plane and coincides with $\mathcal{C}^{\mathrm{M}}\left(\mathrm{i}\omega_n\right)=c_n$ on a finite set of N Matsubara frequencies. We define the corresponding set of tuples $\mathcal{M}=\left\{\left(\mathrm{i}\omega_n,c_n\right)\right\}_{n=0}^{N-1}$. For $N\to\infty$ we would obtain the exact result $\mathcal{F}(z)$ according to the aforementioned theorem.

To construct $\mathcal{F}_N^{\mathcal{P}}(z)$ we use the Padé method. It is based on the assumption that we can express $\mathcal{F}_N^{\mathcal{P}}(z)$ as a rational polynomial or a terminating continued fraction. For the technical realization there exist several classes of Padé schemes. The probably most often used Padé method is Thiele's Reciprocal Difference Method [94, 95]. It represents a class where given the N tuples we directly evaluate $\mathcal{F}_N^{\mathcal{P}}(z)$ for each z individually in terms of continued fractions.

We rely on another method, representing a second class of Padé schemes, which give the coefficients of the continued fractions or rational polynomials instead of implicitly constructing and directly evaluating them. Thus, we obtain $\mathcal{F}_N^{\mathcal{P}}(z)$ as a function. More

specifically, we employ a method by Beach, Gooding and Marsiglio [96] which uses ratios of polynomials. Therefore, we cast $\mathcal{F}_N^{\mathcal{P}}(z)$ as

$$\mathcal{F}_N^{\mathcal{P}}(z) = \frac{P_N(z)}{Q_N(z)} \ . \tag{3.122}$$

Usually we know the asymptotic behavior of $\mathcal{C}^{\mathrm{M}}\left(\mathrm{i}\omega_n\right)$ and can directly adjust the orders of the polynomials (P_N, Q_N) accordingly. In this work we have Green's functions decaying as $1/z$ and dynamical correlation functions of single-body operators which decay as $1/z^2$. Consequently, we make the ansatz with polynomials (P_N, Q_N) of order $(s-1, s)$, $(s-1, s+1)$, respectively. s is given by the integer division $s = \lfloor N/2 \rfloor$. In the following we will first present the method for the $1/z$ Green's function case and then extend it to susceptibilities.

For Green's functions we need an even number $N = 2s$ and expand (3.122) as

$$\mathcal{F}_N^{\mathcal{P}}(z) = \frac{p_0 + p_1 z + \cdots + p_{s-1} z^{s-1}}{q_0 + q_1 z + \cdots + q_{s-1} z^{s-1} + z^s} \ . \tag{3.123}$$

To determine the N coefficients p_i and q_i we set

$$\mathcal{F}_s^{\mathcal{P}}\left(\mathrm{i}\omega_n\right) = c_n \qquad \forall\ 2s \text{ tuples } \left(\mathrm{i}\omega_n, c_n\right) \ . \tag{3.124}$$

With the definition

$$\boldsymbol{\varphi} = \begin{bmatrix} \boldsymbol{p} \\ \boldsymbol{q} \end{bmatrix} \quad \text{and} \quad \boldsymbol{Z} = \begin{bmatrix} z^0 \\ z^1 \\ \vdots \\ z^{s-1} \end{bmatrix} , \tag{3.125}$$

where $\boldsymbol{p}$ and $\boldsymbol{q}$ are s dimensional column vectors of the coefficients q_i, p_i, respectively, and $\boldsymbol{Z}$ is a vector of powers of some complex number z, we can rephrase (3.124) as a system of $N = 2s$ linear equations. For each $z = \mathrm{i}\omega_n$ we have

$$\left(\boldsymbol{q} \cdot \boldsymbol{Z} + z^s\right) \mathcal{F}_s^{\mathcal{P}}(z) = \boldsymbol{p} \cdot \boldsymbol{Z} \ . \tag{3.126}$$

In matrix form (3.126) reads

$$\tilde{\mathcal{F}} = M \boldsymbol{\varphi} \ , \tag{3.127}$$

where

$$\tilde{\mathcal{F}} = \begin{bmatrix} c_0 \left(\mathrm{i}\omega_1\right)^s \\ c_1 \left(\mathrm{i}\omega_2\right)^s \\ \vdots \\ c_{2s-1} \left(\mathrm{i}\omega_{2s}\right)^s \end{bmatrix} \tag{3.128}$$

and

$$M = \begin{pmatrix} 1 & \left(\mathrm{i}\omega_1\right) & \left(\mathrm{i}\omega_1\right)^2 & \dots & \left(\mathrm{i}\omega_1\right)^{s-1} & -c_0 & -c_0\left(\mathrm{i}\omega_1\right) & \dots & -c_0\left(\mathrm{i}\omega_1\right)^{s-1} \\ 1 & \left(\mathrm{i}\omega_2\right) & \left(\mathrm{i}\omega_2\right)^2 & \dots & \left(\mathrm{i}\omega_2\right)^{s-1} & -c_1 & -c_1\left(\mathrm{i}\omega_2\right) & \dots & -c_1\left(\mathrm{i}\omega_2\right)^{s-1} \\ \vdots & & & & & & & & \vdots \\ 1 & \left(\mathrm{i}\omega_{2s}\right) & \left(\mathrm{i}\omega_{2s}\right)^2 & \dots & \left(\mathrm{i}\omega_{2s}\right)^{s-1} & -c_{2s-1} & -c_{2s-1}\left(\mathrm{i}\omega_{2s}\right) & \dots & -c_{2s-1}\left(\mathrm{i}\omega_{2s}\right)^{s-1} \end{pmatrix} \ . \tag{3.129}$$

Hence, we obtain the coefficients q_i, p_i by matrix inversion

$$\mathbf{qp} = M^{-1}\tilde{\mathcal{F}} \tag{3.130}$$

and finally

$$\mathcal{F}_s^{\mathcal{P}}(z) = \frac{\boldsymbol{pZ}}{\boldsymbol{qZ} + z^s} \ . \tag{3.131}$$

The Padé kernel M consists of elements with very different moduli which usually becomes a problem in numerical calculations. To see this, we consider functions $\mathcal{C}^{\mathrm{M}}(\mathrm{i}\omega_n)$ which asymptotically decay with $1/(\mathrm{i}\omega_n)$. Assume that their behaviour roughly resembles $1/(\mathrm{i}\omega_n)$ for all $\mathrm{i}\omega_n$. In that case the ratio of the largest to the smallest element of M is of the order

$$\zeta = \omega_{2s}^s = \left[\frac{\pi}{\beta}(4s - 1)\right]^s \ . \tag{3.132}$$

For the matrix inversion to work reliably we need a numerical range of about ζ^2 which amounts to

$$\mathrm{dps} = 2\log_{10}(\zeta) = 2s\log_{10}((4s-1)\pi/\beta) \tag{3.133}$$

decimal places (the binary precision is roughly given by $3.33 \cdot \mathrm{dps}$). Hence, double precision is clearly not enough providing only 15 decimal places. Therefore, we perform the calculations with arbitrary precision usually using $\mathrm{dps} = 250$.

Green's functions As an example let us apply the Padé method to a Green's function of the two-dimensional Hubbard model. The calculations have been performed with an exact diagonalization impurity solver in DMFT (see next section), which gives direct access to the Lehmann representation. Therefore, we can easily calculate the exact results on both, the Matsubara and real axis. To perform the convergence tests we evaluate the exact expression on the Matsubara frequencies and perform a Padé analytic continuation on the real axis for different number of tuples $(\mathrm{i}\omega_n, c_n)$, where for the $2s$ tuples we choose the first $2s$ fermionic Matsubara frequencies. Figure 3.5 gives the results. The black curve denotes the exact result from exact diagonalization, the colored the Padé approximants. Overall, the Padé approximants work well. Convergence is best for the region around the Fermi level. Already for $2s = 8$ this region is reproduced well. For features at higher frequencies more tuples are needed. For a good approximation $\mathcal{F}_s^{\mathcal{P}}(z)$ and $\mathcal{C}^{\mathrm{M}}(z)$ should have the same number of poles. If the denominator polynomial Q_N has more roots than there are poles in $\mathcal{C}^{\mathrm{M}}(\mathrm{i}\omega_n)$, the additional ones need to be compensated by roots of the numerator P_N. This compensation is, however, not ensured by the method and may lead to spurious poles. If these poles are close enough to the real axis they show as erroneous features in the spectral functions. An example of this behavior is seen for $N = 32$ where the Green's function seems to violate causality, i.e. there is a region of negative spectral weight or positive imaginary part of the Green's function.

For values of $N \geq 128$ the approximation can be deemed converged. Small but stable deviations between the converged Padé and the exact curve are, however, clearly evident.
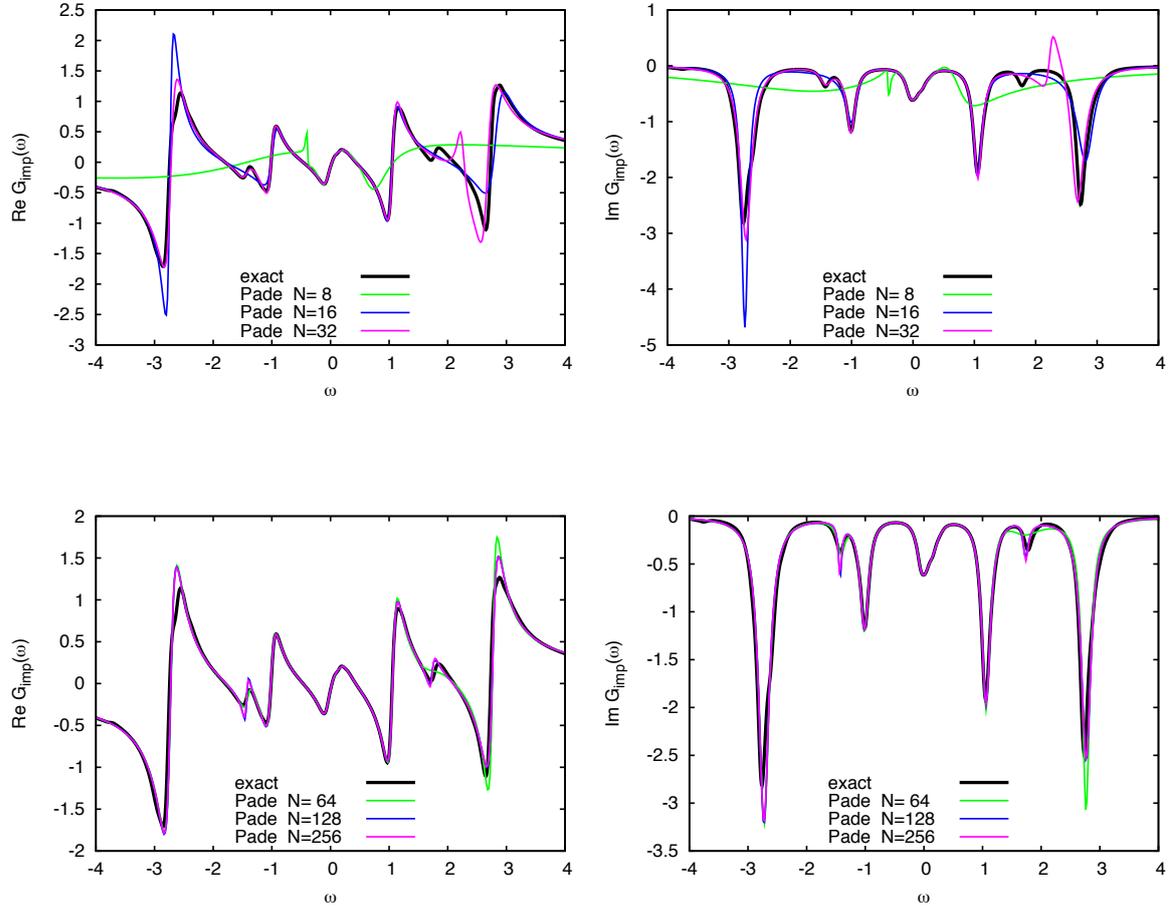
Figure 3.5.: Padé approximants convergence study for the DMFT-impurity Green's function of a 2-dimensional Hubbard model ($U = 4.2$, half-filling, $t = 0.43$, $t' = 0.3t$, $N_b = 4$) for increasing numbers of Matsubara frequencies ($\eta = 0.08$). The real parts are in the left, the imaginary parts in the right column. The black line denotes the exact, the colored lines the Padé approximants. The low energy region around $\omega = 0$ converges first. Already for $N = 8$ the first peak is well resolved. For $N = 32$ we have a region with unphysical negative spectral weight (pos. imaginary part) which however vanishes for higher N. The second row gives the results for higher N which are quite well converged.
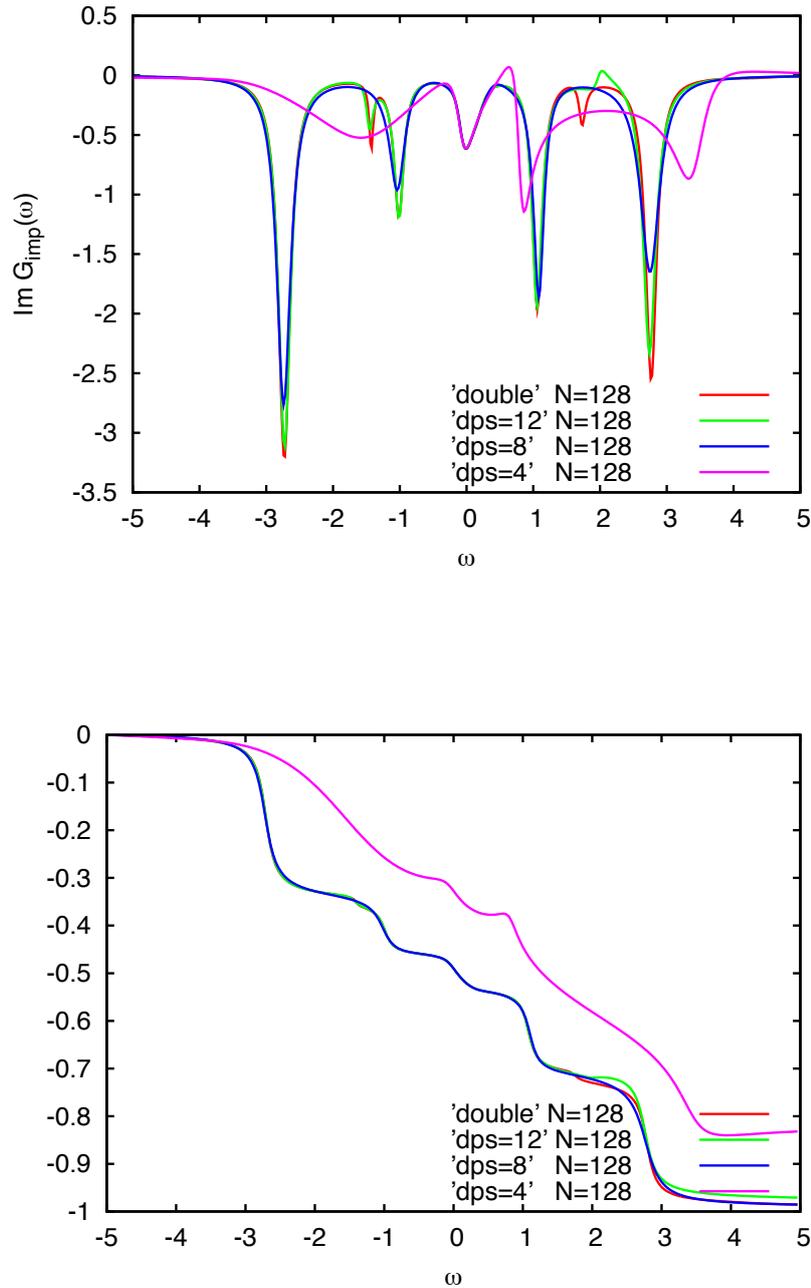
Figure 3.6.: Padé approximants ($2s = 128$) dependence on the accuracy of the input data ($\eta = 0.08$). Example data for an impurity Green's function (upper plot) of a 2-dimensional Hubbard model ($U = 4.2$, half-filling, $t = 0.43$, $t' = 0.3t$, $N_b = 4$) truncated after 4, 8, 12 digits and for double precision (red). The lower plot gives the integral over the imaginary part of the Green's function, showing that the spectral weights are conserved despite the deviations.

While the Padé code operates at arbitrarily high precision this is not true for the exact diagonalization solver which only provides double precision accuracy. Hence, the input data for Padé is inaccurate – in the best case starting from the 15th digit. By artificially truncating the data we can study the effect. The upper plot of figure 3.6 shows the results. For only 4 decimal places (magenta curve) again only the peak at the Fermi energy converges. With 8 we get roughly the correct result, however, we clearly miss peaks. Increasing to 12 decimal places gives more structure but also an unphysical peak with negative spectral weight. Comparing the three curves with dps > 4 and neglecting the lack of poles, we see that the peaks for smaller accuracy are not as high. To check if the spectral weight of the peaks, which captures the physics, is the same, we provide the integrated negative spectral function in the lower plot of figure 3.6. Apart from the negative spectral weight all the curves describe the same physics.

Hence, we conclude that the deviation of the Padé analytically continued curve from the exact result in 3.5 stems from inaccurate input data. Still the spectral weights are essentially converged, i.e. the peaks just might not quite have the correct width.

Susceptibilities   To account for the $1/z^2$ asymptotics we adjust the Padé ansatz

$$\mathcal{F}_N^{\mathcal{P}}(z) = \frac{p_0 + p_1 z + \cdots + p_{s-1} z^{s-1}}{q_0 + q_1 z + \cdots + q_{s-1} z^{s-1} + q_s z^s + z^{s+1}} \, , \qquad (3.134)$$

obviously needing an additional parameter q_s, i.e. an odd number of tuples N. $\boldsymbol{q}$ now becomes a vector of the dimension $s + 1$ and the matrix (3.129) also gains an additional row for $z = \mathrm{i}\omega_{2s+1}$ and an additional column with matrix elements $\left(-c_i \left(\mathrm{i}\omega_{i+1}\right)^s\right)_{i,2s} \quad \forall i = [0, 2s]$.

With these adjustments[2] we perform the analytic continuation of a spin-z correlation function. Figure 3.7 presents the outcome. The black line denotes the result from exact diagonalization and the colored lines the analytically continued Padé approximants. Two curves of like color denote the two branches $\mathrm{Im}\,\chi(\omega)$ and $-\mathrm{Im}\,\chi(-\omega)$. In theory both are identical since retarded/advanced susceptibilities are symmetric and anti-symmetric in the real and imaginary part, respectively.

In fact, for $N = 17$ this symmetry is respected. However, apart from the first pronounced peak no additional structure is resolved and we definitely need more tuples for the analytic continuation. For $N = 65$ and $N = 129$ we obtain more structure. The high-energy peak at about $\omega \approx 4.5$ is reproduced at least qualitatively. We also resolve more information in the intermediate energy range. This additional structure comes at a price of a loss in symmetry.

On the Matsubara axis $\chi(\mathrm{i}\omega)$ is a real-valued function. The imaginary part is theoretically zero by construction. Numerically, we, however, always find a finite value usually

---

[2] Without these adjustments using the Padé method for Green's functions we can also obtain sensible results. For small number of tuples N the correct version tends to give better results. For sufficiently large N, there is little difference in the continuation quality on the frequency range of interest.
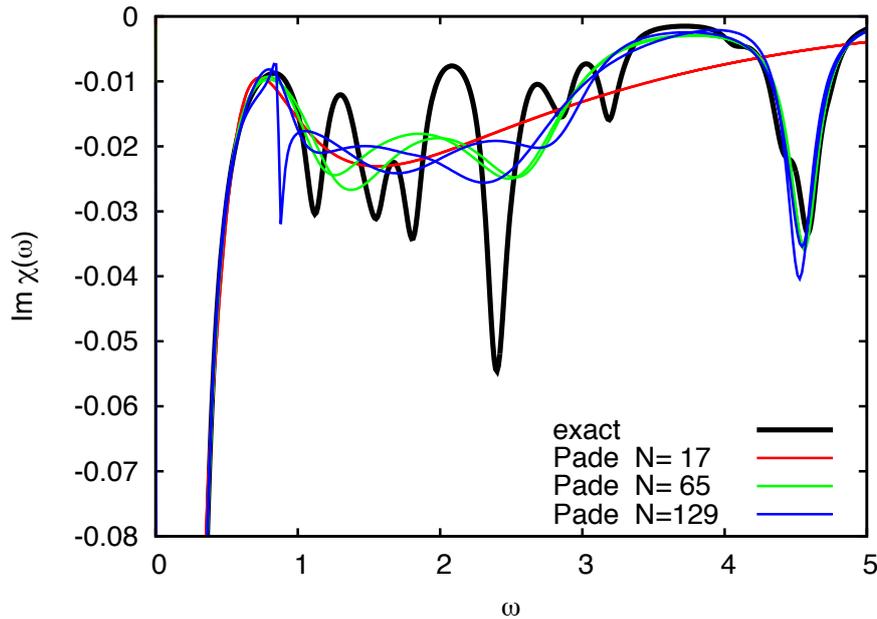
Figure 3.7.: Padé approximants based analytic continuation for the DMFT-impurity
spin-z susceptibility of a 2-dimensional Hubbard model ($U = 4.2$, half-
filling, $t = 0.43$, $t' = 0.3t$, $N_b = 4$) for $N = 17, 65, 129$ tuples ($\eta =
0.08$). The black line denotes the exact, the colored lines the Padé
approximants. Two curves of like color denote $\mathrm{Im}\,\chi(\omega)$ and $-\mathrm{Im}\,\chi(-\omega)$
which theoretically should be identical. For $N = 17$ the identity is
satisfied, however, no peaks apart from the first one are resolved. For
higher N we observe more structure at the expense of symmetry violation
(see text). The high-frequency peak ($\omega \approx 4.5$) converges relatively well.

being of the order of 10^{-15}. For a small number N of tuples (using the first N Matsubara
frequencies) the "zeros" in matrix M and vector $\tilde{\mathcal{F}}$ remain practical zeros. When N
becomes larger, higher frequencies $\mathrm{i}\omega_n$ are exponentiated with higher values of s. The
former practical "zeros" start to have an increasing influence in the inversion (3.130).
This leads to a loss in symmetry and to blurred peaks – especially in the less pronounced,
intermediate-energy peaks.

The double precision floating-point format (IEEE 754) as well as the arbitrary precision
format can encode zero exactly. Since $\mathrm{Im}\,\chi(\mathrm{i}\omega) = 0$ strictly, we exploit this knowledge
and set the imaginary part of the input data to zero. Figure 3.8 shows the corresponding
susceptibilities. Indeed, we find the symmetry retained and a higher-quality resolution
of the intermediate-energy peak structure. We also observe that $N = 65$ gives superior
results to $N = 129$. Hence, using more tuples does not generally make the results better
as error propagation of the inaccurate input data increasingly takes place.

As long as the input data is sufficiently accurate the Padé method can provide a
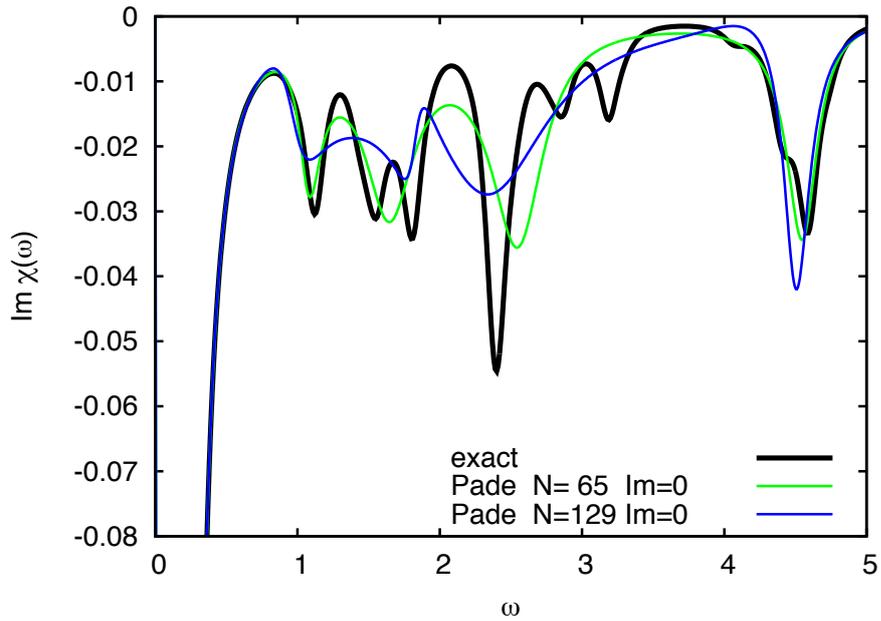
Figure 3.8.: Padé approximants based analytic continuation with $\operatorname{Im}\chi\left(i\omega_n\right)$ explicitly set to zero for the DMFT-impurity spin-z susceptibility of a 2-dimensional Hubbard model ($U = 4.2$, half-filling, $t = 0.43$, $t' = 0.3t$, $N_b = 4$) for $N = 17, 65, 129$ tuples ($\eta = 0.08$). The black line denotes the exact, the colored lines the Padé approximants. The symmetry $\operatorname{Im}\chi\left(\omega\right) = -\operatorname{Im}\chi\left(-\omega\right)$ is restored. Its violation (cf. 3.7) was caused by numerical zeros ($\approx 10^{-17}$) in $\operatorname{Im}\chi\left(i\omega_n\right)$. Moreover, we also observe an improved convergence in for the intermediate energy peak structures with $N = 65$ being superior to $N = 129$.

surprisingly good approximation $\mathcal{F}_N^{\mathcal{P}}(z)$ to $\mathcal{C}^{\mathrm{M}}\left(i\omega_n\right)$. $\mathcal{F}_N^{\mathcal{P}}(z)$ being analytic in the upper half-plane can be readily evaluated along the real axis providing access to real-frequency susceptibilities. Exploiting additional pieces of information about the input data and therewith increasing their accuracy can significantly improve the continuation.

For an application and further discussion of the method see section 3.3.4.

3.2. DMFT

The models used to treat strongly correlated systems are usually drastically simplified but still hard to solve due to their inherent many-body nature. One of the most powerful techniques to make the models solvable is Dynamical Mean-Field Theory (DMFT). It has been used extensively in the last approximately 20 years and gave rise to new insights in the field of strong correlations. In particular the paramagnetic metal-insulator transition within the Hubbard Model has been studied but also interesting correlation effects such as orbital ordering and the interplay between correlations and electron-phonon coupling.

The general idea of DMFT is to map the lattice model to an effective single impurity Anderson model (SIAM). That is a huge decrease in complexity. Even though there are still infinitely many degrees of freedom, the correlations that make the the solution of these systems infeasible, are only present on the impurity with a finite number of local degrees of freedom. The mapping is done self-consistently until the local properties of the original model and the auxiliary SIAM coincide. The situation is very similar to classical mean-field theories. Only now, the mean-field is frequency dependent.

For the sake of brevity we just give a brief introduction and derivation here. For a full review of the DMFT formalism refer to [97] or [98].

3.2.1. Derivation

To motivate DMFT we first consider the classical translationally invariant Ising model

$$H^{\mathrm{IM}} = -J \sum_{\langle ij \rangle} S_i S_j - B \sum_i S_i \, , \tag{3.135}$$

where $J > 0$ is the ferromagnetic coupling constant and B denotes an external magnetic field. In a mean-field treatment [99] all the equivalent sites are decoupled from one another and are subjected to an effective field B^{Weiss}, i.e.

$$H^{\mathrm{MFIM}} = -\sum_i B^{\mathrm{Weiss}} S_i \, . \tag{3.136}$$

The Weiss field contains the external field as well as the mean-field caused by the magnetic moment of all spins on other sites, i.e.

$$B_i^{\mathrm{Weiss}} = B^{\mathrm{Weiss}} = B + J \sum_{\substack{\langle ij \rangle \\ \text{neighbors}}} \langle S_j \rangle = B + JZm \, , \tag{3.137}$$

and due to the translation invariance it is independent of the site $B_i^{\mathrm{Weiss}} = B^{\mathrm{Weiss}}$. In the last term we introduced the coordination number Z and the expectation value of the magnetization $m = \langle S_i \rangle \, \forall i$. A simple calculation evaluating the thermal-expectation value $\langle S_i \rangle$ gives

$$m = \tanh(\beta B + \beta JZm) \, , \tag{3.138}$$

which is an implicit equation for m that has to be solved self-consistently. Hence, we replaced the lattice problem with an effective single-site problem.

It has been known for a long time that the results obtained using the Weiss mean-field theory become exact in the limit of $Z \to \infty$ [100]. For the energy and entropy per site to remain finite J has to be rescaled according to $J = J^*/Z$, where J^* is a constant independent of Z.

These ideas can be generalized to quantum many-body systems. The Hubbard model,

$$H^{\mathrm{HM}} = -t \sum_{\langle ij \rangle \sigma} \left(c_{i\sigma}^\dagger c_{j\sigma} + h.c. \right) + U \sum_i n_{i\uparrow} n_{i\downarrow} \;, \tag{3.139}$$

which we will take as an example, describes the interplay between kinetic and interaction energy. In the limit of $Z \to \infty$ (for a lattice this is equivalent to increasing the dimensionality) U remains constant since it only acts locally. For the kinetic term, however, this is not true and we have to scale the hopping in the kinetic energy to retain a still non-trivial model. For a hypercubic lattice with nearest neighbor hopping only, for instance, we have the dispersion relation

$$\varepsilon_{\boldsymbol{k}} = -2t \sum_{i=0}^{d-1} \cos(k_i) \;. \tag{3.140}$$

The bandwidth $W = 4dt$ increases proportionally with $Z = 2d$. For a generic $\boldsymbol{k}$ in the limit of infinite dimensions (3.140) represents an infinite sum over statistically independently distributed values. According to the central limit theorem the corresponding density of states becomes a Gaussian,

$$D\left(\epsilon\right) = \frac{1}{\sqrt{2\pi Z t^2}} \exp\left(-\frac{\epsilon^2}{2Z t^2} \right) \;. \tag{3.141}$$

Thus, the hopping has to be scaled as $t = t^*/\sqrt{Z}$ in order to have a finite and fixed second moment or variance of the spectrum $\langle \epsilon^2 \rangle = t^{*2}$, which takes the part of the infinite bandwidth W. This scaling applies also to other lattices and was the key insight of Metzner and Vollhardt [101].

In 1989 Müller-Hartmann [102] showed that the self-energy $\Sigma(\omega, \boldsymbol{k})$ loses its k-dependence in this limit. It becomes a purely local but still dynamical quantity $\Sigma(\omega)$. Hence, the local Green's function may be stated as

$$G^{\mathrm{loc}}\left(\omega\right) = \frac{1}{V_{\mathrm{BZ}}} \int_{\mathrm{BZ}} \mathrm{d}^d k \; \frac{1}{\omega + \mu - \varepsilon_k - \Sigma(\omega)} \;. \tag{3.142}$$

Introducing the density of states of the non-interacting system

$$D\left(\epsilon\right) = \frac{1}{V_{\mathrm{BZ}}} \int_{\mathrm{BZ}} \mathrm{d}^d k \; \delta\left(\epsilon - \varepsilon_k\right) \tag{3.143}$$

we can write the Brillouin zone integral into a one-dimensional integral over energies. Equation (3.142) becomes

$$G^{\mathrm{loc}}\left(\omega\right) = \int \mathrm{d}\epsilon \; \frac{D\left(\epsilon\right)}{\omega + \mu - \epsilon - \Sigma(\omega)} \;. \tag{3.144}$$

Introducing the Hilbert transform and its inverse

$$\tilde{D}(\zeta) = \int d\epsilon \, \frac{D(\epsilon)}{\zeta - \epsilon} \tag{3.145}$$

$$R\left[\tilde{D}(\zeta)\right] = \zeta \tag{3.146}$$

we can rewrite G^{loc} as

$$G^{\text{loc}}(\omega) = \tilde{D}(\omega + \mu - \Sigma(\omega)) \,. \tag{3.147}$$

From these ingredients Georges and Kotliar [103], Janiš and Vollhardt [104] and Jarrell [105] developed the "dynamical mean-field theory" in 1992. Following this theory it is possible to single out one lattice site and simulate the effect of the neighbors by coupling it to a dynamic bath, i.e. the model is mapped onto a single impurity Anderson Model (SIAM). In finite dimensions we can use this procedure as an approximation.

The SIAM – or more precisely the bath – has to be chosen such that the (Anderson) impurity Green's function G^{imp} matches the local Green's function of the original lattice G^{loc}. To that end, we write the Green's function in terms of a functional integral over Grassmann variables ϕ and ϕ^* giving

$$G = \frac{1}{\mathcal{Z}_S} \int \mathcal{D}[\phi] \, \mathcal{D}[\phi^*] \, \phi\phi^* \exp\left(-S[\phi, \phi^*, G_b]\right) \,, \tag{3.148}$$

where S is the action on the impurity

$$S[\phi, \phi^*, G_b] = -\int_0^\beta \int_0^{\beta'} d\tau d\tau' \sum_\sigma \phi^*(\tau) G_b^{-1}(\tau - \tau') \phi(\tau') - U \int d\tau \phi_\uparrow^*(\tau)\phi_\uparrow(\tau)\phi_\downarrow^*(\tau)\phi_\downarrow(\tau) \tag{3.149}$$

and $\mathcal{Z}_S$ is the partition function

$$\mathcal{Z}_S = \int \mathcal{D}[\phi] \, \mathcal{D}[\phi^*] \exp\left(-S[\phi, \phi^*, G_b]\right) \,. \tag{3.150}$$

Here G_b plays the role of the Weiss field. It is the non-interacting Green's function of the SIAM. Hence, it completely determines the bath. Intuitively, it describes the creation of a particle on the impurity at time τ and its annihilation at time τ'. Creation and annihilation here should be interpreted as hopping from the bath to the impurity and back.

In analogy to (3.138) equation (3.148) needs to be solved self-consistently.

3.2.2. Self-Consistency Loop in the Hamiltonian Formalism

Equation (3.148) is given in the path integral formalism. For actual calculations using Hamiltonian based methods such as exact diagonalization (ED), dynamical matrix renormalization group (DMRG) [106, 107], Lanczos, or numerical renormalization group (NRG) [108] we need to rewrite (3.148)ff. in a Hamiltonian formalism. To account for the dynamics of the bath we introduce auxiliary degrees of freedom – the bath sites. For

practical calculations in this formalism we are obviously restricted to a finite number of bath sites, whereas in path integral-based methods implicitly infinitely many bath sites are treated.

The general single impurity Anderson model (SIAM) Hamiltonian reads

$$H^{\text{gSIAM}}(\mu) = \sum_{ij\sigma} t^{\text{b}}_{ij\sigma} c^{\dagger}_{i\sigma} c_{j\sigma} + \sum_{i\sigma} \tilde{V}_{i\sigma} \left(f^{\dagger}_{\sigma} c_{i\sigma} + c^{\dagger}_{i\sigma} f_{\sigma} \right) + H^{\text{imp}}(\mu) \,, \qquad (3.151)$$

where the first term denotes the kinetic energy within the (infinite) bath with hopping matrix $t^{\text{b}}_{ij\sigma}$ and $c^{(\dagger)}_{l\sigma}$ being the particle operators of the bath electrons. The second term describes the hybridization of the impurity and the bath with $V_{l\sigma}$ being the hybridization amplitude and $f^{(\dagger)}_{\sigma}$ the impurity particle operators. The (many-body) physics of the impurity is captured in the last term

$$H^{\text{imp}}(\mu) = (\epsilon_{f\uparrow} - \mu)\, n^{f}_{\uparrow} + (\epsilon_{f\downarrow} - \mu)\, n^{f}_{\downarrow} + U n^{f}_{\uparrow} n^{f}_{\downarrow} \,. \qquad (3.152)$$

U denotes the Hubbard-U for the impurity. It coincides with the U of the lattice model. μ is adjusted to reproduce the lattice occupation of a site on the impurity.

This form of the SIAM can be further simplified when diagonalizing the bath-hopping matrix $t^{\text{b}}_{ij\sigma}$. Let $\epsilon_{l\sigma}$ be the eigenenergies of $t^{\text{b}}_{ij\sigma}$ and $\zeta_{l\sigma}$ the corresponding eigenvectors. When transforming the hybridization amplitudes to the eigenbasis of the bath, i.e.

$$V_{l\sigma} = \sum_{i} \tilde{V}_{i\sigma} \zeta_{l\sigma i} \,, \qquad (3.153)$$

we have effectively diagonalized the bath. The former inter-site hopping within the bath is now contained in the new hybridization parameters. Consequently, we can rewrite (3.151) w.l.o.g. as

$$H^{\text{SIAM}}(\mu) = \sum_{l\sigma} \varepsilon_{l\sigma} c^{\dagger}_{l\sigma} c_{l\sigma} + \sum_{l\sigma} V_{l\sigma} \left(f^{\dagger}_{\sigma} c_{l\sigma} + c^{\dagger}_{l\sigma} f_{\sigma} \right) + H^{\text{imp}}(\mu) \,, \qquad (3.154)$$

which describes a star geometry, i.e. each bath site is connected only to the impurity. From now on we drop the spin-index and focus on paramagnetic systems.

Having diagonalized the bath we use the inversion-by-partitioning method (see appendix G) on

$$\hat{G}_b = \frac{1}{\omega - H^{\text{SIAM0}}} \qquad (3.155)$$

with the single particle part of the SIAM Hamiltonian,

$$H^{\text{SIAM0}} = \begin{pmatrix} \epsilon_f - \mu & V_1 & V_2 & V_3 & \dots \\ \hline V_1 & \varepsilon_1 & & & \\ V_2 & & \varepsilon_2 & & \\ V_3 & & & \varepsilon_3 & \\ \vdots & & & & \ddots \end{pmatrix} \,, \qquad (3.156)$$
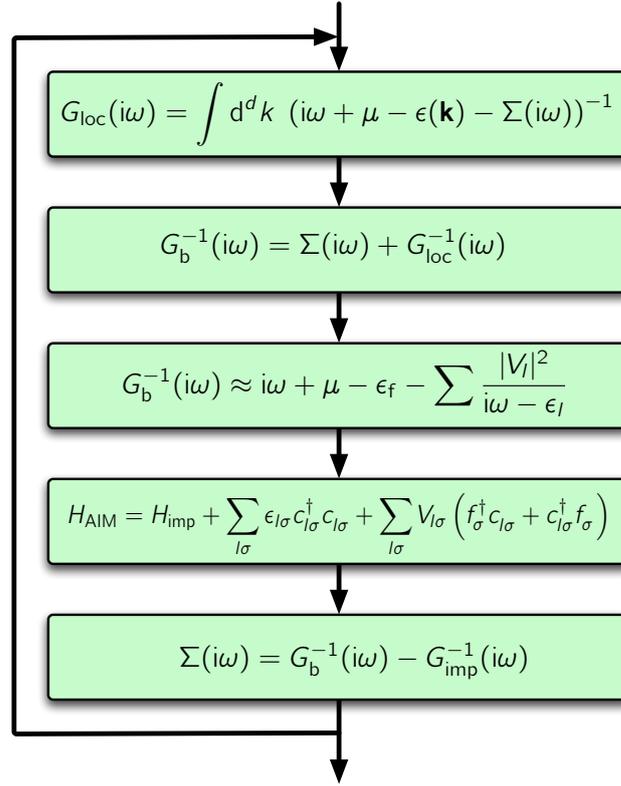
Figure 3.9.: DMFT flow diagram: We start from an arbitrary self-energy Σ; evaluate the lattice G^{loc}, from which we infer the bath Green's function G_b. It defines the associated impurity model, whose solution gives a new self-energy. We iterate until self-consistency is reached.

to directly obtain the free Green's function. It is the bath Green's function G_b from above and reads,

$$G_b^{-1}(\omega) = \omega + \mu - \epsilon_f - \sum_l \frac{|V_{l\sigma}|^2}{\omega - \epsilon_{l\sigma}} \ . \tag{3.157}$$

The last term is called hybridization function

$$\Delta\left(\omega\right) = \sum \frac{|V_l|^2}{\omega - \epsilon_l} \ . \tag{3.158}$$

It contains all bath parameters.

Now we have all ingredients for solving the problem iteratively. Figure 3.9 gives the flow diagram of the DMFT self-consistency loop. Conceptually we start from some arbitrarily chosen self-energy, for instance $\Sigma = 0$, and evaluate the local Green's function of the lattice, equation (3.142). With Dyson's equation

$$G_b^{-1}(\omega) = \Sigma(\omega) + \left[G^{\mathrm{loc}}(\omega)\right]^{-1} \ , \tag{3.159}$$

we obtain the new bath Green's function G_b (Weiss field) which determines the SIAM Hamiltonian. With a Hamiltonian-based impurity solver we diagonalize the Hamiltonian and evaluate the impurity Green's function G^{imp}. Using Dyson's equation again

$$\Sigma(\omega) = G_b^{-1}(\omega) - \left[G^{\text{imp}}(\omega)\right]^{-1} \; , \tag{3.160}$$

we obtain a new self-energy. The loop restarts unless self-consistency is reached, i.e. $G^{\text{imp}} = G^{\text{loc}}$. Technically, however, we usually start from some bath parameters instead of a special choice of the self-energy.

   In the self-consistency loop the information about the physical system we want to study enters via the local Green's function G^{loc}. For the Hubbard model the input that characterizes the system is the dispersion relation ϵ_k or, in the many-band case, the single-particle tight-binding Hamiltonian.

   Using the inverse Hilbert transform instead of the Brillouin zone integrals we have a formal shortcut in the self-consistency loop. From the impurity Green's function we can directly obtain the Weiss field using

$$G_b^{-1}(\omega) = \omega + \mu + G^{-1}(\omega) - R\left[G(\omega)\right] \; . \tag{3.161}$$

This equation becomes practical in cases where the inverse of the Hilbert transform is known analytically. As we will see this is the case for the Bethe lattice in infinite dimensions.

3.2.3. Exact Diagonalization as Impurity Solver

For this project we use an exact diagonalization (ED) impurity solver. ED provides exact solutions with full information on clusters of a finite and in practice quite small number of sites – one of them being the impurity. Since there are only N_b bath sites we have to truncate the sum in (3.158). This restricts the accuracy of the hybridization and hence the bath Green's function. It is practical to think of this restriction as a projection of the real hybridization function on a function subspace spanned by finite sums of the form (3.158). In the limit of $N_b \to \infty$ we recover the correct G_b. For a finite number of bath sites it is in general impossible to strictly satisfy the self-consistency condition $G^{\text{imp}} = G^{\text{loc}}$. In practice we therefore consider the system converged, when the finite number of bath (or Anderson) parameters, i.e. the on-site energies $\epsilon_{l\sigma}$ and hybridization amplitudes V_l, no longer change from iteration to iteration. Figures 3.10 and 3.11 show a comparison of G^{imp} to G^{loc} of a 2-dimensional half-filled Hubbard model (see captions for details). On the real axis we clearly see the differences (first row of 3.10) between both Green's functions. We can think of G^{loc} as a broadened version of G^{imp} where the mollifier is roughly the density of states. On the Matsubara axis agreement seems to be very good (second row). However, the difference plot $\Delta G = G^{\text{imp}} - G^{\text{loc}}$ reveals the differences (see figure 3.11). We clearly observe that the larger N_b the better the (theoretical) self-consistency condition $G^{\text{imp}} = G^{\text{loc}}$ is satisfied. A finite number of bath
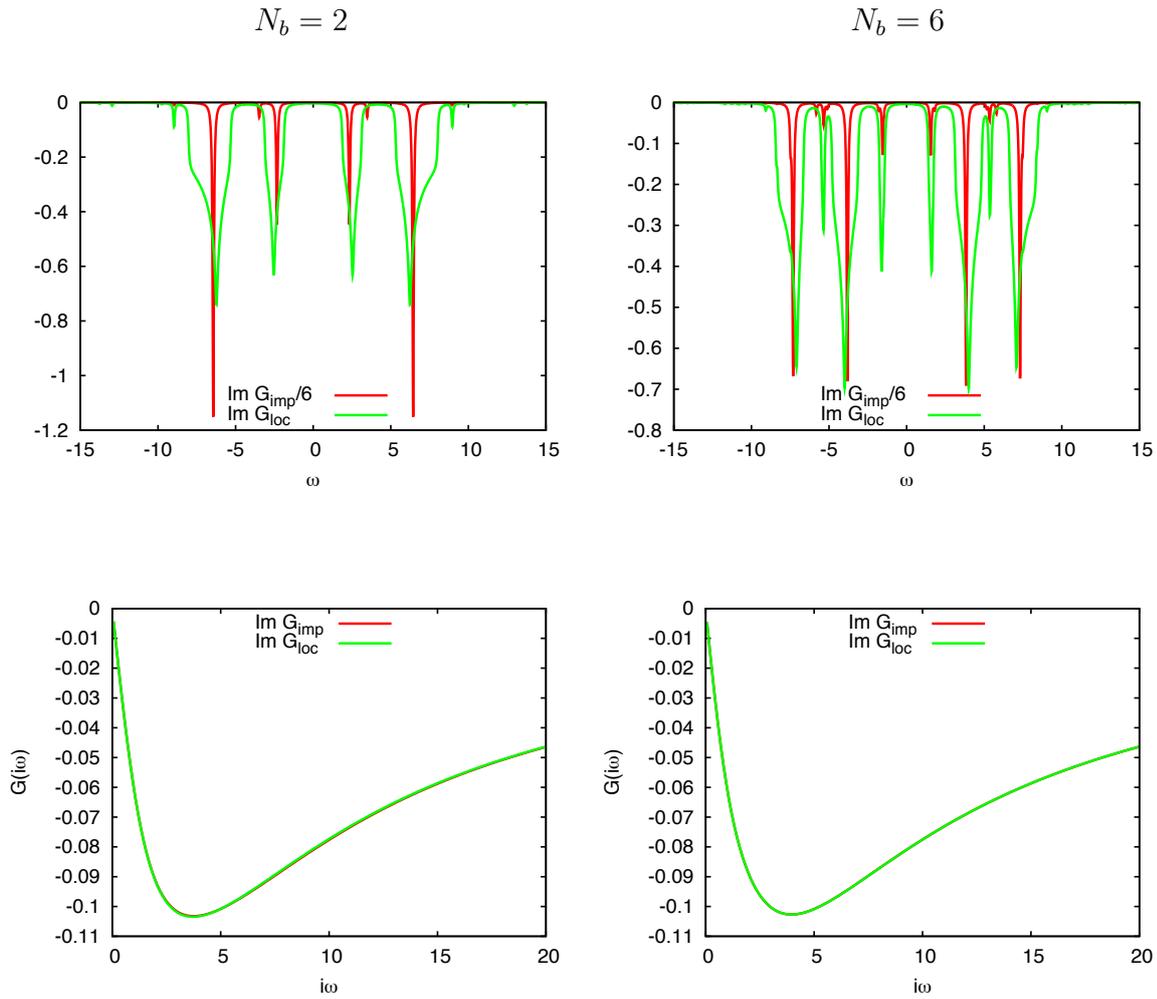
Figure 3.10.: Impurity (red) and lattice (green) Green's function on real (upper row) and Matsubara frequencies (lower row) for 2-dimensional half-filled Hubbard model with next-neighbor hopping only ($\epsilon_{\mathrm{imp}} = 0.0$, $U = 10.6$, $\mu = U/2$, $t = 1$, $\beta = 50$, $\mathrm{num}_k = 64$) mapped on a SIAM with $N_b = 2$ (left column) and $N_b = 6$ (right column). The impurity Green's functions on the real-frequency axis have been scaled for clarity by a factor 6. Roughly speaking we can regard the local Green's function as an impurity Green's function broadened with the density of states. We observe that the self-consistency condition is violated but is better fulfilled the larger N_b. On the Matsubara axis agreement appears to be better. The differences show, however, when looking at the difference $\Delta G = G^{\mathrm{imp}} - G^{\mathrm{loc}}$ plotted in figure 3.11.
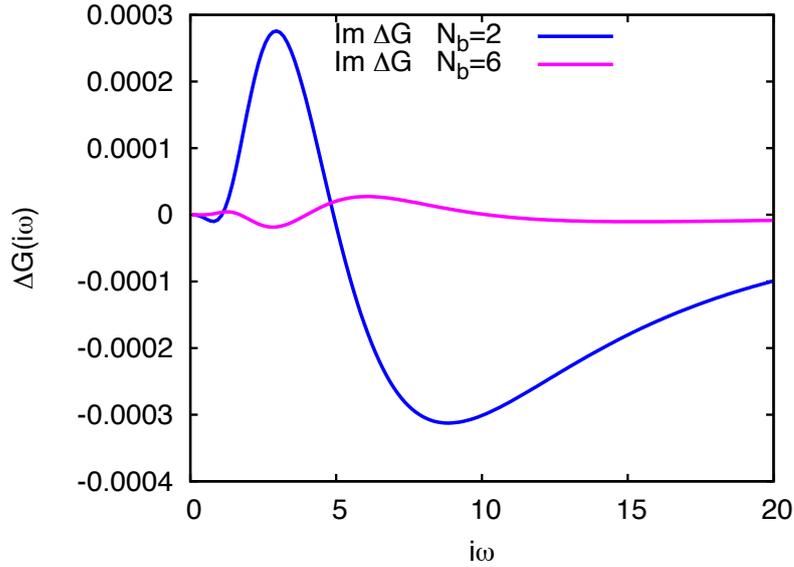
Figure 3.11.: Difference of local and impurity Green's function $\Delta G = G^{\mathrm{imp}} - G^{\mathrm{loc}}$ for $N_b = 2$ (blue) and $N_b = 6$ (magenta) for a 2-dimensional half-filled Hubbard model with next-neighbor hopping only ($\epsilon_{\mathrm{imp}} = 0.0$, $U = 10.6$, $\mu = U/2$, $t = 1$, $\beta = 50$, $\mathrm{num}_k = 64$). This plot reveals the differences apparent in the real frequency representation (see 3.10) but hidden when comparing the Green's functions on the Matsubara frequencies. Obviously, the larger the bath the better the agreement.

sites N_b is the only additional approximation of ED to the DMFT scheme. For small N_b it is therefore of utmost importance to choose the bath parameters well.

After having obtained G_b in each iteration (second step in figure 3.9) we extract the bath parameters. To that end, we isolate the hybridization function $\Delta\,(\mathrm{i}\omega)$ from $G_b\,(\mathrm{i}\omega)$

$$\Delta\,(\mathrm{i}\omega) = \mathrm{i}\omega + \mu - G_b^{-1}\,(\mathrm{i}\omega) \tag{3.162}$$

and fit the result to finite bath version of equation (3.158)

$$\Delta_p\,(\mathrm{i}\omega) = \sum_{l=1}^{N_b} \frac{V_l^2}{\mathrm{i}\omega - \epsilon_l}\ . \tag{3.163}$$

This determines the bath parameters $p = \{V_l, \epsilon_l\}_{l=1}^{N_b}$ and therefore the SIAM.

We perform the fit along the Matsubara axis. The hybridization function obviously has its poles along the real axis which renders the function very spiky and hard to fit along this axis. Using the Matsubara representation instead the hybridization $\Delta\,(\mathrm{i}\omega)$ behaves very smoothly which is favourable for the fit. For illustration figure 3.12 shows the Matsubara in contrast to the real frequency Δ.
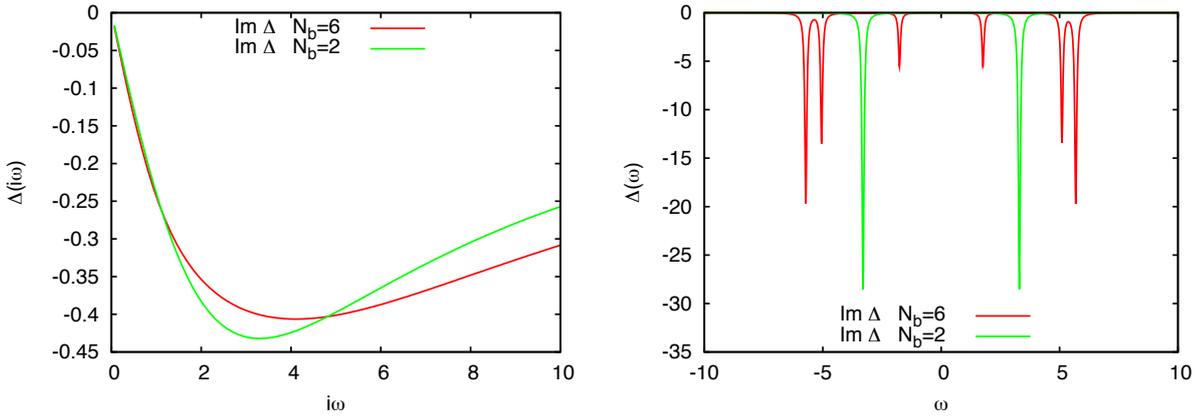
Figure 3.12.: Hybridization function $\Delta(z)$ for 2-dimensional Hubbard model with next-neighbor hopping only (ϵ_{imp}, $U = 10.6$, $\mu = U/2$, $t = 1$, $\beta = 50$, $\text{num}_k = 64$) on Matsubara (left plot) and real axis (right plot) for 7 (red) an 3 sites (green). Obviously the Matsubara version is smoother and favourable to fitting. For larger baths there is significantly more structure to Δ.

Technically the fitting is done employing the conjugate gradients method to find the minimum of the function

$$f_p = \frac{1}{N_{\text{i}\omega}} \sum_{\text{i}\omega_n}^{\text{i}\omega_{\text{max}}} \mathcal{W}\left(\text{i}\omega_n\right) \left|\Delta\left(\text{i}\omega\right) - \Delta_p\left(\text{i}\omega\right)\right|, \tag{3.164}$$

where $N_{\text{i}\omega}$ denotes the number of Matsubara frequencies we use for the fit $[\omega_1, \omega_{\text{max}}]$. $\mathcal{W}$ is a weight function – usually $\mathcal{W}(\text{i}\omega) = 1/(\text{i}\omega_n)^\alpha$. It determines which part of the hybridization function we prefer to fit. For the low/high energy domain we choose higher, lower values of α.

Mainly fitting large ω_n enforces a sum rule [109] which relates the hybridization of the impurity to the bath and the hopping in the physical lattice. To see this, we start from (3.160)

$$G_b^{-1}\left(\text{i}\omega\right) = \Sigma\left(\text{i}\omega\right) + \left\{\frac{1}{N_k} \sum_{\boldsymbol{k}} \left[\text{i}\omega + \mu - \epsilon_{\boldsymbol{k}} - \Sigma\left(\text{i}\omega\right)\right]^{-1}\right\}^{-1} \tag{3.165}$$

and expand it for $\omega \to \infty$ up to third order in $1/\text{i}\omega$. In so doing we neglect the ω dependency of Σ, which for high frequencies goes to zero. Comparing the result to (3.157) and neglecting the ϵ_l, since $\omega_n \gg \epsilon_l$, in the denominator of the hybridization function we obtain the sum rule

$$\sum_l V_l^2 = \frac{1}{N_k} \sum_k \epsilon_{\boldsymbol{k}}^2 = \sum_n Z_n t_n^2, \tag{3.166}$$

where n denotes the nth-nearest neighbor and Z_n and t_n give the coordination number and hopping amplitude, respectively. Intuitively that means that the overall hybridization strength of the impurity to the bath ($\sum_l V_l^2$) has to be consistent with the coupling of the sites among each other in the physical lattice ($\sum_n Z_n t_n^2$). Hence, essentially a single parameter is fixed. The low energy domain on the other hand puts more stress on the on-site energies of the bath. This is because the low energy domain is closer to the poles on the real axis. Thus, it gives the details of the SIAM. Especially for for small N_b this is important.

Table 3.1.: Sum rules for 2-dimensional Hubbard model with next-neighbor hopping only ($\epsilon_{\text{imp}} = 0$, $U = 10.6$, $\mu = U/2$, $t = 1$, $\beta = 50$, $\text{num}_k = 64$) for different values of α and N_b for otherwise fixed convergence criteria. For $\alpha = 1$ more weight is put on the hybridization parameters V_l when fitting. Hence, the V_l are consistently better compared to the results for $\alpha = 2$. For the ϵ_i the opposite is true. Their sum should be 0 due to particle-hole symmetry and half-filling (see figure 3.12). The larger the bath, however, the smaller the differences become. For stricter targets the results improve. α merely puts more weight on a certain energy domain.

sum rule	$\sum_l V_l^2 \overset{!}{=} 4$		$\sum_i \epsilon_i \overset{!}{=} 0$	
α	1	2	1	2
$N_b = 2$	3.4	2.8	1.4×10^{-4}	-2.2×10^{-6}
$N_b = 4$	3.9	3.8	9.6×10^{-3}	4.2×10^{-4}
$N_b = 6$	4.0	3.9	1.8×10^{-4}	1.7×10^{-4}

Table 3.1 gives example results for the sum rule in a 2-dimensional half-filled Hubbard model with next-neighbor hopping. According to (3.166) we expect $\sum_l V_l^2 = 4$. Half-filling and particle hole symmetry means that the energy spectrum of the bath sites should be symmetric around the chemical potential μ. Thus, $\sum_l \epsilon_l = 0$ should hold. Hence, we have a means to directly compare the effect of α on the energy and hybridization accuracy for otherwise fixed convergence criteria. From the table we indeed see that small α prefer the sum rule whereas larger α the bath on-site energies. The larger the bath the less important the choice of α becomes.

The difference f_p is a measure for the quality of the fit of $\Delta(\mathrm{i}\omega)$ with the Anderson parameters and thus of the ED approximation to DMFT. For an infinite bath the fit would be perfect, giving $f_p = 0$.

An alternative way to obtain the Anderson parameters is to use the Padé method described in section 3.1.9.1. Instead of applying the method to a Green's function we can also apply it to the hybridization function $\Delta(\mathrm{i}\omega)$ obtain the polynomials P_N, Q_N whose coefficients determine the coefficients of the equivalent continued fraction (see e.g. [94]). If these coefficients are real, which they should be when converged, then the continued fraction is positive definite. These kind of continued fractions are named J-fraction. They
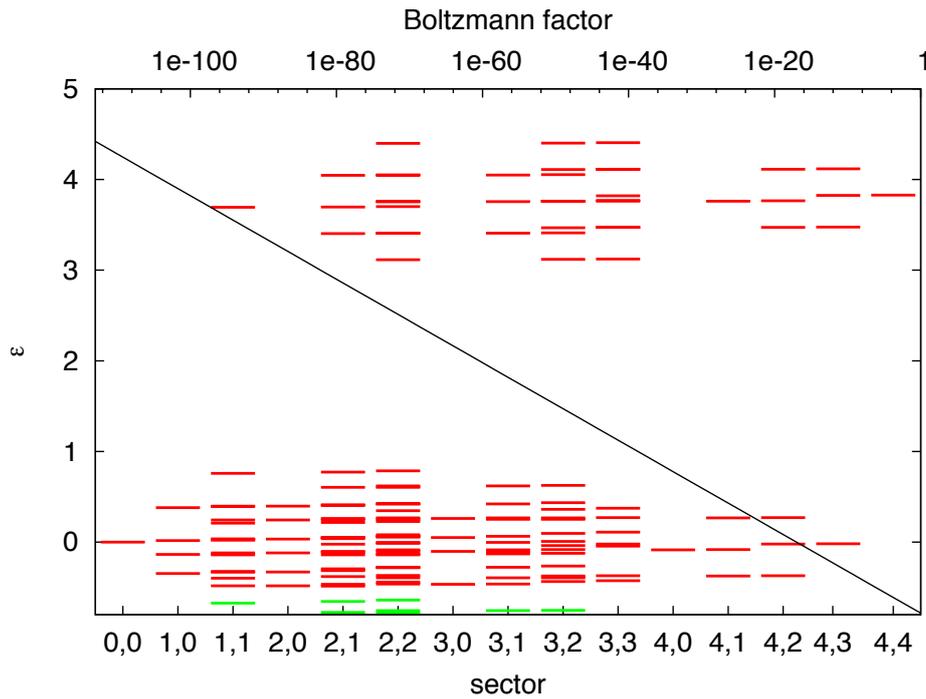
Figure 3.13.: 4-site SIAM spectrum of a 5-dimensional Periodic Anderson Model ($V = 0.2$, $t = 1/\sqrt{10}$, $U = 4$, $\mu = -0.14$, $\epsilon_f = 0.3$) in different sectors $N_\uparrow, N_\downarrow$ (x-axis). The black line gives the Boltzmann factor (see upper x-axis for tics and labels) for a given energy at $\beta = 50$. In the calculation for the Green's function only 'green' levels are taken into account (Boltzmann factor $> 10^{-4}$).

can be expressed as sums over simple poles [110, 111]

$$\Delta_p(z) = \sum_{l=0}^{N_b} \frac{V_l^2}{z - \epsilon_l} \, , \tag{3.167}$$

giving, in principle, direct access to the parameters.

Having determined the parameters we build the SIAM Hamiltonian. Since it is particle conserving, $\left[H^{\mathrm{SIAM}}, N_\sigma\right] = 0$, we can divide its diagonalization in sectors of fixed $N_\uparrow, N_\downarrow$. For all possible combinations (often we can however exploit symmetries) of $N_x \in [0, N_s]$ we derive the Hamiltonian of the sector in matrix form and diagonalize it using standard means yielding the eigenvectors and eigenstates. From here we can directly evaluate the thermal impurity Green's function according to (3.56) and the new self-energy Σ. Often the sector ground states are energetically quite far from each other and we can reduce the computational demand by neglecting terms with low Boltzmann weight (see figures 3.13, 3.14).
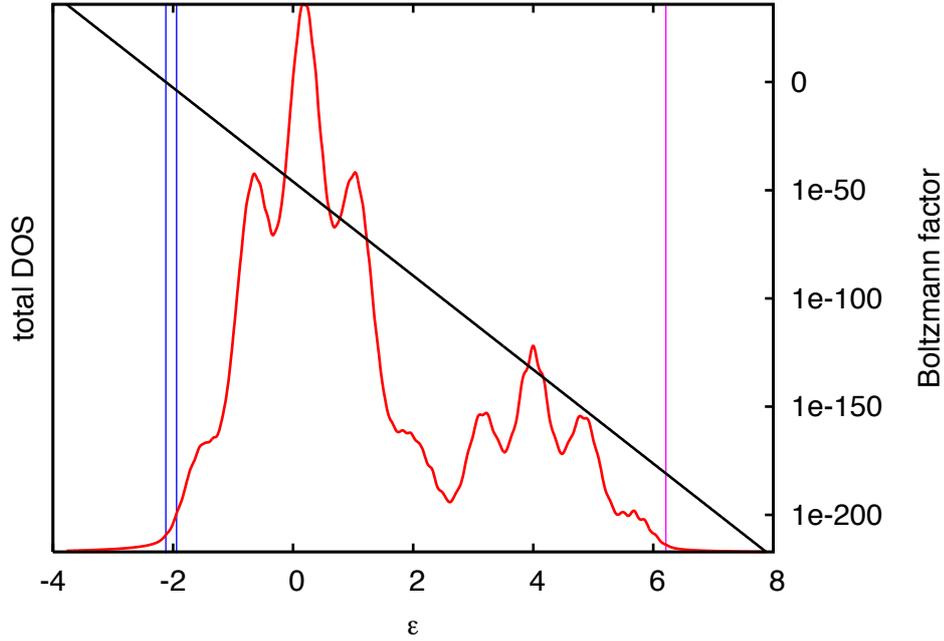
Figure 3.14.: 7-site SIAM many-body DOS of a 5-dimensional Periodic Anderson Model ($V = 0.2$, $t = 1/\sqrt{10}$, $U = 4$, $\mu = -0.14$, $\epsilon_f = 0.3$). The black line gives the Boltzmann factor (see right y-axis for tics and labels) for a given energy at $\beta = 50$. The two blue lines encase the window of states we take into account for the Green's functions (Boltzmann factor $> 10^{-4}$). The very left blue and red line give the ground states, highest state energy, respectively. (The weight below the ground state stems from the finite broadening ($\eta = 0.08$).)

3.2.4. Exact DMFT Limits

In general, DMFT gives an approximation to the local Green's function of the real lattice. However, in the free case, $U = 0$, and in the atomic limit the local Green's functions coincide with the impurity Green's functions and DMFT yields the exact, albeit trivial result.

Free limit   In the free limit, $U = 0$, the self-energy Σ is zero. Hence, the impurity Green's function coincides with the bath Green's function G_b, i.e. $G_{\mathrm{imp}} = G_b$. G^{loc} is just the non-interacting Green's function of the lattice $G^{\mathrm{loc}\,0}$ and independent of the bath.

Atomic limit   In the atomic limit, $t = 0$, there is no hopping in the lattice. From the sum rule (3.166) we see that this translates to no hybridization with the bath in the

SIAM. Hence, all physics is purely local. The integrand in G^{loc} does not depend on k and

$$G^{\text{loc}}(\omega) = \frac{1}{V_{\text{BZ}}} \int_{\text{BZ}} \mathrm{d}^d k \, \frac{1}{\omega + \mu - \varepsilon_k - \Sigma(\omega)} = \frac{1}{\omega + \mu - \varepsilon - \Sigma(\omega)} = G^{\text{imp}} \, . \qquad (3.168)$$

This model is easily solved since we just need to treat a single impurity Hamiltonian in a four dimensional Fock space. We choose $(|\rangle, |\uparrow\rangle, |\downarrow\rangle, |\uparrow\downarrow\rangle)$ as the basis and obtain the finite-temperature Hubbard-I Green's function

$$G(\mathrm{i}\omega_n) = \frac{1 - f}{\mathrm{i}\omega_n + \mu} + \frac{f}{\mathrm{i}\omega_n + \mu - U} \qquad (3.169)$$

with

$$f = \frac{e^{\beta\mu} + e^{\beta(2\mu - U)}}{1 + 2e^{\beta\mu} + e^{\beta(\mu - U)}} \, . \qquad (3.170)$$

3.2.5. Models

Hypercubic lattice   The DMFT method can be applied to different quantum many-body models. Each model is defined on a lattice in a certain dimension. Before we describe two of the most important models we briefly introduce two types of lattices, the hypercubic and the Bethe lattice. It is often advantageous to employ the density of states when calculating G^{loc} because an evaluation in terms of Brillouin zone integrals can be very costly. This is especially true for lattices in high-dimensions.

For a hyper-cubic lattice with next-neighbor hopping only (dispersion relation (3.140)) figure 3.15 gives the density of states for increasing dimension. We can easily identify van-Hove singularities up to about $d = 4$. For higher dimensions these, however, become quite weak. In the limit of infinite dimension the density of states becomes a Gaussian function due to the central limit theorem

$$D(\epsilon) = \frac{1}{\sqrt{2\pi t^{*2}}} \exp\left(-\frac{\epsilon^2}{2t^{2*}}\right) \, , \qquad (3.171)$$

where t^* is defined as above ($t^* = t/\sqrt{Z}$) while for any finite d the density of states vanishes outside the bandwidth. In $d \to \infty$ there obviously is no well-defined bandwidth. This shows in the limit of small to zero filling where the kinetic energy per electron diverges. However, for every finite density the kinetic energy remains finite.

Bethe lattice   The second type of lattice is the Bethe lattice, also known as Cayley tree. It was introduced by Hans Bethe in 1935. Such a lattice is a cycle-free tree where each site is connected to Z neighbors. Figure 3.16 shows the Bethe lattices for $Z = 3$ (left) and for $Z = 5$ (right). For $Z = 2$ the Bethe lattice is a linear chain. This is the only
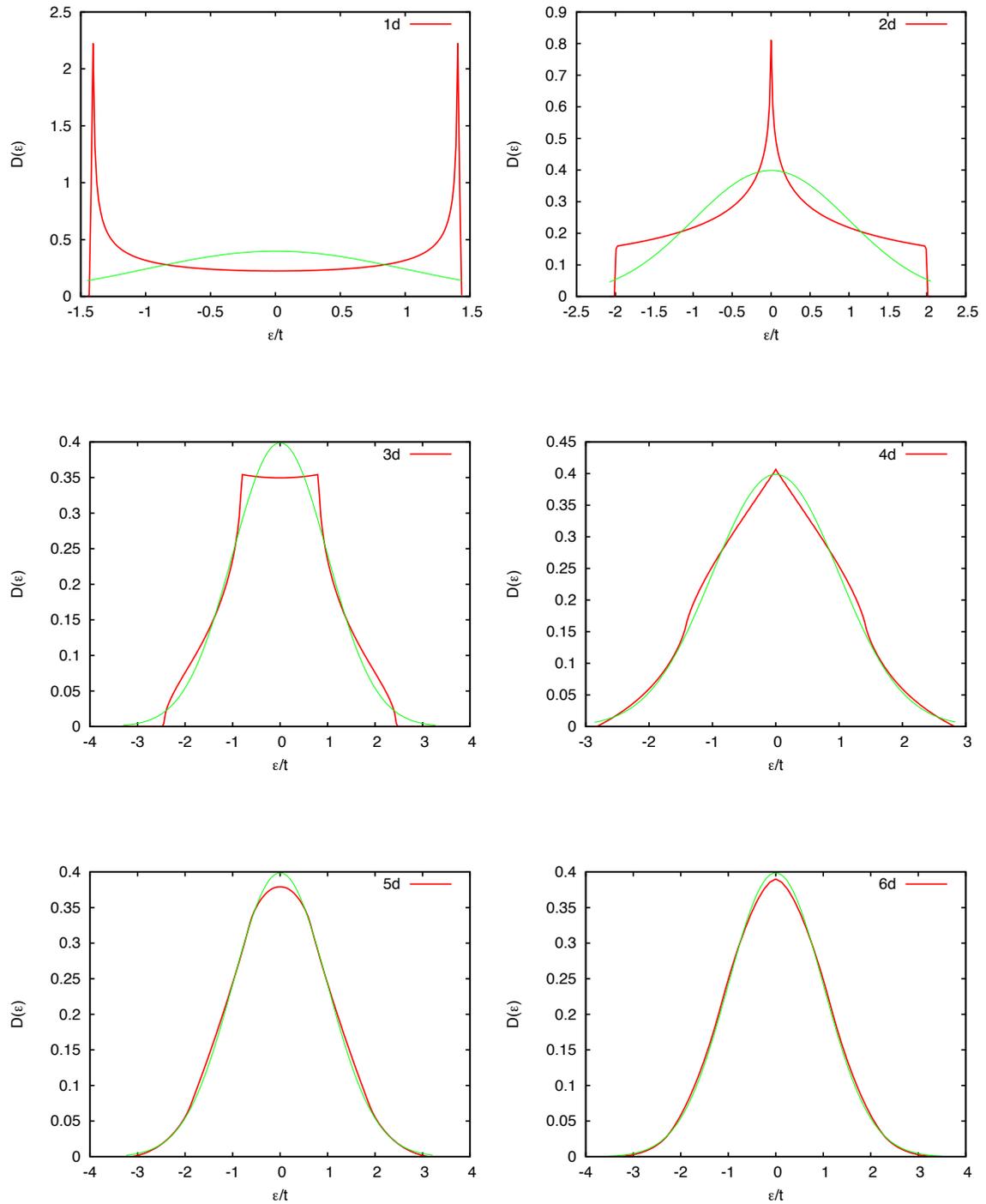
Figure 3.15.: Density of states for a hypercubic lattice from 1 to 6 dimensions with next-neighbor hopping only (dispersion relation: $\varepsilon_{\boldsymbol{k}} = -2t \sum_{i=0}^{d-1} \cos(k_i)$). For $d = 1, 2, 3, 4$ the van-Hove singularities are clearly identifiable. For comparison $d \to \infty$ is plotted in green.
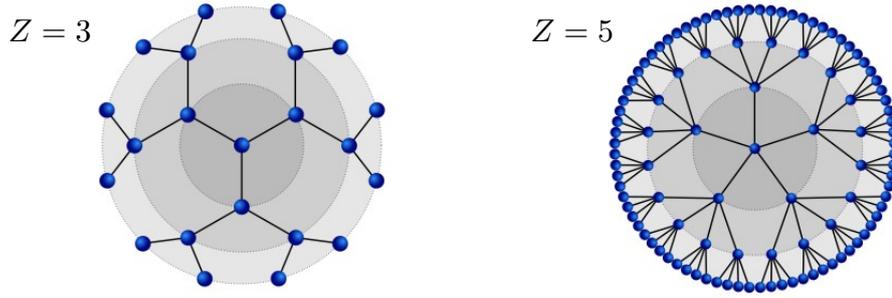
Figure 3.16.: Bethe lattice for $Z = 3$ (left) and $Z = 5$ (right) dimensions. For all values of Z a Bethe lattice is bipartite.

case where there is a simple Fourier transform of the lattice. The density of states for a general Bethe lattice is given by

$$D(\epsilon) = \frac{\sqrt{4(Z-1)t^2/Z - \epsilon^2}}{2\pi \left(t^2 - \epsilon^2/Z\right)} \ . \tag{3.172}$$

In the DMFT limit $Z \to \infty$ this simplifies to the semicircular density of states

$$D^{\text{Bethe } Z \to \infty}(\epsilon) = \frac{\sqrt{4t^2 - \epsilon^2}}{2\pi t^2} \ . \tag{3.173}$$

Moreover, in this limit the Hilbert transform, equation (3.145), assumes a simple and practical form

$$\tilde{D}(\zeta) = \frac{\left(\zeta - \sqrt{\zeta^2 - 4t^2}\right)}{2t^2} \ , \tag{3.174}$$

as does the reciprocal transform

$$R(D) = t^2 G + G^{-1} \ . \tag{3.175}$$

A naïve computer implementation using (3.174) leads to surprising results. Numerically the complex square root function is generally given by the principal square root. For a complex number $z = a + ib$ it is

$$\sqrt{a + ib} = \frac{1}{\sqrt{2}} \left\{ \sqrt{r + a} + i \, \text{sign}(b) \sqrt{r - a} \right\} \ , \tag{3.176}$$

where $r = \sqrt{a^2 + b^2}$ is the modulus of z. From this we can see the branch cut along the negative real axis $a < 0$.

The term $\sqrt{z^2 - 1}$ understood as principal square root has two branch cuts; one along the imaginary axis and the other between ± 1. This apparently leads to non-continuous, non-differentiable behavior of (3.174) in the physically relevant region. An especially
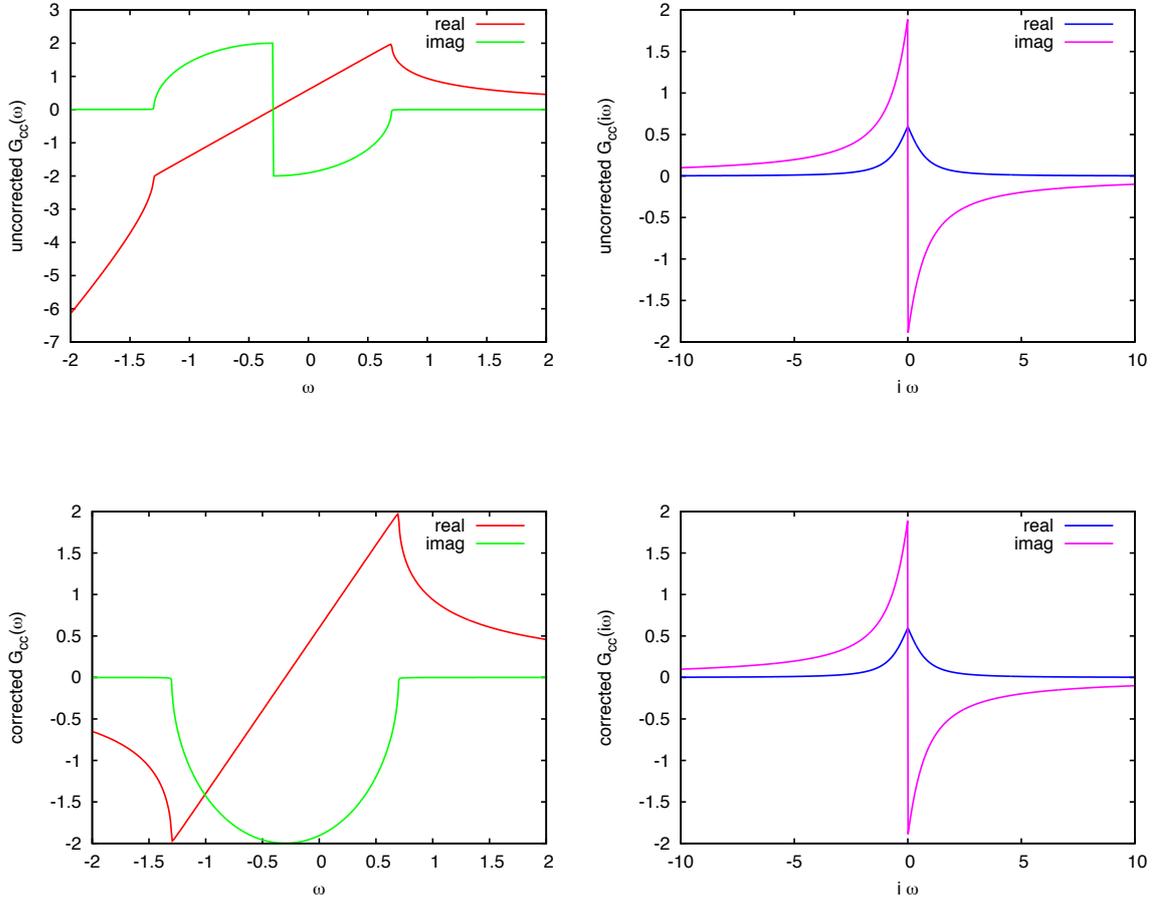
Figure 3.17.: G_{cc} of Bethe lattice in infinite dimensions for $\mu = 0.3$. Naïvly evaluating expression (3.174) numerically gives wrong results due to a branch cut along the imaginary axis (see for instance sign-flip in semicircular DOS (green function upper left plot)). With (3.177) (second row) there is only a single branch cut on the interval $[-1, 1]$ yielding correct results(second row). The second column gives the Matsubara results which are unchanged under the transformation. $\mu = 0.3$ has been taken to have a non-vanishing Matsubara real part.

striking consequence is the sign change in its imaginary part for real-frequencies, the density of states, as shown in the first plot of figure 3.17.

To maintain the symmetry for Matsubara- and fix the discontinuity for real frequencies a single branch cut needs to reside on the real axis between $[-1, 1]$. Using the previous definition of the principal square root this can be readily achieved using

$$\tilde{D}(\zeta) = \frac{\left(\zeta - \sqrt{\zeta - 2t}\sqrt{\zeta + 2t}\right)}{2t^2} \tag{3.177}$$

instead of (3.174). The second row of figure 3.17 gives the result. Indeed we observe the semi-circular density of states for real frequencies and that the Matsubara part is retained.

3.2.5.1. Hubbard Model

We already introduced the Hubbard model in the derivation of the DMFT. It is the simplest model to study the effect of strong correlations. It reads

$$H^{\mathrm{HM}} = -t \sum_{\langle ij \rangle \sigma} \left(c_{i\sigma}^\dagger c_{j\sigma} + h.c.\right) + U \sum_i n_{i\uparrow} n_{i\downarrow} . \tag{3.178}$$

Bethe lattice The simple reciprocal Hilbert transform allows for a shortcut in the self-consistency loop. Inserting (3.175) in (3.161) the bath Green's function simplifies to

$$G_b^{-1} = i\omega + \mu - t^2 G(i\omega) . \tag{3.179}$$

Hence, having the solution of the impurity model we can directly proceed to the fitting function without explicitly calculating Σ and G^{loc}. Usually we set the hopping parameter to $t = 1$ fixing the energy units of the system. Another common convention is to set half the bandwidth to unity, i.e. $W = 2$.

Hypercubic lattice For hypercubic lattices we do not have such a simple form for the reciprocal Hilbert transform. Hence, we use the full self-consistency loop. Since the derivation was based on the Hubbard model all formulæ given in figure 3.9 apply. We just need to choose how to evaluate the local Green's function G^{loc}: using the density of states form, which is numerically less costly, or the Brillouin zone integral which works for every dispersion relation.

Figure 3.10 shows the impurity and local Green's function of a two-dimensional Hubbard model with next-neighbor hopping at $\beta = 50$ and Hubbard model parameters $t = 1$, i.e. the bandwidth $W = 8t$, and $U/W = 4/3$. With $\mu = U/2$ the system is half-filled. For the calculation we used a SIAM with $N_b = 6$ bath sites. The green curve in the plot shows the impurity Green's function of the self-consistent solution. It has a rather spiky appearance due to the small bath. The local lattice Green's function is readily accessible using equation (3.142). We see that the peak positions coincide with the peaks of G^{imp} but are broadened (see discussion in section 3.2.3).

3.2.5.2. Periodic Anderson Model

Systems with f-electrons stemming from lanthanide and actinide ions (open f-shells) often show physics of strong electronic correlations. Some of these compounds are called heavy-fermions, since they have quasiparticle bands with extremely high effective masses m^*. This particularly shows in large values for the specific-heat coefficient. Taking the Fermi liquid expression

$$\gamma = C/T = \frac{m^* k_F}{3} \tag{3.180}$$

where k_F is the Fermi wave vector (note that $k_B = 1$) we see that γ is proportional to m^*, therewith establishing the relation.

The small hybridization of the localized f-electrons with the itinerant conduction electrons of the metallic ions causes these extraordinarily high effective masses. At low temperature the magnetic f-moments are screened by the conduction electrons giving rise to a combined quasiparticle band of either character. The simplest Hamiltonian modelling such systems is the *Periodic Anderson Model* (PAM),

$$H_{\text{PAM}} = H^0_{\text{PAM}} + H_{\text{int}} , \tag{3.181}$$

where

$$H^0_{\text{PAM}} = \sum_{\boldsymbol{k}\sigma} \varepsilon_{\boldsymbol{k}\sigma} a^\dagger_{\boldsymbol{k}\sigma} a_{\boldsymbol{k}\sigma} + V \sum_{l\sigma} \left(f^\dagger_{l\sigma} c_{l\sigma} + c^\dagger_{l\sigma} f_{l\sigma} \right) + \epsilon_f \sum_{l\sigma} f^\dagger_{l\sigma} f_{l\sigma} , \tag{3.182}$$

and

$$H_{\text{int}} = U \sum_l n^f_{l\uparrow} n^f_{l\downarrow} . \tag{3.183}$$

The $f^{(\dagger)}$ and $c^{(\dagger)}, a^{(\dagger)}$ operators act on the f-orbitals with energy ϵ_f and conduction electrons with dispersion relation $\varepsilon_{\boldsymbol{k}}$, respectively. V denotes the hybridization parameter which adjusts the strength of the hybridization. H^0_{PAM} is given in a mixed-representation of $\boldsymbol{k}$- and real space. Fourier transform of the real-space part yields the full $\boldsymbol{k}$-space Hamiltonian,

$$H^0_{\text{PAM}} = \sum_{\boldsymbol{k}\sigma} \varepsilon_{\boldsymbol{k}\sigma} a^\dagger_{\boldsymbol{k}\sigma} a_{\boldsymbol{k}\sigma} + V \sum_{\boldsymbol{k}\sigma} \left(f^\dagger_{\boldsymbol{k}\sigma} a_{\boldsymbol{k}\sigma} + a^\dagger_{\boldsymbol{k}\sigma} f_{\boldsymbol{k}\sigma} \right) + \epsilon_f \sum_{\boldsymbol{k}\sigma} f^\dagger_{\boldsymbol{k}\sigma} f_{\boldsymbol{k}\sigma} . \tag{3.184}$$

We can formally write H^0_{PAM} in this representation as a block matrix of diagonal blocks where the upper left block gives the non-dispersive impurity on-site energies (infinitely narrow band), the lower right block the dispersion of the conduction electrons and the off-diagonal blocks give the constant hybridization. Schematically, the matrix looks like

$$\hat{H}^0_{\text{PAM}} = \begin{pmatrix} \epsilon_f & & & V & & \\ & \epsilon_f & & & V & \\ & & \ddots & & & \ddots \\ \hline V & & & \epsilon_{k_0} & & \\ & V & & & \epsilon_{k_1} & \\ & & \ddots & & & \ddots \end{pmatrix} \tag{3.185}$$

or alternatively in block form

$$\hat{H}^0_{\text{PAM}} = \left(\begin{array}{c|c} \epsilon_f & V \\ \hline V & \epsilon_k \end{array} \right) . \tag{3.186}$$

Formally, we can write the resolvent of the free H^0_{PAM}

$$\hat{G}^0(z) = \frac{1}{z - \hat{H}^0_{\text{PAM}}} . \tag{3.187}$$

Dyson's equation (3.83) gives the relation between the interacting and the non-interacting resolvent. It reads

$$\hat{G}^{-1}(z) = \left[\hat{G}^0(z) \right] - \hat{\Sigma}(z) = z - \hat{H}^0_{\text{PAM}} - \hat{\Sigma}(z) . \tag{3.188}$$

We have seen that within single-site DMFT there is no $\boldsymbol{k}$-dependence in the self-energy Σ. Moreover, we only treat the correlations in the f-orbitals while the conduction electrons are considered as non-interacting. Thus, we effectively assume that Σ is non-zero only in the upper left block , i.e.

$$\hat{\Sigma}^{\text{DMFT}} = \hat{\Sigma} = \left(\begin{array}{c|c} \Sigma \mathbb{1} & 0 \\ \hline 0 & 0 \end{array} \right) . \tag{3.189}$$

Hence, the interacting Green's function reads,

$$\hat{G}(\boldsymbol{k}, z) = \left(\begin{array}{cc} G_{ff} & G_{fc} \\ G_{cf} & G_{cc} \end{array} \right) = \left(\begin{array}{cc} z - \epsilon_f - \Sigma & -V \\ -V & z - \varepsilon_{\boldsymbol{k}} \end{array} \right)^{-1} . \tag{3.190}$$

Using inversion-by-partitioning (see appendix G) we obtain the inverse matrix elements giving the Green's functions on the different subspaces,

$$G_{ff}(\boldsymbol{k}, z) = \left(z + \mu - \epsilon_f - \Sigma(z) - \frac{V^2}{z + \mu - \epsilon_k} \right)^{-1} \tag{3.191}$$

$$G_{cc}(\boldsymbol{k}, z) = \left(z + \mu - \varepsilon_{\boldsymbol{k}} - \frac{V^2}{z + \mu - \epsilon_f - \Sigma(z)} \right)^{-1} \tag{3.192}$$

$$G_{fc}(\boldsymbol{k}, z) = G_{cf}(\boldsymbol{k}, z) = \left(\frac{1}{V} (z + \mu - \varepsilon_{\boldsymbol{k}}) G_{ff}^{-1}(\boldsymbol{k}, z) \right)^{-1} . \tag{3.193}$$

An analogous derivation to the one sketched above for the DMFT of the Hubbard model can be carried out for the Periodic Anderson Model [97]. The effective action for the SIAM reads,

$$S\left[\phi_f, \phi_f^*, G_b \right] = - \int_0^\beta \int_0^{\beta'} \mathrm{d}\tau \mathrm{d}\tau' \sum_\sigma \phi_f^*(\tau) G_b^{-1}(\tau - \tau') \phi_f(\tau')$$
$$- U \int \mathrm{d}\tau \phi_{f\uparrow}^*(\tau) \phi_{f\uparrow}(\tau) \phi_{f\downarrow}^*(\tau) \phi_{f\downarrow}(\tau) . \tag{3.194}$$

where again G_b^{-1} plays the role of the Weiss field and defines the impurity model.

$$\Sigma = G_b^{-1}(\omega) - G^{\text{imp}-1}(\omega) \tag{3.195}$$

is still valid. Self-consistency is reached when the impurity Green's function G^{imp} coincides with the local Green's function of the f-electrons

$$G_{ff}(\mathrm{i}\omega) = \frac{1}{V_{\text{BZ}}} \int_{\text{BZ}} \mathrm{d}k \, G_{ff}(\mathbf{k}, \mathrm{i}\omega) \tag{3.196}$$

$$= \frac{1}{V_{\text{BZ}}} \int_{\text{BZ}} \mathrm{d}k \, \frac{1}{\mathrm{i}\omega + \mu - \epsilon_f - \Sigma(\mathrm{i}\omega) - \frac{V^2}{\mathrm{i}\omega + \mu - \epsilon_k}} \, . \tag{3.197}$$

Using (3.157) in (3.195) we can eliminate Σ from (3.191) giving an alternative form

$$G_{ff}(\mathbf{k}, z) = \left(G^{\text{imp}-1}(z) + \Delta(z) - \frac{V^2}{z + \mu - \epsilon_k} \right)^{-1} , \tag{3.198}$$

where we use the hybridization function Δ as defined in (3.158).

Equation (3.197) is directly related to the local conduction electron Green's function

$$G_{cc}(\mathrm{i}\omega) = \frac{1}{V_{\text{BZ}}} \int_{\text{BZ}} \mathrm{d}k \, \frac{1}{\mathrm{i}\omega + \mu - \frac{V^2}{\mathrm{i}\omega + \mu - \epsilon_f - \Sigma(\mathrm{i}\omega)} - \epsilon_{\mathbf{k}}} \, . \tag{3.199}$$

To see this, we rewrite the integrand of (3.197) by multiplying numerator and denominator with $\mathrm{i}\omega + \mu - \epsilon_k$ and factoring $\rho = \mathrm{i}\omega + \mu - \epsilon_f - \Sigma(\mathrm{i}\omega)$ out. We get

$$\frac{1}{\mathrm{i}\omega + \mu - \epsilon_f - \Sigma(\mathrm{i}\omega) - \frac{V^2}{\mathrm{i}\omega + \mu - \epsilon_k}} = \frac{\mathrm{i}\omega + \mu - \epsilon_k}{\mathrm{i}\omega + \mu - \epsilon_f - \Sigma(\mathrm{i}\omega)} \frac{1}{\mathrm{i}\omega + \mu - \epsilon_k - \frac{V^2}{\mathrm{i}\omega + \mu - \epsilon_f - \Sigma(\mathrm{i}\omega)}} \, .$$

Adding $-V^2/(\mathrm{i}\omega + \mu - \epsilon_f - \Sigma(\mathrm{i}\omega)) + V^2/(\mathrm{i}\omega + \mu - \epsilon_f - \Sigma(\mathrm{i}\omega))$ to the numerator of the first fraction gives

$$\frac{1}{\mathrm{i}\omega + \mu - \epsilon_f - \Sigma(\mathrm{i}\omega) - \frac{V^2}{\mathrm{i}\omega + \mu - \epsilon_k}} = \frac{1}{\rho} + \frac{V^2}{\rho^2} \frac{1}{\mathrm{i}\omega + \mu - \frac{V^2}{\rho} - \epsilon_k} \tag{3.200}$$

Exploiting $\int \mathrm{d}k \, 1 = V_{\text{BZ}}$ we can thus rephrase (3.197)

$$G_{ff}(\mathrm{i}\omega) = \frac{1}{\rho} + \frac{V^2}{\rho^2} G_{cc}(\mathrm{i}\omega) \, . \tag{3.201}$$

Hence, all $\mathbf{k}$-dependence is captured in the conduction electron Green's function.

In terms of the non-interacting density of states of the conduction electrons we can reformulate equation (3.197) in the same way by exploiting $\int \mathrm{d}D(\epsilon) = 1$ and get

$$G_{ff}(\mathrm{i}\omega) = \int_{\mathbb{R}} \mathrm{d}\epsilon \, \frac{D(\epsilon)}{\mathrm{i}\omega - \epsilon_f - \Sigma(\mathrm{i}\omega) - \frac{V^2}{\mathrm{i}\omega - \epsilon}} \tag{3.202}$$

$$= \frac{1}{\rho} + \frac{V^2}{\rho^2} \tilde{D}\left(\mathrm{i}\omega + \mu - \frac{V^2}{\rho} \right) , \tag{3.203}$$

where $\tilde{D}(z)$ denotes the Hilbert transform (3.146).

Bethe lattice For the Bethe lattice in the infinite connectivity limit $Z \to \infty$ we again obtain a shortcut by exploiting your knowledge of the Hilbert transform. We get from (3.203)

$$G_{ff}\left(\mathrm{i}\omega\right) = \frac{1}{\rho} + \frac{V^2}{\rho^2} \frac{\mathrm{i}\omega + \mu - \epsilon_c - \frac{V^2}{\rho} - \sqrt{\left(\mathrm{i}\omega + \mu - \epsilon_c - V^2/\rho\right)^2 - 4t^2}}{2t^2} \; . \qquad (3.204)$$

For a numerical evaluation and the proper choice of the branch cut see section 3.2.5.

Hypercubic lattice The calculation is exactly the one used for the Hubbard model except for the self-consistency condition, i.e. the choice of G^{loc}. Here, G^{imp} has to coincide with the local f-electron Green's function G_{ff} which we can either state in terms of a Brillouin zone integral, see (3.201) and (3.199), or the density of states, see (3.202).

In the following we will briefly cover two example calculations for a 5-dimensional Periodic Anderson Model. In both calculations we scale the hopping matrix element $t = 1/\sqrt{2 \cdot d} = 1/\sqrt{10}$ and choose $U = 4$ and $\epsilon_f = -0.3$. All calculations have been performed with $N_b = 6$.

In the first calculation we used the hybridization $V = 0.2$ and the chemical potential $\mu = -0.14$ giving an impurity occupation of $\langle n_\sigma \rangle \approx 0.44$. Figure 3.18 gives the Green's functions for the conduction electrons (upper plot) and a comparison of the local f-electron with the impurity Green's function (lower plot). We observe that the imaginary part of G_{cc} roughly gives the density of states of the non-interacting electrons. There only is a significant deviation for around $\omega = 0$ and a very small one at $\omega \approx U$. This is due to the relatively small hybridization V, which appears as V^2 in (3.199) and gives the only term deviating from the free case. In the lower plot we see that the agreement of the local f-electron and impurity Green's function is very good. The impurity physics of the PAM almost being in the atomic limit better match the impurity physics of the SIAM. If we increase the hybridization to $V = 0.8$ and keep the impurity occupation fixed $\langle n_\sigma \rangle \approx 0.45$ ($\mu = 1$) we obtain the Green's functions shown in figure 3.19. This probably overly strong hybridization leads to a pronounced deviation from the free behavior in the conduction band and a stronger disagreement between G^{imp} and the local G_{ff}. The almost atomic limit character of the impurity is lost.
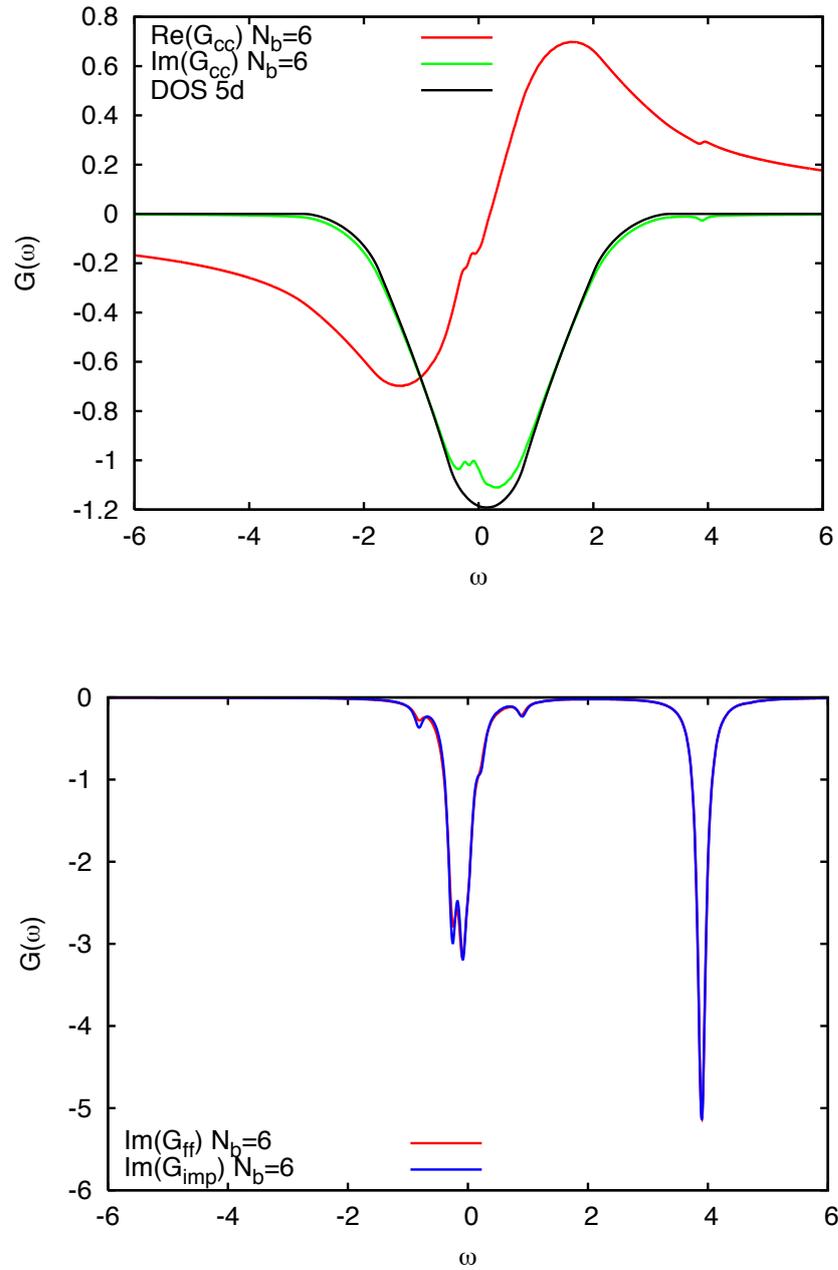
Figure 3.18.: G_{cc} (upper plot) and G_{ff}/G^{imp} (lower plot) of a 5-dimensional PAM with next-neighbor hopping in a hypercubic lattice and parameters $t = 1/\sqrt{2 \cdot d} = 1/\sqrt{10}$, $U = 4$, $\epsilon_f = -0.3$, $V = 0.2$, and $\mu = -0.14$. We observe that the imaginary part of G_{cc} is very similar to the free DOS (black curve). This is due to the small value of V which always appears as V^2. A similar consequence is the very good agreement of G^{imp} and G_{ff}.
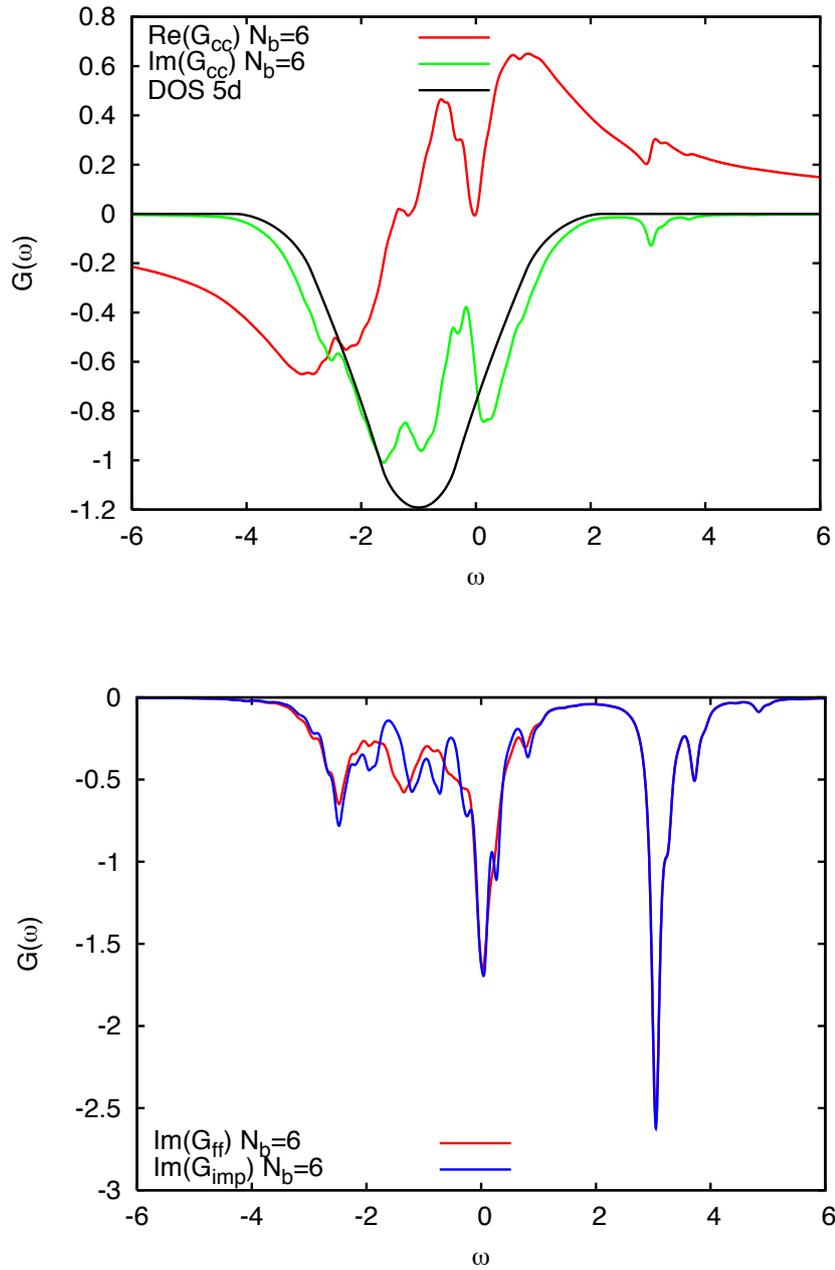
Figure 3.19.: G_{cc} (upper plot) and G_{ff}/G^{imp} (lower plot) of a 5-dimensional PAM with next-neighbor hopping in a hypercubic lattice and parameters $t = 1/\sqrt{2 \cdot d} = 1/\sqrt{10}$, $U = 4$, $\epsilon_f = -0.3$, $V = 0.8$, and $\mu = 1.0$. We observe a strong deviation from the free behaviour in the imaginary part of G_{cc}. It stems from the strong hybridization with the impurity physics on the impurity. In this case also the good agreement of G^{imp} and G_{ff} found in figure 3.18 for $V = 0.2$ is strongly reduced.

3.3. DMFT Dynamical Susceptibilities and Vertex Functions

Even though DMFT works by treating correlations only locally, it is also possible to evaluate lattice response functions with full $\boldsymbol{Q}$-dependence. As we will see in the following chapter the knowledge of the self-energy Σ and the impurity two-particle Green's function suffices to obtain the $\boldsymbol{Q}$-dependent lattice response function (Falicov-Kimball model [112]; Hubbard Model [105, 113, 114, 115]). In principle this makes it possible to study instabilities which are associated with certain $\boldsymbol{Q}$-vectors. The self-energy, within DMFT, on the other hand just contains local information and thus gives only insights into instabilities which occur instantaneously at all wave vectors. The Metal-Insulator Transition (MIT) is the prime example of this kind of instability.

3.3.1. General Formalism and DMFT Approximation

This part is based on the review of Georges, Kotliar, Krauth and Rozenberg [97]. According to equation (3.47) we write the Matsubara response function in a crystal for the operator $\mathcal{O}_1 = \mathcal{O}_2 = \mathcal{O}$ in $\boldsymbol{Q}$-space as

$$\chi\left(\boldsymbol{Q}, \mathrm{i}\Omega_n\right) = \sum_i e^{\mathrm{i}\boldsymbol{Q}\boldsymbol{R}_i} \int_0^\beta \mathrm{d}\tau \, e^{\mathrm{i}\Omega_n \tau} \left\langle \mathcal{T}_\tau \, \mathcal{O}\left(\boldsymbol{R}_i, \tau\right) \mathcal{O}\left(\boldsymbol{0}, 0\right) \right\rangle . \tag{3.205}$$

As discussed in section 3.1.2 we can rewrite this expression in terms of two-particle Green's functions (3.30), yielding

$$\chi(\boldsymbol{Q}, \mathrm{i}\Omega_n) = \sum_{\substack{\boldsymbol{k}\boldsymbol{k}' \\ \sigma\sigma'}} v_{\boldsymbol{k}'\sigma'}^{\mathcal{O}} v_{\boldsymbol{k}\sigma}^{\mathcal{O}} \, \chi_{\boldsymbol{k}\boldsymbol{k}'}^{\sigma\sigma'}(\boldsymbol{Q}, \mathrm{i}\Omega_n) \tag{3.206}$$

with

$$\chi_{\boldsymbol{k}\boldsymbol{k}'}^{\sigma\sigma'}(\boldsymbol{Q}, \mathrm{i}\Omega_n) = \int_0^\beta \mathrm{d}\tau \, e^{\mathrm{i}\Omega_n \tau} \chi_{\boldsymbol{k}\boldsymbol{k}'}^{\sigma\sigma'}(\boldsymbol{Q}, \tau) \tag{3.207}$$

and

$$\chi_{\boldsymbol{k}\boldsymbol{k}'}^{\sigma\sigma'}(\boldsymbol{Q}, \tau) = \left\langle \mathcal{T}_\tau a_{\boldsymbol{k}'\sigma'}^\dagger(\tau) a_{\boldsymbol{k}'+\boldsymbol{Q}\,\sigma'}(\tau) a_{\boldsymbol{k}\sigma}^\dagger(0) a_{\boldsymbol{k}+\boldsymbol{Q}\,\sigma}(0) \right\rangle . \tag{3.208}$$

Equivalently, we can directly use the Matsubara representation of the four-point two-particle Green's function to evaluate (3.207) as shown in section 3.1.8.

If we had the two-particle Green's function $\chi_{\boldsymbol{k}\boldsymbol{k}'}^{\sigma\sigma'}$, we could evaluate all possible dynamical correlation functions (for single particle operators) by the choice of the correct matrix elements $v_{\boldsymbol{k}\sigma}^{\mathcal{O}}$. Here, we are interested in the spin-spin and charge-charge correlation function of paramagnetic systems, whose matrix elements are $\boldsymbol{k}$-independent and given by $v_\sigma^S = \mathrm{sgn}(\sigma)$ and $v_\sigma^C = 1$, respectively.

The two-particle Green's functions are very complicated objects that in general cannot be calculated exactly. Our goal is to derive an approximation to $\chi(\boldsymbol{Q}, \mathrm{i}\Omega_n)$ within DMFT
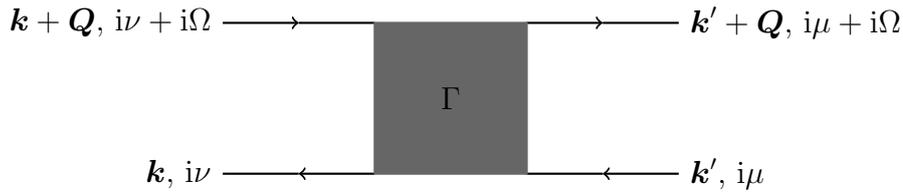
Figure 3.20.: Two-particle vertex function

which allows for their evaluation. To that end, we define a two-particle vertex function $\Gamma_{\boldsymbol{kk'Q}}$ which is irreducible in the particle-hole channel. Its diagram is depicted in figure 3.20. It is chosen such that

$$
\begin{aligned}
\chi_{\boldsymbol{kk'}}\left(\boldsymbol{Q}, \mathrm{i}\Omega_n\right) = & -\frac{1}{\beta} \sum_{\mathrm{i}\nu} G\left(\boldsymbol{k}, \mathrm{i}\nu\right) G\left(\boldsymbol{k}+\boldsymbol{Q}, \mathrm{i}\nu + \mathrm{i}\Omega\right) \\
& + \frac{1}{\beta^2} \sum_{\mathrm{i}\nu\mathrm{i}\mu} G\left(\boldsymbol{k}, \mathrm{i}\nu\right) G\left(\boldsymbol{k}+\boldsymbol{Q}, \mathrm{i}\nu + \mathrm{i}\Omega\right) \\
& \times \Gamma_{\boldsymbol{kk'Q}}\left(\mathrm{i}\nu, \mathrm{i}\mu, \mathrm{i}\Omega\right) G\left(\boldsymbol{k'}, \mathrm{i}\mu\right) G\left(\boldsymbol{k'}+\boldsymbol{Q}, \mathrm{i}\mu + \mathrm{i}\Omega_n\right) + \cdots,
\end{aligned}
\tag{3.209}
$$

where the Green's functions are the full interacting single-particle Green's functions. We can think of (3.209) as a ladder sum as shown in figure 3.21.
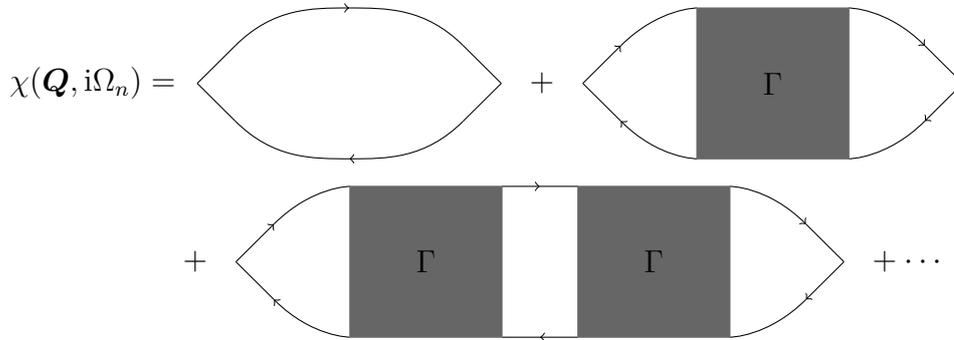
Figure 3.21.: Ladder sum of the dynamical correlation function $\chi(\boldsymbol{Q}, \mathrm{i}\Omega_n)$ with vertices Γ.

It is notationally convenient to introduce a matrix formalism. We rewrite equation (3.209) without the summation over the outermost two internal Matsubara frequencies $\mathrm{i}\mu$ and $\mathrm{i}\nu$ and regard all quantities in (3.209) as matrices in these two indices. Using $[\cdot]$ as notation for those matrices we have the

$$
\chi_{\boldsymbol{kk'}}\left(\boldsymbol{Q}, \mathrm{i}\Omega_n\right) = \frac{1}{\beta^2} \sum_{\mathrm{i}\mu\,\mathrm{i}\nu} \left[\chi_{\boldsymbol{kk'}}\left(\boldsymbol{Q}, \mathrm{i}\Omega_n\right)\right]_{\mathrm{i}\mu\,\mathrm{i}\nu}
\tag{3.210}
$$

with

$$\left[\chi_{\boldsymbol{k}\boldsymbol{k}'}\left(\boldsymbol{Q}, \mathrm{i}\Omega_n\right)\right]_{\mathrm{i}\mu\,\mathrm{i}\nu} = \left[\chi^0_{\boldsymbol{k}\boldsymbol{k}'}\left(\boldsymbol{Q}, \mathrm{i}\Omega_n\right)\right]_{\mathrm{i}\mu\,\mathrm{i}\nu}$$
$$+ \left[\chi^0_{\boldsymbol{k}\boldsymbol{k}''}\left(\boldsymbol{Q}, \mathrm{i}\Omega_n\right)\right]_{\mathrm{i}\mu\,\mathrm{i}\nu'}\left[\Gamma_{\boldsymbol{k}''\boldsymbol{k}'''}\left(\boldsymbol{Q}, \mathrm{i}\Omega_n\right)\right]_{\mathrm{i}\nu'\,\mathrm{i}\mu'}\left[\chi_{\boldsymbol{k}'''\boldsymbol{k}'}\left(\boldsymbol{Q}, \mathrm{i}\Omega_n\right)\right]_{\mathrm{i}\mu'\,\mathrm{i}\nu} ,$$

$$(3.211)$$

where

$$\left[\chi^0_{\boldsymbol{k}\boldsymbol{k}'}\left(\boldsymbol{Q}, \mathrm{i}\Omega_n\right)\right]_{\mathrm{i}\mu\,\mathrm{i}\nu} = -G\left(\boldsymbol{k}, \mathrm{i}\nu\right)G\left(\boldsymbol{k}+\boldsymbol{Q}, \mathrm{i}\nu+\mathrm{i}\Omega_n\right)\beta\delta_{\mathrm{i}\nu\,\mathrm{i}\mu}\delta_{\boldsymbol{k}\boldsymbol{k}'} \qquad (3.212)$$

is a diagonal matrix describing a particle-hole propagator. In this notation we understand the matrix product as a summation/integration over internal indices appearing twice (Einstein-like convention), i.e.

$$\left[X_{\boldsymbol{k}\boldsymbol{k}'}\right]_{\mathrm{i}\nu\,\mathrm{i}\mu}\left[Y_{\boldsymbol{k}'\boldsymbol{k}''}\right]_{\mathrm{i}\mu\,\mathrm{i}\nu'} = \frac{1}{\beta}\sum_{\mathrm{i}\mu}\frac{1}{V_{\mathrm{BZ}}}\int_{\mathrm{BZ}}\mathrm{d}^d k'\left[X_{\boldsymbol{k}\boldsymbol{k}'}\right]_{\mathrm{i}\nu\,\mathrm{i}\mu}\left[Y_{\boldsymbol{k}'\boldsymbol{k}''}\right]_{\mathrm{i}\mu\,\mathrm{i}\nu'} . \qquad (3.213)$$

Almost all of the complexity is now hidden in the two-particle vertex function $\Gamma_{\boldsymbol{k}\boldsymbol{k}'\boldsymbol{Q}}$, which can be expressed in a Dyson-like way as

$$[\Gamma] = \left[\chi^0\right]^{-1} - [\chi]^{-1} . \qquad (3.214)$$

In general, the evaluation of Γ is still intractable. However, in the DMFT limit of infinite dimension $\Gamma_{\boldsymbol{k}\boldsymbol{k}'\boldsymbol{Q}}$ becomes a purely local quantity Γ similar to the self-energy [113][3].

Hence, the $\boldsymbol{k}$-integrals in the matrix product decouple and with the matrix elements v_σ being independent of $\boldsymbol{k}$, we can can perform the integrations over pairs of Green's functions (particle-hole bubbles, see 3.1.8.1). This is a enormous reduction in complexity. Still, the vertex remains a complicated function of three frequencies. Equation (3.211) becomes

$$\left[\chi_{\boldsymbol{Q}, \mathrm{i}\Omega_n}\right] = \left[\chi^0_{\boldsymbol{Q}, \mathrm{i}\Omega_n}\right] + \left[\chi^0_{\boldsymbol{Q}, \mathrm{i}\Omega_n}\right]\left[\Gamma_{\mathrm{i}\Omega_n}\right]\left[\chi_{\boldsymbol{Q}, \mathrm{i}\Omega_n}\right] , \qquad (3.215)$$

where

$$\left[\chi^0_{\boldsymbol{Q}, \mathrm{i}\Omega_n}\right]_{\mathrm{i}\mu\,\mathrm{i}\nu} = -\frac{1}{V_{\mathrm{BZ}}}\int_{\mathrm{BZ}}\mathrm{d}^d k\, G\left(\boldsymbol{k}, \mathrm{i}\nu\right)G\left(\boldsymbol{k}+\boldsymbol{Q}, \mathrm{i}\nu+\mathrm{i}\Omega_n\right)\beta\delta_{\mathrm{i}\nu\,\mathrm{i}\mu} . \qquad (3.216)$$

From (3.215) we see that the momentum dependence of the final quantity $\left[\chi_{\boldsymbol{Q}\,\mathrm{i}\Omega_n}\right]$ stems entirely from $\left[\chi^0_{\boldsymbol{Q}, \mathrm{i}\Omega_n}\right]$, i.e. from the single-particle Green's function.

For a hypercubic lattice with dispersion relation given by equation (3.140) it has been shown [102, 112] that the $\boldsymbol{Q}$-dependence of $\left[\chi^0_{\boldsymbol{Q}, \mathrm{i}\Omega_n}\right]$ and $\left[\chi_{\boldsymbol{Q}, \mathrm{i}\Omega_n}\right]$ is solely given through

$$\mathcal{Q}\left(\boldsymbol{Q}\right) = \frac{1}{d}\sum_{i=0}^{d-1}\cos(Q_i) . \qquad (3.217)$$

---

[3]In fact, Γ does retain some momentum dependence. However, only its local components contribute to to the sum (3.209) [97]. Thus, we can neglect the residual $\boldsymbol{k}$-dependence.

For a generic vector $\boldsymbol{Q}$ the sum is over terms whose signs are random. Thus, they scale like $\mathcal{Q}(\boldsymbol{Q}) \to 1/\sqrt{d}$ yielding $\mathcal{Q}(\boldsymbol{Q}) = 0$ for infinite dimension. Here, generic means for all vectors but a set of measure zero (for instance, containing $\mathcal{Q}(\boldsymbol{0}) = 1$).

Hence, for generic values of $\boldsymbol{Q}$ both functions $\left[\chi^{(0)}_{\boldsymbol{Q},\mathrm{i}\Omega_n} \right]$ coincide with their local version $\left[\chi^{\mathrm{loc}\,(0)}_{\mathrm{i}\Omega_n} \right]$, i.e.

$$\left[\chi^{(0)}_{\boldsymbol{Q},\mathrm{i}\Omega_n} \right] \overset{\mathrm{generic}\ \boldsymbol{Q}}{=} \frac{1}{V_{\mathrm{BZ}}} \int_{\mathrm{BZ}} \mathrm{d}^d Q \; \left[\chi^{(0)}_{\boldsymbol{Q},\mathrm{i}\Omega_n} \right] = \left[\chi^{\mathrm{loc}\,(0)}_{\mathrm{i}\Omega_n} \right] . \tag{3.218}$$

Exploiting this equality in equation (3.215) we can express the vertex function as

$$\Gamma_{\mathrm{i}\Omega_n} = \left[\chi^{\mathrm{loc}\,0}_{\mathrm{i}\Omega_n} \right]^{-1} - \left[\chi^{\mathrm{loc}}_{\mathrm{i}\Omega_n} \right]^{-1} , \tag{3.219}$$

which is now fully $\boldsymbol{k}/\boldsymbol{Q}$-independent. Consequently, we can obtain our target matrix function with [113, 105],

$$\begin{aligned}
\left[\chi_{\boldsymbol{Q},\mathrm{i}\Omega_n} \right]^{-1} &= \left[\chi^0_{\boldsymbol{Q},\mathrm{i}\Omega_n} \right]^{-1} - \Gamma_{\mathrm{i}\Omega_n} \\
&= \left[\chi^0_{\boldsymbol{Q},\mathrm{i}\Omega_n} \right]^{-1} - \left[\chi^{\mathrm{loc}\,0}_{\mathrm{i}\Omega_n} \right]^{-1} + \left[\chi^{\mathrm{loc}}_{\mathrm{i}\Omega_n} \right]^{-1} .
\end{aligned} \tag{3.220}$$

It is important to note that with this equation we have a relation between the lattice $\chi_{\boldsymbol{Q}}$ (LHS) and quantities which are accessible from the impurity alone. For $\left[\chi^0_{\boldsymbol{Q},\mathrm{i}\Omega_n} \right]$ all we need is the lattice Green's function which in DMFT is determined by the local self-energy Σ. The other two quantities are local by construction. They are response functions of the impurity model's effective action.

The final result thus follows from (3.220) by inversion and summation, i.e.

$$\chi_{\boldsymbol{Q}}(\mathrm{i}\Omega_n) = \sum_{\mathrm{i}\nu\,\mathrm{i}\mu} \left[\chi_{\boldsymbol{Q},\mathrm{i}\Omega_n} \right]_{\mathrm{i}\nu\,\mathrm{i}\mu} . \tag{3.221}$$

As a reminder, these equations are only valid in the limit of infinite dimensions. Ultimately we, however, like to treat finite-dimensional lattices. Strictly speaking we cannot identify $\left[\chi^{(0)}_{\boldsymbol{Q},\mathrm{i}\Omega_n} \right]$ with their local versions $\left[\chi^{\mathrm{loc}\,(0)}_{\mathrm{i}\Omega_n} \right]$ for generic vectors, i.e. the equation (3.219) does not hold anymore.

Nevertheless, neglecting the $\boldsymbol{Q}$-dependence in $\Gamma_{\mathrm{i}\Omega_n}$ is a natural approximation. It is similar in spirit to neglecting the momentum dependence in the self-energy. Hence, the DMFT approximation is to retain the formalism of infinite dimensions and apply it to finite dimensional systems. We start with the vertex and therefore need the full and the 'unconnected' two-particle Green's function of the impurity.

For actual calculations of the spin-spin or charge-charge correlation function we see from (3.211) that the matrix elements v_σ only act on the vertex. This is because $\left[\chi^{(0)\,\sigma\sigma'}_{\boldsymbol{Q},\mathrm{i}\Omega_n} \right]$ is diagonal in the spin indices and $v_\sigma^2 = 1$. Thus, for χ^{zz} we have, for instance,

$$\begin{aligned}
\chi^{\mathrm{imp}}_{\mathrm{i}\mu,\mathrm{i}\nu}(\mathrm{i}\Omega_n) = &\frac{1}{4} \int_0^\beta \mathrm{d}\tau_1 \int_0^\beta \mathrm{d}\tau_2 \int_0^\beta \mathrm{d}\tau_3 \int_0^\beta \mathrm{d}\tau_4 \; e^{\mathrm{i}\mu(\tau_1-\tau_2)} e^{\mathrm{i}\nu(\tau_3-\tau_4)} e^{\mathrm{i}\Omega_n(\tau_1-\tau_4)} \\
&\sum_{\sigma\sigma'} (-1)^{\sigma+\sigma'} \langle \mathcal{T}_\tau \, c_\sigma(\tau_1) c_\sigma^\dagger(\tau_2) c_{\sigma'}(\tau_3) c_{\sigma'}^\dagger(\tau_4) \rangle_S .
\end{aligned} \tag{3.222}$$

In the next section we will give the formulæ to evaluate the two-particle Green's function within the ED method and briefly discuss the unconnected part. With these two quantities we can directly obtain the vertex function according to equation (3.219). Finally, we evaluate $\left[\chi^0_{\boldsymbol{Q},\mathrm{i}\Omega_n}\right]$ employing (3.216), where we use the Green's functions for the model under investigation making use of the local Σ.

3.3.2. Explicit Derivation in the ED Framework

The basic building block for the vertex function is the two particle Green's function . We will consider only single-band models, so we drop additional orbital and site indices. Moreover, to shorten the notation we drop the superscript imp. In Matsubara space the two-particle Green's function reads,

$$\chi^{\sigma\sigma'}(\omega_1,\omega_2,\omega_3) = \int\limits_0^\beta d\tau_1 \int\limits_0^\beta d\tau_2 \int\limits_0^\beta d\tau_3 \; e^{\mathrm{i}(\omega_1\tau_1+\omega_2\tau_2+\omega_3\tau_3)} \; \langle \mathcal{T}_\tau\, c_\sigma(\tau_1)c_\sigma^\dagger(\tau_2)c_{\sigma'}(\tau_3)c_{\sigma'}^\dagger(0)\rangle \; .$$

(3.223)

In principle each particle operator could carry its own spin-index. However, for the trace to be finite it is easy to see that only 6 combinations remain, i.e. $\uparrow\uparrow\uparrow\uparrow$, $\uparrow\uparrow\downarrow\downarrow$, $\uparrow\downarrow\downarrow\uparrow$ and the flipped version. The latter two are related by reordering of the operators. Hence, if we have $\chi_{\sigma\sigma'}$ defined as $\chi_{\sigma\sigma'} = \chi_{\sigma\sigma\sigma'\sigma'}$ we can evaluate all non-vanishing two-particle Green's functions.

Due to (imaginary) time translation invariance we have set $\tau_4 = 0$, effectively fixing the right-most operator to $c^\dagger$. At first it might look like we are missing terms since we always start with putting an electron into the system. However, as we will see later in this section the summations over the entire Fock space (explicitly in the trace and implicitly in between the operators) give all permutations.

To carry out the integrations in equation (3.223) we transform the imaginary time-ordering operator into its Θ-function representation. That makes the time-order explicit in the integration boundaries. We obtain $3! = 6$ terms since there are 6 permutations of the three operators at times $\tau_4 = 0 \leq \tau_i \leq \beta$ with $i = 1, 2, 3$. In each of the permutations we need to keep track of the Fermi sign.

It turns out to be practical not to use the standard definition of Fourier transforms for the particle operators (see equation (3.222) above). Instead we use the same sign in the Fourier phase factors for annihilators and creators. In addition, we redefine the frequencies such that each imaginary time τ_i corresponds to a frequency $\mathrm{i}\omega_i$. These frequencies are fermionic, a property they inherit from the particle operators. This is in contrast to the more physical definition where $\mathrm{i}\Omega$ is bosonic and represents an energy transfer. Energy conservation in this notation requires $\omega_1 + \omega_2 + \omega_3 + \omega_4 = 0$. With this definition all these terms can be brought in the same form when we permute the operators along with their frequencies. Using standard Fourier convention we would also have had to permute the minus sign along with frequency ω_2 cluttering the notation and the code.

This unified form of expression (3.223) is given by

$$\chi^{\sigma\sigma'}_{\omega_1,\omega_2,\omega_3} = \frac{1}{Z} \sum_{ijkl} \sum_{\Pi} \quad \Phi\left(E_i, E_j, E_k, E_l; \omega_{\Pi_1}, \omega_{\Pi_2}, \omega_{\Pi_3}\right) \mathrm{sign}(\Pi)$$

$$\langle i|\mathcal{O}_{\Pi_1}|j\rangle\langle j|\mathcal{O}_{\Pi_2}|k\rangle\langle k|\mathcal{O}_{\Pi_3}|l\rangle\langle l|c^\dagger_{\sigma'}|i\rangle \;, \qquad (3.224)$$

where we introduced several energy eigenstate closure relations and defined $\mathcal{O}_1 = c_\sigma$, $\mathcal{O}_2 = c^\dagger_\sigma$ and $\mathcal{O}_3 = c_{\sigma'}$. Φ denotes the Fourier transform with explicit time ordering

$$\Phi\left(E_i, E_j, E_k, E_l; \omega_1, \omega_2, \omega_3\right) = \int\limits_0^\beta d\tau_1 \int\limits_0^{\tau_1} d\tau_2 \int\limits_0^{\tau_2} d\tau_3 \; e^{-\beta E_i} e^{E_{ij}\tau_1} e^{E_{jk}\tau_2} e^{E_{kl}\tau_3} e^{\mathrm{i}(\omega_1\tau_1+\omega_2\tau_2+\omega_3\tau_3)} \;.$$

$$(3.225)$$

Numerically we need to pay attention to degenerate energies which may give rise to vanishing denominators. We treat these terms explicitly and substitute these terms with their proper limit. As a notational abbreviation we define $\not\delta(x) = 1 - \delta(x)$ and $E_{ij} = E_i - E_j$. Straightforward calculation yields

$$\Phi\left(\; E_i, E_j, E_k, E_l; \omega_1, \omega_2, \omega_3\right) = e^{-\beta E_i} \left\{ \frac{\not\delta\left(\mathrm{i}\omega_3 + E_{kl}\right)}{\mathrm{i}\omega_3 + E_{kl}} \left[\frac{\not\delta\left(\mathrm{i}\omega_2 + \mathrm{i}\omega_3 + E_{jl}\right)}{\mathrm{i}\omega_2 + \mathrm{i}\omega_3 + E_{jl}} \right.\right.$$

$$\times \left(\mathcal{C}\left(\mathrm{i}\omega_1 + \mathrm{i}\omega_2 + \mathrm{i}\omega_3 + E_{il}\right) - \mathcal{C}\left(\mathrm{i}\omega_1 + E_{ij}\right)\right) + \delta\left(\mathrm{i}\omega_2 + \mathrm{i}\omega_3 + E_{jl}\right)\mathcal{A}\left(\mathrm{i}\omega_1 + E_{ij}\right)$$

$$- \frac{\not\delta\left(\mathrm{i}\omega_2 + E_{jk}\right)}{\mathrm{i}\omega_2 + E_{jk}} \left(\mathcal{C}\left(\mathrm{i}\omega_1 + \mathrm{i}\omega_2 + E_{ik}\right) - \mathcal{C}\left(\mathrm{i}\omega_1 + E_{ij}\right)\right) - \delta\left(\mathrm{i}\omega_2 + E_{jk}\right)\mathcal{A}\left(\mathrm{i}\omega_1 + E_{ij}\right) \right]$$

$$+ \delta\left(\mathrm{i}\omega_3 + E_{kl}\right)\left[\not\delta\left(\mathrm{i}\omega_2 + E_{jk}\right)\left(\frac{\mathcal{A}\left(\mathrm{i}\omega_1 + \mathrm{i}\omega_2 + E_{ik}\right)}{\mathrm{i}\omega_2 + E_{jk}} - \frac{\mathcal{C}\left(\mathrm{i}\omega_1 + \mathrm{i}\omega_2 + E_{ij}\right) - \mathcal{C}\left(\mathrm{i}\omega_1 + E_{ij}\right)}{\left(\mathrm{i}\omega_2 + E_{jk}\right)^2}\right)\right.$$

$$\left.\left. + \delta\left(\mathrm{i}\omega_2 + E_{jk}\right)\mathcal{B}\left(\mathrm{i}\omega_1 + E_{ij}\right)\right]\right\} \;,$$

$$(3.226)$$

where

$$\mathcal{A}(c) = \int_0^\beta \mathrm{d}\tau \; \tau e^{c\tau} = \not\delta\left(c\right)\left\{\frac{\beta e^{c\beta}}{c} - \frac{e^{c\beta} - 1}{c^2}\right\} + \delta\left(c\right)\frac{\beta^2}{2} \qquad (3.227\mathrm{a})$$

$$\mathcal{B}(c) = \frac{1}{2}\int_0^\beta \mathrm{d}\tau \; \tau^2 e^{c\tau} = \not\delta\left(c\right)\frac{1}{c^3}\left\{e^{c\beta}\left(1 - c\beta + \frac{1}{2}(c\beta)^2\right) - 1\right\} + \delta\left(c\right)\frac{\beta^3}{6} \qquad (3.227\mathrm{b})$$

$$\mathcal{C}(c) = \int_0^\beta \mathrm{d}\tau \; e^{c\tau} = \not\delta\left(c\right)\frac{e^{c\beta} - 1}{c} + \delta\left(c\right)\beta \;. \qquad (3.227\mathrm{c})$$

The actual evaluation of equation (3.224) is computationally very expensive – hence the need for optimization. At first we can use the trick already encountered for the single-particle Green's function (see section 3.1.6). We multiply each term in equation (3.226) with the $\exp\left(-\beta E_i\right)$ Boltzmann factor. Identifying the terms having an exponential

factor with E_x where $x = j, k, l$ and substituting x by i, gives equations (3.228) (see next page) where the superscripts denote the renaming. In this form the full $4! = 24$ permutations of the 4 particle operators are explicit. All terms are now multiplied by the single Boltzmann factor $\exp(-\beta E_i)$ which we factorize out. To speed up the calculation we define a Boltzmann cutoff ϵ_{Boltz} which becomes the more efficient the lower the temperature. Often only a few states have to be taken into account (cf. for example figure 3.13). Of course, in general the details depend on the spectrum and its gaps.

$$\phi^{ii}\left(E_i, E_j, E_k, E_l; \omega_1, \omega_2, \omega_3\right) = \frac{\not\phi\left(i\omega_3+E_{kl}\right)}{i\omega_3+E_{kl}}\left[\frac{\not\phi\left(i\omega_2+i\omega_3+E_{jl}\right)}{i\omega_2+i\omega_3+E_{jl}}\left\{\left(\frac{\not\phi\left(i\omega_1+E_{ij}\right)}{i\omega_1+E_{ij}}-\beta\delta\left(i\omega_1+E_{ij}\right)\right)\left(\frac{\not\phi\left(i\omega_1+E_{ij}\right)}{\left(i\omega_1+E_{ij}\right)^2}+\delta\left(i\omega_1+E_{ij}\right)\frac{\beta^2}{2}\right)\right.\right.$$

$$-\left(\frac{\not\phi\left(i\omega_1+i\omega_2+i\omega_3+E_{il}\right)}{i\omega_1+i\omega_2+i\omega_3+E_{il}}-\beta\delta\left(i\omega_1+i\omega_2+i\omega_3+E_{il}\right)\right)\left\}+\delta\left(i\omega_2+i\omega_3+E_{jl}\right)\left(\left(\frac{\not\phi\left(i\omega_1+E_{ij}\right)}{i\omega_1+E_{ij}}\right)-\left(\frac{\not\phi\left(i\omega_1+i\omega_2+E_{ik}\right)}{i\omega_1+i\omega_2+E_{ik}}-\delta\left(i\omega_1+i\omega_2+E_{ik}\right)\beta\right)\right)\right\}$$

$$-\frac{\not\phi\left(i\omega_2+E_{jk}\right)}{i\omega_2+E_{jk}}\left\{\left(\frac{\not\phi\left(i\omega_1+E_{ij}\right)}{\left(i\omega_1+E_{ij}\right)^2}+\delta\left(i\omega_1+E_{ij}\right)\frac{\beta^2}{2}\right\}\right.$$

$$-\delta\left(i\omega_2+E_{jk}\right)\left(\left(\frac{\not\phi\left(i\omega_1+i\omega_2+E_{ik}\right)}{\left(i\omega_1+i\omega_2+E_{ik}\right)^2}+\delta\left(i\omega_1+i\omega_2+E_{ik}\right)+\delta\left(i\omega_1+i\omega_2+E_{ik}\right)\frac{\beta^2}{2}\right)\right.$$

$$-\delta\left(i\omega_2+E_{jk}\right)\left\{\left(\frac{\not\phi\left(i\omega_1+i\omega_2+E_{ik}\right)}{\left(i\omega_1+i\omega_2+E_{ik}\right)^2}+\delta\left(i\omega_1+i\omega_2+E_{ik}\right)\beta-\frac{\not\phi\left(i\omega_1+E_{ij}\right)}{i\omega_1+E_{ij}}+\delta\left(i\omega_1+E_{ij}\right)\beta\right)\right\}+\delta\left(i\omega_2+E_{jk}\right)\right\}$$

$$+\frac{1}{i\omega_2+E_{jk}}\left(\left(\frac{\not\phi\left(i\omega_1+i\omega_2+E_{ik}\right)}{i\omega_1+i\omega_2+E_{ik}}-\delta\left(i\omega_1+i\omega_2+E_{ik}\right)\beta-\frac{\not\phi\left(i\omega_1+E_{ij}\right)}{i\omega_1+E_{ij}}+\delta\left(i\omega_1+E_{ij}\right)\beta\right)\frac{\beta^3}{6}-\frac{\not\phi\left(i\omega_1+E_{ij}\right)}{\left(i\omega_1+E_{ij}\right)^3}\right\}$$
$$\tag{3.228a}$$

$$\phi^{ji}\left(E_i, E_j, E_k, E_l; \omega_1, \omega_2, \omega_3\right) = \frac{\not\phi\left(i\omega_3+E_{kl}\right)}{i\omega_3+E_{kl}}\frac{\not\phi\left(i\omega_1+E_{ji}\right)}{i\omega_1+E_{ji}}\left[\delta\left(i\omega_2+i\omega_3+E_{il}\right)\left\{\beta-\frac{1}{i\omega_1+E_{ji}}\right\}\right.$$

$$-\frac{\not\phi\left(i\omega_2+i\omega_3+E_{il}\right)}{i\omega_2+i\omega_3+E_{il}}\left[\frac{\not\phi\left(i\omega_2+E_{ik}\right)}{i\omega_2+E_{ik}}-\delta\left(i\omega_2+E_{ik}\right)\right]\left\{\beta-\frac{1}{i\omega_1+E_{ji}}\right\}$$

$$+\delta\left(i\omega_3+E_{kl}\right)\,\text{\color{red}$\exp\left(i\omega_1\beta\right)$}\left[\frac{\not\phi\left(i\omega_2+E_{ik}\right)}{\left(i\omega_2+E_{ik}\right)^2}+\delta\left(i\omega_2+E_{ik}\right)\right\}\frac{\not\phi\left(i\omega_1+E_{ji}\right)}{i\omega_1+E_{ji}}\left\{1-\left(i\omega_1+E_{ji}\right)\beta+\frac{1}{2}\left(i\omega_1+E_{ji}\right)^2\beta^2\right\}\right]$$
$$\tag{3.228b}$$

$$\phi^{ki}\left(E_i, E_j, E_k, E_l; \omega_1, \omega_2, \omega_3\right) = \frac{\not\phi\left(i\omega_2+E_{ji}\right)}{i\omega_2+E_{ji}}\frac{\not\phi\left(i\omega_1+i\omega_2+E_{ki}\right)}{i\omega_1+i\omega_2+E_{ki}}\,\text{\color{red}$\exp\left(\left(i\omega_1+i\omega_2\right)\beta\right)$}\left\{\beta-\frac{1}{i\omega_1+i\omega_2+E_{ki}}-\frac{1}{i\omega_2+E_{ji}}\right\}\delta\left(i\omega_3+E_{il}\right)-\frac{\not\phi\left(i\omega_3+E_{il}\right)}{i\omega_3+E_{il}}$$
$$\tag{3.228c}$$

$$\phi^{li}\left(E_i, E_j, E_k, E_l; \omega_1, \omega_2, \omega_3\right) = \frac{\not\phi\left(i\omega_3+E_{ki}\right)}{i\omega_3+E_{ki}}\frac{\not\phi\left(i\omega_2+i\omega_3+E_{ji}\right)}{i\omega_2+i\omega_3+E_{ji}}\frac{\not\phi\left(i\omega_1+i\omega_2+i\omega_3+E_{li}\right)}{i\omega_1+i\omega_2+i\omega_3+E_{li}}\,\text{\color{red}$\exp\left(\left(i\omega_1+i\omega_2+i\omega_3\right)\beta\right)$}$$
$$\tag{3.228d}$$

Equations (3.228) have ω_i dependent exponential functions emphasized in red. For ω_i's being fermionic Matsubara frequencies these exponentials give $-1/+1$ for an odd/even number of them. For real frequencies after an implicit analytic continuation, however, these exponentials pose a problem. Similar to the Matsubara summation for the particle-hole bubble (see section 3.1.8.1) we have to use our knowledge of ω to bring (3.226) into a form which then can be analytically continued to the desired real-frequency result.

For fermionic Matsubara frequencies, (3.226) simplifies to

$$
\begin{aligned}
\Phi\left(E_i, E_j, E_k, E_l; \omega_1, \omega_2, \omega_3\right) &= \\
\frac{e^{-\beta E_i}}{i\omega_3 + E_{kl}} &\left\{ \frac{\not\!\phi\left(i(\omega_2 + \omega_3) + E_{jl}\right)}{i\left(\omega_2 + \omega_3\right) + E_{jl}} \left[\frac{e^{-\beta E_{ji}} + 1}{i\omega_1 + E_{ij}} - \frac{e^{-\beta E_{li}} + 1}{i(\omega_1 + \omega_2 + \omega_3) + E_{il}} \right] \right. \\
&+ \delta(i(\omega_2 + \omega_3) + E_{jl}) \left[\frac{e^{-\beta E_{ji}} + 1}{(i\omega_1 + E_{ij})^2} - \beta\frac{e^{-\beta E_{ji}}}{(i\omega_1 + E_{ij})} \right] - \frac{1}{i\omega_2 + E_{jk}} \times \\
&\left. \left[\frac{e^{-\beta E_{ji}} + 1}{i\omega_1 + E_{ij}} + \not\!\phi\left(i(\omega_1 + \omega_2) + E_{ik}\right) \frac{e^{-\beta E_{ki}} - 1}{i(\omega_1 + \omega_2) + E_{ik}} + \beta\delta(i(\omega_1 + \omega_2) + E_{ik}) \right] \right\} .
\end{aligned}
$$

$$(3.229)$$

Again factorizing the Boltzmann factor $\exp\left(-\beta E_i\right)$ out gives equations (3.230a-3.230d)[116, 117], which are the simplified versions of equations (3.228a-3.228d).

$$
\phi^{ii}\left(E_i, E_j, E_k, E_l; \omega_1, \omega_2, \omega_3\right) = \frac{1}{i\omega_3 + E_{kl}} \left\{ \frac{\delta\left(i\left(\omega_2 + \omega_3\right) + E_{jl}\right)}{i\left(\omega_2 + \omega_3\right) + E_{ij}} \left[\frac{1}{i\omega_1 + E_{ij}} - \frac{1}{i\left(\omega_1 + \omega_2 + \omega_3\right) + E_{il}} \right] \right.
$$
$$
\left. - \frac{1}{i\omega_2 + E_{jk}} \left[\frac{1}{i\omega_1 + E_{ij}} - \frac{\delta\left(i\left(\omega_1 + \omega_2\right) + E_{ik}\right)}{i\left(\omega_1 + \omega_2\right) + E_{ik}} + \beta\delta\left(i\left(\omega_1 + \omega_2\right) + E_{ik}\right) \right] \right\}
$$
$$
+ \frac{\delta\left(i\left(\omega_2 + \omega_3\right) + E_{jl}\right)}{\left(i\omega_1 + E_{ij}\right)^2}, \tag{3.230a}
$$

$$
\phi^{ji}\left(E_i, E_j, E_k, E_l; \omega_1, \omega_2, \omega_3\right) = \frac{1}{i\omega_3 + E_{kl}} \left\{ \frac{\delta\left(i\left(\omega_2 + \omega_3\right) + E_{il}\right)}{i\left(\omega_2 + \omega_3\right) + E_{il}} \frac{1}{i\omega_1 + E_{ji}} \right.
$$
$$
\left. + \delta\left(i\left(\omega_2 + \omega_3\right) + E_{il}\right) \left[\frac{1}{\left(i\omega_1 + E_{ji}\right)^2} - \frac{\beta}{i\omega_1 + E_{ji}} \right] - \frac{1}{i\omega_2 + E_{ik}} \frac{1}{i\omega_1 + E_{ji}} \right\}, \tag{3.230b}
$$

$$
\phi^{ki}\left(E_i, E_j, E_k, E_l; \omega_1, \omega_2, \omega_3\right) = \frac{-1}{i\omega_3 + E_{il}} \frac{\delta\left(i\left(\omega_1 + \omega_2\right) + E_{ki}\right)}{i\left(\omega_1 + \omega_2\right) + E_{ki}} \frac{1}{i\omega_2 + E_{ji}}, \tag{3.230c}
$$

$$
\phi^{li}\left(E_i, E_j, E_k, E_l; \omega_1, \omega_2, \omega_3\right) = \frac{-1}{i\omega_3 + E_{ki}} \frac{\delta\left(i\left(\omega_2 + \omega_3\right) + E_{ji}\right)}{i\left(\omega_2 + \omega_3\right) + E_{ji}} \frac{1}{i\left(\omega_1 + \omega_2 + \omega_3\right) + E_{li}}. \tag{3.230d}
$$

3.3.2.1. Unconnected Diagrams

To obtain the irreducible vertex using (3.219) we still need the 'unconnected' $\chi^{\mathrm{imp0}}(i\Omega)$. For χ^{zz} we have already given the result in equation (3.96). In the general case, we proceed according to the free case given in section 3.1.7, albeit using fully dressed propagators. Hence, we evaluate

$$
\chi^{\mathrm{imp0},\sigma\sigma'}(\tau_1,\tau_2,\tau_3) = \langle \mathcal{T}_\tau\, c_\sigma(\tau_1)\bar{c}_\sigma(\tau_2)\rangle\langle \mathcal{T}_\tau\, c_\sigma(\tau_3)\bar{c}_\sigma(0)\rangle
$$
$$
- \langle \mathcal{T}_\tau\, c_\sigma(\tau_1)\bar{c}_{\sigma'}(0)\rangle\langle \mathcal{T}_\tau\, c_{\sigma'}(\tau_3)\bar{c}_\sigma(\tau_2)\rangle\ . \tag{3.231}
$$

Fourier transforming $\chi_{\sigma\sigma'}$ and using the sign convention yields

$$
\chi^{\mathrm{imp0},\sigma\sigma'}(\omega_1,\omega_2,\omega_3) = \int_0^\beta d\tau_1\, d\tau_2\, d\tau_3\ e^{i(\omega_1\tau_1+\omega_2\tau_2+\omega_3\tau_3)}\, \chi^0_{\sigma\sigma'}(\tau_1,\tau_2,\tau_3,0)
$$
$$
= \beta\left(\delta_{\omega_1,-\omega_2} - \delta_{\omega_3,-\omega_2}\delta_{\sigma\sigma'}\right) G(i\omega_1)G(i\omega_3)\ . \tag{3.232}
$$

3.3.2.2. Translation to Standard Notation

The Fourier transform convention, we used, is practical for derivation within the exact diagonalization framework. The standard convention, on the other hand, describes the scattering of two particles with energy $\mu+\Omega$, ν and spin σ, σ', respectively. After this process the energy Ω is transferred from the first to the second particle. Figure 3.22 shows the scattering process.

The relations, connecting our (LHS) to the standard (RHS) convention, are

$$
\omega_1 = \mu + \Omega \tag{3.233a}
$$
$$
\omega_2 = -\mu \tag{3.233b}
$$
$$
\omega_3 = \nu\ , \tag{3.233c}
$$
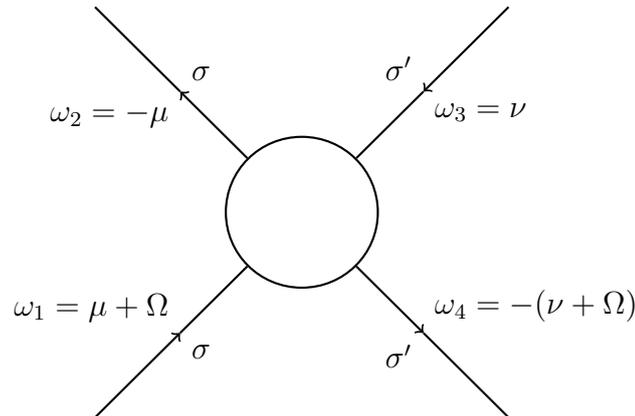
Figure 3.22.: Translation of the Fourier transform definitions for an evaluation with exact diagonalization to the standard definition.

where the minus sign is due to the creation operator. The energy conservation in standard convention is

$$(\mu + \Omega) + \nu = \mu + (\nu + \Omega) \ . \tag{3.234}$$

Hence, for the translation of the expressions from exact diagonalization we have

$$\chi_{i\mu,i\mu}^{\text{imp},\sigma\sigma'} (i\Omega) = \chi^{\sigma\sigma'}(i\mu + i\Omega, -i\mu, i\nu) \tag{3.235}$$

and

$$\chi_{i\mu,i\mu}^{\text{imp0},\sigma\sigma'} (i\Omega) = \beta \left(\delta_{\Omega 0} - \delta_{i\mu,i\nu}\delta_{\sigma\sigma'} \right) G(i\mu + i\Omega)G(i\nu) \ . \tag{3.236}$$

The first term only contributes for $\Omega = 0$ while the other demands $\sigma = \sigma'$.

3.3.3. Properties of the Two-Particle Green's Function and the Vertex

Since the vertex inherits all symmetries from the two-particle Green's function we will only discuss the latter in this section. Its numerical calculation is the most time consuming part of the entire simulation. By exploiting symmetries we can significantly reduce the number of matrix elements that have to be calculated and hence, significantly speed up the entire simulation. For instance, in a paramagnetic system obviously $\chi_{\uparrow\uparrow} = \chi_{\downarrow\downarrow}$ holds, as does $\chi_{\uparrow\downarrow} = \chi_{\downarrow\uparrow}$.

From

$$\chi_{i\mu,i\nu}^{\sigma\sigma'} (i\Omega_n) = \int_0^\beta \mathrm{d}\tau_1 \int_0^\beta \mathrm{d}\tau_2 \int_0^\beta \mathrm{d}\tau_3 \int_0^\beta \mathrm{d}\tau_4 \ e^{i\mu(\tau_1-\tau_2)}e^{i\nu(\tau_3-\tau_4)}e^{i\Omega_n(\tau_1-\tau_4)} \\ \langle \mathcal{T}_\tau \, c_\sigma(\tau_1)c_\sigma^\dagger(\tau_2)c_{\sigma'}(\tau_3)c_{\sigma'}^\dagger(\tau_4) \rangle_S \tag{3.237}$$

we infer

$$\left[\chi_{i\mu,i\nu}^{\sigma\sigma'} (i\Omega_n) \right]^* = \chi_{(i\mu)^*,(i\nu)^*}^{\sigma\sigma'} ((i\Omega_n)^*) \ . \tag{3.238}$$

As a consequence for $i\Omega$ being a Matsubara frequency we just need to evaluate the Green's functions for $i\Omega_n$ with $n \geq 0$. For real Ω, (3.237) still holds. We can use this additional symmetry to reduce the computational demand for a fixed Ω.

Another practical symmetry from the exchange of the two particles is

$$\chi_{i\mu,i\nu}^{\sigma\sigma'} (i\Omega_n) = \chi_{i\nu,i\mu}^{\sigma'\sigma} ((i\Omega_n)) \ . \tag{3.239}$$

For the paramagnetic case we have in addition

$$\chi_{i\mu,i\nu}^{\sigma\sigma'} (i\Omega_n) = \chi_{i\nu,i\mu}^{\sigma\sigma'} (i\Omega_n) \ . \tag{3.240}$$

Figure 3.23 visualizes this paramagnetic case for a fixed Ω. While the symmetry due to equation (3.240) holds for all $\Omega \in \mathbb{C}$ (red line) the one represented by the green line only
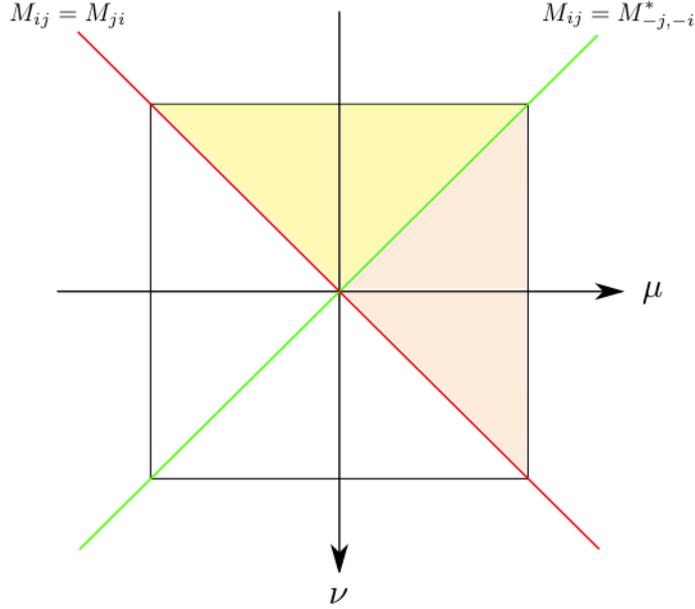
Figure 3.23.: Symmetries of vertex and two-particle Green's function for a fixed Ω. All matrices obey the symmetry shown by the red line where the green line only applies to the $\Omega \in \mathbb{R}$ case. Hence, for $\Omega \in \mathbb{R}$ only the light-orange triangle needs to be calculated whereas in the general case the upper half (yellow + orange triangle) is needed.

applies to real Ω (see equation (3.238)). Thus, for real Ω all we need to calculate is one of the triangles spanned by a red and green line (for instance the light orange one).

Figure 3.24 contains exemplary matrix plots for the two-particle Green's function

$$\chi_{i\mu,i\nu}^{zz}\left(\Omega\right) = \frac{1}{2}\left(\chi_{i\mu,i\nu}^{\uparrow\uparrow}\left(\Omega\right) - \chi_{i\mu,i\nu}^{\uparrow\downarrow}\left(\Omega\right)\right)\ , \tag{3.241}$$

for bosonic Matsubara (left column) and real frequencies (right column). The colors encode the logarithm of the modulus. Comparing with figure 3.23 we see that the symmetries are indeed satisfied.

The region of largest modulus is concentrated around $\mu \approx \nu \approx 0$ for $\Omega \approx 0$. Increasing Ω along the imaginary axis we find that the weight splits into two parts. One remains at $\mu \approx \nu \approx 0$ while the other moves along the diagonal in negative direction. These two strong areas along the diagonal define a cross of less pronounced features, whose bars become the broader the larger n. Formally, the vertices are infinitely large matrices and this shift does not cause problems. Technically, however, we can only treat finite matrix which should be only as large as necessary due to the computational cost of evaluating a matrix element. To capture more of the important part of the vertex we use "roaming vertices". These are vertices moved by a bosonic Matsubara frequency such that the region of largest modulus remains in the center of the matrix. This is done by shifting with $-\Omega_{\lfloor n/2 \rfloor}$ restoring the symmetry $M_{i,j} = M_{-i,-j}^*$ exactly for even n.
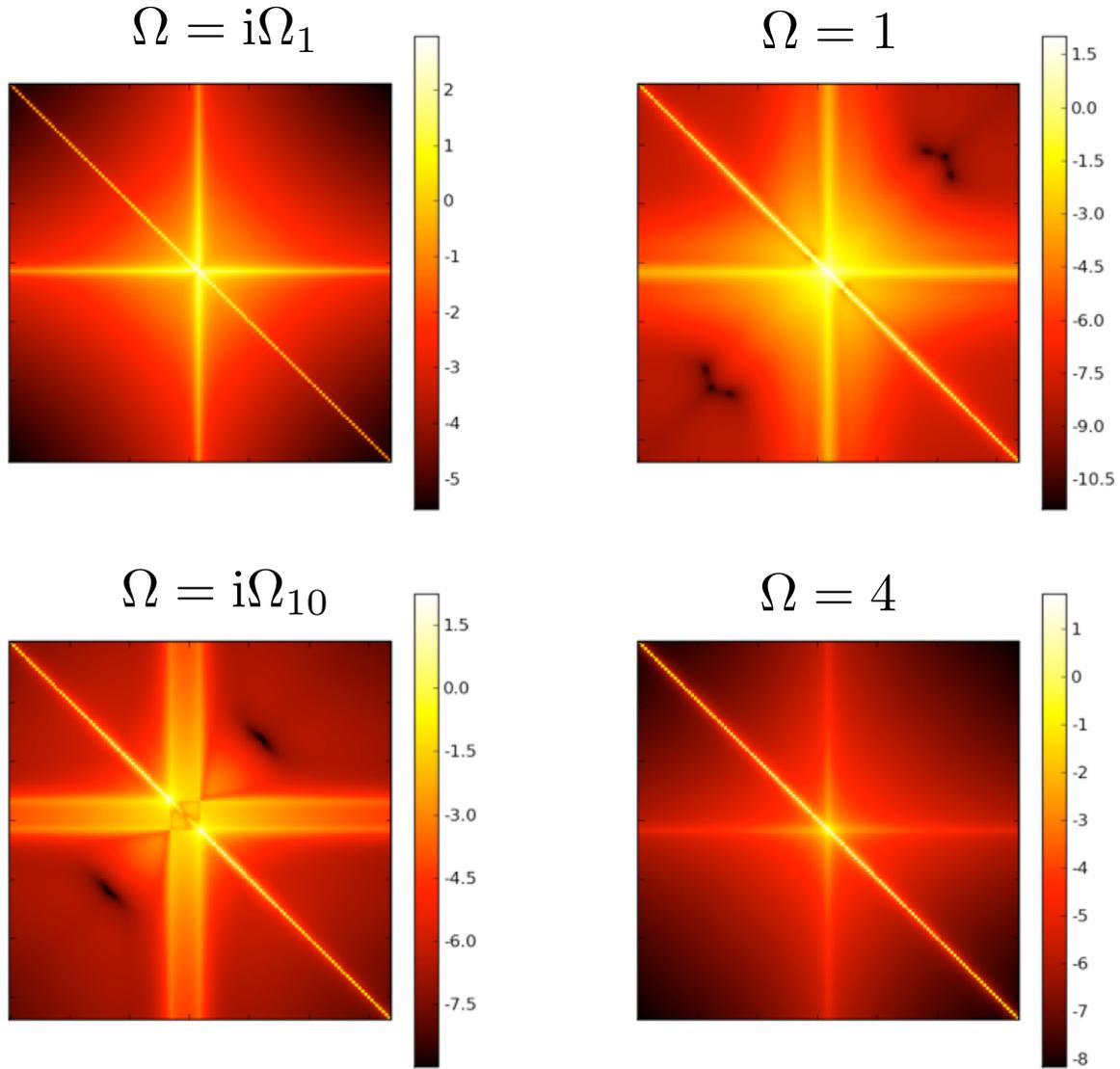
Figure 3.24.: Log plot of the modulus of $\chi^{zz}_{i\mu,i\nu}(\Omega)$ for bosonic Matsubara (left) and real frequencies (right). Example system is a 2-dimensional Hubbard Model ($U = 4.2$, half-filling, $t = 0.43$, $t' = 0.3t$, $N_b = 4$). Obviously the symmetries from figure 3.23 are respected. For real frequencies the region where the modulus is the largest remains in the center, whereas it splits and moves in the case of Matsubara frequencies breaking the symmetry $M_{i,j} = M^*_{-i,-j}$.

3.3.4. Overview of the Actual Calculation & Tests

Having the two-particle Green's function $\chi_{\mathrm{i}\Omega_n}^{\mathrm{loc}\,\sigma\sigma'}$, the generalized $\boldsymbol{Q}$-dependent lattice $\chi_{\boldsymbol{Q},\mathrm{i}\Omega_n}^{0}$, and local bubble $\chi_{\mathrm{i}\Omega_n}^{\mathrm{loc}\,0}$ we can evaluate the spin-spin and charge-charge dynamical lattice correlation function

$$\chi_{\boldsymbol{Q}}^{zz/cc}\,(\mathrm{i}\Omega_n) = \sum_{\mathrm{i}\nu\,\mathrm{i}\mu} \left[\chi_{\boldsymbol{Q},\mathrm{i}\Omega_n}^{zz/cc}\right]_{\mathrm{i}\nu\,\mathrm{i}\mu} \,, \tag{3.242}$$

where

$$\left[\chi_{\boldsymbol{Q},\mathrm{i}\Omega_n}^{zz/cc}\right]^{-1} = \left[\chi_{\boldsymbol{Q},\mathrm{i}\Omega_n}^{0}\right]^{-1} - \left[\chi_{\mathrm{i}\Omega_n}^{\mathrm{loc}\,0}\right]^{-1} + \left[\chi_{\mathrm{i}\Omega_n}^{\mathrm{loc}\,zz/cc}\right]^{-1} \,, \tag{3.243}$$

and

$$\left[\chi_{\mathrm{i}\Omega_n}^{\mathrm{loc}\,zz/cc}\right] = \frac{1}{2}\left\{\left[\chi_{\mathrm{i}\Omega_n}^{\mathrm{loc}\,\uparrow\uparrow}\right] \mp \left[\chi_{\mathrm{i}\Omega_n}^{\mathrm{loc}\,\uparrow\downarrow}\right]\right\} \,. \tag{3.244}$$

Since we have the general analytic formulæ for all ingredients we could imagine that a direct evaluation on the real axis was possible. However, it turns out we run into similar problems already encountered for continuing the bubble in section 3.1.9.

While the ingredients are properly defined in the entire complex plane the summation in equation (3.242) impedes the continuation. Hence, we again have to resort to the Padé method introduced in section 3.1.9.1.

From our previous work on Padé we know that the accuracy of the input data is crucial for a reliable analytic continuation. Therefore, we need means to assess the quality of our simulation and a well-defined test system where we can directly compare to correct results. Obviously such a procedure also tests the correctness of the implementation for the two-particle Green's functions.

Test Procedure   To that end, we calculate the *local* spin-z susceptibility. Its real- and Matsubara frequency version are directly accessible from the exact diagonalization solver using equation (3.65) with operators $\mathcal{O}_1 = \mathcal{O}_2 = S_{\mathrm{imp}}^z$. These results are labelled "exact" from here on. The local spin-z susceptibility can also be calculated by summing over the fermionic Matsubara frequencies in (3.244). Using the trivial identity

$$\left[\chi_{\mathrm{i}\Omega_n}^{\mathrm{loc}\,zz/cc}\right]^{-1} = \left[\chi_{\mathrm{i}\Omega_n}^{\mathrm{loc}\,0}\right]^{-1} - \left[\chi_{\mathrm{i}\Omega_n}^{\mathrm{loc}\,0}\right]^{-1} + \left[\chi_{\mathrm{i}\Omega_n}^{\mathrm{loc}\,zz/cc}\right]^{-1} \,, \tag{3.245}$$

we can test the framework and all ingredients: the two-particle Green's function (3.230a-3.230d), its evaluation (3.224), the unconnected local bubble, and the Matsubara summation (3.242) over the finite roaming matrices. Thus, we check the entire simulation except for the lattice propagator part $\chi_{\boldsymbol{Q},\mathrm{i}\Omega_n}^{0}$.

Direct Analytic Continuation   Evaluating (3.242) for $z = \Omega + \mathrm{i}\eta$ indeed verifies that the mixed representation with Ω being real and $\mathrm{i}\nu$, $\mathrm{i}\mu$ Matsubara frequencies does not give proper physical results. The problem is caused by the summation over Matsubara frequencies, where spurious additional poles in complex plane are generated (cf. section
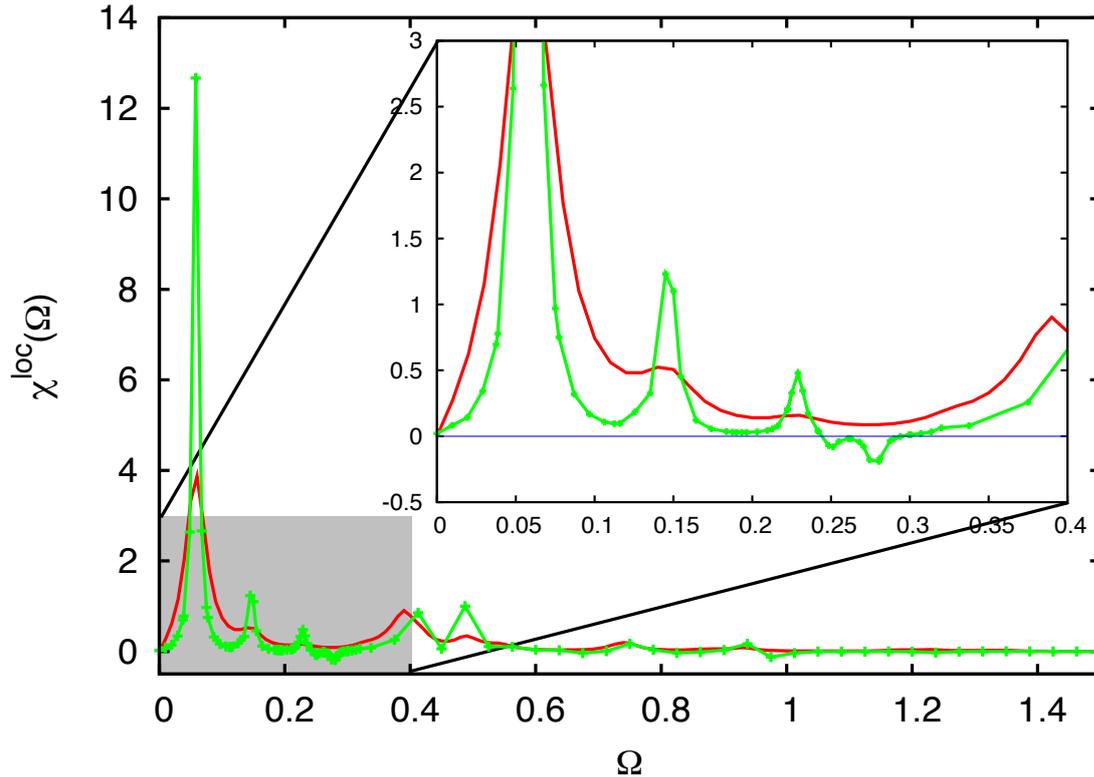
Figure 3.25.: Mixed approach for local spin-z susceptibility in a 3-dimensional periodic Anderson model with ($V = 0.3$, $U = 1.0$, $t = 1.0$, $\beta = 100$, $N_b = 3$ and filling $\langle n_{\mathrm{imp}} \rangle = 0.88$). We indeed find that the summation in (3.242) impedes the analytic continuation, since it implicitly generates spurious poles in the complex plane (cf. 3.1.9). These manifest themselves as poles with negative weight. Surprisingly, the general peak structure is restored regardless.

3.1.9). Figure 3.25 shows the outcome of this mixed approach (green curve) in comparison to the exact result (red curve).

Surprisingly, the peaks are reproduced quite well at first glance. However, a closer analysis shows stable negative and therefore unphysical spectral weight (see inset). Moreover, we cannot systematically improve the results.

Evaluation Technique To use the Padé method we need the Matsubara susceptibility as accurately as possible. The main and foremost accuracy problem arises from the finite matrix size. To overcome this problem we employ the roaming vertex scheme introduced in section 3.3.3. Since the shift is only exact for even Matsubara frequencies we only take those into account. In addition, we perform the calculation of equation (3.242) for different matrix sizes and extrapolate to infinite matrix dimensions. For a fixed Matsubara frequency, an example extrapolation is shown in figure 3.26 for a 5-dimensional periodic
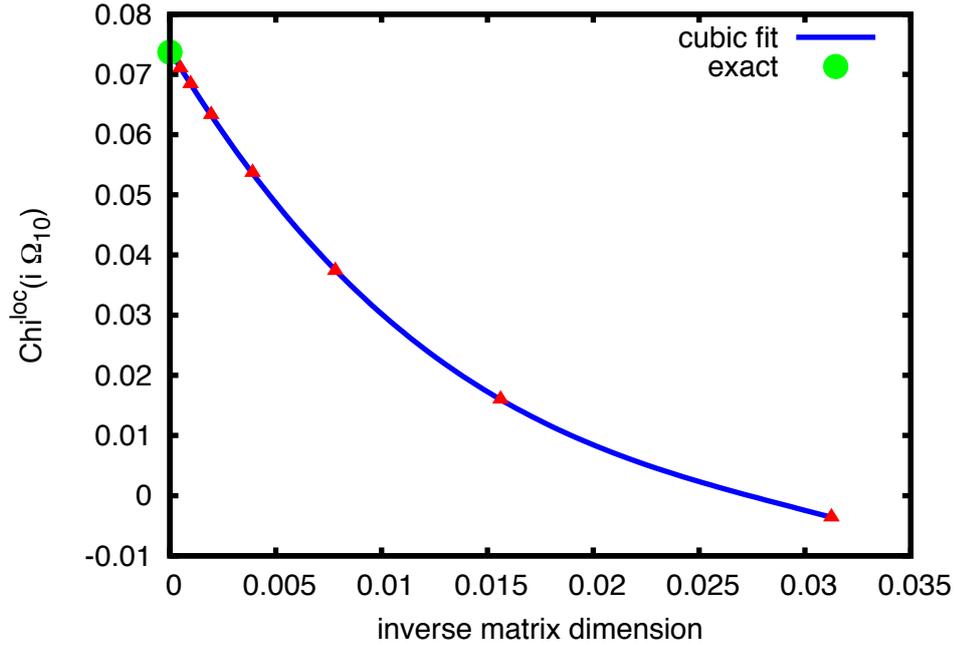
Figure 3.26.: Extrapolation to infinite matrix dimension for the tenth Matsubara frequency of the local spin-z susceptibility in a 5-dimensional periodic Anderson model with $V = 0.8$, $t = 1.0$ and $U = 4.2$ and $\langle n_{\text{imp}} \rangle = 0.88$. The green dot denotes the exact result from ED. For matrix dimensions 32-256 we find a deviation from the exact result of about 1.4%; For 32-2048 it is 0.4%.

Anderson model with $V = 0.8$, $t = 1.0$ and $U = 4.2$ and $\langle n_{\text{imp}} \rangle = 0.88$. The green dot denotes the exact result as derived from an exact diagonalization. We fit the data of different matrix sizes with a cubic function and extrapolate. For matrix dimensions 32-256 we find a deviation from the exact result of about 1.4%. For dimensions 32-2048 the extrapolation improves giving a deviation of about 0.4%. For smaller U smaller matrices suffice. For instance, when $U = 0.5$ we find for the same range of matrix dimension a deviation of about 0.02%. For $U = 0$ the matrix is diagonal.

In our production implementation we evaluate (3.242) for matrix sizes $D_{\text{max}} - n \cdot D_{\text{step}}$, where D_{max} gives the maximal matrix size (e.g. $D_{\text{max}} = 2048$), n usually runs from $n = 0 \to 10$ and D_{step} denotes the step size (e.g. $D_{\text{step}} = 32$).

Since the extrapolations work so well, we also consider higher than cubic fits. Figure 3.27 shows the relative deviation for higher-order polynomial extrapolation from the exact result. The colors red/green/blue/magenta encode third-/forth-/fifth-/sixth-order polynomials. Indeed we find that the higher the order the better the extrapolation. This is quite a remarkable result, as the accuracy improves by about 3 orders of magnitude when going from $D_{\text{max}} = 512$ (squares) to $D_{\text{max}} = 2048$ (triangles). For $D_{\text{max}} = 2048$
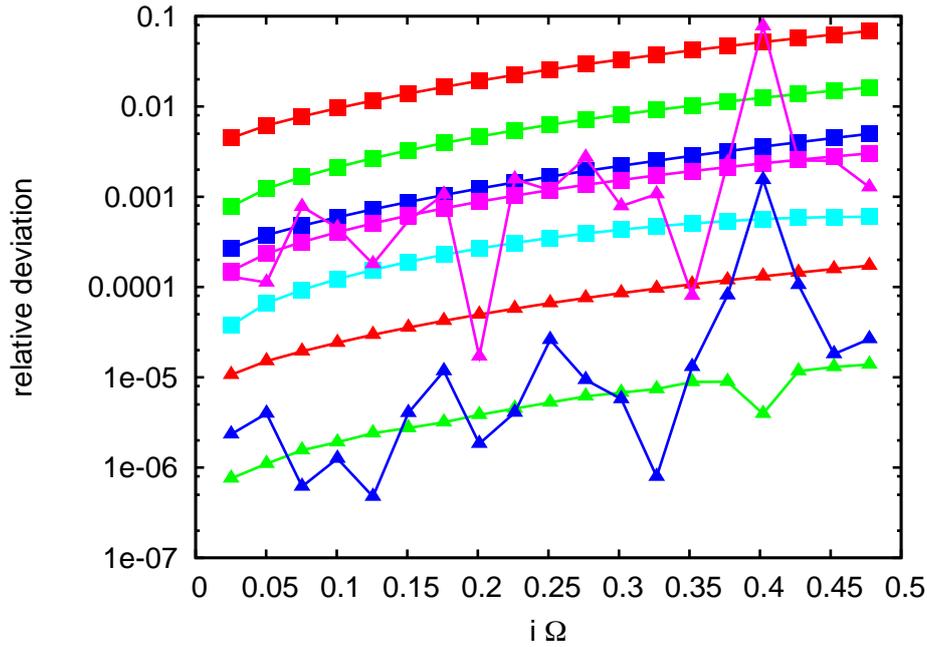
Figure 3.27.: Relative deviation of different extrapolation orders to the exact result for the local spin-z susceptibility in a 3-dimensional periodic Anderson model (model S) with $V = 0.25$, $t = 1.0$ and $U = 1.2$, $\epsilon_{\mathrm{imp}} = -0.4$ and $\langle n_{\mathrm{imp}} \rangle = 0.95$. The colors red/green/blue/magenta encode third-/forth-/fifth-/sixth-order polynomials. Squares and triangles denote matrices with $D_{\max} = 512$ and $D_{\max} = 2048$, respectively. For the squares higher-order extrapolations clearly lead to smaller deviations. For cubic polynomials the larger vertices give results better by about 3 orders of magnitude.

higher-order extrapolations, however, seem to become problematic. For these matrices we obtain the best results for a forth-order extrapolation.

Padé and Stability Analysis   Using only even bosonic Matsubara frequencies and setting the imaginary part of the input data to *exactly* zero (cf. the discussion in section 3.1.9.1) we perform the Padé analytic continuations and compare with the exact results. From figure 3.27 we know that the error in the Matsubara correlation functions increases with $i\Omega$. We therefore have to find a trade-off between the error introduced and information gained by using more frequencies. Technically we employ the Padé method for many different tuples and then take a robust representative curve. For our tests here we choose $N = 17$ and $N = 19$.

The plots in figure 3.28 present our findings for matrices of dimension 2048 (upper
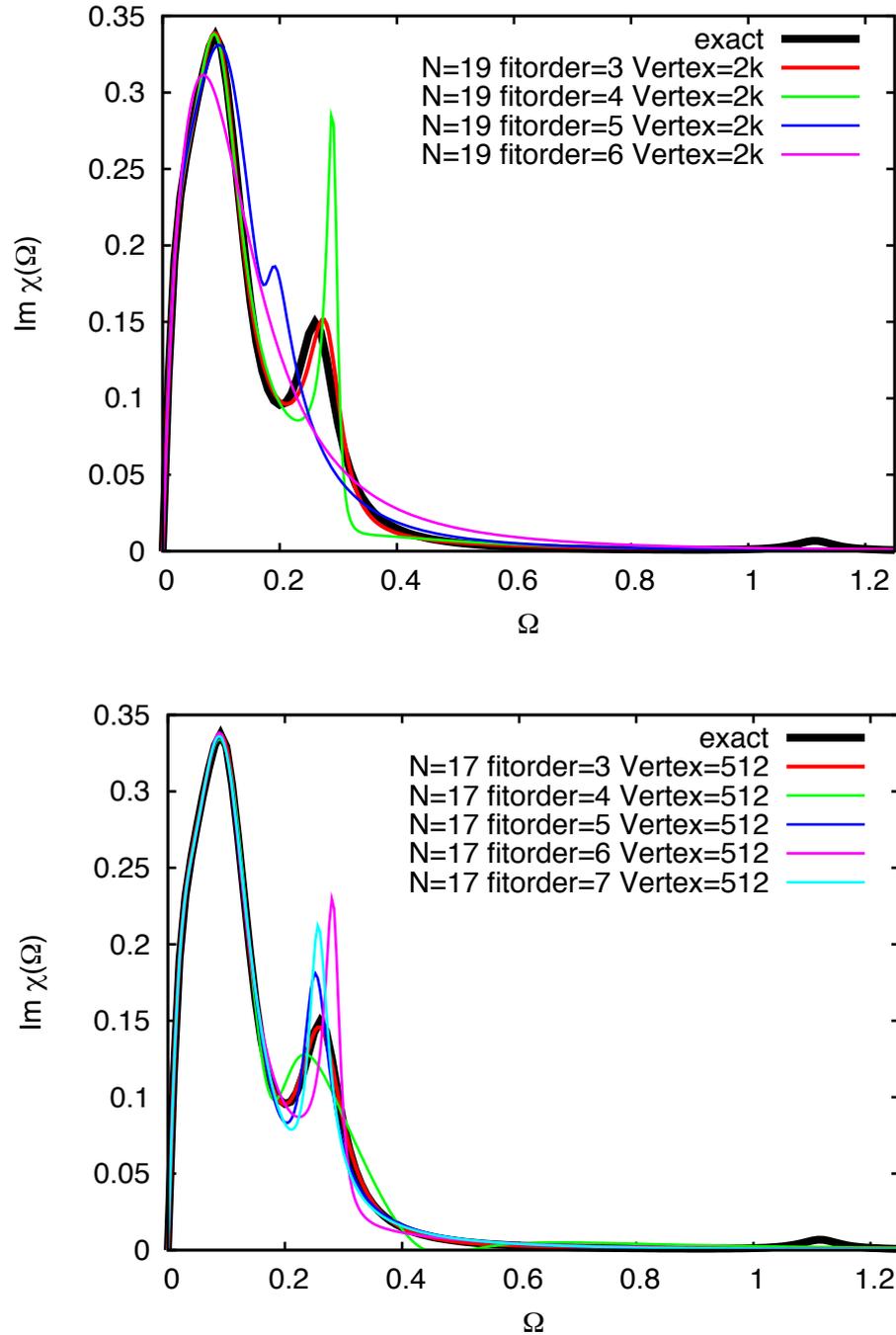
Figure 3.28.: Analytically continued local spin-z susceptibility based on equation (3.242) for a 3-dimensional periodic Anderson model (model S) with $V = 0.25$, $t = 1.0$ and $U = 1.2$, $\epsilon_{\mathrm{imp}} = -0.4$ and $\langle n_{\mathrm{imp}} \rangle = 0.95$. The color codes are consistent with figure 3.27. The matrix sizes are $D_{\mathrm{max}} = 2048$ (upper plot) and $D_{\mathrm{max}} = 512$ (lower plot). Even though the absolute deviation for the higher-order polynomials is smaller, the results from an extrapolation based on cubic polynomials give consistently better results (see text).
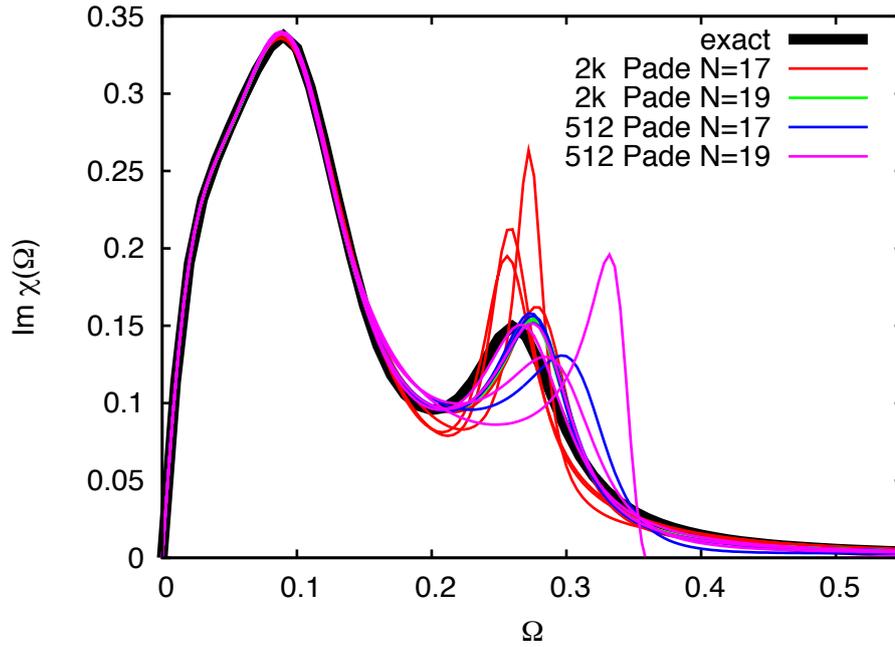
Figure 3.29.: Analytically continued local spin-z susceptibility from figure 3.28 for the cubic polynomial extrapolation with artificially noisy data (uniform noise with amplitude $5 \cdot 10^{-8}$) to assess the stability of the peaks. We find that the low-energy peak is very stable. The second peak is stable enough to determine its position roughly, whereas extracting the $\boldsymbol{Q}$-dependence reliably requires calculations at higher accuracy.

plot) and 512 (lower plot). The colors of the curves coincide with the definitions used in figure 3.27.

Interestingly, we find that the extrapolation using cubic polynomials consistently gives the best results, even though their relative error (cf. figure 3.27) is significantly larger compared to all the other extrapolations. Obviously, an improvement in the absolute deviation itself does not automatically lead to better results after the Padé method's black magic. We also see that the continuation for both matrix sizes agrees very well with the exact result. Interestingly, the continuation based on the smaller vertex gives slightly more accurate data. Both capture the two predominant peaks well but miss the small high-energy feature at about $\Omega = 1.1$. Higher-order extrapolations only describe the low-energy peak except for the sixth-order vertex of dimension 2048. It even fails to reproduce this peak. This is, however, not surprising when we take its strongly fluctuating relative error in figure 3.27 into consideration. Hence, we will use cubic polynomials for the extrapolation from here on.

In order to assess the stability of the analytic continuation we add a small noise on top of the Matsubara input data. The noise is an additive uniformly distributed random variable fluctuating between $\pm 5 \cdot 10^{-8}$. Figure 3.29 gives the results where curves of

like color denote random numbers from different seeds. Under this perturbation the low-energy peak remains stable and therefore can be considered a reliable result even if we had no exact (black) result to compare to. The robustness of this feature stems from the large weight of the peak and, more importantly, its proximity to the real axis. The peak at $\Omega \approx 0.27$ is significantly less stable as mentioned before. While its position can be roughly determined, the weights and consequently the $\boldsymbol{Q}$-dependence is not resolved reliably.

To actually discriminate the good and stable from the bad unstable peaks we need a lot of tests and a thorough stability analysis. The Padé method can give surprisingly accurate results. However, constant vigilance against this magical method is important.

Lattice Susceptibility   We apply the aforementioned evaluation and stability assessing techniques also to the dynamical lattice susceptibility. For the necessary Brillouin zone integrations we employ a Monkhorst and Pack [118] $\boldsymbol{k}$-grid yielding more accurate data. Since absolute errors alone do not necessarily improve the analytic continuation we also try to minimize systematic and fluctuating errors. To that end, we choose all vectors in the lattice bubble to be commensurate with the $\boldsymbol{k}$-grid.

3.4. Application to the 3-dimensional Anderson Model

As an application of our method we evaluate the lattice response functions for the 3-dimensional periodic Anderson model with next-neighbor hopping. The dispersion relation for the conduction electron reads

$$\varepsilon_{\boldsymbol{k}} = -2t \sum_{i=x,y,z} \cos(k_i) \; , \qquad (3.246)$$

where we set $t = 1$. Consequently, their bandwidth is 12. For the Brillouin zone integral we employ a Monkhorst-Pack $(^1/_2, ^1/_2, ^1/_2)$-shift in units of the $\boldsymbol{k}$-mesh.

Table 3.2 provides all periodic Anderson model parameters as well as the self-consistent DMFT results for the associated Anderson impurity model. The corresponding impurity

Table 3.2.: PAM and self-consistent AIM bath parameters

model	S
t	1.000
U	1.200
V	0.245
ϵ_p	0.000
ϵ_f	-0.400
β	500
μ	-0.241
boltz	10^{-6}
α	2.0
$\#k$	48
V_1 / ϵ_1	0.0409/$-$0.0548
V_2 / ϵ_2	0.0117/ 0.0003
V_3 / ϵ_3	0.0430/ 0.0616
$\langle n \rangle$	0.95

and PAM Green's functions are presented in figure 3.30.

We see that the self-consistency condition $G_{\mathrm{imp}} = G_{ff}$ is satisfied quite well. Moreover, the c-electron Green's function closely resembles the 3-dimensional density of states. Only at the excitation energies of the f-electrons we find significant dips originating from the relatively small hybridization V.

Dynamical Local Susceptibilities   From this self-consistent solution for the associated Anderson Impurity Model we calculated the local two-particle Green's function and perform the stability tests already presented in the previous section. We find that the
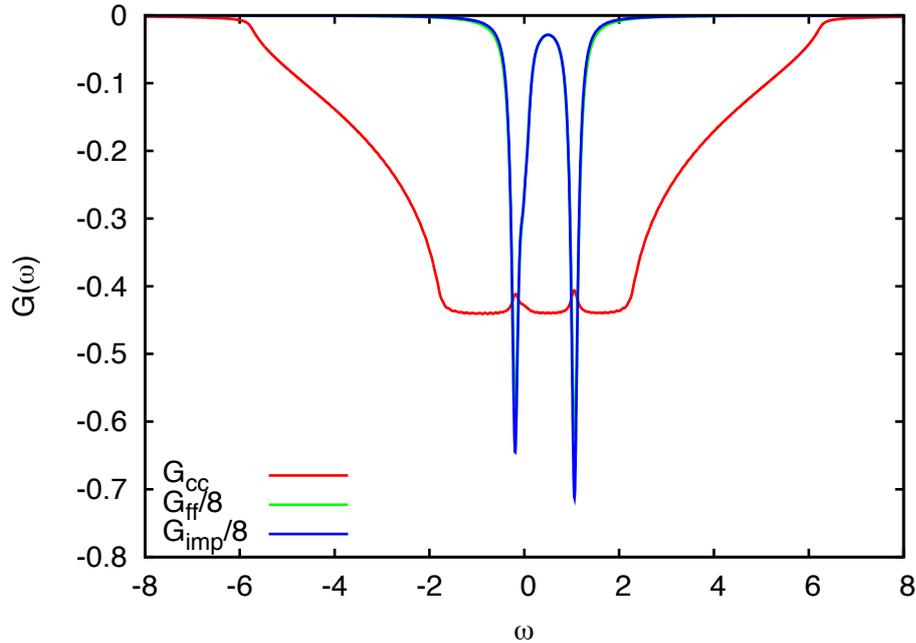
Figure 3.30.: Impurity (blue curve), f-electron (green curve), and c-electron (red curve) Green's functions for the model of table 3.2. We find hardly any deviation between the f-electron and impurity Green's function (self-consistency condition). The c-electron Green's function is close to the 3-dimensional DOS and significantly deviates only at the pronounced excitation energies of the f-electrons. The impurity/local quantities have been scale by a factor of 4 for display purposes.

first pronounced feature (at about $\Omega = 0.1$) in the local spin-z susceptibility is reliable. The existence of a second feature is also confirmed. However, neither its weight nor its exact position can be reliably determined with the current accuracy. With larger and more accurate vertices we could also converge this feature requiring, however, even higher computational efforts.

Due to the small hybridization we expect the vertex correction to the lattice bubble to be similar to the vertex correction to the impurity bubble. A comparison of both impurity functions is given in figure 3.31. We see that the impurity bubble being evaluated on the Matsubara axis can be reliably continued (red curves). This is even true for the high-energy feature at about $\Omega = 1.25$. We observe a strong effect of the vertex correction. The high-energy feature is completely suppressed in the local susceptibility. In the low-energy range we find a redistribution from the second peak at about $\Omega = 0.27$ to the first when correcting χ_0^{loc} obtaining χ^{loc}.
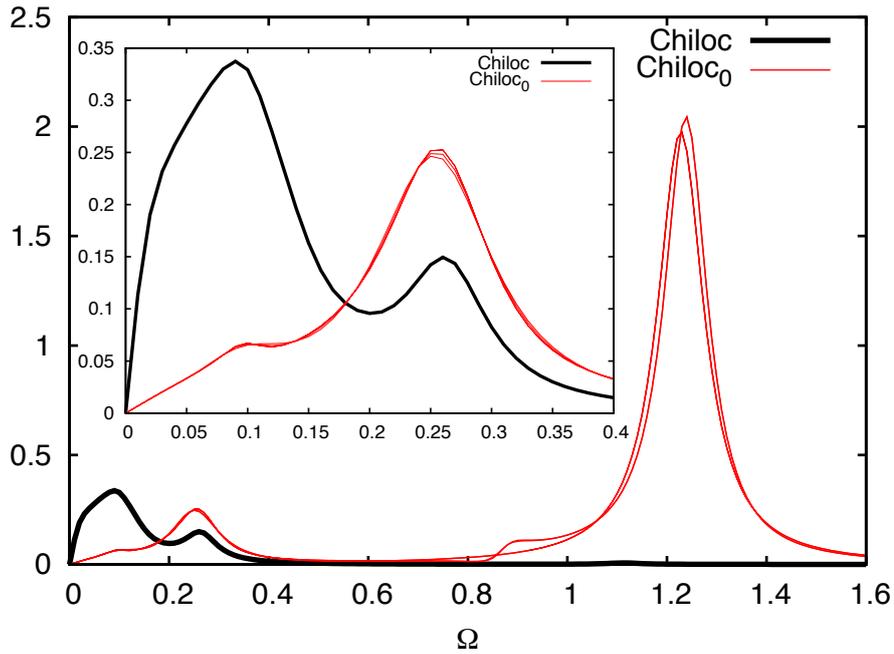
Figure 3.31.: Local susceptibility χ_0^{loc} (red curves denote different number of Matsubara frequencies) and χ^{loc} (black, ED data) for the model of table 3.2. We find that the Padé analytic continuation for χ_0^{loc} works reliably even for the high energy peak. The effect of the vertex correction is to (a) suppress this high-energy peak and to redistribute weight in the low-energy range (inset). There weight from the second peak at about $\Omega = 0.27$ is shifted to the first one. For the lattice susceptibility we expect a similar process to happen due to the small V.

Dynamical Lattice Susceptibilities   The only difference that puts the simulation for different models apart from one another is the self-consistency condition of DMFT and the $\boldsymbol{Q}$-dependent lattice bubble $\chi^0_{\boldsymbol{Q}\text{i}\Omega}(\text{i}\nu)$ given by equation (3.216)

$$\chi^0_{\boldsymbol{Q}\,\text{i}\Omega_n}(\text{i}\nu) = -\frac{1}{N_k}\sum_{\boldsymbol{k}} G(\boldsymbol{k},\text{i}\nu)\,G(\boldsymbol{k}+\boldsymbol{Q},\text{i}\nu+\text{i}\Omega_n) \ . \tag{3.247}$$

For the periodic Anderson model we use the lattice f- electron Green's function

$$G(\boldsymbol{k},\text{i}\nu) = G_{ff}(\boldsymbol{k},\text{i}\nu) = \left(G^{\text{imp}}(\text{i}\nu) + \Delta(\text{i}\nu) + \frac{V^2}{\text{i}\nu + \mu - \epsilon_k}\right)^{-1} \ . \tag{3.248}$$

Figure 3.32 gives the stability analysis from the bubble with respect to different number of tuples. We observe the usual picture: The low-energy peaks are resolved well, whereas
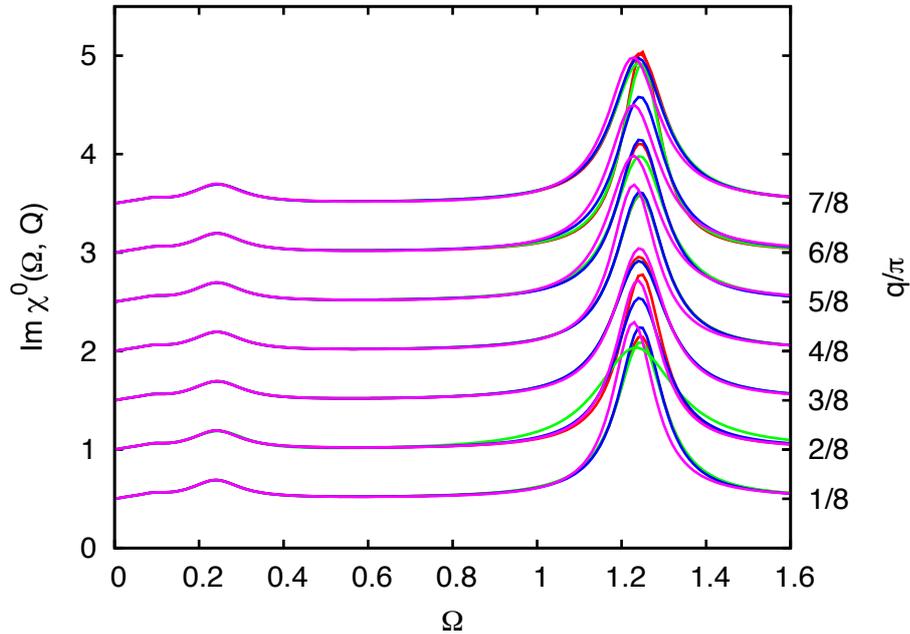
Figure 3.32.: Lattice bubble for the f-electrons of different $\boldsymbol{Q} = q \cdot (\pi, \pi, \pi)^t$ vectors for the model of table 3.2, where the colors denote approximants for different N. We find good agreement with the local bubble χ_0^{loc}. However, here the high-energy peak is not as stable. The lower one is reliably reproduced.

the high-energy peak shows quite a bit of fluctuation. Agreement with the local bubble χ_0^{loc} is good, as we have already expected due to the small hybridization.

From these building blocks we obtain the charge-charge and spin-spin lattice susceptibility. Figure 3.33 shows the stability analysis with respect to different tuples for these two susceptibilities, where the charge susceptibility is in the upper and the spin in the lower plot. We find that the most pronounced feature is stable in both susceptibilities. The small peak in the charge susceptibility, albeit at lower energies, is not so well-converged. The general structure is similar to the local susceptibility. Also for these two lattice correlation functions the peak at 1.25 is suppressed and weight is redistributed in the low-energy region.

To better assess the stability in this region we choose the $N = 29$ tuple Padé approximant and add uniformly distributed noise of amplitude $5 \cdot 10^{-8}$ (see figure 3.34). We find that the first peak of the $S^z S^z$-correlation function remains stable. It is a reliable result. For the dominant (second) peak in the charge response function we observe small fluctuations. For the $q = 7/8$ $\boldsymbol{k}$-vector the deviation can be quite strong. Moreover, the first peak is hardly converged at all.

Finally, figure 3.35 presents the unperturbed results with $N = 29$ for the low-energy
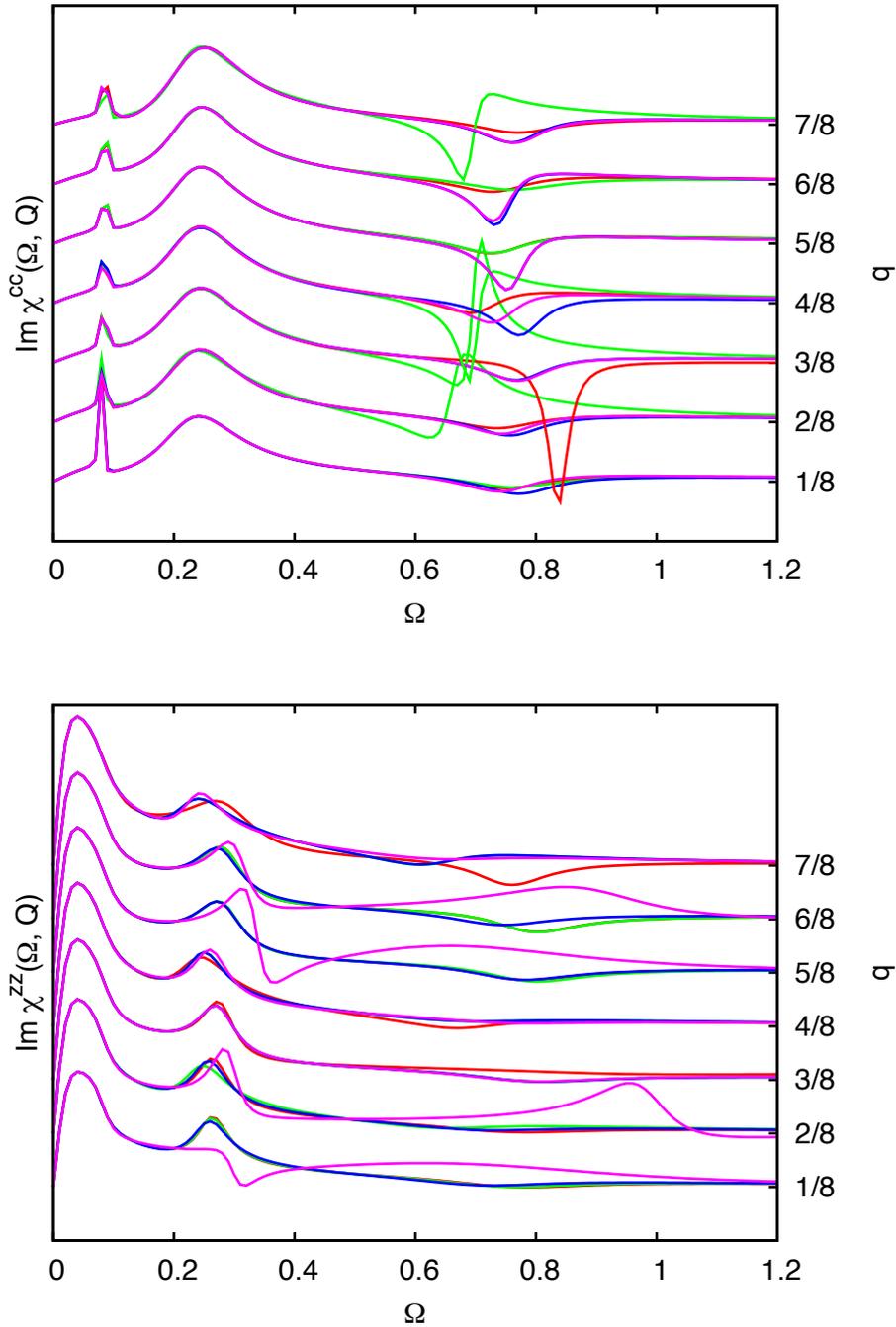
Figure 3.33.: Stability analysis w.r.t. the number of tuples N for the charge (upper plot) and spin (lower plot) dynamical lattice susceptibility of the f-electrons at different $\boldsymbol{Q} = q \cdot (\pi, \pi, \pi)^t$ vectors for the model of table 3.2. We find that for both functions the dominant feature is well-converged. For the charge susceptibility this is the second peak, while the first one still shows some fluctuation. For the spin susceptibility the first coincides with the one carrying the largest weight. At higher Ω the continuation becomes unreliable.
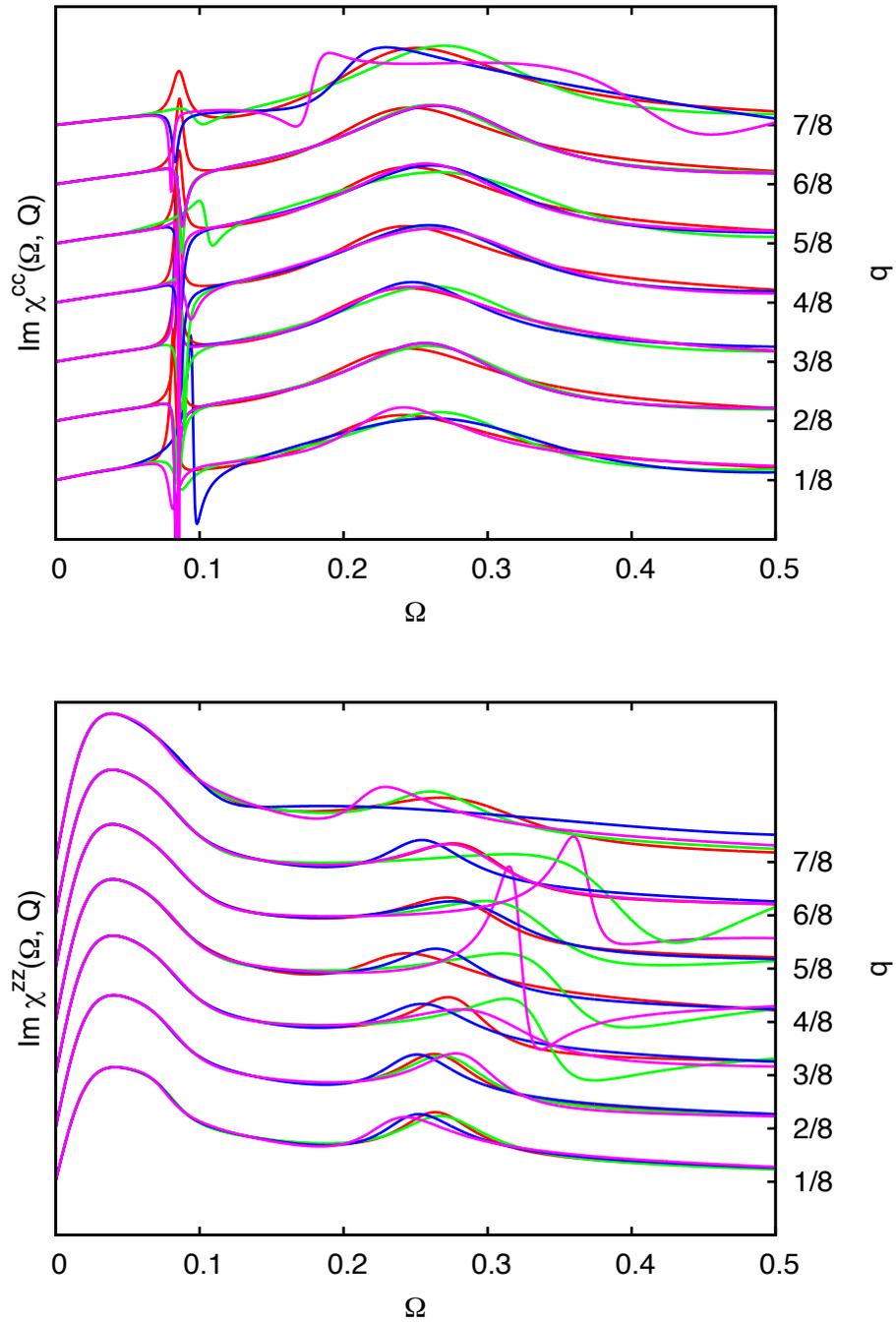
Figure 3.34.: Stability analysis w.r.t. additional uniform noise (amplitude $5 \cdot 10^{-8}$) for the charge (upper plot) and spin (lower plot) dynamical lattice susceptibility (model of table 3.2) in the low-energy region. While the first peak of the spin susceptibility remains stable and can be considered a reliable result, this is not true for the charge susceptibility. The dominant (second) feature is relatively stable except for $q = 7/8$.
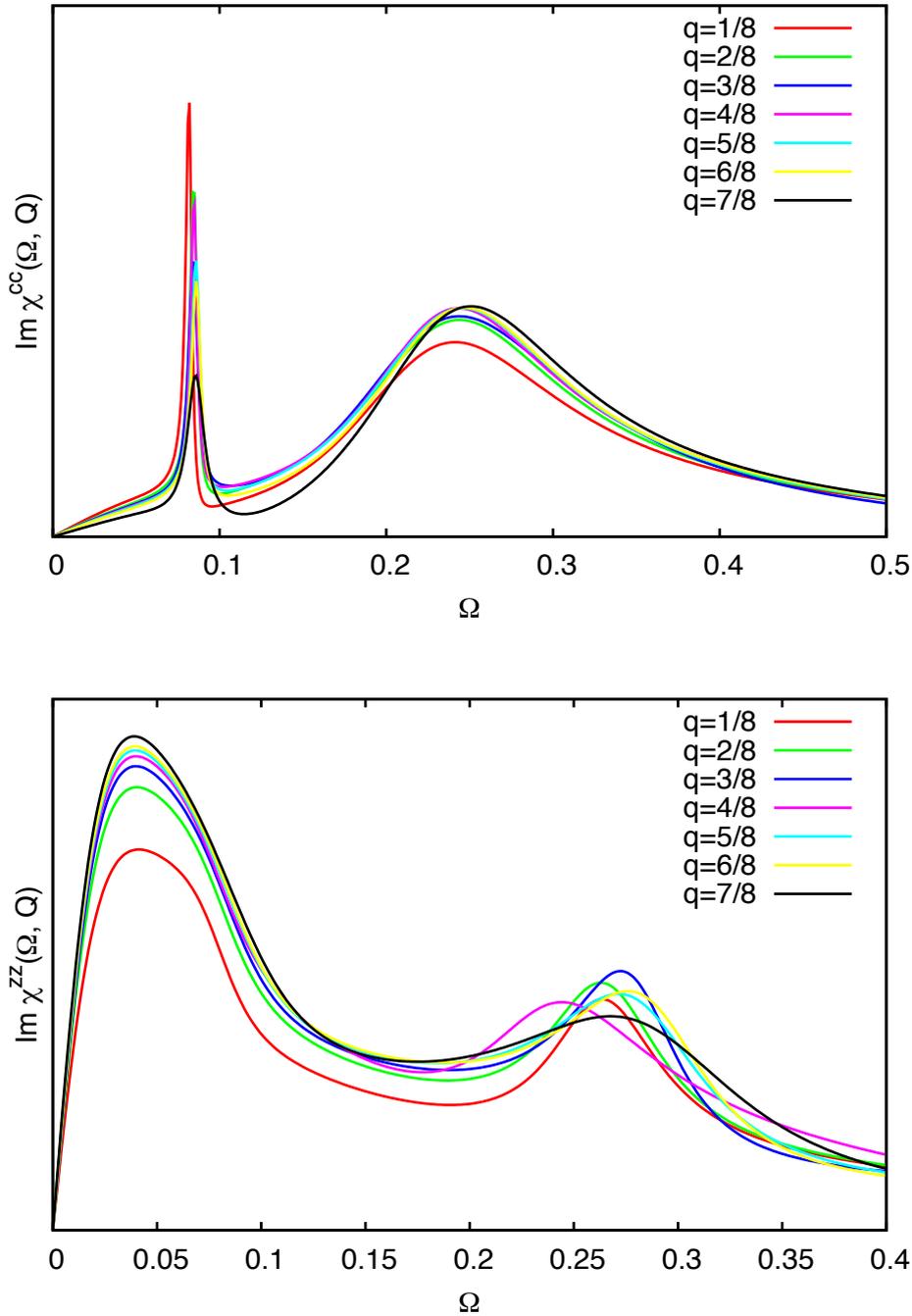
Figure 3.35.: Stable dispersion of dynamical lattice susceptibility for charge (upper plot) and spin (lower plot) of the f-electrons at different $\boldsymbol{Q} = q \cdot (\pi, \pi, \pi)^t$ vectors for the model of table 3.2. For χ^{zz} we find that the first peak gains weight for higher $\boldsymbol{Q}$. The second peak is not stable enough for reliably extracting the $\boldsymbol{Q}$-dependence. For χ^{cc} we can merely determine a rough estimation for the peaks position, while the weights are not sufficiently well converged.

region. Different colors denote different $\boldsymbol{Q}$ vectors. For the charge correlation functions we merely obtain the rough positions of the excitation energies. As seen in the previous tests their weight is also not sufficiently well converged at the current level of accuracy. The spin susceptibility, on the other hand, not only gives accurate positions but also stable weights. We observe a reliable $\boldsymbol{Q}$-dependence in the pronounced first peak. Located at about $\Omega = 0.05$ it becomes the more pronounced the larger q.

3.5. Summary

We now have means to obtain lattice susceptibilities for strongly correlated model systems within the DMFT framework. Even tough we studied the periodic Anderson model as an application, the method is directly generalizable to other models – for instance the Hubbard model. The computations are challenging from the computing perspective and can put thousands of processors to good use. The current bottleneck of the simulation is, however, the analytic continuation. Using the Padé method requires plenty of checks and tests to assess whether its results are reliable or not. We found that even higher accuracy data does not necessarily improve the results. The calculations still have to be tested carefully using the stability analysis we have introduced. In so doing, we are able to tell reliable structures from unstable artefacts of the Padé method.

Summary

Seeking an understanding of one of the most challenging classes of matter, strongly-correlated systems, we try to simulate and predict the interesting processes found in experiments for these compounds. As strongly correlated systems are very sensitive to perturbations, it is of key importance to reliably calculate the corresponding response functions. In this thesis we tackled the problem from two different perspectives: the construction of appropriate models (chapters 1 and 2) and the actual evaluation of lattice response functions (chapter 3).

We devised a method for deriving realistic material-specific parameters for a description of organic molecular crystals in terms of a generalized Hubbard model. The main problem is to properly evaluate the screening of the bare Coulomb integrals. For this we take a three-step route. In the first chapter we deal with the screening contributions of all molecules. Clearly, an approach based on quantum mechanics is infeasible – even for the most powerful supercomputers. Hence, we develop a classical electrostatic method which effectively describes a non-polar molecular crystal (with localized charge distributions at the lattice sites) in terms of a microscopic (polarizable) point-dipole model (MPDM). Within this model we show how to obtain the arrangement of dipole moments and the energy corrections due to screening. In one- and two-dimensional systems we find exotic screening and anti-screening effects, which we can understand in terms of an anti-screening volume argument.

In chapter 2 we discuss the actual method for the derivation of the realistic parameters. We start by constructing a model crystal from unit cells determined by X-ray diffraction experiments. Replacing the molecules in the experimental unit cell by DFT relaxed structures we obtain a well-defined crystal structure. Using FHI-aims we evaluate the hopping parameters as well as the bare- and intra-molecularly screened Hubbard parameters. With a dimer approach the hopping-matrix elements can be directly evaluated from the bonding/anti-bonding splitting of the highest-occupied (donor molecule) or lowest-unoccupied (acceptor molecule) molecular orbital. The bare Coulomb integrals readily follow from density integrations of the molecular orbital. This is the conceptually

first step in our three-step renormalization procedure. Second, to take the Coulomb parameter renormalization due to the electrons inside the molecules into account, we charge a single molecule (for U_0) or a dimer (for V_0), where the energetic response due to the relaxation of the orbitals gives the screening. In the third step we use the MPDM developed in chapter 1.

Applying this procedure to two compounds, TTF-TCNQ and (BEDT-TTF)$_2$I$_3$, we obtain a realistic set of model parameters. Typical of organic crystals, we find relatively small hopping-matrix elements in comparison to the screened Coulomb integrals. For the local Hubbard-U screening is most pronounced, reducing the value to about 30% of the bare integral. Our results for TTF-TCNQ put early estimates given by Hubbard on a solid footing. For both materials we find that the next-neighbor interaction, which is usually neglected in Hubbard model calculations, has a sizable contribution. In (BEDT-TTF)$_2$I$_3$ its values are roughly 40% of the effective Hubbard-U, whereas in TTF-TCNQ it even is about 65%. Evidently, for both longer-range Coulomb interactions should not be neglected.

For TTF-TCNQ we show that the inclusion of V is key to solving a long-standing problem: In former treatments of TTF-TCNQ using the t-U Hubbard model the hopping-matrix element t had to be twice as large as the calculated value in order to match experiments. Including V, we show that its effect is a simple broadening of the spectrum, mimicking the doubling of $2t$. We could also exclude the presence of Hubbard-Wigner-type states suggested by Hubbard. Moreover, using the correct hopping t puts the temperature scale T_J, below which signatures of spin-charge separation are found, into ranges consistent with experiment. For both systems, (BEDT-TTF)$_2$I$_3$ and TTF-TCNQ, we find that sufficient pressure should lead to interesting phenomena. In the former uniaxial pressure might significantly change the t/V-ratio due to its strong dependence on molecular orientations. In TTF-TCNQ hydrostatic pressure should drive the system even closer or across the ferroelectric instability.

Having determined the parameters of the model Hamiltonians we now strive for an understanding of the processes inside these systems. We therefore need a solution to the Hamiltonian and, for comparison with experiment, dynamical lattice susceptibilities. Both problems prove to be difficult.

One of the most successful techniques to tackle these models is dynamical mean-field theory (DMFT), where the lattice Hamiltonian is self-consistently mapped onto an artificial single-impurity Anderson model. By construction this gives a good approximation to local correlations and direct access to local quantities such as the self-energy and susceptibilities. With the self-energy we can readily obtain the lattice Green's function employing the Dyson equation. Lattice susceptibilties are, however, more complicated and cannot be built from the knowledge of the self-energy alone.

We solve this problem by deriving the local vertex function, which is based on the two-particle Green's function of the impurity. From this function and the impurity and lattice particle-hole bubbles we can then, in a Dyson-like way, evaluate the lattice susceptiblities. However, the two-particle Green's function is a very complex quantity which is cumbersome to evaluate. It is constructed by four field-operators acting at, in general, four different times. Assuming time translation invariance and paramagnetism it

is a quantity of three frequency and two spin arguments – still, a challenge to evaluate and process. Even with small numbers of bath sites we can easily make efficient use of thousands of processors of the latest supercomputers.

An advantage of the procedure is that it easily generalizes to other model Hamiltoninans, since it only relies on the solution of the DMFT Anderson impurity model and lattice Green's function.

A direct analytical continuation of lattice susceptibilities to the real-frequency axis was not possible. Hence, we resort to the Padé approximants to continue the Matsubara susceptibilities to the real axis. For this to work reliably we need these functions as accurate as possible. Since in numeric calculations the vertices need to be finite matrices we perform the calculations for different matrix dimensions and extrapolate to the infinite-size limit. Moreover, noticing that the region of largest modulus moves within the complex frequency plane we introduced a "roaming vertex" scheme, to capture this most pronounced region. This enables us to reliably use the Padé method and extract robust susceptibilities on the real axis. As an application we choose a three-dimensional periodic Anderson model, where we resolve the low-energy $\boldsymbol{Q}$-dependence of the spin-spin and charge susceptibility.

Ewald Method

In 1921 Peter Ewald published a fast and flexible summation procedure for calculating the total electrostatic energy of a lattice which works for arbitrary crystal structures [7]. The slowly converging sum is recast into two rapidly converging parts, one in real space and one in reciprocal space, and additional terms.

In this appendix we will derive a generalized version of the Ewald summation due to Bertraut for the total electrostatic energy of a lattice. For more information on extensions and further generalizations of this method refer to the work of Toukmaji and Board [119].

A.1. Generalized Derivation of the Ewald Summation

Thirty years after Ewald's publication Bertraut [120] derived a generalization of the method elegantly expounded in [16]. We start with the calculation of the total electrostatic energy E^{tot} of a lattice of point charges q_j located at $\boldsymbol{r}_j = \boldsymbol{R}_i + \boldsymbol{x}_h$, where the $\boldsymbol{R}_i$ form a Bravais lattice and the $\boldsymbol{x}_h$ denote the vectors to the basis in the unit cell. Hence, $j = (i, h)$ is a multi-index. We can write the electrostatic energy as

$$E^{\mathrm{tot}} = E^{\mathrm{inter}} + E^{\mathrm{self}} \, , \tag{A.1}$$

where we also included the (infinite) self-energy for reasons becoming clear later.

As a consequence of Gauss's theorem we can replace the point charges with non-overlapping spherical charge densities σ_j, which only need to obey the normalization condition

$$\int \mathrm{d}^3 x \, \sigma(|\boldsymbol{x}|) = 1 \, . \tag{A.2}$$

Thus, the total charge density is

$$\varrho(\boldsymbol{x}) = \sum_j q_j \sigma(\boldsymbol{x} - \boldsymbol{r}_j) \ . \tag{A.3}$$

Due to the translational invariance with respect to the lattice vectors $\boldsymbol{R}_i$, it is practical to transform the charge density in reciprocal space. We obtain

$$\varrho(\boldsymbol{r}) = \sum_{\boldsymbol{g}} \varrho_{\boldsymbol{g}} \exp\left(\mathrm{i}\boldsymbol{g} \cdot \boldsymbol{r}\right) \ , \tag{A.4}$$

where

$$\varrho_{\boldsymbol{g}} = \frac{1}{V_{\mathrm{cell}}} \int_{V_{\mathrm{cell}}} \mathrm{d}^3 r \, \varrho(\boldsymbol{r}) \exp\left(-\mathrm{i}\boldsymbol{g} \cdot \boldsymbol{r}\right) = S_{\boldsymbol{g}} \Phi_{\boldsymbol{g}} \tag{A.5}$$

and

$$S_{\boldsymbol{g}} = \sum_{h \in \mathrm{cell}} q_k \exp\left(-\mathrm{i}\boldsymbol{g} \cdot \boldsymbol{x}_h\right) \tag{A.6}$$

$$\Phi_{\boldsymbol{g}} = \frac{1}{V_{\mathrm{cell}}} \int_{V_{\mathrm{cell}}} \mathrm{d}^3 r \, \sigma(\boldsymbol{r} - \boldsymbol{r}_j) \exp\left(-\mathrm{i}\boldsymbol{g} \cdot (\boldsymbol{r} - \boldsymbol{r}_j)\right) \ . \tag{A.7}$$

$S_{\boldsymbol{g}}$ takes the role of the structure factor, whereas $\Phi_{\boldsymbol{g}}$ is similar to the atomic form factor from the basic theory of diffraction. Hence, we can rewrite

$$E^{\mathrm{tot}} = \frac{1}{2} \int_{\mathbb{R}^3} \mathrm{d}^3 r \, \mathrm{d}^3 r' \, \frac{\varrho(\boldsymbol{r}) \, \varrho(\boldsymbol{r} + \boldsymbol{r}')}{|\boldsymbol{r}'|} \tag{A.8}$$

as a sum in reciprocal space:

$$E^{\mathrm{tot}} = 2\pi V_{\mathrm{cell}} \sum_{\boldsymbol{g}} \frac{|\varrho_{\boldsymbol{g}}|^2}{g^2} = 2\pi V_{\mathrm{cell}} \sum_{\boldsymbol{g}} \frac{|S_{\boldsymbol{g}}|^2 |\Phi_{\boldsymbol{g}}|^2}{g^2} \ . \tag{A.9}$$

Inserting the σ-representation of $\varrho(\boldsymbol{r})$, equation (A.4), we obtain the equivalent description

$$E^{\mathrm{tot}} = \frac{1}{2} \sum_{ij} q_i q_j \int_{\mathbb{R}^3} \mathrm{d}^3 x \, \mathrm{d}^3 y \, \frac{\sigma(\boldsymbol{x} - \boldsymbol{r}_j) \, \sigma(\boldsymbol{x} + \boldsymbol{y} - \boldsymbol{r}_i)}{y} \ . \tag{A.10}$$

Using the convolution theorem in the form $f * g = \mathcal{F}^{-1}\left(\mathcal{F}(f) \cdot \mathcal{F}(g)\right)$ we get

$$E^{\mathrm{tot}} = \frac{V_{\mathrm{cell}}^2}{\pi} \sum_{ij} \frac{q_i q_j}{r_{ij}} \int_0^\infty \mathrm{d}k \, \frac{|\Phi_k|^2}{k} \sin\left(k r_{ij}\right) \ , \tag{A.11}$$

where $r_{ij} = r_i - r_j$. To get the electrostatic self-energy we set $r_{ij} \to 0$ and obtain

$$E^{\mathrm{self}} = \frac{V_{\mathrm{cell}}^2}{\pi} \sum_i q_i^2 \int_0^\infty \mathrm{d}k \, |\Phi_k|^2 \ . \tag{A.12}$$

Obviously the interaction energy evaluates to

$$
\begin{aligned}
E^{\text{inter}} &= E^{\text{tot}} - E^{\text{self}} && \text{(A.13)}\\
&= \frac{V_{\text{cell}}^2}{\pi} \sum_{ij} \frac{q_i q_j}{r_{ij}} \int_0^\infty \mathrm{d}k \, \frac{|\Phi_k|^2}{k} \sin(k r_{ij}) - \frac{V_{\text{cell}}^2}{\pi} \sum_i q_i^2 \int_0^\infty \mathrm{d}k \, |\Phi_k|^2 \,, && \text{(A.14)}
\end{aligned}
$$

or equivalently with equation (A.9)

$$
E^{\text{inter}} = 2\pi V_{\text{cell}} \sum_{\boldsymbol{g}} \frac{|S_{\boldsymbol{g}}|^2 \, |\Phi_{\boldsymbol{g}}|^2}{g^2} - \frac{V_{\text{cell}}^2}{\pi} \sum_i q_i^2 \int_0^\infty \mathrm{d}k \, |\Phi_k|^2 \,. \tag{A.15}
$$

Next we allow the spherical charge densities $\sigma(x)$ to overlap. As a result we need to add a correction term C to the interaction energy formula (A.15). Equation (A.14) enables us to evaluate this correction

$$
C = \frac{1}{2} \sum_{ij} \frac{q_i q_j}{r_{ij}} \left[1 - \frac{2 V_{\text{cell}}^2}{\pi} \int_0^\infty \mathrm{d}k \, \frac{|\Phi_k|^2}{k} \sin(k r_{ij}) \right] \,. \tag{A.16}
$$

For the interaction energy we therefore obtain

$$
\begin{aligned}
E^{\text{inter}} &= \frac{1}{2} \sum_{ij} \frac{q_i q_j}{r_{ij}} && \text{(A.17)}\\
&= 2\pi V_{\text{cell}} \sum_{\boldsymbol{g}} \frac{|S_{\boldsymbol{g}}|^2 \, |\Phi_{\boldsymbol{g}}|^2}{g^2} - \frac{V_{\text{cell}}^2}{\pi} \sum_i q_i^2 \int_0^\infty \mathrm{d}k \, |\Phi_k|^2 + C \,. && \text{(A.18)}
\end{aligned}
$$

Hence, the potential of atom h at $\boldsymbol{x}_h$ in the unit cell is

$$
\begin{aligned}
V(\boldsymbol{x}_h) &= \frac{\partial}{\partial q_h} E^{\text{inter}}\\
&= 4\pi V_{\text{cell}} \sum_{\boldsymbol{g}} \frac{\tilde{S}_{\boldsymbol{g}} \, |\Phi_{\boldsymbol{g}}|^2}{g^2} - \frac{2 q_h V_{\text{cell}}^2}{\pi} \int_0^\infty \mathrm{d}k \, |\Phi_k|^2\\
&\quad + 2 \sum_s \frac{q_s}{|\boldsymbol{R}_s - \boldsymbol{x}_h|} \left[1 - \frac{2 V_{\text{cell}}^2}{\pi} \int_0^\infty \mathrm{d}k \, \frac{|\Phi_k|^2}{k} \sin(k |\boldsymbol{R}_s - \boldsymbol{x}_h|) \right] \,, && \text{(A.19)}
\end{aligned}
$$

where

$$
\tilde{S}_{\boldsymbol{g}} = \sum_{s \in \text{cell}} q_s \exp(\mathrm{i} \boldsymbol{g} (\boldsymbol{x}_s - \boldsymbol{x}_h)) \,. \tag{A.20}
$$

The actual choice of the charge distribution $\Phi(k)$ is arbitrary. If we take the Gaussian charge distribution $\Phi(|\boldsymbol{k}|) = \exp(-k^2/4\pi^2\eta^2)/V_{\text{cell}}$, we obtain Ewald's method.

A.2. Ewald Summation for the Dipole Matrix

A general derivation of Ewald's method applied to lattices of point-dipoles in arbitrary dimensions is given in [121]. Cohen and Keffer applied this technique to three dimensions [122]. It has been extended for systems with non-trivial unit cells in a work of Bowden and Clark [123].

The general ansatz is to calculate the series in

$$\Gamma_{\mu\nu}(\mathbf{k}) = \nabla_\mu \nabla_\nu \frac{1}{N} \sum_{j \neq i} e^{-i\mathbf{k} \cdot \mathbf{r}_{ij}} \frac{1}{|r_{ij}|} \tag{A.21}$$

analytically by the Ewald method and then perform the derivatives. With $\boldsymbol{\tau}_{mn} = \boldsymbol{x}_m - \boldsymbol{x}_n$, i.e. the vector from atom m to atom n in the unit cell, this gives for the μ-ν components

$$
\begin{aligned}
\Gamma_{\mu\nu}^{mn}(\boldsymbol{k}) = & -\frac{4\pi}{V_{\text{cell}}} \frac{k^\mu k^\nu}{k^2} \exp\left(-\frac{k^2}{4\eta^2}\right) \\
& -\frac{4\pi}{V_{\text{cell}}} \sideset{}{'}\sum_{\boldsymbol{g}} \frac{(g^\mu + k^\mu)(g^\mu + k^\nu)}{|\boldsymbol{g} + \boldsymbol{k}|^2} \exp\left(-\frac{|\boldsymbol{g} + \boldsymbol{k}|^2}{4\eta^2} - \boldsymbol{g} \cdot \boldsymbol{\tau}_{mn}\right) \\
& + \sideset{}{'}\sum_i \exp\left(i\boldsymbol{k} \cdot (\boldsymbol{R}_i + \boldsymbol{\tau}_{mn})\right) \mathrm{E}_{\mu\nu}^\eta(\boldsymbol{R}_i + \boldsymbol{\tau}_{mn}) + \frac{4\eta^3}{3\sqrt{\pi}} \delta_{\mu\nu} \delta_{mn} ,
\end{aligned}
\tag{A.22}
$$

where

$$
\begin{aligned}
\mathrm{E}_{\mu\nu}^\eta(\boldsymbol{r}_i) = & \frac{2\eta \exp(-\eta^2 \boldsymbol{r}_i^2)}{\sqrt{\pi} \boldsymbol{r}_i^2} \left(\left(3 + 2\eta^2 \boldsymbol{r}_i^2\right) \frac{r_i^\mu r_i^\nu}{\boldsymbol{r}_i^2} - \delta_{\mu\nu}\right) \\
& + \left(3 \frac{r_i^\mu r_i^\nu}{|\boldsymbol{r}_i|^5} - \frac{\delta_{\mu\nu}}{|\boldsymbol{r}_i|^3}\right) \mathrm{erfc}(\eta|\boldsymbol{r}_i|) ,
\end{aligned}
\tag{A.23}
$$

erfc denotes the complementary error function

$$\mathrm{erfc}(x) = 1 - \mathrm{erf}(x) = 1 - \frac{2}{\sqrt{\pi}} \int_0^x \mathrm{d}\zeta \, \exp(-\zeta^2) , \tag{A.24}$$

and η is the Ewald parameter. It determines the pace of convergence. $\eta \approx 2/\lambda$ usually is a good choice, where λ is a characteristic length of the unit cell.

A close look at the first term in equation (A.22) shows that it is non-analytical at $\boldsymbol{k} \to \boldsymbol{0}$. Let us assume a simple cubic structure. If we approach the Γ point from different directions in the $k_1 k_2$-plane, i.e. $k \to 0$ for $\boldsymbol{k} = k(\cos\phi \, \boldsymbol{k}_1 + \sin\phi \, \boldsymbol{k}_2)$, we obtain for the k_1, k_1-component of the first term in (A.22)

$$I_{11}(\phi) \overset{|\boldsymbol{k}| \to 0}{=} -\frac{4\pi}{V_c} \cos^2\phi . \tag{A.25}$$

Thus, by changing the direction this term assumes all values in the interval $[-4\pi/V_c, 0]$. However, diagonalization of the full I matrix yields eigenvalues $-4\pi/V_c$ and 0 for all values of ϕ, leading to a continuous "band structure" as in figure 1.3.

Likewise, the second term is non-analytical when $\boldsymbol{k}$ approaches a reciprocal lattice vector $\boldsymbol{g}$. We also like to mention that the terms converge indeed rapidly due to the Gaussians and the complementary error functions.

Note that for the distributed dipole approach (DDA) used to treat the organics in chapter 2 the dipoles within a molecule do not polarize each other. Equation A.22 treats all dipoles on equal footing. Hence, for the DDA we need a correction term which subtracts the dipole-dipole interaction within the molecules. Introducing the notation M_i where M denotes the molecule and i enumerates its atoms and likewise for N_j we obtain

$$^{\mathrm{DDA}}\Gamma_{\mu\nu}^{M_i N_j}\left(\boldsymbol{k}\right) = \Gamma_{\mu\nu}^{M_i N_j}\left(\boldsymbol{k}\right) - \exp\left(\mathrm{i}\boldsymbol{k}\cdot\boldsymbol{\tau}_{ij}\right)\delta_{MN}\frac{3\,\tau_{ij\mu}\tau_{ij\nu} - \delta_{\mu\nu}\boldsymbol{\tau}_{ij}^2}{\boldsymbol{\tau}_{ij}^5}\ . \tag{A.26}$$

For Coulomb matrix elements in systems with non-isotropic polarizability it is more practical to diagonalize

$$^{\mathrm{DDA}}\tilde{\Gamma}_{\mu\nu}^{M_i N_j}\left(\boldsymbol{k}\right) = [\alpha^{-1}]_{\mu\nu}^{M_i N_j}\,\delta_{MN}\delta_{ij} - {}^{\mathrm{DDA}}\Gamma_{\mu\nu}^{M_i N_j}\left(\boldsymbol{k}\right) \tag{A.27}$$

instead of $^{\mathrm{DDA}}\Gamma_{\mu\nu}^{M_i N_j}\left(\boldsymbol{k}\right)$. In this formulation the zeros of the eigenvalues give rise to the instabilities. $\alpha_{\mu\nu}^{M_i N_j}$ denotes the components of the polarizability tensor for atom i of molecule M.

A.3. Results for Body- and Face-Centered Cubic Lattices

Here, we give some example results for simple lattices with a single dipole per unit cell. The "band structure" of the dipole-dipole matrix in a simple cubic crystal is plotted in figure 1.3 of section 1.1.4. The eigenvalues for the body centered cubic (bcc) crystal and the face centered cubic (fcc) crystal are shown in figures A.1 and A.2, respectively.
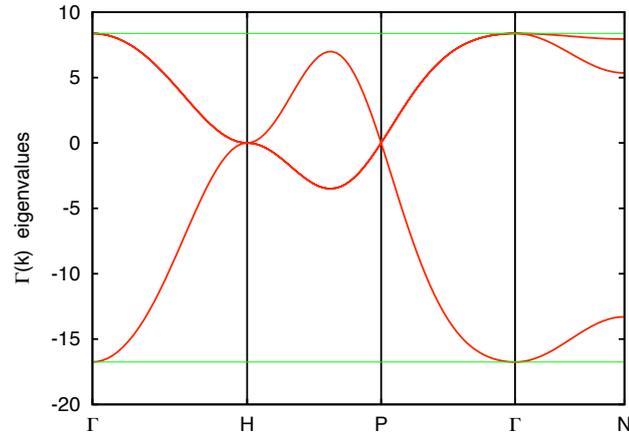
Figure A.1.: $\gamma_{\boldsymbol{k}}$ as a function of $\boldsymbol{k}$ of the dipole-dipole interaction matrix Γ for a body centered cubic (bcc) lattice of polarizable point dipoles. The largest eigenvalue resides at the Γ-point. It is also given by the Clausius-Mossotti relation (green lines).
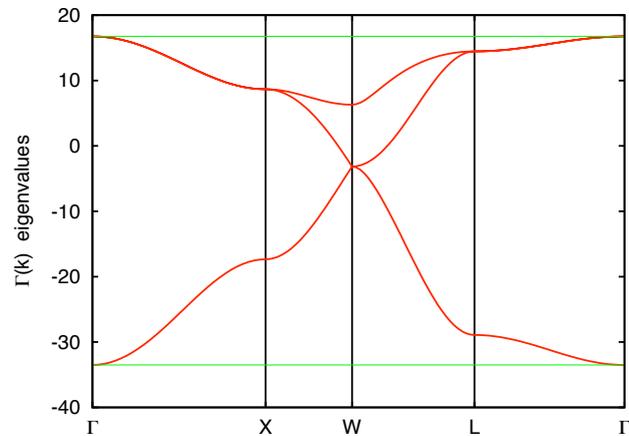
Figure A.2.: $\gamma_{\boldsymbol{k}}$ as a function of $\boldsymbol{k}$ of the dipole-dipole interaction matrix Γ for a face centered cubic (fcc) lattice of polarizable point dipoles. The largest eigenvalue resides at the Γ-point as predicted by the Clausius-Mossotti relation (green lines). For the definition of the high-symmetry points see, for instance, [11, page 703].

Euler Angles

B.1. General Introduction

In order to determine the orientation of a rigid body in three-dimensional space relative to a standard orientation, we need three angles, the Euler angles. A general rotation R can be split into three distinct elemental rotations determined by the three angles $R(\alpha, \beta, \gamma)$ about three different axes, i.e.

$$R(\alpha, \beta, \gamma) = R_{\boldsymbol{a}}(\alpha)\, R_{\boldsymbol{b}}(\beta)\, R_{\boldsymbol{c}}(\gamma) \;, \tag{B.1}$$

where the greek symbols denote the Euler angles and the latin vectors the rotation axes. For the three Cartesian axes the rotation matrices read

$$R_x(\xi) = \begin{pmatrix} 1 & 0 & 0 \\ 0 & \cos(\xi) & \sin(\xi) \\ 0 & -\sin(\xi) & \cos(\xi) \end{pmatrix} \;, \tag{B.2}$$

$$R_y(\xi) = \begin{pmatrix} \cos(\xi) & 0 & -\sin(\xi) \\ 0 & 1 & 0 \\ \sin(\xi) & 0 & \cos(\xi) \end{pmatrix} \;, \tag{B.3}$$

$$R_z(\xi) = \begin{pmatrix} \cos(\xi) & \sin(\xi) & 0 \\ -\sin(\xi) & \cos(\xi) & 0 \\ 0 & 0 & 1 \end{pmatrix} \;. \tag{B.4}$$

For a given orientation the Euler angles obviously depend on the choice of the rotation axes. There is no unique choice and one can choose from 12 different conventions. In this
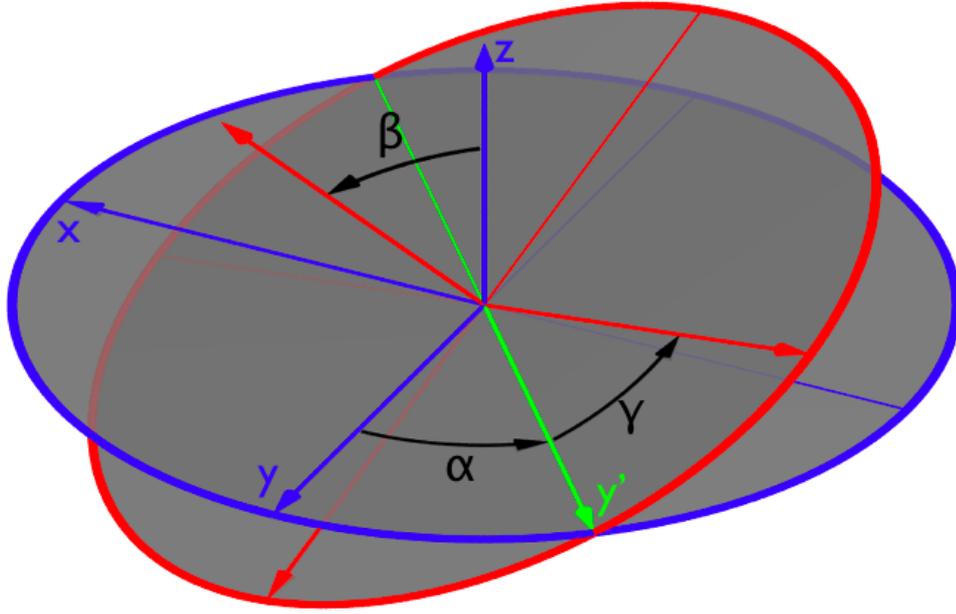
Figure B.1.: Visualization of Euler angles following the (Z, Y', Z'') convention. The original coordinate system is plotted in blue, the final in red.

work we use the (Z, Y', Z'') convention (see for instance Tinkham [124]), since it is the most common in quantum physics of atoms and molecules. It states

$$R(\alpha, \beta, \gamma) = R_{\boldsymbol{Z''}}(\gamma)\, R_{\boldsymbol{Y'}}(\beta)\, R_{\boldsymbol{Z}}(\alpha) \ . \tag{B.5}$$

We start from an initial coordinate system which is space-fixed. It is plotted in blue color in figure B.1. First, we rotate the object about the z axis by an angle $0 \leq \alpha < 2\pi$ described by matrix (B.4). In a coordinate system fixed to the body the Y-axis is thereby transformed to $\boldsymbol{e}_Y = R_z(\alpha)\boldsymbol{e}_y$ which is plotted in green. It serves as the second axis of rotation with the second Euler angle $0 \leq \beta < \pi$. We obtain a new body-Z axis Z'', i.e. $\boldsymbol{e}_{Z''} = R_{\boldsymbol{Y'}}(\beta)R_z(\alpha)\boldsymbol{e}_z$, which with $0 \leq \gamma < 2\pi$ determines the final rotation into the final orientation (see red coordinate system in figure B.1).

Since we know the rotation matrices for the space-fix axes it is desirable to express $R_{\boldsymbol{Z''}}(\gamma)$ and $R_{\boldsymbol{Y'}}(\beta)$ in terms of these. This is simple because

$$R_{\boldsymbol{Y'}}(\beta) = R_{\boldsymbol{z}}(\alpha)R_{\boldsymbol{y}}(\beta)R_{\boldsymbol{z}}^{-1}(\alpha) \tag{B.6}$$

and similarly

$$R_{\boldsymbol{Z''}}(\gamma) = R_{\boldsymbol{Y'}}(\beta)R_{\boldsymbol{z}}(\gamma)R_{\boldsymbol{Y'}}^{-1}(\beta) \ . \tag{B.7}$$

Using equations (B.6), (B.7) and $R_{\boldsymbol{Z}}(\alpha) = R_{\boldsymbol{z}}(\alpha)$ we may rewrite equation (B.5) yielding

$$R(\alpha, \beta, \gamma) = R_{\boldsymbol{Z''}}(\gamma)\, R_{\boldsymbol{Y'}}(\beta)\, R_{\boldsymbol{Z}}(\alpha) = R_{\boldsymbol{z}}(\alpha)\, R_{\boldsymbol{y}}(\beta)\, R_{\boldsymbol{z}}(\gamma) \ . \tag{B.8}$$

In the most right-hand term all rotations refer to fixed-axes. Inserting the matrices we obtain $R(\alpha, \beta, \gamma) =$

$$
\begin{pmatrix}
\cos(\alpha)\cos(\beta)\cos(\gamma) - \sin(\alpha)\sin(\gamma) & \cos(\alpha)\cos(\beta)\sin(\gamma) + \sin(\alpha)\cos(\gamma) & -\sin(\beta)\cos(\alpha) \\
-\sin(\alpha)\cos(\beta)\cos(\gamma) - \cos(\alpha)\sin(\gamma) & -\sin(\alpha)\cos(\beta)\sin(\gamma) + \cos(\alpha)\cos(\gamma) & \sin(\alpha)\sin(\beta) \\
\sin(\beta)\cos(\gamma) & \sin(\beta)\sin(\gamma) & \cos(\beta)
\end{pmatrix} .
$$

With the restrictions for the angles the Euler angles are uniquely determined in general. There is, however, an exception for $\beta = n\pi$, where $n = 0, 1, 2, \cdots$, which describes a pure rotation about the z axis with angle $\alpha + \gamma$. This situation is referred to as *gimbal lock*.

B.2. Extracting Euler angles

Imagine we have a general rotation matrix and we would like to extract the Euler angles – For instance to obtain the relative orientations of two objects in space.

From the element $R_{2,2} = R_{2,2}(\alpha, \beta, \gamma)$ [1] we directly obtain the angle $\beta = \arccos(R_{22})$. If $\beta = 0$, the gimbal lock occurs and thus $(\alpha, \beta, \gamma) \to T$ is not locally invertible. We solve this ambiguity by setting $\gamma = 0$. The matrix elements R_{01}, R_{00} simplify to $cos(\alpha)$, $\sin(\alpha)$, respectively. Thus, alpha is uniquely given by $\alpha = \arctan2(R_{01}, R_{00})$. If $\beta > 0$, we obtain $\alpha = \arctan2(R_{12}, -R_{02})$ and $\gamma = \arctan2(R_{21}, R_{20})$, where $\arctan2(y, x)$ denotes the arctangent of y/x – similar to arctan – but within the range of $(-\pi, \pi]$. It thus determines the angle between the positive x axis and the vector $(x, y)^T$. It gives, for instance, the argument of a complex number, i.e. $z = x + iy = r \exp(i\phi)$ with $\phi = \arctan2(y, x)$.

Finally the angles are folded back into the range of $[0, 2\pi)$ for α and γ and $[0, \pi)$ for β. A Python script providing this operation is printed in listing B.1.

```
1  def RotMat2Euler(T):
       """

3      T : input rotation matrix (numpy or compatible array)

5      Returns the tuple of the three Euler angles determined by rotation
       matrix T and the (Z, Y', Z'') convention. In the gimbal lock case
7      the third Euler angle about Z'' is set to zero to obtain uniqueness.
       """

9
       # sanity check: Is T a three by three matrix?
11     if T.shape != (3,3):
           raise "T parameter must be a 3x3 matrix"

13
       beta = arccos(T[2,2])
15     alpha = gamma = 0.
```

---

[1]For compatibility with the appended Python script we start counting the rows and columns by 0. The first matrix element thus is R_{00}.

```
17      if abs(beta) > 0.000001:
            alpha = arctan2(T[1,2],−T[0,2])
19          gamma = arctan2(T[2,1],T[2,0])
        else: # gimbal lock
21          gamma = 0.
            alpha = arctan2(T[0,1],T[0,0])

23

        if alpha < 0: alpha += 2*pi
25      if beta  < 0: beta  += 2*pi
        if gamma < 0: gamma += 2*pi

27

        return (alpha,beta,gamma)
```

Listing B.1: RotMat2Euler(T) python function. See comments in the docstring. This code requires the numpy library [125].

FHI-aims: Basis Sets

Table C.1.: Radial basis functions beyond the minimal tier used by FHI-aims for hydrogen, carbon, nitrogen, and oxygen (`aims_standard.pre-CPC`). H(nl, Z) denotes a hydrogen-like radial function for the bare Coulomb potential Z/r for quantum numbers n and l. ionic(nl, r) adds a free-ion like radial function where n and l also give the quantum numbers and r the onset radius of the confining potential.

	H	C	N	O
tier 1	H($2s$, 2.1)	H($2p$,1.7)	H($2p$,1.8)	H($2p$, 1.8)
	H($2p$, 3.5)	H($3d$,6.0)	H($3d$,6.8)	H($3d$, 7.6)
		H($2s$,4.9)	H($3s$,5.8)	H($3s$, 6.4)
		H($4f$,9.8)	H($4f$,10.8)	H($4f$, 11.6)
tier 2	H($1s$, 0.85)	H($3p$,5.20)	H($3p$,5.8)	H($3p$, 6.2)
	H($2p$, 3.70)	H($3s$,4.30)	H($1s$,0.8)	H($3d$, 5.6)
	H($2s$, 1.20)	H($5g$,14.4)	H($5g$,16.0)	H($5g$, 17.6)
	H($3d$, 7.00)	H($3p$,6.20)	H($3d$,4.9)	H($1s$, 0.75)
tier 3	H($4f$, 11.20)	H($2p$,5.6)	H($3s$,16)	ionic($2p$, 9.4486)
	H($3p$, 4.80)	H($2s$,1.4)	ionic($2p$,9.4486)	H($4f$, 10.8)
	H($4d$, 9.00)	H($3d$,4.9)	H($3d$,6.6)	H($4d$, 4.7)
	H($3s$, 3.20)	H($4f$,11.2)	H($4f$,11.6)	H($2s$, 6.8)
tier 4		H($2p$,2.1)	H($2p$,4.5)	H($3p$, 5.0)
		H($5g$,16.4)	H($2s$,2.4)	H($3s$, 3.3)
		H($4d$,13.2)	H($5g$,14.4)	H($5g$, 15.6)
		H($3s$,13.6)	H($4d$,14.4)	H($4f$, 17.6)
		H($4f$,17.6)	H($4f$,16.8)	H($4d$, 14.0)

Table C.2.: Radial basis functions beyond the minimal tier used by FHI-aims for sulfur and iodine (`aims_standard.pre-CPC`). H(nl, Z) denotes a hydrogen-like radial function for the bare Coulomb potential Z/r for quantum numbers n and l. ionic(nl, r) adds a free-ion like radial function where n and l also give the quantum numbers and r the onset radius of the confining potential.

	S	I
tier 1	ionic(3d,9.4486)	H(3d,4)
	H(2p,1.8)	H(4f,6.4)
	H(4f,7)	H(2p,1.6)
	ionic(3s,9.4486)	ionic(5s,9.4486)
tier 2	H(4d,6.2)	H(5g,9.4)
	H(5g,10.8)	H(4f,18.4)
	H(4p,4.9)	H(6h,12.4)
	H(5f,10)	H(4p,4.4)
	H(1s,0.8)	H(4d,5.4)
		H(3s,3.0)
tier 3	H(3d,3.9)	H(5f,15.2)
	H(3d,2.7)	H(5d,15.2)
	H(5g,12)	H(5g,12)
	H(4p,10.4)	H(6h,14.4)
	H(5f,12.4)	ionic(5p,9.4486)
	H(2s,1.9)	H(1s,6.6)
tier 4	H(4d,10.4)	
	H(4p,7.2)	
	H(4d,10)	
	H(5g,19.2)	
	H(4s,12)	

Atomic units

Practical electronic structure calculations are usually done in atomic units, a. u. for short. The motivation for introducing atomic units is to simplify the equations. For example, in SI units the Hamiltonian of a hydrogen atom is

$$H = -\frac{\hbar^2}{2m_e}\nabla^2 - \frac{e^2}{4\pi\epsilon_0 \, r} \; . \tag{D.1}$$

To avoid having to keep track of the constants, we would like to simplify this to

$$H = -\frac{1}{2}\nabla^2 - \frac{1}{r} \; . \tag{D.2}$$

To this end we invent units in which the *numerical values* of the electron mass m_e, the elementary charge e, the Planck-constant $\hbar$, and the dielectric constant $4\pi\epsilon_0$ are all equal to one. This immediately tells us: 1 a.u. mass $= m_e$ and 1 a.u. charge $= e$. To complete the set of basis units we still need the atomic unit of length, which we call a_0, and time, t_0. To find the values of a_0 and t_0 we write $\hbar$ and $4\pi\epsilon_0$ (using simple dimensional analysis) in atomic units: $\hbar = 1 \, m_e a_0^2/t_0$ and $4\pi\epsilon_0 = 1 \, t_0^2 e^2/(m_e a_0^3)$. Solving this system of equations, we find

1 a.u. length $=$	a_0	$= 4\pi\epsilon_0\hbar^2/m_e e^2$	$\approx 5.2918 \cdot 10^{-11}$	m
1 a.u. mass $=$	m_e	$=$	$\approx 9.1095 \cdot 10^{-31}$	kg
1 a.u. time $=$	t_0	$= (4\pi\epsilon_0)^2\hbar^3/m_e e^4$	$\approx 2.4189 \cdot 10^{-17}$	s
1 a.u. charge $=$	e	$=$	$\approx 1.6022 \cdot 10^{-19}$	C
1 a.u. energy $=$	$\frac{m_e e^4}{(4\pi\epsilon_0)^2\hbar^2}$	$=$	$4.3598 \quad \approx 10^{-18}$	$\cdot$ J

As the unit of energy in the *Système International* (SI) is given by $\mathrm{kg\,m^2/s^2}$, in atomic units it is $m_e a_0^2/t_0^2 = m_e e^4/(4\pi\epsilon_0)^2\hbar^2$. Because of its importance the atomic unit of energy has a name, the Hartree. One Hartree is minus twice the groundstate energy of the hydrogen atom (D.1), about $27.211\,\mathrm{eV}$.

The SI unit of the electrical dipole moment charge · length is C · m. In these units atomic polarizabilites are inconveniently small. A more practical unit is the Debye D, named after Peter Debye. It is often used in atomic and molecular physics and chemistry. A Debye is defined as D $= 10^{18}$ stratcoulomb centimeter $= 10^{10} \cdot 0.1$ Am/c $\approx 3.3 \cdot 10^{-30}$ Cm. The dipole moment unit in a.u. is $e\,a_0$ which relates to Debye as 1 a.u. ≈ 2.54 D. The polarizability is also often given in terms of atomic units, i.e. in e a_0^2/Ha $= a_0^3$.

Massively Parallel Lanczos Solver

The key ingredient of the Lanczos algorithm is the sparse matrix vector multiplication. Already for quite small systems this operation takes most of the execution time, and increasing the size of the many-body vector, it dominates ever more. Thus, this is the focus our parallelization efforts. On shared memory systems this matrix-vector multiplication is embarrassingly simple but we are restricted to relatively small memories. To use the memory that is needed to reduce finite-size effects, we have to find an efficient distributed memory implementation.

The kinetic energy term of the Hamiltonian of the Hubbard model

$$H = - \sum_{i \neq j\, \sigma} t_{ij} c_{i\sigma}^\dagger \, c_{j\sigma} + U \sum_i n_{i\uparrow} n_{i\downarrow} + V \sum_{<ij>} n_i n_j \; . \tag{E.1}$$

has non-diagonal terms and therefore leads to non-local memory access patterns. To obtain an efficient distributed memory implementation we use a simple yet important observation: As pointed out above, the kinetic energy term conserves spin. Thus, performing the up-electron hopping takes only different up-hopping configurations into account while the down-electron configuration remains unchanged. If we group all up configurations for a fixed down configuration together in a single process, this hopping can thus be carried out locally: for a fixed index $i_\downarrow$, all $i_\uparrow$ configurations follow and can be stored in a process. We see that this basis can be naturally indexed by a tuple $(i_\downarrow, i_\uparrow)$ instead of a single index. We can therefore equivalently regard the vectors as matrices $v(i_\downarrow, i_\uparrow)$ with indices $i_\downarrow$ and $i_\uparrow$. Now it is easy to see that a matrix transpose reshuffles the data elements such that the down configurations are sequentially in memory and local to the process. Therefore, the efficiency of the sparse matrix-vector multiplication rests on the performance of the matrix transpose operation. We implement it with `MPI_Alltoall`. This routine expects, however, the data packages which will be sent to a given process to
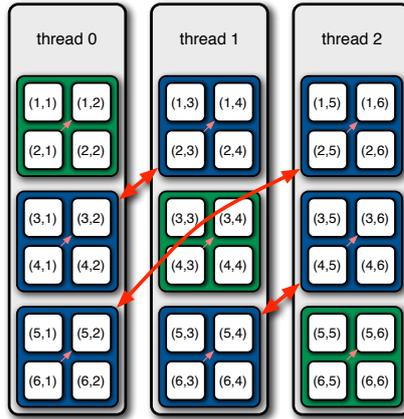
Figure E.1.: Transpose operation that makes memory access thread-local when cal-
culating the operation of the Hamiltonian on the state-vector. The
communication (red arrows) is realized by a call to `MPI_alltoall`, which
is very efficiently implemented on BlueGene/P. The small pink arrows
indicate the local operations needed to complete the matrix-transpose.

be stored contiguously in memory. This does not apply to our case, since we would like to
store the spin-down electron configurations sequentially in memory. Thus, the matrix is
stored column wise. For `MPI_Alltoall` to work properly, we would have to bring the data
elements in row-major order. This could be done by performing a local matrix transpose.
The involved matrices are, however, in general rectangular, leading to expensive local-copy
and reordering operations. We can avoid this by calling `MPI_Alltoall` for each column
separately. After calling `MPI_Alltoall` for each column (red arrows in figure E.1) only a
local strided transposition has to be performed (small pink arrows) to obtain the fully
transposed matrix or Lanczos vector [71, 126]. The speed up (figure E.2) shows that
collective communication is indeed very efficient on Jugene, a BlueGene/P supercomputer.
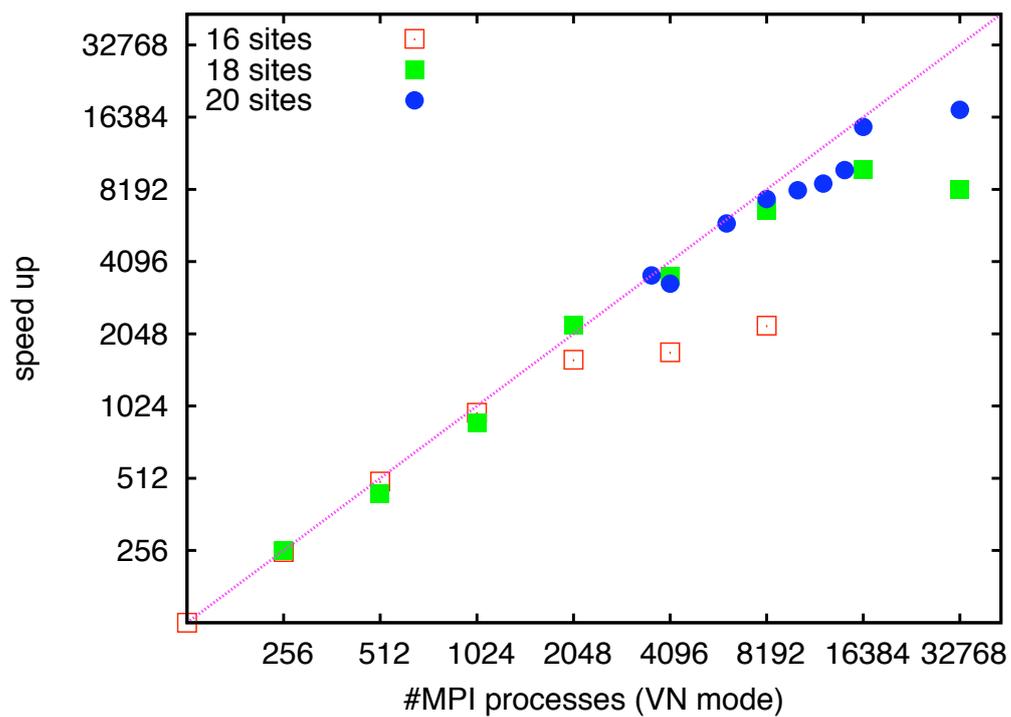
Figure E.2.: ParLa (Parallel Lanczos) speed up on JUGENE (BlueGene/P) in virtual node mode (VN); state vectors for the half-filled Hubbard model with 16, 18, and 20 are 1.23, 17.61, and 254.32 GB in double precision, respectively. When the message size becomes too small latency cannot be neglected and the speed up levels off.

Fourier transforms & Friends

We give a brief review of different Fourier-related transforms. We focus on one dimension since generalizations to higher dimension follows trivially.

F.1. Infinite Continuous Fourier Transform

Let $f(x)$ be a sufficiently well behaved integrable function. The Fourier transform of $f(x)$ reads

$$\mathcal{F}[f(x)](k) = F(k) = \kappa_k \int_{-\infty}^{\infty} \mathrm{d}x\, f(x)e^{-\mathrm{i}kx} \; . \tag{F.1}$$

Its inverse is

$$\mathcal{F}^{-1}[F(k)](x) = f(x) = \kappa_x \int_{-\infty}^{\infty} \mathrm{d}k\, F(k)e^{\mathrm{i}kx} \; . \tag{F.2}$$

$\kappa_x \cdot \kappa_k = 1/(2\pi)$ needs to be satisfied. The exact choice depends on convention. For $\kappa_x = \kappa_k = 1/\sqrt{2\pi}$ the Fourier transform becomes a unitary transformation. This is the natural choice for quantum mechanics. In classical mechanics we often use $\kappa_k = 1$ and therefore $\kappa_x = 1/(2\pi)$.

F.2. Infinite Discrete Fourier Transform

Assume an infinite discrete one-dimensional lattice with sites $x_m = ma$, $m \in \mathbb{Z}$. The first Brillouin zone in reciprocal space is consequently given by $(-\pi/a, \pi/a]$ with the volume $V_{\mathrm{BZ}} = 2\pi/a$. A function f with values f_m at the lattice sites m has the Fourier transform

$$f(k) = \sum_m e^{-ikx_m} f_m \ , \tag{F.3}$$

where $k \in (-\pi/a, \pi/a]$. The inverse Fourier transform reads

$$f_m = \frac{1}{2\pi/a} \int_{-\pi/a}^{\pi/a} \mathrm{d}k \, e^{ikx_m} f(k) \ . \tag{F.4}$$

From the orthogonality relation we obtain the Kronecker delta for the real space

$$\delta_{mn} = \frac{1}{2\pi/a} \int_{-\pi/a}^{\pi/a} \mathrm{d}k \, e^{ik(x_m - x_n)} \ , \tag{F.5}$$

and the Laue function $\Delta(k) = \sum_j \delta(k - 2\pi j/a)$ in reciprocal space

$$\Delta(k - k') = \sum_m e^{-i(k-k')x_m} \ , . \tag{F.6}$$

F.3. Relationship between Continuous and Discrete Fourier Transforms

Instead of a lattice we can also regard the discrete Fourier transform of the preceding section as a sampling in real space. Let $f(x)$ be a continuous function with Fourier transform $F(k)$ and $f_m = f(ma)$ the sampling of $f(x)$. The Poisson summation enables us to relate $F(k)$ with the discrete Fourier transformation $f(k)$ of f_m. A generalized Poisson summation formula is

$$\sum_{m=-\infty}^{\infty} f(ma) \, e^{-ikma} = \frac{1}{a} \sum_{g=-\infty}^{\infty} F\left(k + \frac{2\pi}{a}g\right) \ , \tag{F.7}$$

where $k \in (-\pi/a, \pi/a]$. We note that the LHS is $f(k)$ (see (F.3)) and the RHS gives a periodization of the continuous Fourier transform $F(k)$ with periodicity $2\pi/a$, the extent of the first BZ.

F.4. Convolution Theorem and Autocorrelation function

Let f and g be complex functions of some real variable ω. We define the convolution as the integral of the product of these functions where one is reversed and shifted, i.e.

$$(f * g)(\Omega) = \int_{-\infty}^{\infty} d\omega \, f(\omega)g(\Omega - \omega) . \tag{F.8}$$

The cross-correlation function is defined in a similar way without reversing one function and an additional complex conjugation.

$$(f \star g)(\Omega) = \int_{-\infty}^{\infty} d\omega \, f^*(\omega)g(\Omega + \omega) . \tag{F.9}$$

Obviously, $(f \star g) = (\bar{f} * g)$ with $\bar{f}(\omega) = f^*(-\omega)$. Thus, if either f or g is Hermitian then convolution and cross-correlation function are identical $(f \star g) = (f * g)$.

A special case is the autocorrelation function, the cross-correlation of a function with itself $(f \star f)(\Omega)$.

$$\mathcal{F}[f * g] = \mathcal{F}[f] \cdot \mathcal{F}[g] \tag{F.10}$$

is the convolution theorem which relates the Fourier transformation of a convolution of two functions with the product of their Fourier transforms. Analogous to the convolution theorem the cross-correlation function satisfies

$$\mathcal{F}[f \star g] = \mathcal{F}[f]^* \cdot \mathcal{F}[g] . \tag{F.11}$$

F.4.1. Similar relations used in Condensed Matter Physics

The autocorrelation-like function we encountered in section 3.1.8 when deriving expressions for the particle-hole bubble can be considered as a cross-correlation function of $(G^* \star G)$ – hence, it almost is the autocorrelation function. From the viewpoint of the convolution it is $(\tilde{G} * G)$ with $\tilde{G}(\omega) = G(-\omega)$.

From this it is straightforward to show

$$\mathcal{F}[G(t)G(-t)](\Omega) = \left(\tilde{G} * G\right)(\Omega) = \int d\Omega \, G(\omega)G(\omega + \Omega) . \tag{F.12}$$

$G(\tau)$ in imaginary time is pseudo-periodic in τ allowing for a Fourier series expansion

$$G(\tau) = \frac{1}{\beta} \sum_{i\omega} \exp(-i\omega\tau) \, G(i\omega) \tag{F.13}$$

instead of the full integration. Hence,

$$\mathcal{F}[G(\tau)G(-\tau)](i\Omega) = (G^* \star G)(i\Omega) = \frac{1}{\beta} \sum_{i\omega} G(i\omega)G(i\omega + i\Omega) . \tag{F.14}$$

Inversion by Partitioning

The inversion by partitioning technique is commonly used in condensed matter physics. Here we employ it to derive the Weiss function in DMFT for the Anderson Impurity Model (see 3.2.2) and in the derivation for the Green's functions of the f- and conduction electrons in the Periodic Anderson Model (see 3.2.5.2).

We start with a partitioning of the Hilbert space into two subspaces, e.g. f- and c-states, and format the Hamiltonian in block matrices accordingly, i.e.

$$H = \begin{pmatrix} F & V_{fc} \\ V_{cf} & C \end{pmatrix} . \tag{G.1}$$

F, C denote the blocks of interest (here the f-, c-electrons) and V_{fc}, V_{cf} the transitions (hybridization) between both subspaces. The Green's function is partitioned likewise

$$G(\omega) = \begin{pmatrix} G_{ff} & G_{fc} \\ G_{cf} & G_{cc} \end{pmatrix} = (\omega - H)^{-1} = \begin{pmatrix} \omega - F & -V_{fc} \\ -V_{cf} & \omega - C \end{pmatrix}^{-1} . \tag{G.2}$$

Evaluating the inverse of this 2×2 block matrix can be done straightforwardly taking into account that the submatrices do not commute. The situation in 3.2.5.2 is a special case with the submatrices being numbers.

We obtain

$$G_{ff} = \left((\omega - F) - V_{fc}(\omega - C)^{-1}V_{cf} \right)^{-1} \tag{G.3}$$

$$G_{fc} = G_{ff} \cdot \left(V_{fc}(\omega - C)^{-1} \right) , \tag{G.4}$$

$$G_{cf} = \left(C^{-1}V_{cf} \right) \cdot G_{ff} , \tag{G.5}$$

$$G_{ff} = (\omega - C)^{-1} + \left((\omega - C)^{-1}V_{cf} \right) \cdot G_f f \cdot \left(V_{fc}(\omega - C)^{-1} \right) . \tag{G.6}$$

For more information and alternative forms refer to chapter 2.7.4 of [127].

Inversion by partitioning is also the basis of the downfolding technique. It is used to integrate out high-energy degrees of freedom for effective low-energy models. For a discussion of this important method refer to appendix B of [128].

Bibliography

[1] E. Schrödinger, *An Undulatory Theory of the Mechanics of Atoms and Molecules*, Phys. Rev. **28**, 1049 (1926). (cited in (document).)

[2] P. A. M. Dirac, *Quantum Mechanics of Many-Electron Systems*, Proceedings of the Royal Society of London **123**, 714 (1929). (cited in (document).)

[3] R. Resta, *Berry's Phase and Geometric Quantum Distance: Macroscopic Polarization and Electron Localization*, Troisième Cycle de la Physique en Suisse Romande , 121 (1999-2000). (cited in 1.)

[4] P. B. Allen, *Dipole interactions and electrical polarity in nanosystems: The Clausius–Mossotti and related models*, The Journal of Chemical Physics **120**, 2951 (2004). (cited in 1.1.2, 1.1.4.)

[5] P. B. Allen, *Dipole Interactions In Nanosystems*, arXiv:cond-mat/0309392v1 (2003). (cited in 1.1.2.)

[6] J. M. Luttinger and L. Tisza, *Theory of Dipole Interaction in Crystals*, Phys. Rev. **70**, 954 (1946). (cited in 1.1.2, 1.1.4.)

[7] P. P. Ewald, *Die Berchnung optischer und elektrostatischer Gitterpotentiale (Evaluation of optical and electrostatic lattice potentials)*, Ann. Phys. (Leipzig) **64**, 253 (1921). (cited in 1.1.4, A.)

[8] W. Smith, *18 CCP5 Newsletter No. 46 Point Multipoles in the Ewald Summation (Revisited)*. (cited in 1.1.4.)

[9] O. Mossotti, Memorie di Mathematica e di fisica della Societa Italiana della Scienza Residente in Modena **24** (1850). (cited in 1.1.4.)

[10] R. Clausius, *Die mechanische Wärmtheorie II* (Vieweg, Braunschweig, 1897). (cited in 1.1.4.)

[11] A. P. Cracknell, *Group theory in solid-state physics is not dead yet alias some recent developments in the use of group theory in solid-state physics*, Advances in Physics **23**, 673 (1974). (cited in 1.3, A.2.)

[12] J. A. Sauer, *Magnetic Energy Constants of Dipolar Lattices*, Phys. Rev. **57**, 142 (1940). (cited in 1.1.4.)

[13] S. J. White, M. R. Roser, J. Xu, J. T. van der Noordaa and L. R. Corruccini, *Dipolar Magnetic Order with large Quantum Spin Fluctuations in a Diamond Lattice*, Phys. Rev. Lett. **71**, 3553 (1993).

[14] J. van den Brink and G. A. Sawatzky, *Non-conventional screening of the Coulomb interaction in low-dimensional and finite-size systems*, Europhys. Lett. **50**, 447 (2000).

[15] J. Topping, *On the Mutual Potential Energy of a Plane Network of Doublets*, Royal Society of London Proceedings Series A **114**, 67 (1927). (cited in 1.3.1.)

[16] M. L. Glasser and I. J. Zucker, *Lattice Sums in Theoretical Chemistry*, in *Theoretical Chemistry - Advances and Perspectives*, edited by Henry and D. E. Henderson Vol. 5, pp. 67–139, Academic Press Inc, 1980. (cited in 1.3.1, A.1.)

[17] L. Lorenz, Tidskr Mat. **1**, 97 (1871). (cited in 1.3.1.)

[18] J. D. Jackson, *Classical Electrodynamics* (John Wiley & Sons, Inc., 1962). (cited in 1.4.1, 1.4.1.)

[19] C. Kittel, *Introduction to Solid State Physics* (John Wiley & Sons, Inc., 1996). (cited in 1.4.1.)

[20] N. W. Ashcroft and N. D. Mermin, *Solid State Physics* (Saunders College, Philadelphia, 1976). (cited in 1.4.1.)

[21] D. E. Aspnes, *Local-field effects and effective-medium theory: A microscopic perspective*, Am. J. Phys. **50**, 704 (1982). (cited in 1.4.1.)

[22] J. van Kranendonk and J. Sipe, *Foundations of the Macroscopic Electromagnetic Theory of Dielectric Media* Progress in Optics XV (North Holland, 1977). (cited in 1.4.1.)

[23] G. D. Mahan, *Nanoscale dielectric constants: Dipole summations and the dielectric function in nanowires and quantum dots of cubic materials*, Phys. Rev. B **74**, 033407 (2006). (cited in 1.4.1.)

[24] D. R. Hartree, *The Wave Mechanics of an Atom with a Non-Coulomb Central Field. Part I. Theory and Methods*, Mathematical Proceedings of the Cambridge Philosophical Society **24**, 89 (1928). (cited in 2.1.1.)

[25] V. Fock, *Näherungsmethode zur Lösung des quantenmechanischen Mehrkörperproblems*, Zeitschrift für Physik A Hadrons and Nuclei **61**, 126 (1930). (cited in 2.1.1.)

[26] C. D. Sherrill and H. F. S. III, *The Configuration Interaction Method: Advances in Highly Correlated Approaches*, , Advances in Quantum Chemistry Vol. 34, pp. 143 – 269, Academic Press, 1999. (cited in 2.1.1.)

[27] R. J. Bartlett, *Coupled-cluster approach to molecular structure and spectra: a step toward predictive quantum chemistry*, The Journal of Physical Chemistry **93**, 1697 (1989). (cited in 2.1.1.)

[28] C. Møller and M. S. Plesset, *Note on an Approximation Treatment for Many-Electron Systems*, Phys. Rev. **46**, 618 (1934). (cited in 2.1.1.)

[29] L. H. Thomas, *The calculation of atomic fields*, Mathematical Proceedings of the Cambridge Philosophical Society **23**, 542 (1927). (cited in 2.1.1.)

[30] E. Fermi, Atti Accad. Naz. Lincei, Cl. Sci. Fis., Mat. Nat. **6**, 602 (1927). (cited in 2.1.1.)

[31] P. Hohenberg and W. Kohn, *Inhomogeneous Electron Gas*, Phys. Rev. **136**, B864 (1964). (cited in 2.1.1.)

[32] M. Levy, *Electron densities in search of Hamiltonians*, Phys. Rev. A **26**, 1200 (1982). (cited in 2.1.1.)

[33] E. H. Lieb, *Density Functionals for Coulomb Systems,* Physics as Natural Philosophy: Essays in Honor of Laszlo Tisza on His 75th Birthday (MIT Press, Cambridge, 1982). (cited in 2.1.1.)

[34] W. Kohn and L. J. Sham, *Self-Consistent Equations Including Exchange and Correlation Effects*, Phys. Rev. **140**, A1133 (1965). (cited in 2.1.1.)

[35] E. Wigner and F. Seitz, *On the Constitution of Metallic Sodium. II*, Phys. Rev. **46**, 509 (1934). (cited in 2.1.1, 2.4.3.2.)

[36] D. M. Ceperley and B. J. Alder, *Ground State of the Electron Gas by a Stochastic Method*, Phys. Rev. Lett. **45**, 566 (1980). (cited in 2.1.1.)

[37] J. P. Perdew and Y. Wang, *Accurate and simple analytic representation of the electron-gas correlation energy*, Phys. Rev. B **45**, 13244 (1992). (cited in 2.1.1.)

[38] J. P. Perdew, K. Burke and M. Ernzerhof, *Generalized Gradient Approximation Made Simple*, Phys. Rev. Lett. **77**, 3865 (1996). (cited in 2.1.1.)

[39] W. Kohn, Y. Meir and D. E. Makarov, *van der Waals Energies in Density Functional Theory*, Phys. Rev. Lett. **80**, 4153 (1998). (cited in 2.1.1.)

[40] P. L. Silvestrelli, *Van der Waals Interactions in DFT Made Easy by Wannier Functions*, Phys. Rev. Lett. **100**, 053002 (2008). (cited in 2.1.1.)

[41] V. Blum *et al.*, *Ab initio molecular simulations with numeric atom-centered orbitals: FHI-AIMS*, CPC (preprint) (2008). (cited in 2.1.2.1.)

[42] V. Blum *et al.*, *Ab initio molecular simulations with numeric atom-centered orbitals*, Computer Physics Communications **180**, 2175 (2009). (cited in 2.1.2.1, 2.1.2.1, 2.1.2.4.)

[43] J. Huang and M. Kertesz, *Intermolecular transfer integrals for organic molecular materials: can basis set convergence be achieved?*, Chemical Physics Letters **390**, 110 (2004). (cited in 2.3.1.)

[44] C. Mattheus, *Polymorphism and electronic properties of Pentacene*, PhD thesis, Rijksuniversiteit Groningen, 2002. (cited in 2.11, 2.3.1.)

[45] C. C. Mattheus *et al.*, *Polymorphism in pentacene*, Acta Crystallographica Section C **57**, 939 (2001). (cited in 2.11, 2.3.1.)

[46] J. F. Janak, *Proof that $\partial E/\partial ni = \epsilon$ in density-functional theory*, Phys. Rev. B **18**, 7165 (1978). (cited in 2.3.2.2.)

[47] U. von Barth, *Lecture Notes for the Gent Summer School 1982*, in *NATO Advanced Study Institute on the Electronic Structure of Complex Systems*, edited by W. Temmerman and P. Phariseau, Plenum, New York, 1982. (cited in 2.3.2.2.)

[48] M. Springer and F. Aryasetiawan, *Frequency-dependent screened interaction in Ni within the random-phase approximation*, Phys. Rev. B **57**, 4364 (1998). (cited in 2.3.2.2.)

[49] M. R. Pederson and A. A. Quong, *Polarizabilities, charge states, and vibrational modes of isolated fullerene molecules*, Phys. Rev. B **46**, 13584 (1992). (cited in 2.3.2.3.)

[50] G. Mazur and P. Petelenz, *Charge transfer excitons in perylenetetracarboxylic dianhydride - microelectrostatic calculations*, Chemical Physics Letters **324**, 161 (2000). (cited in 2.3.2.3.)

[51] H. Reis, M. G. Papadopoulos, P. Calaminici, K. Jug and A. M. Koster, *Calculation of macroscopic linear and nonlinear optical susceptibilities for the naphthalene, anthracene and meta-nitroaniline crystals*, Chemical Physics **261**, 359 (2000). (cited in 2.3.2.3.)

[52] R. S. Mulliken, *Electronic population analysis on LCAO-MO molecular wave functions*, J. Chem. Phys. **110**, 1833 (1955). (cited in 2.3.2.3, 2.5.2.1.)

[53] Hirshfeld, Theor. Chim Acta **44**, 129 (1977). (cited in 2.3.2.3.)

[54] J. Behler, B. Delley, S. Lorenz, K. Reuter and M. Scheffler, *Dissociation of O2 at Al(111): The Role of Spin Selection Rules*, Phys. Rev. Lett. **94**, 036104 (2005).

[55] P. H. Dederichs, S. Blügel, R. Zeller and H. Akai, *Ground States of Constrained Systems: Application to Cerium Impurities*, Phys. Rev. Lett. **53**, 2512 (1984).

[56] J. Behler, B. Delley, K. Reuter and M. Scheffler, *Nonadiabatic potential-energy surfaces by constrained density-functional theory*, Phys. Rev. B **75**, 115409 (2007).

[57] J. Ferraris, D. O. Cowan, V. Walatka and J. H. Perlstein, *Electron transfer in a new highly conducting donor-acceptor complex*, Journal of the American Chemical Society **95**, 948 (1973). (cited in 2.4.)

[58] L. B. Coleman *et al.*, *Superconducting fluctuations and the Peierls instability in an organic solid*, Solid State Communications **88**, 989 (1993). (cited in 2.4.)

[59] F. Zwick *et al.*, *Band Mapping and Quasiparticle Suppression in the One-Dimensional Organic Conductor TTF-TCNQ*, Phys. Rev. Lett. **81**, 2974 (1998). (cited in 2.4.)

[60] T. Ito *et al.*, *Temperature-Dependent Luttinger Surfaces*, Phys. Rev. Lett. **95**, 246402 (2005). (cited in 2.4.)

[61] J. B. Torrance, Y. Tomkiewicz and B. D. Silverman, *Enhancement of the magnetic susceptibility of TTF-TCNQ (tetrathiafulvalene-tetracyanoquinodimethane) by Coulomb correlations*, Phys. Rev. B **15**, 4738 (1977). (cited in 2.4.)

[62] R. Claessen *et al.*, *Spectroscopic Signatures of Spin-Charge Separation in the Quasi-One-Dimensional Organic Conductor TTF-TCNQ*, Phys. Rev. Lett. **88**, 096402 (2002). (cited in 2.4.)

[63] M. Sing *et al.*, *Electronic structure of the quasi-one-dimensional organic conductor TTF-TCNQ*, Phys. Rev. B **68**, 125111 (2003). (cited in 2.4.)

[64] H. Benthien, F. Gebhard and E. Jeckelmann, *Spectral Function of the One-Dimensional Hubbard Model away from Half Filling*, Phys. Rev. Lett. **92**, 256401 (2004). (cited in 2.4, 2.4.3.)

[65] J. Fraxedas *et al.*, *Characterization of the unoccupied and partially occupied states of TTF-TCNQ by XANES and first-principles calculations*, Phys. Rev. B **68**, 195115 (2003). (cited in 2.4.)

[66] S. Kagoshima, H. Anzai, K. Kajimura and T. Ishiguro, *Observation of the Kohn Anomaly and the Peierls Transition in TTF-TCNQ by X-Ray Scattering*, Journal of the Physical Society of Japan **39**, 1143 (1975). (cited in 2.4.)

[67] L. Cano-Cortés *et al.*, *Spectral broadening due to long-range Coulomb interactions in the molecular metal TTF-TCNQ*, The European Physical Journal B - Condensed Matter and Complex Systems **56**, 173 (2007). (cited in 2.4, 2.4.3.2.)

[68] J. Hubbard, *Generalized Wigner lattices in one dimension and some applications to tetracyanoquinodimethane (TCNQ) salts*, Phys. Rev. B **17**, 494 (1978). (cited in 2.4, 2.4.3.2.)

[69] S. Mazumdar and A. N. Bloch, *Systematic Trends in Short-Range Coulomb Effects among Nearly One-Dimensional Organic Conductors*, Phys. Rev. Lett. **50**, 207 (1983). (cited in 2.4.)

[70] T. J. Kistenmacher, T. E. Phillips and D. O. Cowan, *The crystal structure of the 1:1 radical cation–radical anion salt of 2,2'-bis-l,3-dithiole (TTF) and 7,7,8,8-tetracyanoquinodimethane (TCNQ)*, Acta Crystallographica Section B **30**, 763 (1974). (cited in 2.4.1, 2.25.)

[71] A. Dolfen, *Massively parallel exact diagonalization of strongly correlated systems*, Master's thesis, Forschungszentrum Juelich, 2006. (cited in 2.4.3.1, 2.4.3.2, 2.4.3.2, E.)

[72] H. J. Schulz, *Interacting fermions in one dimension: from weak to strong correlation*, ArXiv Condensed Matter e-prints (1993), [arXiv:cond-mat/9302006]. (cited in 2.4.3.1.)

[73] T. Takahashi, *13C-NMR studies of charge ordering in organic conductors*, Synthetic Metals **133-134**, 261 (2003), Proceedings of the Yamada Conference LVI. The Fourth International. (cited in 2.5.)

[74] Y. Takano, K. Hiraki, H. M. Yamamoto, T. Nakamura and T. Takahashi, *Charge disproportionation in the organic conductor, [alpha]-(BEDT-TTF)2I3*, Journal of Physics and Chemistry of Solids **62**, 393 (2001). (cited in 2.5.)

[75] E. B. Yagubskii *et al.*, *Superconductivity at atmospheric pressure in the organic metal bis(ethylenedithiolo)tetrathiofulvalene triiodide ((BEDT-TTF)$_2$I$_3$)*, Pis'ma Zh. Eksp. Teor. Fiz. Pis'ma Zh. Eksp. Teor. Fiz. Pis'ma Zh. Eksp. Teor. Fiz. **39**, 12 (1984). (cited in 2.5.)

[76] H. Schwenk *et al.*, *New, organic, volume superconductor at ambient pressure*, Physical Review B **31** (1985). (cited in 2.5.)

[77] A. Nothardt *et al.*, *Investigations of quantum oscillations in* $\Theta-$ *and* Θ_T*-(BEDT-TTF)$_2$I$_3$*, Journal of Low Temperature Physics **142**, 539 (2006). (cited in 2.5.)

[78] T. Mori, *Structural Genealogy of BEDT-TTF-Based Organic Conductors I. Parallel Molecules: β and β″ Phases*, Bulletin of the Chemical Society of Japan **71**, 2509 (1998). (cited in 2.5.)

[79] T. Mori, H. Mori and S. Tanaka, *Structural Genealogy of BEDT-TTF-Based Organic Conductors II. Inclined Molecules: θ, α, and κ Phases*, Bulletin of the Chemical Society of Japan **72**, 179 (1999). (cited in 2.5.)

[80] T. Mori, *Structural Genealogy of BEDT-TTF-Based Organic Conductors III. Twisted Molecules: δ and αᵖrime; Phases*, Bulletin of the Chemical Society of Japan **72**, 2011 (1999). (cited in 2.5.)

[81] R. Shibaeva and E. Yagubskii, *Molecular Conductors and Superconductors Based on Trihalides of BEDT-TTF and Some of Its Analogues*, Chemical Reviews **104**, 5347 (2004). (cited in 2.5.)

[82] K. Brake, B. Powell, R. McKenzie, M. Pederson and T. Baruah, *First-principle density-functional calculation of the Raman spectra of BEDT-TTF*, J. Phys. IV France **114**, 293 (2004). (cited in 2.9, 2.5.1.1.)

[83] E. Demiralp and W. A. Goddard, *Ab Initio and Semiempirical Electronic Structural Studies on Bis(ethylenedithio)tetrathiafulvalene (BEDT-TTF or ET)*, Journal of Physical Chemistry **98**, 9781 (1994). (cited in 2.5.1.1.)

[84] B. Salameh *et al.*, *Electronic properties of the organic metals Θ-(BEDT-TTF)$_2$I$_3$ and Θ_T-(BEDT-TTF)$_2$I$_3$*, Phys. Rev. B **75**, 054509 (2007). (cited in 2.5.1.2, 2.5.2.1.)

[85] T. Mori, *Estimation of Off-Site Coulomb Integrals and Phase Diagrams of Charge Ordered States in the Θ-phase Organic Conductors.*, Bull. Chem. Soc. Jpn. **73**, 2243 (2000).

[86] T. Matsubara, *A New Approach to Quantum-Statistical Mechanics*, Progress of theoretical physics **14**, 351 (19551000). (cited in 3.1.1.)

[87] J. W. Negele and H. Orland, *Quantum Many-Particle Systems (Frontiers in Physics)* (Perseus Books, 1988). (cited in 3.1.2, 3.1.3.)

[88] A. Altland and B. Simons, *Concepts of Theoretical Solid State Physics*, 2001. (cited in 3.1.2.)

[89] A. A. Abrikosov, L. P. Gorkov and I. E. Dzyaloshinski, *Methods of Quantum Field Theory in Statistical Physics* (Dover Pubn Inc, 1975). (cited in 3.1.3.)

[90] A. L. Fetter and J. D. Walecka, *Quantum Theory Of Many-Particle Systems* (Dover Pubn, INC., 2003). (cited in 3.1.3.)

[91] P. Nozieres, *Theory of Interacting Fermi Systems (Advanced Book Classics)* (Perseus, 1997). (cited in 3.1.5.)

[92] E. S. Fradkin, *The green's function method in quantum statistics*, Nuclear Physics **12**, 465 (1959). (cited in 3.1.6.)

[93] D. Gorkov, Abrikosov, *On the application of Quantum field theory methods to problems of quantum statistics at finite temperature*, Sov. Phys. JETP **9**, 636 (1959). (cited in 3.1.6.)

[94] G. A. Baker, *Essentials of Padé Approximants* (Academic Press, New York, 1975). (cited in 3.1.9.1, 3.2.3.)

[95] H. J. Vidberg and J. W. Serene, *Solving the Eliashberg equations by means ofN-point Padéapproximants*, Journal of Low Temperature Physics **29**, 179 (1977). (cited in 3.1.9.1.)

[96] K. S. D. Beach, R. J. Gooding and F. Marsiglio, *Reliable Padé analytical continuation method based on a high-accuracy symbolic computation algorithm*, Phys. Rev. B **61**, 5147 (2000). (cited in 3.1.9.1.)

[97] A. Georges, G. Kotliar, W. Krauth and M. J. Rozenberg, *Dynamical mean-field theory of strongly correlated fermion systems and the limit of infinite dimensions*, Rev. Mod. Phys. **68**, 13 (1996). (cited in 3.2, 3.2.5.2, 3.3.1, 3.)

[98] T. Pruschke, M. Jarrell and J. K. Freericks, *Anomalous normal-state properties of high-Tc superconductors: intrinsic properties of strongly correlated electron systems?*, Advances in Physics **44**, 187 (1995). (cited in 3.2.)

[99] P. Weiss, *L'hypothèse du champ moléculaire et la propriété ferromagnétique*, J. de Phys **6**, 661 (1907). (cited in 3.2.1.)

[100] R. Brout, *Statistical Mechanical Theory of Ferromagnetism. High Density Behavior*, Phys. Rev. **118**, 1009 (1960). (cited in 3.2.1.)

[101] W. Metzner and D. Vollhardt, *Correlated Lattice Fermions in $d = \infty$ Dimensions*, Phys. Rev. Lett. **62**, 324 (1989). (cited in 3.2.1.)

[102] E. Müller-Hartmann, *Correlated fermions on a lattice in high dimensions*, Zeitschrift für Physik B Condensed Matter **74**, 507 (1989). (cited in 3.2.1, 3.3.1.)

[103] A. Georges and G. Kotliar, *Hubbard model in infinite dimensions*, Phys. Rev. B **45**, 6479 (1992). (cited in 3.2.1.)

[104] V. Janiš and D. Vollhardt, *Comprehensive Mean Field Theory For The Hubbard Model*, International Journal of Modern Physics B **6**, 731 (1992). (cited in 3.2.1.)

[105] M. Jarrell, *Hubbard model in infinite dimensions: A quantum Monte Carlo study*, Phys. Rev. Lett. **69**, 168 (1992). (cited in 3.2.1, 3.3, 3.3.1.)

[106] S. R. White, *Density matrix formulation for quantum renormalization groups*, Phys. Rev. Lett. **69**, 2863 (1992). (cited in 3.2.2.)

[107] U. Schollwöck, *The density-matrix renormalization group*, Rev. Mod. Phys. **77**, 259 (2005). (cited in 3.2.2.)

[108] K. G. Wilson, *The renormalization group: Critical phenomena and the Kondo problem*, Rev. Mod. Phys. **47**, 773 (1975). (cited in 3.2.2.)

[109] E. Koch, G. Sangiovanni and O. Gunnarsson, *Sum rules and bath parametrization for quantum cluster theories*, Phys. Rev. B **78**, 115102 (2008). (cited in 3.2.3.)

[110] H. S. Wall, *Analytic theory of continued fractions* (Chelsea Publishing Co., 1948). (cited in 3.2.3.)

[111] W. B. Jones and W. J. Thron, *Continued Fractions: Analytic Theory and Applications*, Encyclopedia of Mathematics and its Applications Vol. 11 (Addison-Wesley Publishing Company, 1984). (cited in 3.2.3.)

[112] U. Brandt and C. Mielsch, *Thermodynamics and correlation functions of the Falicov-Kimball model in large dimensions*, Zeitschrift für Physik B Condensed Matter **75**, 365 (1989). (cited in 3.3, 3.3.1.)

[113] V. Zlatic and B. Horvatic, *The local approximation for correlated systems on high dimensional lattices*, Solid State Communications **75**, 263 (1990). (cited in 3.3, 3.3.1, 3.3.1.)

[114] T. Pruschke, D. L. Cox and M. Jarrell, *Transport Properties of the Infinite-Dimensional Hubbard Model*, EPL (Europhysics Letters) **21**, 593 (1993). (cited in 3.3.)

[115] T. Pruschke, D. L. Cox and M. Jarrell, *Hubbard model at infinite dimensions: Thermodynamic and transport properties*, Phys. Rev. B **47**, 3553 (1993). (cited in 3.3.)

[116] H. Hafermann *et al.*, *Superperturbation solver for quantum impurity models*, EPL (Europhysics Letters) **85**, 27007 (6pp) (2009). (cited in 3.3.2.)

[117] A. Toschi, A. A. Katanin and K. Held, *Dynamical vertex approximation: A step beyond dynamical mean-field theory*, Physical Review B (Condensed Matter and Materials Physics) **75**, 045118 (2007). (cited in 3.3.2.)

[118] H. J. Monkhorst and J. D. Pack, *Special points for Brillouin-zone integrations*, Phys. Rev. B **13**, 5188 (1976). (cited in 3.3.4.)

[119] A. Y. Toukmaji and J. A. Board, *Ewald summation techniques in perspective: a survey*, Computer Phys. Comm. **95**, 73 (1996). (cited in A.)

[120] F. Bertaut, *L'énergie électrostatique de réseaux ioniques*, J. Phys. Radium **13**, 499 (1952). (cited in A.1.)

[121] A. Aharony and M. E. Fisher, *Critical Behavior of Magnets with Dipolar Interactions. I. Renormalization Group near Four Dimensions*, Phys. Rev. B **8**, 3323 (1973). (cited in A.2.)

[122] M. H. Cohen and F. Keffer, *Dipolar Sums in the Primitive Cubic Lattices*, Phys. Rev. **99**, 1128 (1955). (cited in A.2.)

[123] G. J. Bowden and R. G. Clark, *Fourier transforms of dipole-dipole interactions using Ewald's method*, Journal of Physics C: Solid State Physics **14**, L827 (1981). (cited in A.2.)

[124] M. Tinkham, *Group Theory and Quantum Mechanics* (McGraw-Hill, 1975). (cited in B.1.)

[125] T. E. Oliphant, *Python for Scientific Computing*, Computing in Science & Engineering **9**, 10 (2007). (cited in 29.)

[126] A. Dolfen, E. Pavarini and E. Koch, *New Horizons for the Realistic Description of Materials with Strong Correlations*, Inside **1** (2006), http://inside.hlrs.de/htm/Edition_01_06/article_05.htm. (cited in E.)

[127] W. H. Press, S. A. Teukolsky and W. T. Vetterling *Numerical Recipes 3rd Edition: The Art of Scientific Computing*, Vol. 3, (Cambridge University Press, 2007). (cited in G.)

[128] A. Dolfen and E. Koch, *Electronic Correlations*, in *41. IFF Springschool - Correlation Phenomena, Exotic Phases and Novel Functionalities*, edited by R. W. C. S. Stefan Blügel, Thomas Brückel Vol. 13, Forschungszentrum Jülich GmbH, Institut für Festkörperforschung, 2010. (cited in G.)

Acknowledgements

Thanks to the assistance of many helping brains and hands it is finally accomplished.

First and foremost I would like to thank my supervisor Prof. Dr. Erik Koch for introducing me to the fascinating world of strongly correlated systems, for his patience when answering my innumerable questions, his continuing support, constructive comments and suggestions, and for opening up many opportunities. Without you this work would not have been possible.

I would also like to thank Prof. Dr. Eva Pavarini for being the second referee of this thesis and for many helpful comments.

Next, I would like to express my gratitude to my hosts at the Fritz-Haber Institute in Berlin, Prof. Dr. Karsten Reuter and, in particular, Dr. Volker Blum, for getting me started with FHI-aims development and answering all the many DFT and FHI-aims related questions.

I am also grateful to Prof. Dr. Gabriel Kotliar, Rutgers University, USA, for his hospitality, for fruitful discussions, and helping me with all the necessary organizational details. I thank Dr. Cedric Weber, Dr. Alberto Camjayi, Park Hyowon, and Kim Kyoo for their help and enlightening discussions. I would also like to thank ICAM that made this research stay possible.

I am especially grateful to the strenuous proofreaders: Sebastian Reuschel, Swantje Heers, Dr. Binh Trieu, Dr. David Heilmann, Andreas Gierlich, Andreas Flesch, and those who prefer not to be named.

Special thanks go to *the* "office team", Swantje Heers, Andreas Gierlich, and Manfred Niesert for encouragements, their deep and sincere friendship, that extended far beyond our professional lives. I would also like to thank my more recent office-mates Martin Schlipf and Clemens Adolphs for their help with all the small things. Thanks also to all the fellow PhD and diploma students for the many interesting, inspiring, and pleasant conversations as well as the board-gaming events and soccer games.

I further appreciate the discussions with all present and past members of the IFF theory department, in particular Dr. Clemens Gugenberger, Dr. Christoph Friedrich, and all

other people that are too many to mention here. Special thanks also go to Ute Winkler, the soul of the theory I department, for her organizational support.

I also like to thank the Many-Core Group, formerly known as the Cell Group, at the JSC, in particular, Willi Homberg and Inge Gutheil for the interesting discussions concerning Cell and computing in general.

Finally, I would also like to thank Prof. Dr. Stefan Blügel and the Institut für Festkörperforschung, that funded the first part of my work, and the German Research School for Simulation Sciences for the second part.